Microscopic Visualization of Alamethicin Incorporation into Model Membrane Monolayers

Roman Volinsky,[†,‡] Sofiya Kolusheva,[†,‡] Amir Berman,*[,†,§] and Raz Jelinek*[,†,‡]

Ilse Katz Center for Nano- and Mesoscience and Technology, Department of Chemistry, and Department of Biotechnology Engineering, Ben Gurion University of the Negev, Beer-Sheva 84105, Israel

Received September 8, 2004

Lipid interactions and cooperative assembly properties are fundamental determinants for the action of antimicrobial membrane-active peptides. Here we analyze the interactions and aggregation properties of alamethicin, an antimicrobial pore-forming peptide, with films formed at the air/water interface. Surface-area/pressure isotherms, Brewster angle microscopy, and fluorescence-confocal microscopy provided detailed information on the morphologies and structural properties of the peptide and its effect on the film components. The pressure−area analysis and microscopy experiments facilitated unprecedented visualization of the structural consequences of alamethicin association at the air/water interface, with pure phospholipid films, and within mixed phospholipid/polydiacetylene (PDA) films. The analysis exposed the kinetic features and the interplay between the peptide aggregates and film constituents. In particular, the results demonstrate the use of phospholipid/PDA film assemblies for studying membrane−peptide association and interactions within two-dimensional films.

Introduction

The biological activities of antimicrobial membrane-active peptides are determined to a large part by their interactions with the phospholipid bilayer comprising the plasma membrane and the mutual structural effects induced within the peptide and lipid molecules.[1,2] Indeed, the amphipathic nature of many antimicrobial peptides, which are short, mostly helical sequences, generally dictate a high affinity to lipid assemblies. Furthermore, numerous studies have shown that membrane environments significantly affect the structural properties and functionality of membrane-active peptides.[3,4] Thus, elucidating the dynamical and structural characteristics of antimicrobial peptide incorporation within lipid assemblies is highly important for understanding their mechanisms of action and biological effects.

We present a microscopic analysis of the association and interactions of alamethicin with lipid-containing films formed at the air/water interface. Alamethicin is a 20-amino acid antimicrobial peptide, produced by the fungus *Trichoderma viride*.[5] The peptide exhibits a very high affinity to phospholipid bilayers and exhibits a-helical structure in hydrophobic environments.[6,7] The overall amphipathic character of alamethicin is due to the distribution of polar and nonpolar amino acid residues between the lateral sides of the helix. The peptide has been studied using varied model membranes and is believed to form voltage-gated ion channels in lipid membranes according to the "barrel-stave" model.[8−11] Previous studies have also employed Langmuir monolayers for analysis of alamethicin association with lipid assemblies.[12−14] Pore formation processes induced by alamethicin were recently investigated in a two-dimensional phospholipid/water interface.[15,16]

Here we report on the analysis of interactions and association properties of alamethicin within different films at the air/water interface by surface pressure−area isotherms[15,16] and through application of advanced microscopy techniques, specifically Brewster angle microscopy[17−20] and confocal fluorescence microscopy.[15,21−23] In particular, we have explored the insertion of alamethicin into phospholipid/polydiacetylene (PDA) two-dimensional assemblies. Polymerized diacetylenic lipids, first synthesized by Wegner in 1969,[24] exhibit unique chromatic properties, specifically the occurrence of blue-to-red irreversible color transitions that can be induced by external

* To whom correspondence should be addressed: e-mail razj@bgumail.bgu.ac.il (R.J.); aberman@bgumail.bgu.ac.il (A.B.).
† Ilse Katz Center for Nano- and Mesoscience and Technology, Ben Gurion University of the Negev.
‡ Department of Chemistry, Ben Gurion University of the Negev.
§ Department of Biotechnology Engineering, Ben Gurion University of the Negev.

(1) Shai, Y. *Biochim. Biophys. Acta* **1999**, *1462*, 55−70.
(2) Kessel, A.; Ben-Tal, N. *Curr. Top. Membr.* **2002**, *52*, 205−253.
(3) Hancock, R. E. W.; Diamond, G. *Trends Microbiol.* **2000**, *8* (9), 402−410.
(4) Blondelle, S. E.; Lohner, K.; Aguilar, M.-I. *Biochim. Biophys. Acta* **1999**, *1462*, 89−108.
(5) Meyer, P.; Reusser, F. *Experimentia* **1967**, *23*, 85−86.
(6) Banerjee, U.; Chan, S. I. *Biochemistry* **1983**, *22*, 3709.
(7) North, C. L.; Barranger-Mathys, M.; Cafiso, D. S. *Biophys. J.* **1995**, *69*, 2392−2397.
(8) Hall, J. E.; Vodyanov, I.; Balasubramanian, T. M.; Marshall, G. R. *Biophys. J.* **1984**, *45*, 233−247.
(9) Sansom, M. S. *Q. Rev. Biophys.* **1993**, *26*, 365−421.
(10) Ojcius, D. M.; Young, J. D. *Trends Biochem. Sci.* **1991**, *16*, 225−229.
(11) Yang, L.; Harroun, T. A.; Weiss, T. M.; Ding, L.; Huang, H. W. *Biophys. J.* **2001**, *81*, 1475−1485.
(12) Doty, P.; Shulman, J. H. *Discuss. Faraday Soc.* **1949**, *6*, 21−27.
(13) Colacicco, G. *J. Colloid Interface Sci.* **1969**, *29*, 345−364.
(14) Brockman, H. *Curr. Opin. Struct. Biol.* **1999**, *9*, 438−443.
(15) Ionov, R.; El-Abed, A.; Angelova, A.; Goldmann, M.; Peretti, P. *Biophys. J.* **2000**, *78* (June), 3026−3035.
(16) Ionov, R.; El-Abed, A.; Goldmann, M.; Peretti, P. *J. Phys. Chem. B* **2004**, *108*, 8485−8488.
(17) Honig, D.; Mobius, D. *J. Phys. Chem.* **1991**, *95* (12), 4590−4592.
(18) Henon, S.; Meunier, J. *Rev. Sci. Instrum.* **1991**, *64* (4), 936−939.
(19) Lipp, M. M.; Lee, K. Y. C.; Zasadzinski, J. A.; Waring, A. J. *Rev. Sci. Instrum.* **1997**, *68* (6), 2574−2582.
(20) Frey, W.; William, R.; Schief, J.; Vogel, V. *Langmuir* **1996**, *12*, 1312−1320.
(21) McConlogue, C. W.; Vanderlick, T. K. *Langmuir* **1997**, *13* (26), 7158−7164.
(22) Uwaha, M.; Saito, Y. *Phys. Rev. A* **1989**, *40*, 4716.
(23) Lipp, M. M.; Lee, K. Y. C.; Takamoto, D. Y.; Zasadzinski, J. A.; Waring, A. J. *Phys. Rev. Lett.* **1998**, *81* (8), 1650−1653.
(24) Wegner, G. *Z. Naturforsch., B: Chem. Sci.* **1969**, *24*, 824.

10.1021/la0477486 CCC: $27.50
Published on Web 11/03/2004

parameters such as temperature,[25] pH change,[26,27] lateral friction, interfacial pressure,[28,29] and others. PDA assemblies further possess intriguing fluorescence profiles; the blue PDA phase is weakly fluorescent while the red phase of the polymer strongly fluoresces at around 560 and 650 nm (excitation at 488 nm).[30]

Vesicles composed of phospholipids and PDA have recently attracted interest as colorimetric sensors for studying a variety of membrane processes, such as peptide−membrane interactions,[31,32] ion transport,[33] antibody−epitope recognition,[34] and others.[35,36] These studies indicated that the phospholipid/PDA surface could serve as a model platform for studying biological membrane processes in vitro. While most recent studies have focused on mixed vesicular aggregates of phospholipids and PDA, two-dimensional assemblies of these molecular components might represent promising avenues as platforms for studying membrane events, because they allow application of advanced spectroscopic and microscopic characterization. Recently, we have reported on a study of the organization and chromatic properties of mixed Langmuir films composed of phospholipids and PDA.[37,38] In the present study we assess for the first time the insertion, interactions, and chromatic effects of biological compounds reacting directly with phospholipid/PDA films.

The experiments reported here reveal the characteristics of alamethicin association and aggregation within lipid films. The investigation demonstrates the formation of microscopic peptide domains within varied film environments at the air/water interface and examines the effects of the inserted peptides upon the film components and film properties. This work also shows that two-dimensional film assemblies containing PDA could provide important information on the cooperative properties of membrane-active peptides and might constitute the basis for varied biosensor applications.

Materials and Methods

Materials. 10,12-Tricosadiynoic acid (TRCDA) was purchased from GFS Chemicals (Powell, OH) and purified by dissolving the powder in chloroform, filtrating the resulting solution through a 0.45-μm nylon filter, and evaporation of the solvent. Dimyristoylphosphatidylcholine (DMPC; Avanti Polar Lipids, Alabaster, AL) was used as received. Mixed DMPC/diacetylene films were formed by dissolving DMPC and TRCDA (1:9 mole ratio) in chloroform at a total concentration of 2 mM.

The fluorescent probe, *N*-(7-nitrobenz-2-oxa-1,3-diazol-4-yl)-1,2-dihexadecanoyl-*sn*-glycero-3-phosphoethanolamine, triethylammonium salt (NBD-PE) in HPLC-grade purity was purchased from Molecular Probes, Inc. (Eugene, OR, U.S.A.) and was used as received. For making mixed NBD-PE/DMPC/diacetylene films, NBD-PE was dissolved in chloroform to a concentration of 0.5 mM and was added to the DMPC/TRCDA solution to a final concentration of 2 mol %.

Alamethicin was purchased from Sigma and was dissolved in ethanol at a concentration of 1.5 mg/mL. All solvents were HPLC-grade pure.

Doubly purified water (18.3 mΩ resistivity; Barnstead D7382 water purification system (Barnstead Thermolyne Corp., Dubuque, IA, U.S.A.) was used as the subphase in all experiments.

Surface Pressure−Area Isotherms. All surface pressure−area isotherms were measured with a computerized Langmuir trough (NIMA model 611, Nima Technology, Ltd., Coventry, U.K.). The experiments were carried out at 25 °C using a thermostated Teflon film balance (7 × 50 cm^2). The surface pressure was monitored using 1-cm-wide filter paper as a Wilhelmy plate. For each isotherm experiment, total of 70 nmol of the lipid mixture or 8.2 nmol of alamethicin were spread on the water subphase (pH = 6.3). The film was allowed to equilibrate for 15 min after spreading. Compression was conducted at a constant barrier speed of 5 cm^2 min^{-1}. The surface pressure measurements were repeated at least three times, using a fresh mixture in each experiment. The isotherms shown in the figures represent three experimental runs, which were reproducible within ±3 Å^2·molecule^{-1}.

Adsorption of Alamethicin from Solution at the Air/Water and Lipid/Water Interfaces. Adsorption experiments were carried out at 25 °C using a Nima 611 Teflon trough. Aliquots from the peptide solution were injected into the gently stirred water subphase, using only the dipping well (total volume of 50 cm^3) through a short vertical tube, yielding different initial protein concentrations used in the experiments. The adsorption isotherms ($\Delta\pi$−time) of alamethicin at constant air/water interfaces area were monitored using the Wilhelmy plate. The error in the measurements was ±0.5 mN m^{-1}.

In the experiments where alamethicin penetration into lipid films was examined, the chloroform lipid solution was spread over the clean air/water interface and allowed to equilibrate for 20 min, reaching the desired initial surface pressure (π_i). Alamethicin (dissolved in ethanol) was then injected close to the magnet stirrer, approximately 2 cm beneath the lipid monolayer. In the case of peptide insertion into the DMPC/PDA films, initial compression of the film to 16 mN/m was carried out followed by polymerization of diacetylene by irradiation at 254 nm for 15 s using a Pen-Ray ultraviolet source 5 cm above the film surface. The water subphase underneath the film was separated from the subphase outside the film by insertion of specially made Teflon motionless barriers that go to the trough bottom, thus, constructing an isolated chamber. The appropriate amounts of peptide in buffer (pH = 7.4) were then injected into the subphase.

Preparation of Substrates for Film Deposition. Glass slides were dipped in a cleaning (piranha) solution consisting of 70 mL of H_2SO_4 and 30 mL of H_2O_2 for 30 min at 70 °C, followed by sonication in the same solution for 10 min, rinsed thoroughly with pure water, and dried at 70 °C. Self-assembly of hydrophobic monolayers on the surface was carried out by immersion of the glass slide in 3.00 μL/mL OTS in a cyclohexane solution for 12 h. Glass slides were then rinsed with cyclohexane to remove noncovalently bound OTS. In the fluorescence and UV−visible spectroscopy experiments, samples were prepared by transferring the polymerized DMPC/PDA films to the glass slides using the Langmuir−Schaefer method (horizontal touch method).[39,40] Spectra were acquired following exposure of the slides to a buffered solution (pH = 7.4) containing the appropriate alamethicin concentrations.

Brewster Angle Microscopy. A Brewster angle microscope (BAM; NFT Co., Göttingen, Germany) mounted on a Langmuir film balance was used for in situ analysis of the films. The light source of the BAM was a frequency-doubled Nd:YAG laser with a wavelength of 532 nm and 20−70-mW primary output power in a collimated beam. The BAM images were recorded with a

(25) Wenzel, M.; Atkinson, G. H. *J. Am. Chem. Soc.* **1989**, *111* (16), 6123−6127.
(26) Chance, R. R. *Macromolecules* **1980**, *13*, 386.
(27) Cheng, Q.; Stevens, R. C. *Langmuir* **1998**, *14* (8), 1974−1976.
(28) Tomioka, Y.; Tanaka, N.; Imazeki, S. *J. Chem. Phys.* **1989**, *91*, 5694−5700.
(29) Rubner, M. F. *Macromolecules* **1986**, *19* (8), 2129−2138.
(30) Kobayashi, T.; Yasuda, M.; Okada, S.; Matsuda, H.; Nakanishi, H. *Chem. Phys. Lett.* **1997**, *267*, 472−480.
(31) Kolusheva, S.; Boyer, L.; Jelinek, R. *Nat. Biotechnol.* **2000**, *18* (February), 225−227.
(32) Wang, S.; Leblanc, R. M. *Biochem. Biophys. Acta* **1999**, *1419*, 307−312.
(33) Kolusheva, S.; Shahal, T.; Jelinek, R. *J. Am. Chem. Soc.* **2000**, *122* (5), 776−780.
(34) Kolusheva, S.; Kafri, R.; Katz, M.; Jelinek, R. *J. Am. Chem. Soc.* **2001**, *123* (3), 417−422.
(35) Evrard, D.; Touitou, E.; Kolusheva, S.; Fishov, Y.; Jelinek, R. *Pharm. Res.* **2001**, *18* (7), 943−949.
(36) Jelinek, R.; Kolusheva, S. *Biotechnol. Adv.* **2001**, *19* (2), 109−118.
(37) Gaboriaud, F.; Golan, R.; Volinsky, R.; Berman, A.; Jelinek, R. *Langmuir* **2001**, *17* (12), 3651−3657.
(38) Volinsky, R.; Gaboriaud, F.; Berman, A.; Jelinek, R. *J. Phys. Chem. B* **2002**, *106*, 9231−9236.
(39) Gaines, G. L., Jr. *Insoluble Monolayers at Liquid-Gas Interfaces*; Wiley-Interscience: New York, 1966.
(40) Tscharner, V.; McConell, H. M. *Biophys. J.* **1981**, *36*, 421−427.

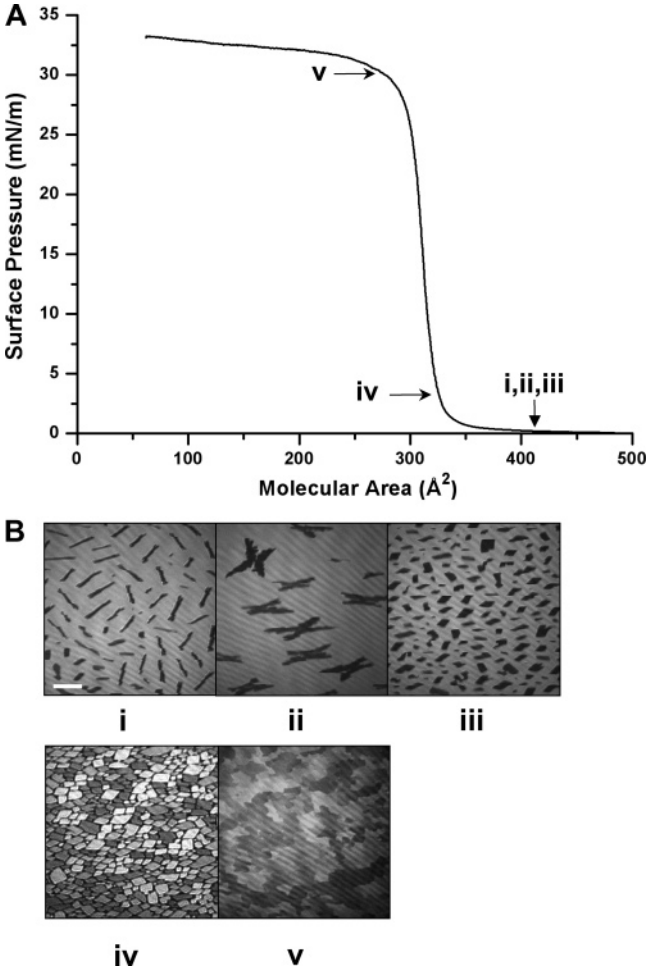

Figure 1. (A) Surface pressure−area isotherm of an alamethicin monolayer, recorded at 25 °C. (B) BAM images recorded at the indicated points within the isotherm. The bar represents 50 μm.

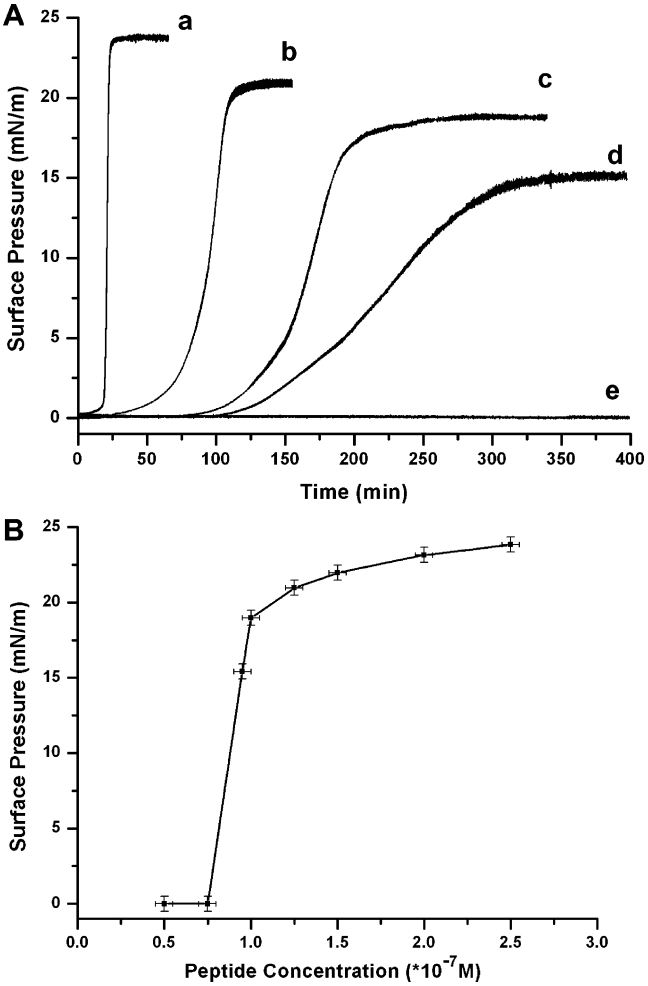

Figure 2. (A) Adsorption isotherms (surface pressure versus time) of alamethicin at the air−water interface, obtained for different peptide subphase concentrations: (a) 2.5×10^{-7}, (b) 1.25×10^{-7}, (c) 1.0×10^{-7}, (d) 9.5×10^{-8}, and (e) 7.5×10^{-8} M. (B) Maximal surface pressures (plateau values) π recorded for different alamethicin subphase concentrations.

charge-coupled device camera. The scanner objective was a Nikon superlong working distance objective with a nominal 10× magnification and was diffraction limited, with a lateral resolution of 2 μm. The images were corrected to eliminate ratio image distortion, originating from the nonperpendicular line of vision of the microscope.

Fluorescence Microscopy. Fluorescence images were acquired with an oil objective PlApo x 60 (N.A. = 1.4) on an Olympus IX70 microscope (Japan) connected to a FV500 (Fluoview) laser scanning confocal microscope. Excitation was performed using an argon laser at 488 nm. Emitted light was collected through a BA 520−550-nm filter (for observing mainly NBD-PE fluorescence) and BA 660IF (observing the PDA fluorescence).

UV−Vis Spectroscopy. Spectroscopic analyses of glass-slide-supported DMPC/PDA films were carried out using a Jasco V-550 UV−vis spectrophotometer (JASCO Corp., Tokyo, Japan). The spectral range was between 400 and 700 nm.

Fluorescence Spectroscopy. Fluorescence spectra of the glass-supported DMPC/PDA films were acquired using an FL920 spectrometer (Edinburgh Instruments, Scotland, U.K.). Excitation was at 480 nm, and the emission range was 530−700 nm.

Results

1. Alamethicin at the Air/Water Interface. To characterize alamethicin properties at the air/water interface and the structural features of the peptide in film environments, we initially examined the interfacial behavior of the peptide in the pure water subphase (Figures 1 and 2). Figure 1A depicts the surface pressure−area isotherm of alamethicin deposited at the air−water interface at 25 °C. The compression isotherm exhibits the expected threshold at a molecular area of approximately 320 Å^2 corresponding to the projected area of an alamethicin α-helix oriented parallel to the water surface.[15,16] The steep rise of the isotherm was followed by a plateau region at π = 33 mN/m (Figure 1A), indicating that in higher surface pressures the peptide monolayer collapsed and formed multilayers rather than reoriented into vertical helical positions.[15,16]

Remarkable microscopic features of the alamethicin assemblies at the air/water interface could be observed in BAM experiments, Figure 1B. The BAM pictures were recorded in situ on the Langmuir trough at different molecular areas (indicated with arrows on the isotherm in Figure 1A). Specifically, images i−iii were acquired at approximately zero surface pressure prior to the pressure offset in Figure 1A and picture iv was recorded during the initial stage of the steep rise in pressure, while image v (Figure 1B) was taken right after initiation of the monolayer collapse at a surface pressure of approximately 30 mN/m. The dark patches apparent in the BAM images in Figure 1B(i−iii) correspond to two-dimensional alamethicin aggregates. The representation in Figure 1B of *darker* surface domains of alamethicin within a *brighter background* (corresponding to the water subphase) is due to the low reflectance of the alamethicin domains on the water surface, particularly at low surface pressures, making them almost visually indistinguishable using

regular BAM imaging conditions. Accordingly, to improve visibility and contrast in the images, the polarizer position was set to enhance reflectance from the *water* surface, resulting in the appearance of the darker alamethicin domains (Figure 1B).

The images in Figure 1B(i−iii) show that distinct peptide domains appear at the air/water interface even at zero surface pressure, indicating that the alamethicin aggregates are well below the liquid-expanded/liquid-condensed transition temperature for air−water interface monolayers. The appearance of long rodlike structures (i), "butterfly" shapes (ii), and irregular rectangles (iii) was reproducible, and, furthermore, these structures coexisted in the *same* film. The different condensed domains are most likely related to nonequilibrium (e.g., kinetic) aggregation of the highly amphiphilic peptide.[41,42] The intriguing BAM image recorded close to the molecular area threshold of 320 Å^2 [Figure 1B(iv)] indicates the onset of physical contact and interactions among the alamethicin domains. The different tones of the individual domains in Figure 1B(iv) are due to the distinct orientations of the peptide aggregates, consistent with ordering of the helical peptides parallel to the water surface.[15,16] After the rapid increase in surface pressure, the water surface became a mixture of interconnected dark and bright peptide domains [Figure 1B(v)].

We have further characterized the kinetic profiles of alamethicin aggregation and film formation on an aqueous subphase at different alamathicin concentrations (Gibbs monolayers; Figure 2). Figure 2A depicts the time dependence of the surface pressure buildup isotherms (also denoted "adsorption isotherms") of alamethicin at the air−water interface following injection of the peptide into the water subphase. The gradual increase in pressure over time observed in the sigmoidal curves in Figure 2A,a−d corresponds to the time needed for peptide diffusion and association and migration of peptide aggregates to the water surface. In particular, the variable lag periods before the initiation of pressure increase most likely correspond to the duration required for the injected peptides to reach the threshold surface concentration inducing a detectable surface pressure.[43] This interpretation is consistent with the absence of the surface pressure increase when the alamethicin concentration in the water subphase was too low (5.0×10^{-8} M, curve e in Figure 2A). At this concentration there are minimal interactions between the alamethicin domains formed at the air/water interface, suggesting that full surface coverage is not yet reached.

The relationship between peptide concentrations and the maximal surface pressures measured at the plateaus, shown in Figure 2B, confirm the existence of a concentration threshold at approximately 7.5×10^{-8} M below which no surface pressure increase could be detected. The existence of a concentration/pressure threshold again reflects the minimal concentration of alamethicin in the water subphase that facilitates peptide aggregate formation, diffusion to the air/water interface, and sufficiently significant interactions among the peptide domains.[44−46]

2. Alamethicin Interactions with DMPC Monolayers. The interactions of antimicrobial peptides such as alamethicin with lipid assemblies in membranes are critical parameters for their biological activities. Figure 3 depicts the kinetic and structural analyses of alamethicin incorporation into phospholipid monolayers deposited at the air/water interface. Figure 3A shows the adsorption isotherms recorded after injection of alamethicin into the water subphase underneath the DMPC monolayers compressed to different (initial) surface pressures. Importantly, the peptide concentration used in the experiments depicted in Figure 3A was 5.0×10^{-8} M, a concentration for which *no increase* in surface pressure was observed in water (Figure 3A, curve a). Thus, the increase in surface pressure over time observed in Figure 3A, curves b−d,

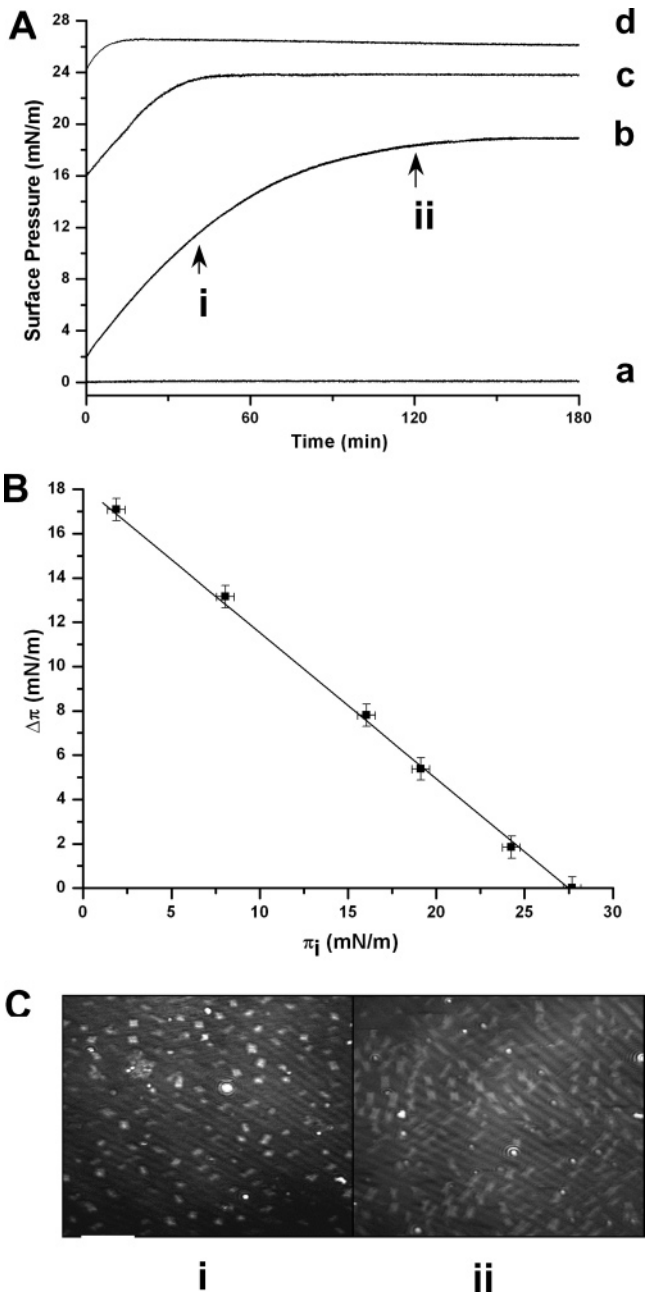

Figure 3. (A) Adsorption isotherms (surface pressure versus time) of alamethicin in DMPC monolayers at different initial surface pressures π_i; (B) graph correlating $\Delta\pi$, the difference between the maximal increase in surface pressure and the initial pressure of the DMPC monolayer after injection of alamethicin into the water subphase (5.0×10^{-8} M subphase concentration), as a function of initial pressure of the DMPC monolayer π_i; (C) BAM images recorded at the indicated points within the adsorption isotherm. The bar represents 50 μm.

(41) Vollhardt, D. *Colloids Surf., A* **1998**, *143*, 185−195.
(42) Vollhardt, D. *Mater. Sci. Eng., C* **2002**, *22*, 121−127.
(43) Sun, Y.; Wang, S.; Sui, S. *Colloid Surf., A* **2000**, *175*, 105−112.
(44) Maget-Dana, R.; Brack, A. *Biopolymers* **1999**, *49*, 415−423.
(45) Baumruk, V.; Huo, D.; Dukor, R. K.; Keiderling, T. A.; Lelievre, D.; Brack, A. *Biopolymers* **1994**, *34* (8), 1115−1121.
(46) Javadpour, M. M.; Barkley, M. D. *Biochemistry* **1997**, *36* (31), 9540−9549.

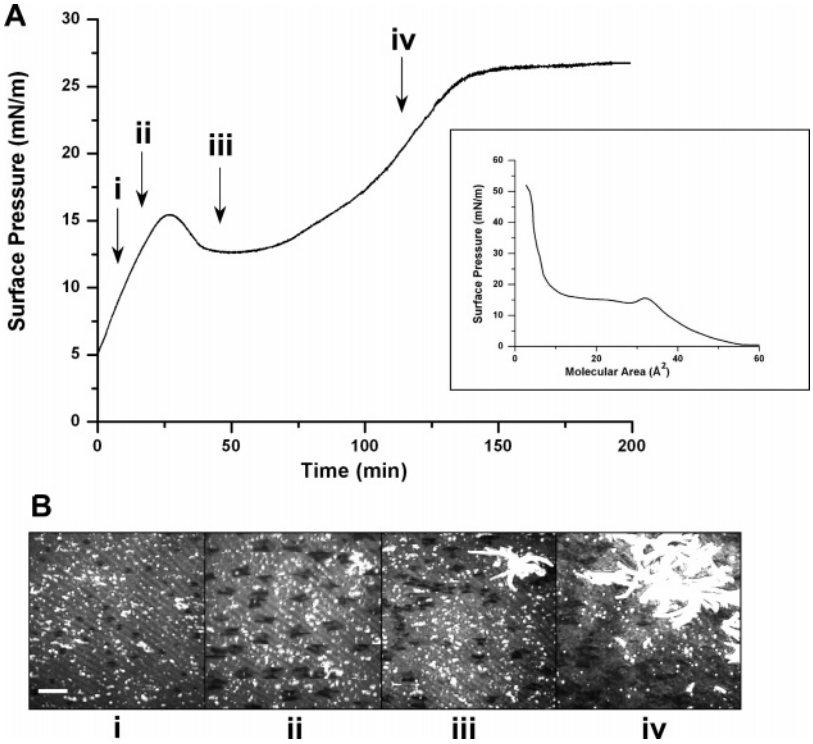

Figure 4. (A) Adsorption isotherm (surface pressure versus time) for alamethicin onto the DMPC/diacetylene film (1:9 mole ratio). The inset shows the surface area−pressure isotherm of the DMPC/diacetylene film at the same mole ratio. (B) BAM images recorded at the indicated points within the adsorption isotherm. The bar represents 50 μm.

were specifically due to insertion of alamethicin into the phospholipid monolayers.[47]

The adsorption isotherms in Figure 3A display other important differences compared to the profiles recorded in pure water (Figure 2A). Specifically, no lag times prior to pressure increase were observed after injection of the peptide into the water subphase, most likely because of the high affinity of alamethicin to the phospholipid monolayers. In addition, the *extent* of the overall pressure increase (i.e., difference between the initial pressure and final equilibrium pressure) following alamethicin insertion into the lipid film clearly depended upon the initial pressure of the phospholipid monolayer. Figure 3B depicts the linear dependence of the difference between equilibrium pressure and initial pressure ($\Delta\pi$) and the initial film pressure (π_i). The intersection of the straight line in Figure 2B to the x (π_i) axis yields the exclusion pressure $\pi_{ex} \approx 27.5$ mN/m in which the peptide no longer penetrated into the DMPC monolayer. This value is in agreement with the surface pressure in which the alamethicin film collapse was observed (Figure 1A) and indicates that the alamethicin domains are essentially immiscible within the phospholipid monolayers.

We have further analyzed the structural features of alamethicin inserted into the phospholipid monolayers by BAM, which further illustrates the immiscibility of the alamethicin aggregates within the phospholipid film (Figure 3C). Figure 3C shows BAM images recorded at two different pressures in the same film that was initially compressed to 2 mN/m (indicated by the arrows in Figure 3A). The images were obtained 30 and 120 min, respectively, after injection of the peptide into the water subphase. The BAM pictures in Figure 3C indicate that the alamethicin microdomains that appeared within the phospholipid monolayer were different both in size and shape compared to the corresponding alamethicin aggregates observed in pure water (Figure 1B). Specifically, very small peptide patches approximately 10 μm in size were detected at the lower surface pressure [Figure 3C-(i)], while slightly bigger and elongated aggregates were observed at the higher pressure [Figure 3C(ii)]. The appearance of significantly smaller peptide domains in Figure 3C demonstrates the considerable structural effect of the phospholipid monolayer on peptide aggregates at the air/water interface. This result is probably also related to the higher affinity of alamethicin to the phospholipid film apparent in Figure 3A.

3. Alamethicin Interactions with Phospholipid/Diacetylene Films. To obtain a systematic overview on alamethicin aggregation properties and microstructures within lipophilic environments, we investigated the interaction and insertion of the peptide into mixed films of DMPC and diacetylene. The benefits of employing phospholipid/diacetylene films for studying peptide interactions stem from the unique chromatic properties of polymerized diacetylene (PDA).[24] In particular, the colorimetric (blue-red) and fluorescence transitions induced in phospholipid/PDA vesicle assemblies by membrane-active peptides[31,32] point to the potential use of PDA-containing films as biosensors for detection and analysis of peptide−membrane interactions. Previous studies have characterized the organization and thermodynamic properties of two-dimensional phospholipid/diacetylene arrays.[37,38]

Figure 4A depicts the adsorption isothem of alamethicin injected into the water subphase (concentration of 1.0×10^{-7} M) underneath a DMPC/diacetylene monolayer (1:9 mole ratio). The initial surface pressure of the monolayer at the time of peptide injection was 5 mN/m. Figure 4A shows that the surface pressure immediately increased as a result of peptide adsorption into the monolayer, similar to the situation observed for a pure DMPC film (Figure 3A). However, at the approximate pressure 15

(47) Maget-Dana, R. *Biochem. Biophys. Acta* **1999**, *1462*, 109−140.

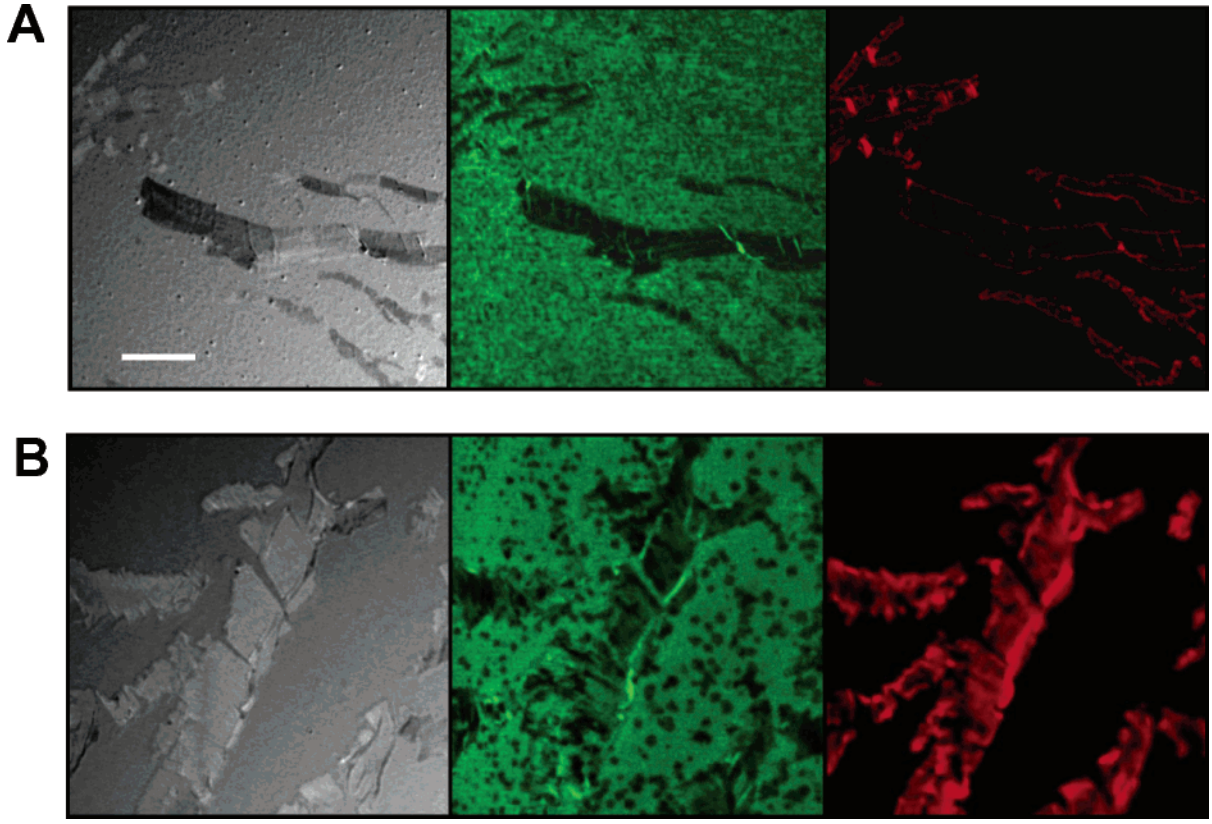

Figure 5. (A) Fluorescent images of polymerized NBD-PE/DMPC/PDA films (0.2:0.8:9 mole ratio). The subphase underneath the film consisted of phosphate buffered saline (PBS) (1.0×10^{-3} M) at pH = 7.4; (B) polymerized NBD-PE/DMPC/PDA films after injection of alamethicin at a concentration of 5.0×10^{-8} M. The bar represents 10 μm. All films were transferred to glass slides prior to image acquisition.

mN/m, a collapse was observed leading to lower surface pressure (Figure 4A). The surface pressure bottomed at around 12.5 mN/m, gradually increasing up to a plateau at a pressure of 27.5 mN/m. The collapse observed in the DMPC/diacetylene film coincides with the monolayer/solid-trilayer transition of diacetylene, shown in the surface pressure−area isotherm of a DMPC/diacetylene film having the same mole ratio[37,38] (Figure 4A, inset). The collapse observed in the isotherm shown in Figure 4A was induced by the alamethicin incorporated into the film, thus, increasing the surface pressure and giving rise to the diacetylene monolayer-to-trilayer transition.

The microscopy data shown in Figure 4B illustrate the morphological relationship between the peptide and the other film components. Figure 4B depicts BAM images recorded at different times (indicated by the arrows on the adsorption isotherm in Figure 4A) after injection of alamethicin into the water subphase underneath the DMPC/diacetylene film. The dark alamethicin domains were clearly apparent in all films [Figure 4B(i−iv)], and their emergence shortly after peptide injection could be explained by the presence of the phospholipids in the film (see discussion of alamethicin insertion into the DMPC monolayer, Figure 3 above). Indeed, the peptide aggregates observed in the DMPC/diacetylene films were smaller compared to the alamathicin patches formed in pure water (Figure 1) and most likely accounted for the different environment in which aggregation took place.

Importantly, the emergence and growth of the visible bright dendritic patterns in the BAM images [Figure 4B-(ii−iv)] points to the formation of diacetylene trilayers following incorporation of alamethicin into the mixed film. Very similar structures, induced by the monolayer−multilayer transformations of diacetylene, were observed in a previous BAM investigation of DMPC/diacetylene films.[38] The formation of solid diacetylene structures induced by incorporation of alamethicin at the water/mixed-film interface (Figure 4B) echoes the film collapse recorded in the surface pressure experiment depicted in Figure 4A.

Close inspection of the BAM data in Figure 4B indicates that alamethicin domains were not formed *inside* the bright diacetylene areas but rather were solely distributed within the darker *phospholipid* background. This result confirms that the peptide did not insert into the diacetylene matrix even in its unpolymerized state but rather was incorporated within the liquid-phase phospholipid monolayer. Exclusion of alamethicin from the multilayered diacetylene domains was similarly observed in experiments employing pure diacetylene films that did not contain phopholipids (data not shown). Overall, even though alamethicin did not penetrate into the diacetylene assemblies, the increased pressure resulting from peptide migration and domain formation within the phospholipid monolayer induced the compression and collapse of diacetylene, pointing to the indirect effect of the peptide.

4. Alamethicin Interactions with Phospholipid/PDA Films. To gain a further insight into alamethicin incorporation within the DMPC/diacetylene film and to probe the effects of the peptide on the film constituents, we carried out fluorescence microscopy experiments employing films in which the diacetylene was polymerized by ultraviolet irradiation, forming blue PDA (Figure 5). The film analyzed in Figure 5 also contained the fluorescence dye NBD-PE which was distributed only within the phospholipid monolayer,[35] thus, facilitating microscopic visualization of the DMPC domains in the films. Application of fluorescence microscopy for studying the

properties of PDA-containing films is further aided by the unique fluorescence properties of the polymer: the blue PDA phase is only weakly fluorescent, while the structurally transformed red PDA strongly fluoresces, with peaks around 560 and 650 nm.[30]

Figure 5 depicts phase contrast (left panels) and fluorescence microscopy images obtained using a 520−550-nm band-pass filter (middle panels) and >660-nm filter (right panels) of the NBD-PE/DMPC/PDA film prior to incorporation of alamethicin (Figure 5A) and after injection of alamethicin into the water subphase (concentration of 0.5×10^{-7} M, Figure 5B). The microscopy experiments facilitate visualization of the distinct film components and, particularly, the remarkable structural and chromatic effects induced by peptide insertion into the film. Figure 5A shows the features of the glass-deposited DMPC/PDA film following compression to 16 mN/m, in which a collapse occurred and diacetylene trilayers formed (see discussion of Figure 4A, above). The abundant green fluorescence shown in the middle panel of Figure 5A arises from the NBD-PE dye molecules distributed only within the DMPC monolayer but not within the PDA multilayers, which appear as darker "islands" in the film.[38] The borders of the PDA domains in the middle panel in Figure 5A, however, gave rise to faint fluorescence from the polymer which existed mostly, but not exclusively, in the initial blue phase. Similarly, very weak fluorescence at the higher wavelength (above 660 nm) was also detected on the borders of the PDA domains (right panel, Figure 5A) because the PDA multilayers were still in the blue phase.

Dramatic transformations in the fluorescence distribution and intensities were induced following alamethicin accumulation and interaction with the NBD-PE/DMPC/PDA film, Figure 5B. The NBD fluorescence microscopy image (Figure 5B, middle panel) demonstrates that numerous alamethicin aggregates formed within the phospholipid monolayer. Distinct peptide microdomains appeared as dark patches within the green fluorescence background because the peptide aggregates essentially ejected the fluorescence marker (Figure 5B, middle panel). Figure 5C depicts the fluorescence image of the same film area recorded at higher wavelengths (above 660 nm), showing a pronounced fluorescence signal (shown in red) from the PDA domains (Figure 5B, right panel). The fluorescence emission in the PDA regions correlated with the appearance of the alamethicin domains and corresponds to the structural transformations of the polymer that were induced by the increasing surface pressure.[48] The fluorescence microscopy images in Figure 5B complement the BAM pictures shown in Figure 4B which depicted the appearance of distinct peptide and diacetylene microstructures following alamethicin insertion.

The local fluorescence transformations of the PDA patches, illuminated in the images in Figure 5, were also apparent macroscopically in fluorescence spectroscopy experiments, Figure 6. The fluorescence spectra presented in Figure 6 were acquired from DMPC/PDA films deposited on glass slides, following addition of varied alamethicin quantities. Importantly, the fluorescence signal arising from peptide−lipid interactions (curves c−e, Figure 6) could be distinguished from the response of the DMPC/PDA film to the buffer solution not containing the peptide (curve b, Figure 6). Moreover, the emission spectra depicted in Figure 6 demonstrate the direct relationship between alamethicin brought into contact with the DMPC/

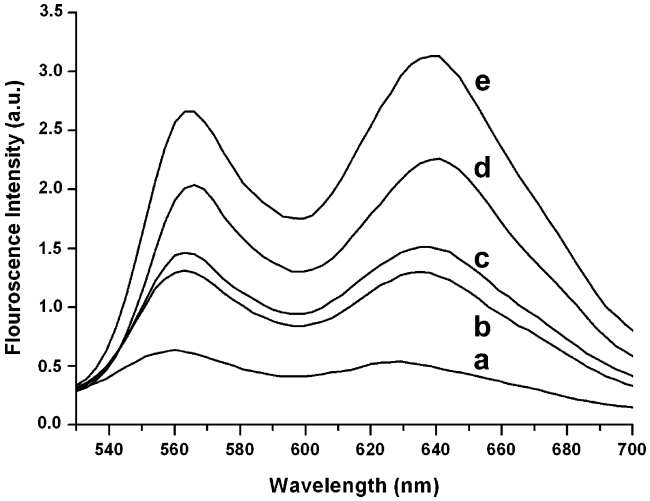

Figure 6. Fluorescence emission spectra of DMPC/PDA films (1:9 mole ratio) transferred onto glass slides. (a) Initial fluorescence from film; (b) addition of buffer (10 mM PBS, pH = 7.4); (c) addition of alamethicin at a concentration of 1.0×10^{-8} M in buffer; (d) addition of alamethicin at a concentration of 2.5×10^{-8} M in buffer; and (e) addition of alamethicin at a concentration of 5.0×10^{-8} M in buffer.

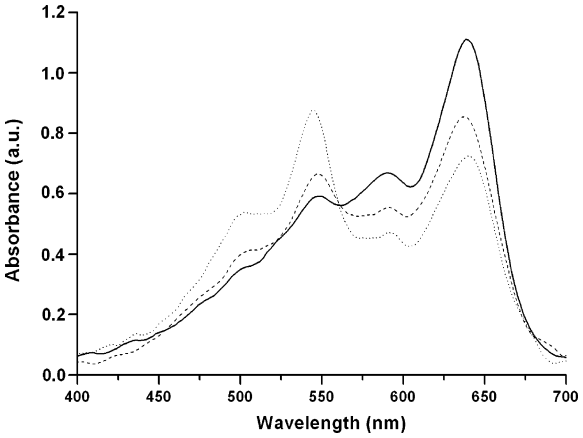

Figure 7. UV−vis spectra of the DMPC/PDA film (solid spectrum) transferred onto a glass slide; the DMPC/PDA film after addition of PBS, pH = 7.4 (10 mM) (dashed line); and the DMPC/PDA film after addition of alamethicin in PBS, pH = 7.4, and at a concentration of 2.5×10^{-8} M (dotted line).

PDA and the fluorescence emission from the film. The fluorescence data show that higher quantities of alamethicin consistently increased the fluorescence peaks at approximately 560 and 650 nm. The spectra in Figure 6 point to the possibility of using the DMPC/PDA film assembly as a platform for detection of lipid−peptide interactions.

The potential of the polymerized DMPC/PDA film for optical analysis of peptide−membrane interactions is further exemplified in Figure 7, depicting the colorimetric response of the film to alamethicin. Similar to the fluorescence spectroscopy analysis (Figure 6), the UV−vis spectra shown in Figure 7 were recorded using polymerized DMPC/PDA films deposited on glass slides. The solid-line spectrum in Figure 7 corresponds to the blue-phase PDA within the initially prepared, unperturbed DMPC/PDA film.[49,50] A slight blue-to-red transition was induced by the buffer solution (dashed-line spectrum,

(48) Carpick, R. W.; Sasaki, D. Y.; Burns, A. R. *Langmuir* **2000**, *16* (3), 1270−1278.

(49) Wang, S.; Ramirez, J.; Chen, Y.; Wang, P. G.; Leblanc, R. M. *Langmuir* **1999**, *15*, 5623−5629.

(50) Hupfer, B.; Ringsdorf, H. *Chem. Phys. Lipids* **1983**, *33*, 263−282.

Figure 7), apparent as the small increase in the relative intensity of the shoulder at around 550 nm and corresponding decrease of the 650-nm peak. Placing the alamethicin solution on the DMPC/PDA film had a much more pronounced colorimetric effect compared to the buffer (dotted spectrum, Figure 7). In particular, following peptide addition the signal at 550 nm became higher than the peak at approximately 650 nm, giving the film a strong reddish appearance.

Discussion

Investigation of alamethicin properties in different film environments revealed distinct structural and kinetic features. The surface pressure−area isotherms and adsorption isotherms in pure water indicated that a concentration threshold was needed for forming sufficiently abundant peptide aggregates to induce measurable surface pressures (Figures 1A and 2A). However, deposition of phospholipid monolayers at the air/water interface significantly promoted the incorporation of alamethicin into the films (Figures 3A and 4A). Indeed, the high affinity of alamethicin to the phospholipid monolayers eliminated the "concentration threshold" observed in water, instead giving rise to instantaneous and rapid peptide adsorption into the film and an increase in surface pressures.

The microscopy analysis provided insight into the organization and structural features of alamethicin assemblies at the air/water interface. BAM revealed a significant propensity of the peptide toward association and domain formation on the water surface. Figure 1B, for example, indicates that formation of solid domains of alamethicin occurred even in zero surface pressure at a molecular area of 450 Å^2. Indeed, the BAM results demonstrate that alamethicin was essentially immiscible both in water and within hydrophobic phospholipid environments. Interesting morphologies of peptide domains at the air/water interface were observed. In pure water, the peptide formed different anisotropic shapes within the *same* film (Figure 1B), a result that might correspond to thermodynamic instabilities of the alamethicin aggregates in water. Alamethicin microdomains of different sizes and shapes were similarly detected in DMPC monolayers (Figure 3B) and within mixed DMPC/diacetylene films (Figure 4B). The microscopy data, thus, point to distinct sensitivities of the association properties of alamethicin toward the film constituents and surface pressures. Similar aggregation and crystallization phenomena of alamethicin at the air/water interface and within lipid films were previously detected by other surface techniques including X-ray diffraction and atomic force microscopy.[15,16]

Fluorescence microscopy experiments (Figure 5) explored alamethicin organization and surface effects when the peptide penetrated into films was composed of phospholipids and polymerized diacetylene. The fluorescence images demonstrated that alamethicin formed discrete microdomains within the phospholipid monolayer in the mixed DMPC/PDA film. Peptide insertion into the film, however, had a profound effect on the PDA multilayers interspersed within the phospholipid monolayer. Specifically, the increased pressure in the film following peptide association resulted in induction of fluorescence from the polymer domains, corresponding to structural transformation of the PDA framework.

The fluorescence and visible spectroscopy experiments in Figures 6 and 7 echo the microscopy data in Figure 5 and, furthermore, point to the unique potential of DMPC/PDA films in studies of peptide−membrane interactions in film environments and in biosensor applications. The sensitivity and dose−response dependence of both the fluorescence and visible spectral signals might be employed for detection and analysis of peptide−membrane interactions in particular and identification of membrane-active species in general.

Conclusions

In this study, we investigated the interactions and aggregation properties of alamethicin, a representative membrane-active antimicrobial peptide, in different films deposited at the air/water interface. Peptide properties were dependent upon the constituents of the films; both the kinetic profiles of the films and the structures of the peptide domains and the other film constituents were modified according to peptide concentration in the water subphase and the presence and initial pressure of phospholipid monolayers. Brewster angle microscopy and fluorescence confocal microscopy provided dramatic images of the peptide aggregates and their effects on the other film components. The experiments elucidated the kinetic profiles of peptide adsorption at the air/water interface and exposed the significant enhancement of peptide aggregation within phospholipid monolayers.

An important result obtained in our experiments was the observation of indirect effects of the peptides on diacetylene moieties within mixed phospholipid/diacetylene films. Formation of peptide microdomains in such films was accompanied by an increase in surface pressure that in turn transformed the diacetylene into the blue-phase trilayer state and eventually into the red-phase PDA. Significantly, the induction of the blue-to-red and fluorescence transitions of the polymerized diacetylene in mixed phospholipid/PDA films can be implemented in biosensor constructs for the detection of specific membrane interactions. This study demonstrates that, although the PDA domains are inert by themselves to membrane interactions, they are sensitive to variations in surface pressure in their immediate surroundings and serve as efficient reporters of membrane processes.

Acknowledgment. This publication has been funded by the Reimund Staedler Minerva Center. Minerva is funded through the BMBF. R.J. acknowledges financial support of the Israel Science Foundation [Grant 2001/0168].

LA0477486

Carbohydrate Biosensors

Raz Jelinek* and Sofiya Kolusheva

Department of Chemistry and Staedler Minerva Center for Mesoscopic Macromolecular Engineering, Ben Gurion University of the Negev, Beersheva 84105, Israel

Received January 12, 2004

Contents

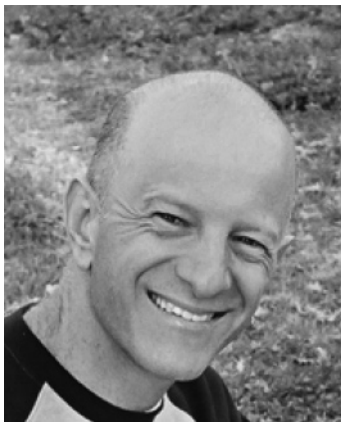

Raz Jelinek was born in 1964 in Beersheva, Israel. He obtained his B.Sc. in chemistry (summa cum laude) at the Hebrew University, Jerusalem, Israel, in 1988 and went on to get his Ph.D. in chemistry at the University of California, Berkeley, in 1993, where he did research under the guidance of Alex Pines on solid-state NMR of zeolites and molecular sieves. During his postdoctorate at the University of Pennsylvania, he switched to structural biology, doing NMR on peptides in membrane environments. In 1996, Raz returned to Beersheva to take a position at Ben Gurion University, where he is conducting research on biosensor development and biomimetic cellular systems.

Sofiya Kolusheva received her M.Sc. degree in biology from Tashkent State University (Uzbekistan) in 1989 (magna cum laude) and her Ph.D. degree in biology from the Institute of Bioorganic Chemistry (Tashkent, Uzbekistan) in 1994. She then took a postdoctoral fellowship at the Ben Gurion University of the Negev (Beersheva, Israel) in 1997. She is currently a Senior Researcher in the Biophysical Laboratory, Ilse Katz Center for Nano- and Mesoscience and Technology, Ben Gurion University of the Negev. Her current scientific interests focus on supramolecular polydiacetylene/lipid assembles and their application as membrane biosensors.

1. Introduction

Carbohydrates (denoted also oligosaccharides or polysaccharides) constitute a large and diverse class of compounds present in varied materials and have major roles in applications in chemistry, biology, materials science, and related fields. In the context of biological systems, in particular, carbohydrate research has emerged as the "new frontier" for elucidating fundamental biochemical processes and for identifying new pharmaceutical substances. Beside nucleic acids and proteins, carbohydrates appear to play critical roles in determining biological functions and affecting wide-ranging physiological processes, thus, their study and characterization have become increasingly important.

This review aims to provide a comprehensive overview of recent scientific activity pertaining to systems, methods, and devices designed to detect carbohydrates. In addition, we discuss biosensor assemblies in which carbohydrates comprise essential

* To whom correspondence should be addressed. E-mail: razj@bgumail.bgu.ac.il. Fax: +972-8-6472943. Telephone: +972-8-6461747.

10.1021/cr0300284 CCC: $48.50
Published on Web 10/28/2004

parts of the biological recognition systems. We have particularly tried to discuss in depth several topics that we believe define the current status of the carbohydrate biosensors field and point to possible future avenues. We have not attempted to cover all aspects of carbohydrate chemistry and biology, carbohydrate-detection methods, or issues concerning molecular processes involving carbohydrates; these aspects are broad and prolific fields of study, and the reader is referred to relevant literature.[1] We have also not discussed here the highly technologically and commercially important field of glucose sensing, an active area of research because of the profound health effects of aberrant glucose levels in diabetes, as glucose is technically a *mono*saccharide rather than a carbohydrate. We do, however, include a description of monosaccharide biosensors, where such devices represent important concepts in biosensor designs, for example, biosensors employing carbohydrate−lectin recognition. Similarly, this review does not address the large body of commercially oriented literature (i.e., patents) related to polysaccharide biosensors. Overall, we tried to limit the scope of this review to more recent published reports, rather than providing a historical perspective of the field. Related reviews on the subject have appeared in the literature in the past.[2]

Biosensors are generally defined as multifunctional assemblies composed of matrix-bound bioactive substances responsible for the specific recognition of the species of interest, which are directly coupled to a physicochemical transducer supplying the output signal. In this review, however, the term "biosensor" has been used in a somewhat broader sense, including systems that can be characterized as biochemical "assays". Because of space and scope considerations, we have not provided here a complete description of all biological assays in which carbohydrates have been directly or indirectly involved; we have focused instead on assemblies in which carbohydrates constitute the critical or central sensing components and discussed in more depth systems which define or represent special and novel functions of their carbohydrate constituents. Similarly, only representative publications were cited in the text when we discuss assay systems that are widely applied.

The review is divided into two sections. In the first part, we discuss schemes for detection of carbohydrates, where the sensors are designed to detect the sugar molecules by themselves or as parts of larger biological or chemical entities (for example, glycolipids and glycoproteins). Subsections focus on the significance of lectin−carbohydrate interactions in biosensor design (section 2.2) and the analysis of carbohydrate derivatives such as lipopolysacharides (LPS) and other glycolipids and glycoproteins for toxin, pathogen, and cancer detection (section 2.4). Certain overlap exists among the subtopics; for example, some pathogen-detection schemes utilize carbohydrate−lectin recognition. A subsection was devoted to the emerging field of "polysaccharide nanobiosensors" (section 2.5), recognizing the contributions and unique scientific and technological potential of "nanotechnology" in carbohydrate biosensor research.

The second part of the review summarizes biosensors and bioassays intended not to *detect* carbohydrates but in which the carbohydrates constitute essential components in the biosensor design, either as recognition elements or as the building blocks within the sensor template. We discuss biosensor schemes that employ specific biomolecular interactions such as lectin−carbohydrate affinities, carbohydrates as substrates in enzymatic processing reactions, and solid carbohydrate matrixes incorporated within sensing devices. A subsection is devoted to the large body of experimental work utilizing surface plasmon resonance (SPR) biosensors that have been widely used in recent years for studying interactions and molecular recognition processes involving carbohydrates.

2. Detection and Analysis of Carbohydrates in Biological Systems

2.1 Identification of Carbohydrates and Carbohydrate Derivatives

2.1.1 General Procedure

The primary requirements facing new biosensor technologies include maximization of the sensitivity, selectivity, and reproducibility within the experimental setup. These issues have been predominant in biosensor design and construction. In that regard, the complexity of carbohydrate structures and the diversity of their chemical properties and molecular context pose particular and significant bioanalytical challenges. These have led to the development of a large number of biosensors and bioassays for carbohydrate identification and analysis using spectroscopic, biochemical, or electrochemical methods.

The use of enzymatic digestion has been among the first and most common assay approaches for carbohydrate analysis.[3−7] In such techniques, carbohydrate detection generally relies on enzymatic catalysis of saccharide substrates by immobilized glycoenzymes.[3−5] Because the detected signal in enzyme-based biosensors originates from the reaction products of the enzyme action, a critical requirement in such sensors is the maintenance and optimization of the biological activity of the enzyme. This could be particularly demanding because in most sensing applications and devices the enzymes have to be immobilized on solid supports.[3] Immobilization of glycosylated enzymes through binding to lectins has been reported.[3−5] This approach has certain advantages over surface binding of the enzymes using means of covalent linkage, particularly because the latter technique might interfere with the stability and biological viability of the enzyme. Furthermore, the high lectin−carbohydrate affinity constituting the basis for the immobilization procedure contributes to the stability of the biosensor assembly and its resistance to varied external degrading factors, such as heat or chemical/biological denaturation.

Frequently, the output signals produced by enzyme-based-detection methods are relatively low, and

amplification of the sensor response is necessary. Magnification of enzymatic signals has been achieved through multiple glycoenzyme layering.[5] Such lectin-based immobilization methods have opened the way to assemblies with higher glycoenzyme affinities and better load factors. Varied synthetic developments have focused on identification of solid matrixes that facilitated repetitive layering of glycoenzymes and lectins.[3−5] Such "multiple bioaffinity layering" exhibited superior analytical capabilities compared to other glycoenzyme-immobilization approaches.[3−5] Some technical challenges, however, are inherent in detection schemes utilizing multiple glycoenzyme layering using immobilized lectins, primarily the need for several preparative steps while retaining the catalytic activities of the enzymes in the solid-supported environments.

The multiple glycoenzyme-layering technique further necessitates careful selection of the solid supports. The appropriate matrixes should be sufficiently reactive to allow derivatization with the lectin, have to exhibit relatively large and accessible surface area, and should not interfere with the catalytic domains of the immobilized glycoenzyme layers.[5] Biospecific sorbent matrixes were reported.[3−5] Importantly, from a biosensing point of view, lectin-based multilayering methods do not dictate which *detection* schemes are to be used for measuring the enzymatic activity. Thus, different sensing methods based on enzymatic digestion in lectin-based "multilayer" environments were described in the literature, including flow-microcalorimetry, in which changes in heat capacity induced by the catalytic action of a glycoenzyme were recorded.[5] Other methods employed coupling between several enzymatic processes that produce spectroscopically detected species.[7]

Signal amplification inherent in the multilayering approach was employed toward achieving sensor prototypes that could identify carbohydrates within complex mixtures. An important consequence of this property is the feasibility of miniaturization within devices based on multienzyme assemblies. Technical advances in this field have led to fabrication of microfabricated biosensors containing lectin-bound glycoenzyme layers coupled to silicon chips.[6] Such achievements could open the way to diverse biosensing applications, such as the fabrication of flow channels within the biosensor chip.[6]

Immobilization of sugar-digesting enzymes within miniaturized biosensor devices has been achieved by other methods. An enzyme-based disaccharide microdetector sensor prototype included enzyme-derivatized agarose beads placed within wells etched on a silicon chip. Miniaturization in this kind of device allows the simultaneous analysis of carbohydrate mixtures.[7] Practical advantages of enzyme-based biosensor chips include the very low sample volumes required (often in the range of nanoliters), the feasibility for presentation of different enzymes on a single chip, which facilitates parallel analysis of complex oligosaccharides or multicomponent systems, translated into significant cost reduction, and the availability of mass production.[6−10]

Varied electrochemical methods have been applied for carbohydrate detection in biological and pharmaceutical samples. A major impetus for development of electrochemical approaches as compared to other bioanalytical techniques has been the observation that carbohydrates do not generally contain intrinsic chromophores (neither fluorescent nor emitting in the UV−visible range). Recent advances in the design and application of electrochemistry in saccharide assays were extensively reviewed.[11] Two electrochemical carbohydrate-detection strategies, in particular, have been thoroughly explored: enzyme-based electrodes and direct oxidation at electrode surfaces, mostly employed in postseparation analysis in liquid chromatography or capillary electrophoresis schemes.

Historically, enzyme-based electrochemical detection strategies for carbohydrates were developed because *direct* analyses of saccharide compounds were traditionally hampered by the unfavorable redox properties of many sugars.[11] In the most basic amperometric enzyme electrode, glucose was oxidized within an immobilized layer of glucose oxidase and then determined at a conducting platinum or carbon electrodes by measuring the current resulting either from oxidation of hydrogen peroxide or reduction of diatomic oxygen consumed by the enzymatic reaction.[12] Overall, the underlying concept of enzymatic electrodes for carbohydrate analysis involves the highly specific conversion of mostly monosaccharide analytes into more conveniently oxidized species (such as H_2O_2).

Immobilization of carbohydrate-digesting enzymes onto electrode surfaces without impairing their functionalities and mediation of the electron transfer to the electrode surface have been among the practical impediments for implementation of enzyme-based electrochemical techniques. Accordingly, a number of electrochemical biosensing approaches have utilized direct oxidation of carbohydrates at electrode surfaces. Many of these techniques require for the oxidation to occur electrochemical potential conditions for which many electrode materials are inadequate.[11] Accordingly, a critical issue in such applications has been the proper selection of electrode composition.[13] Most direct-oxidation detection schemes have combined electrochemical processing of the carbohydrates with liquid ion-exchange chromatography for compound separation.[14,15]

Complex carbohydrates or multicomponent mixtures pose particular challenges for application of electrochemical detection methods. In such systems, the issue of selectivity and/or separation often has to be addressed in parallel with the actual detection process. Varied methods have been developed for achieving these goals, roughly divided into two main approaches: the first relies on the actual selectivity of the chemical/biological component recognizing or reacting with the carbohydrate to be analyzed (such as the enzyme for which the carbohydrate is the substrate); the second group of detection schemes combines the electrochemical analysis with separation techniques such as capillary electrophoresis (CE) or liquid chromatography (LC).[11] Development of

separation methods for carbohydrates is particularly important, because it has been found that, unlike proteins or other macromolecules, a large size or high molecular weight does no significantly impair the capability of electrochemical methods to accurately detect the molecule.[11]

Coupling of electrochemical detection to CE has attracted interest in recent years because of the power of the technique to resolve and identify carbohydrates in complex mixtures.[16,17] Actual analysis of the carbohydrates is similar to other electrochemical methods in which the redox reactions take place at metal electrode surfaces, while the function of CE is separation of the compounds within the mixtures. However, a specific technical problem that has to be surmounted in such devices concerns the electronic separation between the electrophoretic and electrochemical processes. This is due to the fact that current leakage between the two electrical circuits has to be avoided and minimized, because the detection potential is usually much smaller than the capillary electrohoresis voltages.[11]

Several techniques were described in the literature that similarly rely on compound separation but use detection schemes other than electrochemistry, for example, UV absorbance.[18] A carbohydrate-detection technique employed in conjunction with a separation method was denoted polarized photometric detection (PPD).[19] The sensor apparatus of the PPD unit consisted of placing two light polarizers at opposite sides of a conventional UV−vis spectrophotometer flow cell. This arrangement allowed the measurement of optical rotation of chiral compounds through the change in absorbance. Despite its crude mechanism, application of PPD was claimed to achieve extremely high detection sensitivity for oligosaccharides through the different rotations exerted by the molecules.[19]

Even though carbohydrate detection schemes that are combined with compound separation are generally satisfactory in achieving high-sensitivity compound identification, their main drawback is the ultimate dependence upon the separation technique for efficient application. Thus, many of the generic prototypes and published experimental data required, to some degree, prior knowledge of the type of oligosaccharide mixture to be analyzed. Accordingly, the majority of reported differential-elution/detection methodologies have been applied toward analysis of simple sugars.

Fluorescence spectroscopy has had an important contribution to development of carbohydrate biosensors, mostly through the use of fluorescent labels.[20−22] Such "carbohydrate fingerprinting" techniques usually consist of several stages. The analysis includes attachment of nonspecific fluorescent tags that bind to monosaccharide building blocks within the sugar molecule, breaking the larger saccharide into smaller fluorescent-tagged units mostly by enzymatic digestion and application of separation procedures (for example, liquid chromatography) for complete assignment.[20,22] The coupling of the carbohydrate analyte with additional molecular entities (the fluorescent tags) might interfere with both the fragmentation of the larger molecule (a prerequisite for separation and analysis), as well as affect the elution of the components. These constraints naturally pose challenges to the successful use of this methodology. Other fluorescence-based assays were developed not only for identification of individual oligosaccharides but also to characterize biochemical processes in which carbohydrates participate. A fluorescence-labeling technique has been introduced to study the gelation properties and cell-wall localization of alginate, the major cell-wall carbohydrate of brown algae.[23] Specifically, the fluorescent dye fluorescein was conjugated to short polygluronate chains and used to target the gelling subunits of the carbohydrate. The method allowed rapid labeling and probing of distinct cellular regions from varied algae sources.

Several carbohydrate-detection schemes based on boronic acid were reported in the literature, often utilizing fluorescent tags attached to the boronic acid moieties.[24−27] The three primary building blocks comprising such photoinduced electron transfer (PET) biosensors are the fluorophore, the carbohydrate receptor, and a molecular spacer separating them.[27] In particular, saccharide detection achieved with the use of these molecular assemblies rely on the reactivity of boronic acid with vicinal *cis*-diols of carbohydrates.[24,27] Boronic acid PET biosensors exhibit notable advantages and disadvantages. On one hand, the criteria for molecular design allow significant flexibility in determining saccharide ligand binding thorough shape selectivity, chiral recognition, allosteric discrimination, and other factors.[27] On the other hand, functionality of the biosensor generally requires high pH environments to produce ionization of the boronic acid units (yielding boronate anions), a feature that limits the usefulness of such assays.

Varied boronic-acid-based biosensor designs included polymer hydrogels coupled to pendant boronic acid units.[24] Such biosensors conform to the "classic" biosensor design in that the recognition event between the sensor (the hydrogel−boronic acid conjugate) and the carbohydrate analyte gives rise to a detectable physical change in the system, a shift of the visible wavelength of light diffracted by the hydrogel.[24] Swelling of the hydrogel (responsible for the change in the diffraction wavelength) is induced in the sensor assembly by the increased osmotic pressure occurring from the decrease of pK_a of the boronic acid following binding to the carbohydrate. This carbohydrate-detection scheme is simple, robust, and quite sensitive (lower than 50 μM carbohydrate analyte detected).[24] The system was demonstrated primarily for detection of simple sugars, such as glucose, although conceptually, it could be generally applied for more complex carbohydrates. Similar biosensor constructs utilizing boronic acid derivatives consisted of a fluorophore and boronic acid attached to an amine moiety.[25,26] When a saccharide analyte binds to the boronic acid, the boron atom becomes more acidic, leading to an enhanced Lewis acid−base interaction with the amine nitrogen. This reduces the interaction of the nitrogen lone pair with the fluorophore, thus suppressing the PET process and increasing the fluorescence.

Detection methods employed in boronic-acid-based biosensors were not limited to fluorescence techniques. Indeed, the use of the chemical reaction between the saccharide and boronic acid as the defining feature of a biosensor facilitates the application of a plethora of sensing approaches that were recently reviewed.[25] Specific bioanalytical techniques included chiral saccharide recognition using circular dichroism (CD) and liquid crystalline suspensions,[25,28] the use of colorimetric carbohydrate receptors,[29,30] electrochemical detection via coupling of the boronic acid recognition assembly to a redox unit such as ferrocene,[31,32] and others.

Several carbohydrate-sensing schemes have been based on recently developed chemical and biophysical techniques. Molecularly imprinted polymers (MIPs), for example, have attracted an increasing interest as templates for carbohydrate-detection assays. Molecular imprinting creates recognition sites in polymers by using template molecules; the templates are prepared by initiation of the polymerization processes, while molecules of a particular analyte are incorporated within the solidifying material.[33,34] Following the removal of the embedded analyte molecules, the polymer essentially becomes a porous framework that selectively adsorbs only the analyte molecules within the pre shaped binding sites.[35] This kind of "templating biosensing" approach could be particularly well-suited for carbohydrate detection and analysis because the imprinting procedure might be able to distinguish between different functional units and/or saccharide moieties within complex carbohydrates.

"Proofs of concept" for the application of MIPs for detection of simple sugars were described in several publications. Quartz crystal microbalance (QCM, see more in-depth description of the technique below) coated with MIPs was recently synthesized for detection of sialic acid, the cell-surface receptor of influenza virus.[36] That design built upon template imprinting of sialic acid moieties via boronic acid-derivatized polymer for construction of a QCM sensor. The significance of this type of study lies in the demonstration of a MIP as viable technology for use in fundamental biosensor design. In fact, the representative QCM−MIP sensor points to a primary criterion in the design of MIP-based biosensors, which is the choice of the detection scheme. Specifically, one of the important issues underlying MIP sensors is how would the sensors respond to the specific binding of analytes in general, carbohydrate analytes in particular, and how would the signal produced within the biosensor be recorded. Detection of binding interactions to the polymer template through embedded fluorescence tags could be the technology of choice, albeit this approach could pose significant technical and synthetic challenges. Coupling between imprinted polymer technology and fluorescence-based detection of carbohydrates was reported in a representative study.[37] In that work, the researchers synthesized a fluorescent monomer that facilitated detection of *cis*-diols, which was then successfully assembled into an imprinted polymer, preserving its fluorescence-sensing capabilities for carbohydrate derivatives adsorbed onto the polymer framework. The key methodological requirements successfully demonstrated in that report were, first, the synthesis of a functional fluorescent monomer displaying strong binding interactions with particular structural elements in carbohydrates (*cis*-diols) and, second, retaining the discrimination capabilities of the fluorophore and its fluorescence sensitivity inside the polymer framework. Gao et al. attained these goals for detecting fructose with the use of a monomer-conjugated boronic acid monomer.[37]

A practical weakness encountered in MIP applications, particularly saccharide-templated materials, has been the low reloading capacity of the analytes. To overcome this limitation, some studies proposed to enhance the binding capability of the polymer matrix through chemical manipulations, for example, by increasing the polarity of the polymer backbone, thus enabling multiple hydrogen bonding between the polymer framework and the incorporated carbohydrate guest molecules.[38] Specifically, the researchers explored the effects on saccharide rebinding of inclusion of multiple metal cations, such as Cu^{II}_2, within the polymer template and the use of polar cross linkers such as pentaerythritol within the polymer matrix. Improved performance of the MIP was indeed demonstrated for several polysaccharides, indicating that varied synthetic routes could be employed to optimize the bioanalytical performance of MIP-based sensors.

Carbohydrate detection using whole-cell biosensors has been also an active field of research in recent years. Even though the technique was so far employed almost only for detection of mono- and disaccharides,[39] it holds promise as a highly generic approach for carbohydrate analysis in natural samples. In contrast to simple, modular carbohydrate biosensors, the interest in development of cell-based carbohydrate is precisely due to the intrinsic sophisticated, cooperative properties of whole cells. Indeed, living cells are routinely engaged in converting complex substrates into smaller molecular units through distinct metabolic pathways. Cells are also capable to continuously repair their enzymatic cascades, including those involved in carbohydrate digestion.[39−41] Whole-cell biosensors could have advantages over simplified carbohydrate-detection methods such as enzyme-based sensors because cell assays generally monitor *sum parameters* such as toxicity or oxygen uptake, rather than individual molecular analytes in solution.

Held et al. constructed a microbial biosensor array consisting of immobilized *Escherichia coli* bacterial mutants lacking specific metabolic systems for individual carbohydrates.[40] The sensor components included an electrode for monitoring electrochemical potential arising from the reduction of molecular oxygen. The oxygen for its part was produced by *E. coli* mutants immobilized within a solid matrix and was indicative of the metabolic activity of the bacteria. In particular, the bacterial mutants used were deficient in translational pathways for specific carbohydrates; thus, addition of those carbohydrates resulted in increased metabolic activities and higher

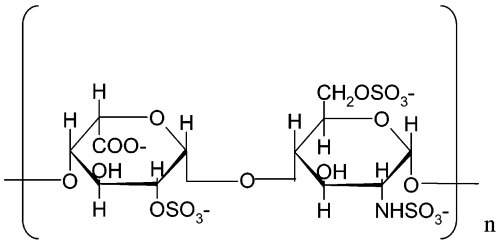

Figure 1. Most common disaccharide unit in the heparin structure.

production of O_2. This microbial biosensor featured high selectivity among different saccharides and was also noteworthy for its overall stability, a general difficulty encountered when working with living systems. A different method was proposed by Svitel et al. consisting of a cell-based biosensor, which utilized an oxygen electrode coated with membrane-containing microorganisms (such as *Gluconobacter oxydans* and *Saccharomyces cerevisiae*) in which the carbohydrate analytes were enzymatically oxidized.[42]

2.1.2 Heparin Detection

An example of an intensive biosensor research focusing on a particular family of carbohydrates is the effort to achieve sensitive and real-time monitoring of the anticoagulant compound heparin. Heparin, a linear sulfated carbohydrate (Figure 1) and its heparinoid derivatives are abundant constituents of the extracellular matrixes of most cell types.[43] Heparin and its derivatives function as modulators and effectors for the activities of important signaling molecules such as chemokines, extracellular matrix proteins, growth factors, and cellular receptors mostly through binding to these biological macromolecules.[43] In a clinical setup, it is critical to maintain heparin levels that on one hand are sufficient to prevent thrombosis but on the other hand avoid risks of bleeding. Real-time monitoring of heparin concentrations was reported during cardiopulmonary bypass surgery and other invasive procedures.[44] However, a limitation for practical commercial and mass use of heparin biosensors has been the requirement for additional reagents and/or specialized laboratory equipment. Considering the fact that more than half of a billion doses of heparin are used annually, there have been intensive efforts to develop simple sensor systems that could detect heparin directly in blood or serum samples.[45]

Several methods for heparin detection were described in the literature. A particular emphasis in the efforts to develop new detection methods has been the introduction of rapid, preferably one-step methods that would facilitate detection of heparin through simple means, for example, a visible color change. An indicator displacement assay for heparin was developed in the laboratory of Anslyn.[46] A colorimetric displacement assay of the type described in that work, shown schematically in Figure 2, is based on generation of colorimetric changes induced by replacement of a receptor-embedded indicator molecule by the analyte.[47] The critical requirement of such a biosensor is the design of a synthetic receptor that would display satisfactory selectivity between the

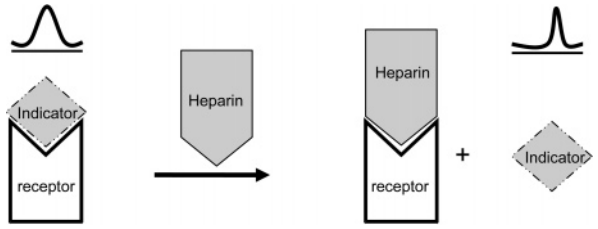

Figure 2. Schematic representation of a colorimetric displacement assay for heparin detection. Different visible spectra are recorded when the indicator molecule is bound to the synthetic receptor (left) and when the indicator is ejected by heparin from the binding site (see the text).

desired analyte and compounds similar to it (as well as the initially incorporated indicator molecule). In the reported heparin biosensor,[46] the synthesis of a receptor containing a boronic acid derivative made possible both an easy replacement of the colorimetric dye by heparin as well as a sufficient selectivity among saccharides with a similar structure. The order-of-magnitude differences between the binding constant of heparin and other glycosaminoglycan derivatives examined were ascribed to the anionic charge densities on the compounds, pointing to negative charge as an important determinant affecting heparin binding and affinity.

Electrostatic interactions indeed played a significant role in other heparin biosensor designs. Heparin detection was carried out through interactions between the negatively charged carbohydrate (average charge of -70) and positive electrode surfaces in ion-channel sensor assemblies.[48] Binding of fibroblast growth factor (FGF) to specific heparin sequences was analyzed by using a radioactive-labeling technique.[49] FGF selectivity among particular glycosaminoglycans was determined through displacement of H^3-labeled heparin by unlabeled carbohydrates, complemented by competitive binding assays using radioactive-labeled and unlabeled saccharide moieties.[49] SPR (see subsection 3.4 below) has been often used as a sensor technique for heparin detection and analysis.[50]

The QCM technique has been applied for heparin detection. QCM biosensors drew interest because of technological progress in producing precisely cut piezoelectric quartz crystal resonators.[51] The QCM sensor is constructed by immobilization of a recognition element (antibody, receptor, carbohydrate-binding protein, and others) onto the surface of a transducer. Selective binding of the desired molecule to the QCM transducer results in mass and consequent changes of its oscillation frequency, which could be detected electrically.[52] Detection of minute changes in the mass of the films allows application of the QCM biosensor for studying varied biomolecular recognition events.[53] QCM has been applied for detection and kinetic analysis of heparin binding to protamine-adsorbed surfaces.[54] This report examined the effect of receptor (protamine) coverage on the gold electrode on the sensitivity of the biosensor toward heparin and the adsorption profiles of heparin at different concentrations. Even though the QCM frequency reached a steady-state condition after a relatively long time (several minutes), admittedly a

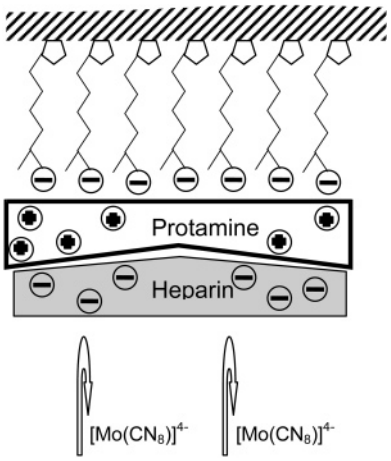

Figure 3. Schematic representation of an ion-channel biosensor for heparin. Heparin−protamine binding at the electrode surface disrupts the attachment of the metal complexes, thus modifiying the redox potential of the electrode.

deficiency of the system, the sensitivity achieved using that sensor was within the clinically required range.[54]

Achieving sufficient detection sensitivity has been a major factor in shaping development of heparin biosensors. Ion-channel sensor methods were shown to detect heparin in very low concentrations in various solutions.[55] The principle of ion-channel sensing, depicted schematically in Figure 3, resembles the displacement assay described above in that detection relies on replacement of a signal-producing molecular species by the analyte. Specifically, negatively charged heparin modulates the electrical voltage developing at an electrode surface through prevention of redox reactions between ionic metal complexes, such as $[Mo(CN)_8]^{4-}$, and an electrode.[55] In the case of heparin, the physical or electrostatic exclusion of the electroactive ions or molecules (referred to as markers) is usually carried out through covalent or electrostatic attachment of specific receptors of the saccharide, such as protamine, to the electrode.[55,56] Heparin is particularly amenable to such applications because of its high negative charge facilitating a low-concentration detection threshold. Gadzekpo et al., for example, demonstrated a dynamic range of between 0.6 and 3.0 μg/mL for heparin, which is well below the values encountered in biomedical applications.[55] A recurring problem of using ion-channel electrodes for heparin biosensing has been the decrease in reproducibility and precision of the determined concentrations after repeated use of the electrode.[55] A partial solution to this deficiency was the removal and reincorporation of the protamine receptor in addition to the heparin analytes. Naturally, this electrode regeneration method could not be applied in the case of covalently attached protamine, leading to development of specially designed surface-attached heparin receptors having superior detection limits and reproducibility properties.[55]

Potentiometric detection methods using polymeric membrane-based electrodes were used for heparin detection. These devices originate from the observation that binding of biological polyions, such as heparin, to the electrode surfaces induce large non-equilibrium potentiometric responses.[57] Such electrodes have been utilized extensively in clinical studies because of their adaptability for rapid and selective detection of ions in blood and plasma liquids.[58] Modification of polymer ion-selective membrane electrodes for heparin detection was reported.[59] Methods for construction of ion-selective heparin biosensors based on irreversible exchange of the carbohydrate polyanion with monovalent ions at the electrode surface were also described in the literature.[60,61] Binding of heparin to the electrode was facilitated in such sensors through doping the electrode surface with lipophilic substances such as quaternary ammonium salts.[57,59] Indeed, the choice of the ion-exchanger dopant incorporated within the polymer determined the biosensor sensitivity and performance to a large extent. One of the important advantages of polymeric-based potentiometric biosensors has been the possibility to use such techniques for determination of heparin levels in whole blood samples, in actual operation environments. An obvious disadvantage is the irreversibility of detection, which mandates that the technology be used mainly in disposable devices.[57]

The irreversibility of heparin binding requires carrying out electrode renewal using varied chemical or physical means, such as heparin displacement by high-concentration Cl^- solutions, that are often elaborate and cumbersome. To overcome this limitation, a reversible heparin sensor employing an additional H^+ ionophore within the electrode membrane was reported.[62] Specifically, doping the biosensor membrane with the ionophore allowed displacement of heparin from the electrode surface by simply increasing the pH of the solution. The addition of the H^+ carrier might make the sensor somewhat more complex; however, the reversibility of the heparin-detection scheme through this elegant design is a noteworthy advantage.

The high concentration of negative charges on heparin has been a basis for other sensing techniques, such as the detection of variations in charge densities in porous membranes mounted on an ion-selective field effect transistor (ISFET).[45,63] The ISFET essentially measures the stepwise change in the potential between the membrane and the bulk solution, following the binding of the analyte (in this case heparin) to the affinity receptor, generally protamine.[45] Indeed, the strong electrostatic attraction between protamine and heparin amplifies the change in surface-charge densities within the ISFET-placed membrane. Heparin biosensors utilizing the ISFET concept exhibited very high sensitivity thresholds of between 0.1 and 1 units/mL;[63] however, drifts of the recorded potential occurred at long incubation times, and optimal pH conditions of the analyte solutions (such as blood plasma) had to be determined before application of the device.[45,63]

A recent study pointed to the feasibility of heparin biosensing applications based on binding of the carbohydrate to glycoproteins.[64] In that study, Borza and Morgan examined the properties and the re-

markable pH sensitivity of the interaction between heparin and plasma histidine−proline-rich glycoprotein (HPRG). The extraordinary abundance of histidine residues in the protein sequence makes it highly sensitive to the solution pH through protonation of the histidines. Because the heparin-binding site spans some of the histidines, the sensitivity of the protein to heparin association could be fine-tuned through controlling the pH. The researchers further demonstrated that heparin binding to HPRG was highly dependent on metal ions; little binding of HPRG to heparin was detected at physiological pH in the absence of metals, but the interaction was promoted by nanomolar concentrations of zinc and copper.[64] Indeed, the frequently encountered high affinities between particular protein classes (such as lectins, see below) and their carbohydrate ligands (heparin or others) has been thoroughly exploited for carbohydrate analysis.

2.1.3 Carbohydrate Structures

Deciphering the organization and order of the monosaccharide units within oligosaccharides poses as one of the most formidable analytical challenges in glycobiology. Varied approaches and generic techniques were applied to facilitate accurate analysis of the individual monomers in complex carbohydrates.[65] Gel electrophoresis methodologies were modified for extraction, separation, and analysis of bacterial cell-surface (capsular) polysaccharides.[66] Enzymatic processing of carbohydrates and glycoconjugates has been frequently used for determination of carbohydrate structures and sequences because of the overall accuracy of the technique and the requirement of small sample quantities.[67] Recent studies have concentrated on the integration of advanced separation and detection methods for achieving fast and accurate oligosaccharide sequencing. Simultaneous detection by UV absorbance and electrospray ionization−mass spectrometry (ESI−MS), for example, provide important structural information on the oligosaccharide components of mixtures.[68]

Detailed structural analysis of bacterial capsular carbohydrates has been achieved by "enzymatic fingerprinting" procedures combining high-performance anion-exchange/pulsed-amperometric detection liquid chromatography, fluorophore-assisted carbohydrate electrophoresis, and matrix-assisted laser-desorption ionization time-of-flight (MALDI−TOF) mass spectrometry (MS).[69] This carbohydrate profiling technique made possible rapid identification of plant-cell-wall mutants and was proposed as a viable alternative for more cumbersome genetic or biochemical phenotyping methods.[69] Specifically, Lerouxel et al. explored the advantages and disadvantages of application of the bioanalytical techniques for the capsular oligosaccharide analysis, particularly in terms of speed, reliability, and accuracy. The researchers asserted that MALDI−TOF MS offers an efficient and rapid method for carbohydrate analysis.[69] This claim could be somewhat problematic because of the fact that prior knowledge of specific carbohydrate components is necessary for the correct interpretation of MALDI−TOF MS. On the other hand, the technique could indeed serve as an excellent tool for initial fast analysis of cell-wall carbohydrates. Combining MALDI−TOF MS with other separation and detection methods and the construction and use of relevant databases could make enzymatic fingerprinting a powerful tool for analysis and sequencing of complex carbohydrates.

Enzyme digestion was also used in a high-throughput assay by which *Arabidopsis thaliana* stems were hydrolyzed with driselase or trifluoroacetic acid (TFA).[70] Specifically, driselase, a mixture of fungal enzymes, hydrolyzes cellulose (to glucose) and all of the major matrix carbohydrates, while TFA hydrolyzes the matrix carbohydrates but not cellulose to monosaccharides. The application of the two substances together yielded a carbohydrate profile of the cell wall, facilitating, for example, identification of mutants with differing compositions of cellulose, xyloglucan, or xylan.[70]

Enzymatic digestion and electrochemical detection of the enzymatic cleavage products have been widely utilized for determination of oligosaccharide structures.[71−73] The chemical profiles of carbohydrate moieties expressed on several glycopeptides were determined by enzymatic desialylation and deglycosylation combined with analytical separation.[73] Another representative report described identification and analysis of carbohydrates by using an enzyme array/amperometric-detection scheme.[72] The technique could decipher structures of complex carbohydrates by direct quantification of monosaccharides released by enzymatic reactions (carried out within the "enzyme array") through pulsed amperometric detection at a gold electrode, rather than determination of the uncleaved carbohydrate moieties. The enzyme array electrochemical detection method does not require any separation or prior labeling of oligosaccharides.[72] However, this method faces several limitations. First, the ultimate resolution power of the sensor is determined by the size and diversity of the enzyme array, and one could anticipate a situation when similar oligosaccharides would produce nondistinguishable cleavage products. Moreover, correct interpretation of the sensor output depends on the assumption that the tested carbohydrates are pure, rather than complex mixtures. The use of an array setup, however, is promising in that it opens the way to high-throughput screening applications and the inclusion of database analysis as an integral part of the biosensor usage. Array-inspired bioanalytical methods in which enzymatic digestion was coupled to fluorescence detection of specific attached markers were applied for carbohydrate structural analysis.[20−22]

Other bioanalytical techniques were developed to elucidate carbohydrate sequences. Nuclear magnetic resonance (NMR) spectroscopy has been highly useful for determination of carbohydrate and glycoconjugate sequences, conformations, and dynamics.[74,75] CD spectroscopy is another important bioanalytical technique that was applied for analysis of oligosaccharide secondary structures and conformational dynamics.[76] Similarly, MS was also applied for obtaining structural information on oligosaccharides.[77] The use of permethylation combined with gas chromatography−

mass spectrometry (GC−MS) for linkage and sequence analysis of oligosaccharides was reviewed.[78] SPR was also successfully applied to glycoconjugate analysis (see detailed discussion in section 3.4 below).

A generic and elegant methodology for carbohydrate biosensor design has been the construction of *neoglycolipids*. These new molecular composites, based on the coupling of oligosaccharides to lipid residues, constitute a chemical-synthesis route for deciphering carbohydrate sequences and structures. The attachment of hydrophobic lipid moieties to carbohydrates opens the way for applications of versatile immobilization methods.[79,80] There are several important advantages of the neoglycolipid approach for biosensor purposes. First, neoglycolipids contain preselected *single* lipid residues rather than the heterogeneity of acyl chains encountered in natural glycolipids, which often adds to the complexity of analysis of saccharide derivatives from natural sources. Another inherent strength of neoglycolipid-based assays is the selective reactivity of different carbohydrates in heterogeneous mixtures following their chemical derivatization, facilitating their separation through varied analytical means. In addition, surface display of carbohydrates immobilized through their lipid chains is well-suited to probing directly the biological roles of oligosaccharide sequences as antigens, ligands, or other recognition elements, thus providing valuable information on the "glycome", the entire spectrum of glycans produced by the cell. Furthermore, neoglycolipids are particularly adaptable for modern microarray applications for high-throughput evaluation of the specificities of oligosaccharide-recognizing proteins (see below).

In an extension of the original neoglycolipid concept, chemical derivatization techniques utilizing *fluorescent* glycoconjugates were developed to decipher carbohydrate components in complex mixtures, particularly focusing on ligand discovery within varied mixtures of neutral and acidic oligosaccharides.[81] The important advantage of this approach is that it adds to the *detection* capabilities for employing neoglycolipids, which by themselves do not contain chromophores other than the saccharides. Further strength of the technique is the analysis of carbohydrates through fluorescence emitted *directly* from the saccharide-coupled fluorophore (rather than indirect detection of fluorescent substances that bind to the neoglycolipid). A recent report described conjugation of an aminolipid 1,2-dihexadecyl-sn-glycero-3-phosphoethanolamine (DHPE) and the fluorescent label anthracene.[81] This reagent is highly fluorescent and can form neoglycolipids by reaction with diverse oligosaccharides through reductive amination. Such conjugates can be resolved by thin-layer chromatography (TLC) and high-performance liquid chromatography (HPLC) and quantified either spectroscopically or through scanning densitometry.

Overall, neoglycolipid technology offers a comprehensive carbohydrate characterization approach, whereby an oligosaccharide ligand population is detected and isolated through selective chemical derivatization. The construction of new and discrete chemical entities containing hydrophobic lipid moieties and saccharides can thus be complemented by analytical methods such as MS and enzymatic digestion for complete structural analysis. In reality, the limitations of neoglycolipids for generic biosensor applications can be traced to their origin in synthetic organic chemistry. For example, one has to verify the sufficient yields of the lipid-coupling reactions, as well as the efficient immobilization of the neoglycolipid products onto the solid matrixes, prior to putative application as carbohydrate-detection devices. In addition, the technique generally requires several preparative and analysis steps that limit its applicability in faster biosensing uses.

While neoglycolipids are created synthetically, studying carbohydrate structures and properties within naturally occurring glycoconjugate entities, such as glycoproteins or glycolipids, is often critical for understanding the biological functions of such assemblies. Evaluation of carbohydrate organization and structures within aggregates of collagen, an abundant fibrous protein localized in various tissues, has been carried out by photometric measurements of textural birefringence.[82] That research has shown that the extent of optical retardations because of birefringence was indicative of the ordering conferred to collagen fibers by the attached carbohydrate moieties. The birefringence measurements exposed the important role played by collagen-bound carbohydrate molecules in the ordered aggregation of collagen fibers and subsequent attachment of other structured macromolecules to the fibers.

2.2 Lectin-Based Biosensors

Lectins constitute a broad family of proteins involved in diverse biological processes, occasionally having potent toxic properties.[83−85] Lectins generally exhibit strong binding to specific carbohydrate moieties (glycans), and this property has been extensively exploited as a basis for biosensor design. Furthermore, particular structural profiles of glycans and their recognition by lectins have been attributed to disease progression, making analysis of saccharide−lectin binding processes important as a diagnostic tool.[86] Glucose biosensor designs, for example, have frequently utilized the specificity and high affinity of different lectins to this monosaccharide. Varied detection methods based on lectin−glucose recognition have been reported in the literature, including electrochemical detection of the monosaccharides via immobilization of lectins on electrode surfaces,[87] and glucose-sensing based on the competitive reversible binding of a mobile fluorophore-labeled lectin concanavalin-A (con A) to immobile pendant glucose moieties within Sephadex beads.[88] Lectins also exhibit high potential in peripheral biotechnology industries, such as food safety; their unique recognition properties are finding promising applications in detecting microorganisms and carbohydrate additives in foods. Reported data suggest that the use of certain lectins may provide a simple and rapid alternative to traditional methods of bacterial analysis and screening.[89]

The high affinity of lectins to saccharide units has been attributed to multivalency and spatial organiza-

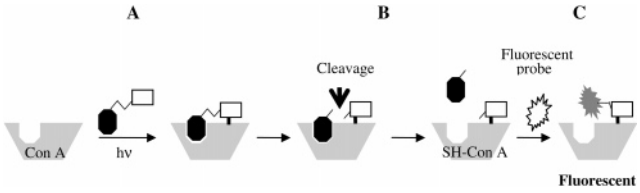

Figure 4. Schematic description of a biosensor design using the post-photoaffinity-labeling modification technique. A synthetic guest is incorporated within the binding site of con A and covalently linked by UV irradiation (A). After cleavage (B), the guest is released and the fluorescent moiety is attached through covalent bonding with a free thiol (SH) residue in proximity to the binding site (C). Binding of the actual carbohydrate guest to con A would change the fluorescent emission from the dye.

tion of the oligosaccharide ligands.[90] The selective binding of lectins to terminal carbohydrate moieties on cell surfaces and protein aggregates has been widely exploited in physiological and pathological research.[91,92] A number of histo- and cytochemical assays have used a series of lectin−enzyme (generally horseradish peroxidase) conjugates, which yielded color reactions upon enzyme processing, following the occurrence of lectin−carbohydrate binding.[93] These techniques enable not only visualization of carbohydrate distribution patterns within tissues and cell systems but also probe the different saccharide compositions expressed by the cells examined. Various staining techniques have been similarly based on lectin−carbohydrate binding. Lectin-based histochemical assays, for example, provide a platform for tissue visualization through binding between stained lectins and cells expressing lectin-reactive glycoproteins.[94]

Lectin-based immunosensor techniques have been routinely used for identifying pathogen and viral species expressing particular carbohydrates on their surface. For example, ELISA methods utilizing immobilized lectins were developed for detection of the human immunodeficiency virus (HIV).[95] Such techniques rely upon the high selectivity of particular lectins, for example, con A or the snowdrop lectin GNA, for capturing the carbohydrate antigens of the envelope glycoproteins displayed on the surface of the virus.[95,96]

con A, a disaccharide-binding lectin, is one of the most widely used lectins in sacchride-detection schemes. Several schemes have used synthetic organic chemistry pathways for coupling of con A to fluorescent moieties, thus creating fluorescence biosensors. The goal of these efforts was to combine the ligand selectivity of con A (as well as other lectins) with the intrinsic sensitivity of fluorescence phenomena, thus forming powerful platforms for carbohydrate biosensors. The laboratory of Hamachi reported the construction of saccharide biosensors in which a fluorescent label was attached in proximity to the binding site of con A, yielding a fluorescent con A in which the degree of fluorescence was modified by saccharide binding[97−99] (Figure 4). The technique, denoted "post photoaffinity labeling modification", relied on UV-induced coupling of a carbohydrate fluorescent dye (having a photoreactive site) within the binding site of con A.[97,98] The fluorescent con A

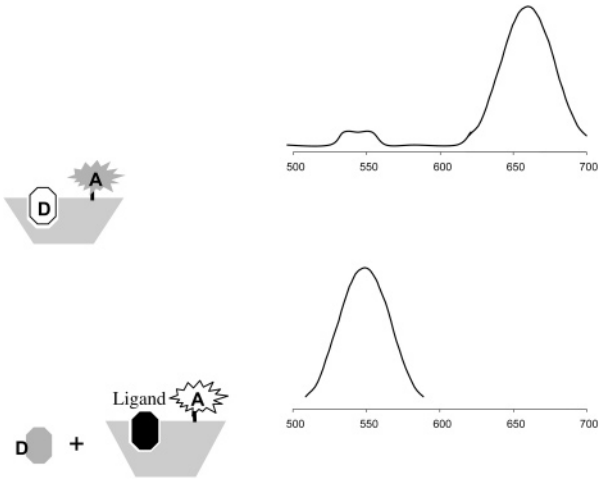

Figure 5. FRET experiment. Initially, a fluorescent donor molecule (D) is located within the binding site of the lectin, leading to a fluorescence energy transfer to an acceptor molecule (A) in close proximity and the observation of an emission spectrum from the acceptor (top). After binding of the ligand analyte (bottom), the donor molecule is released and fluorescence energy is no longer transferred to the acceptor. Thus, the emission spectrum observed (at a lower wavelength) is from the donor.

thus contained the chromophore within the binding site; however, the modified lectin retained its high affinity to various saccharides.[97] Accordingly, the interaction of the fluorescent lectin with its native saccharide ligands led to displacement of the fluorophore, which resulted in a significant decrease of the fluorescence signal.

Lectin-based carbohydrate biosensors have taken advantage of advanced fluorescence techniques, such as fluorescence resonance energy transfer (FRET, Figure 5).[100,101] Application of FRET in the carbohydrate biosensor context hinges on labeling a lectin molecule (for example, con A) with a fluorescent donor close to the binding site, while a lectin-bound carbohydrate ligand (dextran) is labeled with a fluorescent receptor. In the absence of a saccharide analyte, the binding between the lectin and the labeled carbohydrate allows a high FRET efficiency. However, the fluorescence energy transfer is decreased upon displacement of the bound ligand by the carbohydrate analyte, thus facilitating sensing of the soluble saccharide.[100,102]

The selectivity of saccharide binding to con A was the basis of an electrical-oscillation biosensor.[103] In the experimental setup reported in that research, the electrical oscillations across two electrode plates immersed in a con A solution were recorded. These oscillations were shown to depend on the presence of different carbohydrates in solution, presumably because of changes in solution capacitance following carbohydrate-lectin binding. These empirical data are intriguing because they indicate that the different mobility of bound versus free carbohydrate in aqueous solution are significant enough to form a basis for a biosensor. An interesting question arises as to whether different lectin−carbohydrate pairs would produce different signals in the electrical oscillator sensor.

A flow-microcalorimetry bioassay based on mutiple layers of con A and the glycoenzyme invertase was shown to give rise to superior catalytic response of this affixed enzyme.[5] The research demonstrated an almost 10-fold increase of the catalytic activity of the immobilized invertase through the alternating bioaffinity layering of lectin and glycoenzyme and amplification of the microcalorimetry signal. Inhibition tests of hemagglutinating activity were used as assays for monitoring oligosaccharide−lectin binding.[104] The hemagglutinating inhibition technique examines the retardation of erythrocyte agglutination by influenza virus hemagglutinin (HA), a sialic-acid-binding protein.[105] The same assay has been used to assess lectin binding to carbohydrate derivatives on a synthetic glycopeptide.[106]

Lectin−carbohydrate biomolecular recognition constitutes the core of other oligosaccharide biosensor designs. A lectin-coated piezoelectric crystal biosensor was developed for oligosaccharide analysis.[97] Piezoelectric-crystal-detection methods rely on the response of a resonating crystal following analyte binding because of either the increased mass of the crystal or changes in its viscoelastic properties.[107] The piezoelectric crystal sensor developed by Nagase et al., in which the lectin was immobilized on a quartz surface connected to a silver electrode, was used for detection of dissolved sugars and for erythrocyte identification with a detection limit approaching 100 cells.[97] Indeed, the use of lectin−carbohydrate binding in biosensor design offers significant detection sensitivity. A lectin-based biosensor capable of detecting subnanomolar concentrations of glycogen was reported.[108] The sensor concept underlying that study was the occurrence of rapid transients of the surface potential at bi- and monolayer lipid membranes. The selective binding between the lectin and its carbohydrate ligand was shown to induce sizable, rapid potassium ion current fluctuations across the bilayer membranes in a manner that was periodic and reproducible.

Lectin-based biosensors are routinely used as essential tools in biochemical research. Resonant mirror biosensor technology, for example, was applied for sophisticated kinetic rather than thermodynamic analysis of molecular interactions involving carbohydrates. The technique facilitated evaluation of the binding profiles of a carbohydrate antigen with five different lectins.[109] The experiment determined kinetic parameters such as the on rate (k_{on}) and off rate (k_{off}) of the oligosaccharide, as well as the extent of binding at equilibrium. Other applications of the resonant mirror biosensor technology concentrated on probing the difference among the binding strengths of several lectins and proteins with particular carbohydrate ligands.[110−112]

Some studies have expanded upon the concept of lectin−carbohydrate recognition as the basis for original sensory and diagnostic methods. Saccharide-presenting neoglycoprotein probes were introduced to measure the cellular capacity for binding glycan epitopes and human lectins.[108] These newly developed chemical constructs could serve as sensors for endogenous binding sites and as diagnostic tools.[113] Another application employed incorporation of a heparin-specific lectin into a temperature-sensitive gel, in which the presence of the carbohydrate could be detected through modification of the temperature-dependent shrinkage properties of the gel following binding.[114]

The binding selectivity of lectins among related carbohydrate structures forms the basis for varied biosensor designs. Hasegawa et al. evaluated the saccharide composition of several glycopeptides by using SPR (see section 3.4 below).[115] The glycopeptides were immobilized on the sensor surface, and their binding properties to various lectins were monitored following progressive trimming of their carbohydrate moieties by glycosidase digestions.[115] The use of lectins as recognition elements in diverse biosensor applications is also discussed in other sections in this review (for example, sections 2.3 and 3.4).

2.3 Glycoprotein and Glycosylation Biosensors

Glycoproteins and protein glycosylation have attained prominence in recent years as key constituents in varied cellular processes.[116,117] The exact roles of the carbohydrate moieties in such molecules, however, have not been determined yet. Protein-bound saccharides were suggested to contribute to nonprimary functions of proteins, such as nonspecific interactions with other carbohydrates or macromolecules, stabilization of protein conformations, or protection from proteolysis. Nonspecificity of the expressed saccharides is consistent with both the similarity of carbohydrate structures appearing within diverse glycoproteins and the frequent structural microheterogeneity of carbohydrate chains at given sites.[116] This concept is further supported in its overall outline by the viability of cells whose glycosylation processes have been globally disrupted by pharmacological inhibitors.[116,118] Other studies, on the other hand, have revealed the existence of specific receptors for discrete oligosaccharide structures on glycoproteins. Such receptors seem to be either important for compartmentalization of the glycoprotein or for positioning of the cells on which the glycoproteins are located.[116,119] N-linked glycans are believed to play pivotal roles in targeting, transport, and compartmentalization of glycoproteins in cells.[120] Oligosaccharides were also proposed as antigenic determinants of glycoproteins.[121]

Varied schemes for glycoprotein detection have been reported.[122] Such applications are particularly important from a therapeutic standpoint because changes in expression and abundance of glycoproteins in cellular environments are often associated with tumor proliferation (see section 2.4.3 below). Several immunosensing techniques were used for glycoprotein analysis. Ma et al. reported the application of an amperometric impedance biosensor for detection of a human mammary tumor-associated glycoprotein through binding to a monoclonal antibody.[123] The experiment demonstrated that the alternating current from an antibody-functionalized gold electrode was modified after binding of the specific carbohydrate antigen to a monoclonal anti-

body immobilized on the sensor surface. Other approaches utilized more conventional constituents for saccharide recognition and binding such as lectins (section 2.2) for assaying glycoprotein composition and glycosylation. Several reviews summarize lectin overlay assays in which the sugar moieties were initially detached from the protein residues by enzyme digestion procedures.[124,125] The effectiveness and clinical potential of lectin-based assays for studying subtle changes in serum protein glycosylation, particularly associated with disease onset, have been reviewed.[126]

An intriguing technique for creating potential glycoprotein sensors based on Langmuir−Blodgett films of fullerene−glycodendron conjugates was described by Cadullo et al.[127] The authors constructed monolayers at the air−water interface that were comprised of fullerene−dendrimers covalently attached to glycodendron headgroups. The noteworthy achievement of the researchers was the prevention of fullerene aggregation within the monolayers, accomplished by optimization of the hydrophilic/hydrophobic structure of the fullerene−dendrimer conjugates. The absence of aggregation and consequent display of the carbohydrate units at the film surface could be potentially applied to glycoprotein detection.

Interactions between viral envelope glycoproteins and host cells play fundamental roles in viral penetration into cells and viral pathogenesis.[128,129] Accordingly, studying the molecular recognition and interactions between cellular receptors and viral envelope glycoproteins showing receptor-binding activity are of great importance both for understanding the molecular basis of virus entry, as well as for developing antiviral drugs and diagnostic tools. Bertucci et al. have used an optical biosensor to study the binding of recombinant glycoproteins of herpes simplex virus (HSV) to an immobilized recombinant form of the human cellular receptor for HSV.[130] The mode of action of the biosensor was based on detection of changes in the refractive index close to the sensor surface, which was dependent upon the mass of the adsorbed species. The resonant mirror technology utilized in the research represents a class of biosensor technologies that essentially detect binding events and biomolecular interactions in real time. The strengths of the resonant mirror biosensor are mainly traced to the increased sensitivity (nano- to microgram range for glycoproteins), the short time required to perform the experiment (less than an hour), and the fact that there is no need for additional labeling of the analytes.[131] The biosensor could be regenerated after measurements through washing of the bound species, although some decrease of the reproducibility of the results was observed after repeated use.[130]

Envelope glycoproteins of the HIV, in particular gp41 and gp120, have been implicated in viral entry to various cell types.[132,133] Glycosylation of these two proteins is believed to play an important role in their antigenicity and cell-surface interactions, and specific assays were developed to decipher the structure and molecular interactions of the carbohydrates attached to these glycoproteins.[134] The association of gp120 with glycopeptides and glycolipids and contribution of the carbohydrate moieties to gp120 interactions were evaluated with bioanalytical techniques such as enzyme-linked immunosorbent assay (ELISA).[135] Assays measuring the effect of glycosylation on the immunoreactivity of glycoprotein hormones were also evaluated.[136] Different techniques have been developed to determine hemoglobin glycosylation, believed to provide an accurate index of long-term blood glucose control in diabetes mellitus, including ion-exchange chromatography, electrophoresis, isoelectric focusing, thiobarbituric acid colorimetry, and affinity chromatography.[137,138]

Protein glycosylation by chemically modified oligosaccharides ("oligosaccharide tags") could become a useful tool for investigating protein and peptide targeting in cellular processes. Analysis of glycosylation patterns of glycopeptide enzyme substrates was carried out by glucosylation of a set of the glycan substrates *in vitro*, followed by determination of glucose composition by MS.[139] Synthesis of maleimide-activated carbohydrates as site-specific tags for peptides and proteins was also reported.[140] This work built upon the high reactivity of maleimide with thiol groups, making possible attachment of maleimide-activated mono- and polysaccharides to cysteine-containing peptides. Even though technically this method essentially creates "artificial glycopeptides", tagging peptides with different saccharide moieties could be useful for detection of carbohydrate-recognition sites and carbohydrate receptors on cell surfaces.

Diverse glycosylation processes occur on cell surfaces, and elucidating cellular carbohydrate expression and glycosylation pathways is essential for understanding varied cellular events.[92,141] Elegant biochemical techniques were developed for probing oligosaccharide compositions and carbohydrate processes at cell surfaces. Bertozzi and others have expanded upon the concept of "chemical glycobiology" as a generic approach for deciphering biochemical processes in which carbohydrates constitute central components and for studying structure−function relationships involving surface-expressed oligosaccharides.[92,142] The approach, which was also denoted "metabolic oligosaccharide engineering" involves chemical modification of specific saccharide units. These unnatural carbohydrates could then be incorporated into various cell compartments and locations via the biosynthetic machinery of the cell.[142] In particular, it was shown that interference with biochemical and metabolic pathways contributing to oligosaccharide biosynthesis could shed light on the progression and significance of such processes.[92,143]

Chemical intervention in biochemical processes occurring at cellular levels has other important features. The method allows, for example, insertion of varied reactive functional groups and labels onto the cell; some studies demonstrated incorporation of glycoconjugates containing sensor probes into the cell wall, facilitating analysis of distinct reactions and transformations involving the carbohydrate molecules.[143] Charter et al. showed that unnatural sialic acid analogue containing levulinoyl moieties can be incorporated into neuronal cell surfaces. The ketone

group within levulinoyl could then be used for cell imaging using biotin, facilitating insight into metabolic pathways involving adhesion molecules (containing sialic acid) on the cell surface.[143]

Biosynthetic construction of unnatural saccharide assemblies in surfaces of living cells could aid exploration of complex processes involving carbohydrates and contribute to the search for inhibitors, agonists, and antagonists to various carbohydrate and glycoconjugate receptors. Predetermined and controlled modification of cell-surface glycans might lead to promising diagnostic applications, particularly because varied diseases are associated with altered cell glycosylation patterns (see section 2.4.3 below). A possible metabolic carbohydrate engineering approach can be conceived for discrimination of tumor cells through their altered surface glycan expression.[142,144] Additionally important in term of carbohydrate biosensor development, the ability to chemically modify glycoproteins on cell surfaces could open the way for molecular or whole-cell imaging and high-throughput screening in proteomics, "glycomics", and "cellomics" applications.

The compositions and structural features of carbohydrates expressed on cell surfaces have been employed as a tool for cell visualization and physiological research. Cytochemical methods have been applied to probe the localization and distribution of glycoproteins expressed on cell surfaces by utilizing the targeting of specific carbohydrate moieties by lectins or antibodies.[91,145] Researchers utilized both lectins that bind specifically to terminal disaccharides as well as monoclonal antibodies against carbohydrate epitopes.[91] Comparative staining based on these molecular systems differentiated and partially characterized several glycoconjugates in various sites and allowed evaluation of the relationship between chemical heterogeneity and neural speciation.

Advanced high-sensitivity MS approaches have been increasingly used for deciphering glycoprotein structures. MS has been capable to elucidate the primary structures of highly complex glycoprotein mixtures, and the technique could provide an insight into post-translational protein modification processes in particular and structural glycobiology in general.[146] Recent technical advances in MS, specifically fast atom bombardment (FAB), ESI, and MALDI considerably increased the analytical capabilities of the technology to analyze complex carbohydrates and glycoconjugates. For an in-depth discussion of the subject, the reader is referred to a recent comprehensive review.[146]

2.4 Pathogen and Cancer-Detection Assays

2.4.1 Pathogen Identification

Development of biosensors and rapid detection kits for microorganisms such as *E. coli*, *Salmonella typhimurium*, and others are highly desirable because of the adverse and often devastating health effects of pathogen infection.[147] In recent years, diverse techniques have been introduced aiming to detect pathogens in shorter times and with maximal potential sensitivity.[148] Varied techniques for pathogen detection are based on the use of antibodies specific to enzymes or other proteins expressed by the microorganism to be examined.[149] Such methods, however, often require prior knowledge of the identity of the pathogenic species to be analyzed. The search for rapid, low-cost diagnostic pathogen techniques has also focused on the use of oligosaccharides, which constitute primary molecular components and markers on pathogen surfaces. The diversity and broad knowledge base regarding surface-displayed carbohydrates could aid the design of diagnostic tests for specific bacteria. Rapid agglutination assays have been routinely used for detection of microorganisms through binding of their surface carbohydrates to varied external substances, such as antibodies and receptors. The latex agglutination test (LAT), for example, utilizes latex beads coated with polyclonal antibodies against the capsular carbohydrate of particular bacteria. Aggregation of the beads can be observed via the solution turbidity, indicating the presence of bacteria. The technique facilitated, for example, identification of *mycoplasma* in an early development stage within farm animals.[150]

Optimization and enhancement of conventional agglutination tests were reported. Application of ultrasonic standing waves in conjunction with immunoagglutination has significantly enhanced the speed and sensitivity of the assay.[151,152] In that diagnostic technique, the researchers suspended antibody-coated microparticles in an acoustic field, physically promoting interactions between the antibodies and sugar antigens and accelerating formation of aggregates. Using the ultrasound-enhanced agglutination procedure, more than a 50-fold increase in sensitivity was observed for bacterial carbohydrates, approaching the detection levels obtained by the polymerase chain reaction (PCR).

Other immuno-based techniques, such as the widely used ELISA, were applied for pathogen detection by employing cell-displayed (capsular) carbohydrates. While some assays were designed to detect the capsular carbohydrates themselves, most ELISA applications utilize the carbohydrates within the sensor framework as recognition elements designed to bind to carbohydrate-specific antibodies.[153] Published ELISA methods employing saccharide−antibody binding have mostly used carbohydrate immobilization onto the solid support, while variations exist regarding the immobilization procedures. Among the methods summarized were biotinylation of the carbohydrates,[153] conjugating to poly-L-lysine polypeptide for coating the microtiter plates,[154] and others.

Varied techniques have been developed to facilitate rapid detection of pathogen-displayed carbohydrates that could also be applied in field conditions at high sensitivity. A fluorescence polarization assay (FPA) was successfully applied for serological diagnosis of brucellosis in cattle and other farm animals through antibody binding of the capsular carbohydrate epitopes of several *Brucella* strains.[155] The FPA technology is based on the rotational differences between a solubilized fluorescent-labeled free antigen and the antigen molecule bound to its antibody. In principle, a small molecule will rotate randomly at a rapid rate,

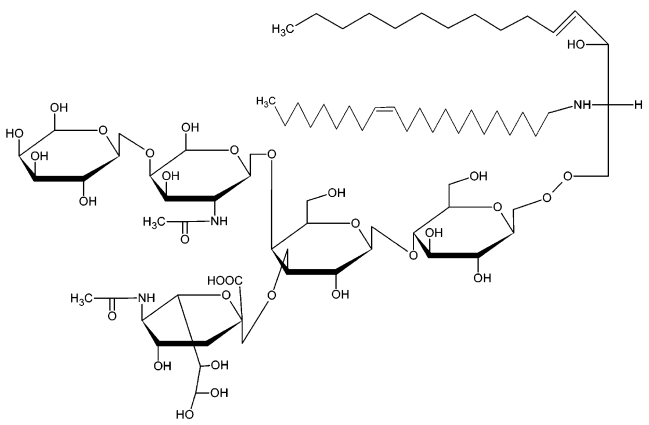

Figure 6. Ganglioside GM1 structure.

resulting in fast depolarization of light, while a larger complex would depolarize light at a reduced rate because of the slower reorientation in water.

An optical biosensor based on a resonant mirror technology was applied for studying physiological interactions of *Helicobacter pylori*, a human pathogen colonizing the gastrointestinal tract.[156] The biosensor technique could be used for actual detection of the bacterial presence. The sensing assembly described in the study utilized immobilized human gastric mucin as the recognition element, and modification of the surface refraction index resulting from bacterial binding could be easily detected. This microbiological study suggests that the suitable choice of molecular recognition determinants has a significant effect on the performance of the resonant mirror biosensor (and other technologies for that matter). The data further demonstrated that addition of sialylated and sulfated oligosaccharides, generally displayed on gastric mucins, interfered with the bacterial binding, confirming the important role of carbohydrates in bacterial surface interactions.[108]

Pathological conditions and bacterial infection could be also detected through analysis of protein glycosylation patterns. Specifically, it was shown that inflammations and infections often lead to alterations in glycosylation patterns of glycoproteins and that such modifications are generally dependent upon the particular disease encountered.[157] Carbohydrates and increased levels of particular glycoproteins have been also used as indicators of disease progression. Laminin and the high-molecular weight carbohydrate hyaluronate, for example, were suggested as biochemical markers of liver fibrosis in clinical practice.[158] Production of specific immunogenic carbohydrates was also observed by molds, a major cause for food deterioration and consequent adverse health effects.[159] Varied ELISA-based assays employing secreted immunogenic carbohydrates have been developed for detecting molds in foods.[160]

Cholera toxin (CT) is the universal marker and binding ligand of the cholera-inducing pathogen.[161,162] The cell-surface ligand of CT is the ganglioside GM1 (Figure 6), and many methods for detection of CT were based on the multivalent binding between the toxin and GM1. Indeed, the strong binding and recognition specificity of this ligand/receptor pair have made the use of this system particularly attractive both as a basis for actual biosensor design and also for demonstrating the proof of concept for putative biological- and pathogen-detection schemes. Several representative reports are described herein. Cooper et al. developed a SPR sensor chip to which ganglioside-displaying vesicles were attached, facilitating the binding of CT to the chip surface.[163] GM1 was reconstituted within model lipid bilayers in other vesicle-based assays.[164] Several studies presented sensor arrangements in which GM1 molecules were incorporated within phospholipid-covered microspheres, onto which specific binding of CT occurred.[165]

Detection of CT using FRET (Figure 5) as the generator of optical signal was reported in several biosensor schemes.[166,167] One example was a flow cytometry assay based on glass beads coated with phospholipids, which served as the scaffold for the fluorescence-labeled GM1 units.[166] Binding of CT to the GM1-coupled donor and acceptor dyes modified the distance between the fluorophores and consequently affected the fluorescence energy transfer. This biosensor arrangement achieved a high detection sensitivity of the toxin, less than 10 pM. Other studies employed the CT−GM1 pair as a model system for construction of biosensors based on FRET pathways.[166−169] Song et al. have presented several sophisticated detection schemes exemplified with the CT−GM1 system. An elegant experiment showed CT detection by FRET, where a protein−carbohydrate binding event induced distance-dependent fluorescence self-quenching and/or resonant-energy transfer processes.[169] Another study focused on the design of a "two-tier FRET" biosensor, in which the excitation spectra of the donor and acceptor were sufficiently separated to minimize the background fluorescence signal because of indirect excitation of the acceptor fluorescence.[167] Energy transfer in that arrangement was achieved through an intermediate fluorophore, also covalently bound to GM1. These reports point to the feasibility of very high detection sensitivities, specificities, and reliability when advanced fluorescence techniques are employed within an integrated detection system consisting of an appropriate biological recognition system.

A gravimetric sensor in which GM1 was incorporated as the target molecule on a QCM surface chip was reported.[170] In that application, a biomimetic film containing glycolipids was shown to attract bacterial toxins and whole cells, facilitating binding and kinetic analysis. A similar device in which self-assembled monolayers (SAMs) of GM1 were immobilized on gold surfaces was used in a QCM setup for detection of CT and the closely related heat-labile enterotoxin of *E. coli* in a continuous-flow cell.[171] Because of its high intrinsic sensitivity, QCM could be a useful reporter technology in pathogen-detection schemes based on carbohydrate recognition. However, like other techniques that rely on specific binding, applicability of the method requires a sufficiently high concentration of the capture agents for the analytes, in this case GM1.

The latter study by Spangler and Tyler[171] points to the utilization of SAMs as a promising design feature of carbohydrate biosensors. Indeed, deposition

of glycoconjugate films on solid surfaces has been a generalized technique for pathogen biosensor designs, and the construction of biofunctional and biocompatible interfaces on solids to generate models of cell and tissue surfaces may have numerous scientific and practical applications.[172,173] Mixed monolayers of thiol-terminated poly(ethylene glycol) (PEG) and thioacetyl GM1 deposited on gold crystals might be used as potential biosensor arrays.[172] Such assemblies could satisfy several key prerequisites in biosensor design: the display, flexibility, and accessibility of the recognition elements (the ganglioside moieties in the case of CT detection), the relatively facile transduction of the analyte-binding signal (through the PEG residues) to the reporting unit, which is associated with the solid surface, and the possibility for surface regeneration. The SAM architectures reported by Nyquist et al. are robust and readily controlled to provide a network of the receptor GM1 in the PEG-terminated matrix.[172] However, the extent of nonspecific protein binding to such film assemblies is still a primary concern for future biosensor applications.

An original approach for detection of pathogenic toxins via thin films of lipid and glycolipid mixtures deposited on the surface of a resonant mirror biosensor was reported.[174] The small quantities of glycolipid ligands incorporated within the films were responsible for generation of the optical signals following binding of the protein receptors. The experimental analysis indicated that the response of the films was sensitive to external parameters, such as pH. On the other hand, lipid/glycolipid deposition generally afforded surface regeneration through simple chemical procedures, enhancing the potential applicability of the biosensor. Another sensing device exploited optically tagged glycolipid ligands embedded within a fluidic phospholipid bilayer formed on the surface of a planar optical waveguide.[175] Multivalent binding of the CT to the film triggered FRET, resulting in a two-color optical change that was monitored through recording the emitted luminescence above the waveguide surface.

A significant hurdle for biosensor applications based on molecular recognition is the amplification of the signal because of the binding event over nonspecific background interactions. Several surface-biosensor designs introduced a transduction concept that relied on induction of structural modifications within biomimetic films in which the recognition events have occurred.[157] Specifically, Bardeau et al. have developed sensor devices that detect signals generated by shifts in the phase-transition temperatures of phospholipid/ganglioside films.[176] Such transitions, probed by IR vibrational spectroscopy, were induced by the highly specific GM1−CT interactions within the hybrid assembly of the glycolipid receptors and phospholipids. This method could have potential applications for signal amplification in biosensor design.

Original pathogen colorimetric sensors that respond to molecular recognition phenomena through the occurrence of rapid color transitions have been recently reported.[177,178] Several laboratories have

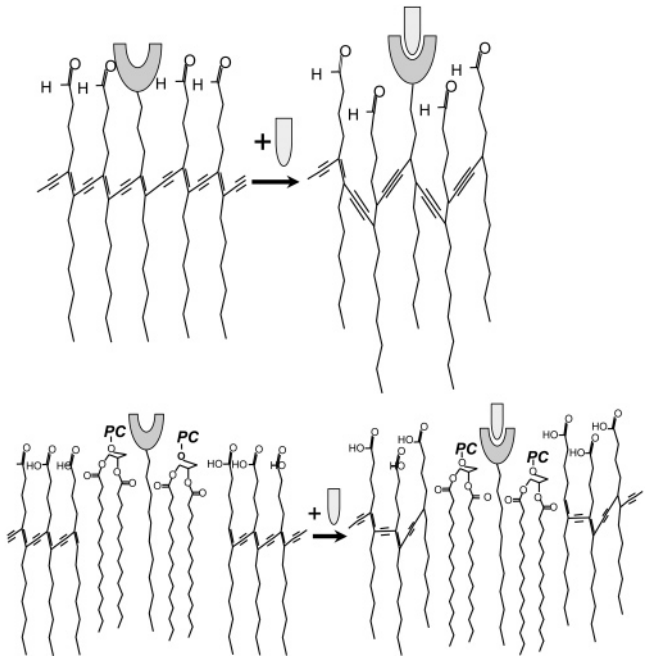

Figure 7. Schematic figures of colorimetric biosensors based on polydiacetylene (PDA). (A) Recognition element is covalently attached at the surface of the PDA framework (which appears blue to the eye). Interaction with the ligand induces a structural transition within the conjugated ene−yne polymer backbone, changing the conjugation length within the polymer network, with a consequent blue−red transition (see the text). (B) Recognition molecule is physically incorporated within phospholipids (phosphocholine, PC) domains in the PDA matrix. Ligand−receptor interaction indirectly induces the structural transformation of the polymer (see the text).

demonstrated that artificial cell membranes made from conjugated lipid polymers (polydiacetylene or PDA) can, on a simple level, mimic membrane surfaces allowing both the occurrence and consequent detection of molecular recognition processes (Figure 7).[177,179−185] Specifically, the ene−yne conjugated backbones of several polydiacetylene species absorb light at the visible region of the electromagnetic spectrum, thus exhibiting visible colors (in most cases, appearing intense blue). Furthermore, it was shown that external perturbations to the polymer induce structural transformations within the conjugated backbone of PDAs, giving rise to dramatic colorimetric transitions (blue−red). In a biological context, it was demonstrated that the blue−red transitions of PDA can be induced by ligand−receptor interactions occurring between soluble molecules and ligands embedded within the PDA matrix. The display of the ligands could be either achieved through covalent binding at the PDA headgroup region (Figure 7A)[177−179] or through physical incorporation of the recognition element within lipid domains assembled in the PDA framework (Figure 7B).[182−185] In PDA-based biosensors, the conjugated polymer backbone essentially acts as a built-in reporter of binding events, measurable by a chromatic change in the visible absorption spectrum. Such assemblies may provide a general approach for direct assays and biosensing devices for varied biological substances and biomolecular recognition events.

Some PDA-based biosensor applications reported on the covalent attachment of the ganglioside GM1 within polydiacetylene liposomes. In this arrangement, specific interactions between GM1 and CT at the interface of the liposomes resulted in a change of the vesicle color (from blue to red) because of conformational changes in the conjugated (ene−yne) polymer backbone induced by the molecular binding.[178,186] Such "chromatic liposomes" might be used as simple colorimetric sensors for screening of recognition processes involving carbohydrates and other biomolecules. A similar PDA-based colorimetric sensor was constructed in a Langmuir−Blodget film format, rather than the vesicle assemblies discussed above.[187] The film assay exhibited the blue−red transformations induced by biomolecular recognition and by other lipid-perturbing processes occurring at membrane surfaces. Song et al. have similarly reported the incorporation of gangliosides or sialic acid moieities in thin films, which permitted the colorimetric detection of CT or influenza virus, respectively.[187]

Sialic acid, the primary ligand for the hemagglutinin coat protein of influenza virus, has been also employed as a key component in colorimetric biosensor designs. Langmuir−Blodgett films as well as liposomes of polydiacetylenes derivatized with sialic acid were shown to undergo blue−red transitions that were specifically induced by binding to influenza virus particles.[179] Construction of sol−gel biosensors containing sialic acid as the recognition element for influenza virus was also reported.[188] In that technique, the researchers have incorporated blue PDA liposomes (see above) functionalized with sialic acid on their surface within transparent sol−gel matrixes. The entrapped liposomes still exhibited the blue−red transition following interaction of the sol−gel biosensor with influenza virus.[188] Indeed, the sol−gel matrix provided higher stability to the colorimetric biosensor compared to the more conventional soluble vesicle assemblies.

2.4.2 LPS Biosensors

Carbohydrate-based pathogen biosensors increasingly rely on detection of LPS moieties (also denoted endotoxins) on pathogen surfaces. LPS molecules, which consist of carbohydrates covalently attached to a lipid A moiety (Figure 8),[189] are located on the outer cell surface of various pathogens.[190] LPS plays a major role in conferring resistance of Gram-negative bacteria toward toxic agents, most likely by participating in the formation of an effective permeability barrier at the outer membrane.[191,192] Varied biosensor assemblies have utilized biomolecular recognition between surface-expressed LPS and lectins or other proteins. Ertl et al. described electrochemical biosensor arrays that facilitated *E. coli* subspecies detection through con A−LPS interactions[193] or through LPS binding to other lectins.[194] In particular, the researchers examined whether different lectins could *selectively* bind LPS moieties on surfaces of different bacteria. The construction of devices based on lectin recognition took advantage of the selective and reversible binding between the surface-immobilized lectins and the oligosaccharide groups. Electrochemical detection was facilitated through changes in the redox potential within the bacterial respiratory chain, following pathogen surface immobilization through the lectin−carbohydrate binding.[193,194] It should be emphasized that, even though carbohydrate recognition served in these biosensors only as an *indirect* means for bacterial detection, the high affinity between LPS and the lectin could generally ensure high sensitivity and fidelity of the sensor. Furthermore, the availability and diversity of known lectins and their carbohydrate ligands could facilitate the construction of sensor arrays for identification of several pathogens through their "signature response" in such arrangements.

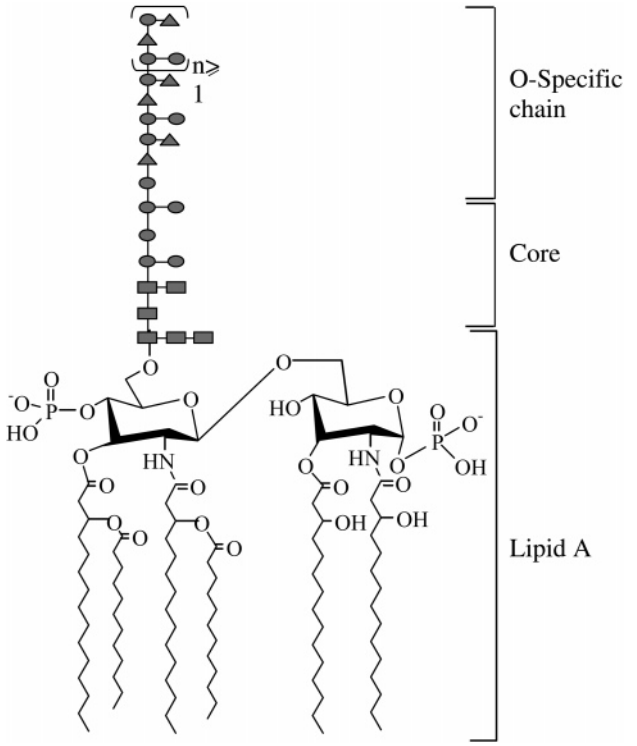

Figure 8. LPS structure.

Innovative LPS biosensors based on protein engineering have been developed.[195] A recent study illustrated a sensor concept in which the sequence of green fluorescent protein (GFP), a common fluorescent marker for protein targeting in intact cells, was modified to accommodate binding sites for either the lipid A moiety or the saccharide headgroup of LPS.[195] The engineered binding sites were localized in the vicinity of the chromophore of GFP, thus inducing fluorescence quenching following LPS binding. The research demonstrated the occurrence of a decrease of the fluorescence yield through association of the mutant proteins with lipid A or with LPS, exhibiting dissociation constants at the micromolar range.[195] The technique suggests that the use of genetic and protein engineering methods could assist in designing novel fluorescence carbohydrate biosensors. This approach could be attractive because it would take advantage of the vast knowledge base on protein structures and *de novo* structure design, increasing ligand affinities in protein-binding sites through residue modification and other factors. In

principle, integrating protein chemistry into carbohydrate-detection schemes could truly revolutionize the development of carbohydrate and pathogen biosensors.

A modified disposable QCM sensor for detection of LPS was reported.[196] The strategy undertook by the research was conceptually different than most other carbohydrate-detection schemes, focusing on detecting changes in the *solution viscosity* close to the sensor surface, rather than recording actual binding to *surface-immobilized* species. Specifically, it was shown that binding between the endotoxins and soluble *Limulus amebocyte* lysate (LAL) led to alterations in the acoustic load impedance at the sensor surface. One of the technical questions in this detection method concerns its intrinsic sensitivity, the extent of modification (damping) of the quartz oscillations induced by the changes in solution viscosity and density. The researchers claimed detection of LPS concentrations approaching 10 fg/mL, which is a rather low threshold. Increasing the hydrophilicity of the sensor might even improve the sensitivity further. Other bioanalytical assays in which LPS was an essential component were described. An ELISA approach using a phage LPS antigen was developed for identification of immunoglobulin antibodies to *Salmonella*.[197]

2.4.3 Cancer Diagnostics

Modification of carbohydrate expression and glycosylation patterns on cellular surfaces is a common feature of cancer cells.[198,199] A majority of human carcinomas are associated with altered expression of oligosaccharides on membrane glycoproteins, for example, in breast cancer,[200] adenocarcinomas of the pancreas,[201] cervical cancers,[202] and others. There have been intensive efforts toward development of diagnostic techniques for tumor identification utilizing carbohydrate markers on cancer cells.[199,203] Dwek et al., for example, have reported an immunohistochemical approach for early tumor detection.[199] Monoclonal antibodies (mAbs) identifying altered glycosylation of specific glycoproteins associated with tumor appearance were used as a diagnostic tool.[200,204]

Changes in the localization and relative abundance of carbohydrate species on cell surfaces can be monitored with the aid of specific carbohydrate-binding proteins, such as lectins. Lectin histochemistry has been utilized to identify modulation of the expression of sialic acid on human cervical carcinomas.[202] Plzak et al. employed biotinylated galactoside-binding (metal-ion-independent) animal lectins (galectins) to detect domains of increased differentiation in human carcinoma tumors.[205]

Sialylated Lewis antigens (SLeAs) and their enhanced cell-surface expression are recognized markers for various malignancies and metastatic processes.[206] SLeAs (a representative antigen, Silaylated Lewis^x, is shown schematically in Figure 9) have been frequently used as molecular targets in immunohistochemical and serological cancer assays.[207,208] MAbs have been raised and tested against SLeAs with the goal of developing immunoassays for the detection and management of malignancies.[209] An electrochemical biosensor approach for determination of the tumor-marker-bound sialic acid (b-SIA) was reported.[210] The sensor consisted of a copolymer-immobilized bilayer containing the enzyme sialidase, placed in contact with a H^+-selective poly(vinyl chloride)−poly(vinyl acetate) indicator membrane. The release of sialic acid, an α-ketocarboxylic acid with a pK_a of 2.6, following enzymatic cleavage resulted in a local pH change monitored by the proton-sensitive indicator electrode. This electrochemical sensor was shown to be capable of differentiating between pathological and nonpathological levels of b-SIA within a relatively short detection time (3−5 min) and in reasonable accuracy. The cancer marker Sialylated Lewis^x antigen and its mimetic structures have been comprehensively characterized through analysis of their binding to selectin, a natural lectin.[211]

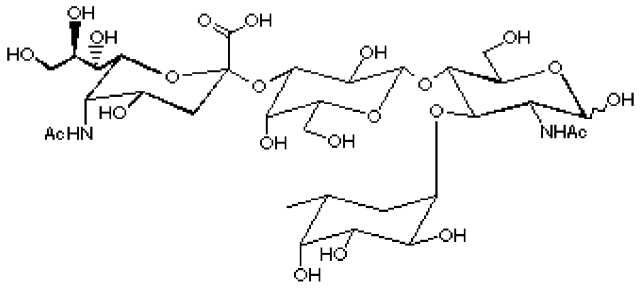

Figure 9. Silaylated Lewis^x structure.

Mucins, a class of highly glycosylated circulating proteins, were also investigated and utilized as biological markers of cancer.[212] Mucins have attracted particular attention as highly specific serum tumor markers because they could differentiate between epithelial ovarian carcinoma and benign growths. Mucin-based assays have significantly increased the specificity and sensitivity of cancer detection, having a significant potential for cancer patient management and tumor detection.[212]

2.5 Carbohydrate Nanobiosensors

The recent emergence of "nanotechnology" as a promising scientific and technological avenue has led to an expanding activity toward development of "nanobiosensors". Some studies have focused on the integration between carbohydrates and nanometer-size systems and devices, while other efforts have attempted to integrate advanced nanotechnology-oriented instrumentation within carbohydrate biosensors. You et al. described an amperometric biosensor facilitating high-sensitivity detection of sugar moieties through embedding nickel nanoparticles within a graphite-film electrode.[213] The authors reported that the dispersion of Ni nanoparticles within the carbon film yielded an order-of-magnitude improvement in the sugar-detection limit compared to conventional electrode arrangements. The use of nanoparticles was not directly related to the actual detection of the carbohydrate molecules but rather as a way for improving the technical performance of the electrode. Another study has employed nanosize amphiphilic C60 dendrimers for achieving better interactions between the sensor surface and the

carbohydrate analytes.[127] Binding was achieved through deposition of ordered Langmuir monolayers of the bucky-ball conjugated with glycodendron headgroups at the air−water interface. The films could be further transferred to solid quartz surfaces, pointing to their potential applications in biosensor design.

Atomic force microscopy (AFM) has been a major driving force in nanotechnology research and development. AFM is conceptually similar to the way old "long-play" records were read by the stylus of a phonograph, where the AFM tip acts like a "stylus" capable to image molecules and atoms on solid surfaces.[214] Among the most widespread applications of AFM in carbohydrate research has been imaging of single carbohydrate molecules and surface characterization of oligosaccharide assemblies.[213,214] An example of the practical application of AFM was its use for evaluation of the structure and texture of food carbohydrates.[215]

AFM has been explored as a tool for varied biosensor-related applications, such as determination of carbohydrate heterogeneity on bacterial surfaces[216] or the observation of a nonhomogeneous distribution of specific oligosaccharide units on the surface of yeast cells through derivatization of the AFM tip with lectins.[217] Such studies illustrate both the capabilities as well as the significant hurdles for application of single-molecule imaging and force measurements in biosensors. On one hand, the atomic-level resolution of AFM could provide unique "carbohydrate imaging fingerprinting" for bacterial and other cellular surfaces. One can conceive, in principle, the construction of an AFM image database for bacterial surfaces that might be used for rapid pathogen identification. Further contributions could be envisaged from integration of computer-aided image analysis into AFM-biosensor applications. However, the particular strength of AFM as a single-molecule-imaging technique rather than characterizing large-population ensembles could raise formidable difficulties in using this method for sufficiently fast and reliable detection. For example, the carbohydrate heterogeneity exposed by Camesano and Abu-Lail[216] could make any interpretation of AFM images of unknown pathogens inconclusive and highly complex. Furthermore, the very high sensitivity of AFM to environmental factors, such as temperature, salt types, and concentrations, etc., might lead to impracticality as a biosensing method.

The capability of AFM to resolve chemical and physical events involving single molecules has led to exploration of other potential biosensor applications. AFM was used for characterizing structural properties of a single xanthan molecule on a solid surface.[218] AFM was also employed for detection of bacterially secreted carbohydrates in river sediments.[219] A novel saccharide "force fingerprinting" technique, based on the single-molecule-imaging capabilities of AFM was reported.[124] The method has built upon the variability of force-induced conformational transitions of the pyranose ring, which are also dependent upon the glycosidic linkages in the molecules. These transitions yield characteristic force-spectrum fingerprints for specific carbohydrates.[124]

The AFM methodology can further identify individual carbohydrate molecules in solution, contributing to its bioanalytical applicability. For example, the capability of AFM to distinguish among chair-twist−boat conformational transitions of the pyranose ring within different α-(1,4)-linked carbohydrates could serve as a "nanomechanical" fingerprinting of different oligosaccharides.[220] AFM was also used to evaluate minute differences in the forces between carbohydrate moieties on bacterial cell walls and biopolymer surfaces, pointing to its use as a tool for bacterial detection.[221]

2.6 Miscellaneous Carbohydrate Bioassays

A large number of bioanalytical techniques are used for routine carbohydrate analysis. Detection methods of carbohydrates in food products, particularly fruit, have been reviewed.[222] The majority of saccharide analysis schemes in food processing combine compound separation, mostly chromatography, and detection. GC has been popular for carbohydrate analysis because it has the advantage of speed, although this technique generally requires carbohydrate prederivatization.[223] TLC is relatively inexpensive; however, it lacks in resolution and quantification information.[224,225] Other techniques have been used, primarily HPLC using polar and nonpolar columns,[226] anion-exchange columns,[222] or cation-exchange columns.[227,228]

Theoretical analyses have been employed in conjunction with carbohydrate biosensor studies. Fractal analysis was used to characterize the binding kinetics between cell-surface receptors (such as bacterial-displayed oligosaccharides) and external soluble analytes.[229] Such theoretical treatments could be of use in interpreting oligosaccharide-binding data and for optimization of sensor performance.

3. Carbohydrate Components in Biosensors

3.1 Carbohydrate Recognition Elements

Carbohydrates often constitute fundamental parts within biosensor devices, either comprising the recognition elements or as scaffold components of the sensor matrixes. Such applications take advantage of two important (and unrelated) properties of carbohydrates. The first is the participation of numerous oligosaccharides in molecular recognition phenomena, which could make them ideal for targeting specific analytes. Another oft-encountered characteristic of molecular framework arrays constructed from saccharide assemblies is their stability and rigidity, making them attractive components in biosensor design.

Films composed of synthetic saccharide derivatives for potential biosensor applications have been constructed.[230] That study presented a detailed physicochemical characterization of the organization and cooperative properties of lipo/glycohomopolymer and random lipo/glycocopolymer monolayers assembled at the air−water interface. The researchers have further proposed utilization of the molecular recognition properties of such films in carbohydrate-based biosensor designs.[230] Similar surface-deposited films of

glycopolymer conjugates were prepared.[231] This research achieved adsorption of SAMs of glycopolymers, specifically polystyrenes carrying maltooligosaccharides with different chain lengths and lactose-carrying polymers with polystyrene and polyphenylacrylamide main-chain structures, which were investigated by QCM.

Other innovative approaches for fabrication of glycoconjugate-containing monolayers and films were described. A recent study focused on the insertion of P glycoprotein (P-gp) into planar lipid bilayers formed either by liposomes disassembled on amorphous carbon film surfaces or as Langmuir−Blodgett monolayers.[232] Specifically, P-gp, a membrane drug pump, was incorporated in model membranes obtained by fusing P-gp-containing vesicles onto two hydrophobic supports: amorphous carbon films or Langmuir−Blodgett lipid monolayers. The researchers demonstrated that the glycoprotein retained its functionality and recognition properties in these model systems, most likely because of the supported lipid bilayer scaffolding. Another important factor contributing to the recognition capabilities of the films and potential utilization is the type and quality of the solid surface, which was shown to intimately affect the vesicle fusion and protein display.[232]

"Surface glycoengineering" methods that could produce carbohydrate-recognition films were reported. Chevolot et al. demonstrated a strategy for chemical immobilization of saccharides through diazirine derivatization.[233] The technique employed synthesis of aryl diazirine coupled to mono- and disaccharide moieties; illumination of the diazirine resulted in covalent binding of the carbohydrates to the polystyrene surface. Even though covalent binding of carbohydrates to surfaces has been achieved using varied methods,[234] *photo*immobilization has the potential to produce well-defined patterns, feasible through the advanced microprinting technologies prevalent in the electronic and semiconductor industries. Further pointing to the integration of electrooptics and carbohydrate biosensors, chemical conjugation of carbohydrates to a sensor surface was carried out for construction of the chemiluminescence-based optical fiber immunosensor.[235] This assembly was designed to identify anti-pneumococcal antibodies, in which pneumococcal cell-wall carbohydrates were covalently attached to optical fiber tips. The optical immunosensor system was shown to be an accurate and sensitive method for detection of antipneumococcal antibodies in specimens such as saliva and urine.

A generic design for biosensor application using immobilized carbohydrates for molecular binding is shown in Figure 10. The key for construction of such biosensor is the efficient immobilization and display of the carbohydrate ligands on the surface, facilitating both interactions with soluble analytes, as well as transduction of the analyte binding to the sensor surface for generation of a measurable signal. Optimization of the deposition and adhesion properties of carbohydrates on solid surfaces are critical to construction and applicability of biosensors. Several investigations focused on characterization of the

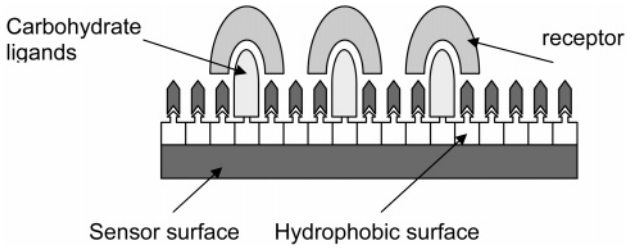

Figure 10. Schematic representation of a generic binding assay containing surface-immobilized carbohydrates. The carbohydrate ligand is displayed within a biocompatible layer, which is placed on the transducer surface of the biosensor.

factors affecting carbohydrate attachment onto solid surfaces and the binding specificity and adhesion properties of biomolecules onto carbohydrate-derivatized surfaces.[236,237] A comparative study has identified key properties that make specific carbohydrate coatings resistant to the adsorption of proteins.[237] Dutra et al. have devised a method for immobilization of a pneumococcal carbohydrate onto silicon oxide wafers for use in surface acoustic wave biosensors in which the sugar molecules were attached to the surface through their specific binding to protein A, which was chemically adsorbed to the solid surface.[238]

Some applications have utilized the strong affinity of ionic carbohydrates to particular metal ions in the design of voltammetric-sensing devices.[239] The electrochemical biosensor was composed of an ion sensor for copper and lead by means of incorporating pectic and alginic acids and heparin onto copper electrodes. The accumulated metal ions in such assemblies modified the recorded voltage, thus allowing high sensitivity and reproducible cation detection. Even though (or perhaps because) this method reports upon the presence of the carbohydrate indirectly (through density of the metal ions), the sensitivity of the biosensor was quite satisfactory.

Novel colorimetric detection methods for toxins and pathogens based on the affinities of carbohydrate ligands embedded within sensor assemblies to their soluble molecular counterparts were reported.[181,240] The sensing schemes consisted of carbohydrate derivatives (lipopolysaccharides and gangliosides) incorporated within a polydiacetylene matrix undergoing dramatic blue−red transitions induced by binding between the embedded carbohydrate moieties and soluble macromolecules or intact pathogens (Figure 7, above). Examples of the applications of this technology include the detection of CT,[178] endotoxin binding,[186] and screening of LPS-binding antimicrobial peptides.[181] Other sensors consisting of chromatic scaffold materials were developed, including a family of glycopolythiophenes containing sialic acid or mannose ligands that exhibited binding to lectins, influenza virus, and bacteria.[241] Similar to the PDA-based sensors, the ligand−receptor binding in these polymers resulted in an unusual red shift of the visible absorption spectra.

Other design principles employed in biosensor development take advantage of the unique assembly properties of cell-surface glycoconjugates. Several publications reported on the construction of ampero-

metric enzyme sensors for sucrose based on bacterial cell-surface layers (S layers) as immobilization matrix for the biological recognition elements.[242,243] S layers, consisting mainly of identical glycoprotein (or other protein) subunits displaying organized and oriented functional groups,[244] represent ideal matrixes for display of enzymes and other functional macromolecules as required for biosensor development and applications. A recent study demonstrated immobilization of S-layer glycoproteins through activation of the hydroxyl groups of the carbohydrate chains with cyanogen bromide or their conversion into carboxyl groups by succinylation.[245] These S-layer-mimicking templates were further coupled to saccharide-degrading enzymes such as glucose oxidase, β-fructosidase, and mutarotase and incorporated within amperometric and fiber-optic biosensor prototypes. Similar experiments utilized two-dimensional glycoprotein crystals as patterning elements and immobilization matrixes for the development of biosensors.[246]

Construction of oligosaccharide arrays has opened the way for coupling glycochemistry with high-throughput screening applications. A novel carbohydrate array has been recently used for profiling and identifying anti-glycan antibodies.[247] In this study, an immobilized glycan array was created by covalently linking the oligosaccharides to a solid surface via a long linker at their reducing ends. The carbohydrates were thus presented to the medium with a well-defined orientation and were accessible for specific binding by glycan-binding proteins, antibodies, and lectins. In preliminary experiments, the researchers used the technique to identify a novel anticellulose antibody that binds specifically to β4-linked saccharides with a preference for glucopyranose over galactopyranose residue. Also discovered in that study were antibodies against mono- and oligosaccharides displayed on surfaces of common bacteria. The introduction of this array biosensor emphasizes the crucial role of clever chemistry for achieving optimal recognition and sensing conditions. The carbohydrate array approach could be employed for high-throughput screening of glycan-binding proteins, pathogen detection, and putative bacterial adhesion substances.

Molecular recognition of oligosaccharides by specifically raised antibodies constitutes the basis for new chemiluminescence-based optical fiber immunosensors.[235] In that technique, chemiluminscence was induced within derivatized antibodies following their binding to immobilized carbohydrates. The concept was demonstrated by chemically conjugating pneumococcal cell-wall carbohydrates to an optical fiber tip, detecting accurately anti-pneumococcal antibodies. This optical immunosensor system might be applied to monitor antibodies in specimens such as saliva and urine.

3.2 Carbohydrate Scaffolds

A number of carbohydrate molecules have been used as rigid components in biosensors. The glycopolymer agarose and cellulose are likely the most widely used constituents of rigid matrixes and gels

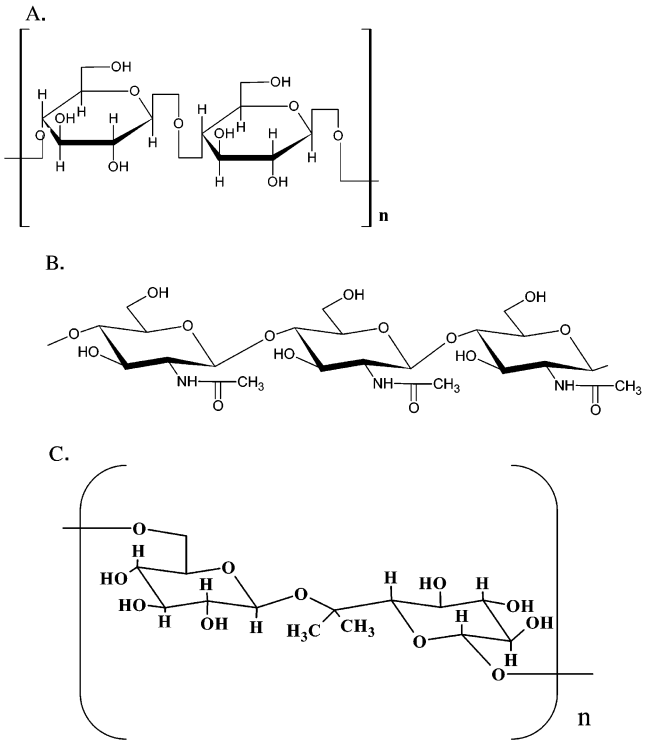

Figure 11. (A) Cellulose structure. (B) Chitin structure (fragment). (C) Dextran structure.

for numerous bioanalytical applications.[248] Cellulose is an abundant natural glycopolymer (Figure 11A), and its distinct physicochemical properties, in particular, its rigid structure, have made it an abundant component in biosensors. Hartmann et al. reported the fabrication of cellulose−antibody films for highly specific evanescent wave immunosensors.[249] Cellulose was recruited for this particular biosensor design as a substrate for deposition of highly stable antibody films on the sensor surface.

Chitin (Figure 11B), a major component of the outer shells of crustaceans, has been also used as a framework constituent for immobilization of recognition elements in various sensor devices.[250,251] The excellent biocompatible properties and relative biological and chemical inertness of chitin and chitosan, its deacetylated derivative, have made these compounds attractive as matrixes for enzyme sensors [250] and potentially implantable devices.[252] Chitin-constructed membranes further exhibit attractive protein entrapment properties and favorable oxygen and glucose permeability profiles, making them highly compatible for biosensor design.[253] The use of chitin in sensor frameworks assists in maintaining the stability and durability of the biosensor system.

Similar to chitin, dextran has been employed as a template and backbone component in numerous biosensor designs. Dextran (Figure 11C) has a repeating uncharged glucose chain structure making this carbohydrate particularly attractive as an inert structural element in biosensors. Dextran assemblies are mostly incorporated as layers or films supporting biological interactions essential to the sensing capabilities.[254] Derivatized dextran polymers have been used as matrixes for affinity biosensors.[255] In another application, highly wettable, covalently grafted, dex-

tran coatings were applied to flat silicon wafer surfaces to be used in potential sensor devices.[256]

Other representative biosensor applications of dextran include its use as a substrate for β-cyclodextrin immobilization in immunosensors,[254] as a material used for functionalization of novel carbon nanotubes in electronic sensors,[257] and for enzyme immobilization.[258] Several schemes utilized fluorescently labeled dextran. Dextran labeled with fluoroscein isothiocyanate (FITC) was used as a framework for a glucose biosensor using the FRET technique.[259] Dextran was co-entrapped with a hydrolytic enzyme in sol−gel films developed for pH sensing.[260] Fluorescently labeled dextran was deployed in conjunction with the lectin con A in a hydrogel arrangement for glucose sensing,[102] employed as a surface-functionalizing agent facilitating antibody immobilization in chemoluminescent immunosensors,[261,262] and as the constituent of a coating layer in surface acoustic waveguide (SAW) biosensors.[263]

Cyclodextrins, macrocyclic carbohydrates with nonpolar internal cavities that participate in numerous chemical systems and applications, have been also widely used in biosensor design.[264] These inclusion compounds have generally appeared in sensor schemes as framework elements facilitating immobilization of other molecular species that are essential for the functionality of the sensor. A representative cyclodextrin-based biosensor was described by David et al., constructing an immunosensor by grafting amino-β-cyclodextrin onto functionalized gold surfaces.[254] The incorporation of additional dextran-derivatized adamantyl groups (adamantane derivatives being the common ligand of cyclodextrins) enabled the coupling of antibodies as the biological recognition elements within the biosensor. Other cyclodextrin-templated biosensors were reported, including cross-linked cyclodextrin films within dopamine biosensors[265] and β-cyclodextrin derivates impregnated in graphite paste for enzyme immobilization in amperometric enantioselective drug biosensors.[266]

Other carbohydrates have been used as substrates in gel constructs for detection of reactant species in the mobile phase. Carboxymethyl (CM)-curdlan, a carbohydrate linked with a chromatic dye, was assembled within polyacrylamide gels for facilitating rapid colorimetric detection of glucanases.[267] Beside applications in which carbohydrates have been directly involved in biochemical reactions, saccharides have been incorporated in sensor assemblies as chemically inert species, albeit essential to the functionality of the systems. Brinkman et al., for example, reported on the construction of hydrogels comprised of poly(vinyl alcohol) and heparin.[268] On one hand, the cross-linked assembly was shown to resist nonspecific protein permeation, an important requirement for biosensor design but, on the other hand, facilitated slow release of the incorporated heparin, thus pointing to potential biosensor applications. Saccharide derivatives were also examined for their ability to form solid gels for cell-based biosensors.[269] O'Connor et al. examined the entrapment of neuronal cells in a three-dimensional matrix constructed from a novel sugar poly(acrylate) hydrogel.[269] A significant hurdle to such biosensor applications has been an insufficient adsorption of the cells to the saccharide template.[269]

Novel uses for carbohydrates as templating agents were reported in the framework of molecular-imprinting technology.[270,271] Shi et al. described a template-imprinted matrix for protein recognition in which the protein-binding sites were molded by a disaccharide framework.[270] The carbohydrate molecules were particularly important in that setup, providing added synthetic flexibility and analyte specificity. This experimental achievement is noteworthy because it points to a generic synthetic pathway for constructing molecularly imprinted protein biosensors, a highly challenging goal in recent years.

Several studies have addressed theoretical aspects pertaining to carbohydrate-containing biosensors. Griesser et al. investigated the interfacial forces between carbohydrate surfaces and adsorbed proteins.[237] When theoretical predictions and experimental approaches such as X-ray photoelectron spectroscopy (XPS), MS, and AFM are combined, the researchers have established key parameters responsible for the resistance of particular polymer coatings to the adsorption of proteins, an important feature of varied biosensor arrangements.

3.3 Biosensors Utilizing Protein–Carbohydrate Interactions

Molecular recognition and interactions between carbohydrates and proteins play key roles in many biochemical processes. The participation of specific oligosaccharide sequences in protein targeting and folding and in propagating infection and inflammation processes through interactions with receptors and antibodies have become increasingly apparent.[1] Studying such interactions is also desirable for development of therapeutic substances that would mimic or interfere with the recognition process. Various approaches have been introduced to probe carbohydrate−protein binding and to utilize such recognition events in the action mechanism of biosensors. However, elucidation and understanding of the bioactive domains within oligosaccharides and their protein-binding properties pose distinct bioanalytical and chemical challenges.

From the standpoint of biosensor design, protein−carbohydrate binding has been employed as a platform for extraction and analysis of varied proteins. In most of these applications, the biosensor operation relies on immobilization of carbohydrate species, which generally function as the recognition elements, followed by generation of measurable signals induced by association with their complementary macromolecules. Construction of carbohydrate-modified recognition surfaces is synthetically demanding because of the structural complexity of oligosaccharides. Distinct problems have been encountered because of the multiplicity of hydroxyl groups that might make specific binding difficult, as well as the requirement of appropriate linker systems to facilitate display and access to the immobilized oligosaccharides.[250] The two most common carbohydrate immobilization tech-

niques employed in such sensors exploit the high affinity of the biotin−avidin pair[272] or the deposition of alkane thiolate monolayers on gold surfaces.[273]

Biosensor technologies based on surface immobilization of oligosaccharides have to address critical technical and fundamental issues. A primary requirement concerns the feasibility of attaching the generally hydrophilic carbohydrate molecules to solid transducer surfaces. In that regard, most surface-layering strategies use hydrophobic chemical interactions. Consequently, many sugar immobilization methods require chemical modification of the saccharide molecular units. Such chemical treatments, however, should not interfere or adversely affect the biological properties of the examined carbohydrates, in particular, molecular recognition by soluble macromolecules. Furthermore, any proposed biosensor design has to exhibit high sensitivity and sufficient versatility for allowing detection of a wide range of proteins and other biomolecular analytes.

A recent development with potentially significant implications for glycobiology research in general and studying carbohydrate−protein interactions in particular has been the fabrication of carbohydrate arrays as a tool for rapid analysis of sugar-binding events and carbohydrate interactions. Examples for such applications include array carbohydrates that are first immobilized on pretreated surfaces, followed by addition of fluorescently labeled carbohydrate-binding proteins; binding occurrence can then be monitored by fluorescence spectroscopy.[274] The challenges for wide applications of such methodologies, however, are mostly synthetic, i.e., the construction of diverse enough, analyte-accessible immobilized carbohydrate arrays.

An elegant and important demonstration of noncovalent immobilization of a carbohydrate antigen array on glass surfaces was recently reported.[26] The researchers assembled dextran polymers produced by *Lactobacillaceae* bacteria on nitrocellulose-coated glass slides and examined binding of anti-dextran antibodies to the slides using fluorescence scanning. Immobilization and specific antibody−antigen binding were detected in this configuration. Glass-immobilized carbohydrate microarrays could have significant diagnostic and clinical applications, including rapid detection of specific antibodies in physiological solutions and "antibody profiling" of such solutions, identification of cross-reactive antibodies and antigens, and quantitative determination of carbohydrate diversity within microorganisms. The platform developed by Wang et al. is particularly robust and involves relatively straightforward preparative steps, facilitating rapid analysis of complex solutions through simple and sensitive detection schemes. Furthermore, this method intrinsically enables the display of a large repertoire of cellular carbohydrates and carbohydrate antigens on a single slide, approaching the capacity to include oligosaccharides encountered in most common pathogens.

Varied chemical strategies were introduced for fabrication of carbohydrate arrays for high-throughput screening applications. As a parallel to the more widely used "DNA chips", "carbohydrate chips" could facilitate rapid evaluation of protein−saccharide interactions. Carbohydrate chips for evaluation of lectin binding and glycoenzyme substrate specificities were prepared by saccharide immobilization onto SAMs of cyclopentadiene conjugates via the Diels−Alder reaction[275] or through coupling of the carbohydrates to thiol moieties.[276] The functionalized monolayers in those studies contained chemical entities such as benzoquinone[275] or maleimide[276] for covalently bonding the carbohydrate derivatives but also displayed ethylene glycol for minimization of nonspecific protein attachment to the surface. Such surface engineering strategies might find uses in sensor applications for analysis of complex carbohydrate structures. However, the ultimate utility of such "biochip" designs would most likely depend on the detection method to be used, its sensitivity, reproducibility, and technical limitations. For example, fluorescence microscopy could provide high sensitivity and spatial resolution; however, this technique might incur problems of bleaching, background signals, and surface regeneration.

Progress in carbohydrate array research has been also achieved through the creation of microarrays of *neoglycolipids* and their display on solid surfaces.[277] Neoglycolipids, comprised of oligosaccharides chemically conjugated to lipids, can be readily immobilized on solid matrixes through their hydrophobic lipid residues, thus facilitating the surface display of the carbohydrate molecules for rapid screening of binding interactions.[81] Immobilized neoglycolipid assemblies could achieve higher avidity of protein analytes because of lipid clustering and surface oligomeric organizations of the oligosaccharides.[81] The microarrays constructed by Fukui et al.[277] contained neoglycolipids prepared from diverse physiological and synthetic sources (including extracts from whole organs). That exploratory and potentially groundbreaking study demonstrated that carbohydrate-recognizing proteins bound their ligands not only within arrays of homogeneous oligosaccharides but also within mixture of heterogeneous carbohydrate species. The technology could have much more general diagnostic appeal, as a tool for profiling carbohydrate-binding proteins from different sources, for discovery of new carbohydrate-binding proteins within cellular targets, and for large-scale analysis of protein-binding characteristics of the glycome.

A recently reported screening assay for protein−carbohydrate recognition utilized surface immobilization of sulfated carbohydrates.[278] The technique, denoted sulfated carbohydrates coating ELISA (SPC-ELISA) employed initial coating of sulfated carbohydrates followed by binding with different target proteins, consequently detected by a conventional ELISA method. Complementing carbohydrate immobilization and immunosorbent detection in SPC-ELISA has some advantages over other frequently applied immunosensing techniques, including its compatibility with automation in general and high-throughput screening methodologies and equipment in particular and the versatility of the technique with regard to molecular-target variability and detection methods.

A novel technique for the screening of carbohydrate−peptide interactions through phage-display selection of peptide binding to mirror-image sugars has been developed.[279] The researchers used phage display to identify peptides that bind to surface-immobilized synthetic L-type saccharide enantiomers; the corresponding *mirror image* peptides that bind the D-type saccharides could then be identified through application of SPR. The technique was demonstrated for detection of saccharide binding to high-affinity antibodies.

Interactions between proteins and glycolipids are of particular importance in carbohydrate-based biosensor design. The lipid moieties of glycolipids are generally buried within the hydrophobic membrane bilayer, leaving on one hand, the oligosaccharide components exposed to the solution but, on the other hand, close enough to the bilayer surface facilitating ligand presentation. Furthermore, the structural features of immobilized glycolipids might play pivotal roles in shaping carbohydrate−protein binding. This is mostly due to the observations that *multivalent* interactions rather than the relatively weak monovalent affinities are prevalent between proteins and carbohydrates.[280] Studies of protein−saccharide recognition and the effects of the membrane environment on these phenomena are in their infancy.[281] The presence of the acyl chains could be further advantageous for immobilization of the carbohydrate recognition elements within varied hydrophobic surfaces in potential membrane-mimic biosensor designs. The creation of surface patterns of glycolipid targets and biosensor arrays[282] would be a natural extension of the immobilization capabilities.

Pathogen detection is an important field in which glycolipid−carbohydrate interactions could be of particular importance. The interactions between gangliosides and CTs have been widely studied and included in biosensor designs, in many instances using surface immobilization of GM1 (see section 2.4.1, above). A multiarray evanescent wave biosensor for detection of CT was described in which gangliosides immobilized at discrete locations on the surface of an optical waveguide.[282] Rapid and easy detection of the fluorescent-labeled CT or tracer antibodies was achieved using the same technique.[157] Other examples for the use of the CT−GM1 recognition pair in biosensor design are described above (see section 3.3, pathogen detection). The binding between globotriaosylceramide (Gb3) and *E. coli* verotoxins could similarly constitute the core of diverse bacterial detection schemes.[281]

Heparin−protein binding constitutes the basis of varied peptide and protein bioassays. A range of techniques has exploited surface expression and the selective protein-binding properties of heparin and its derivatives in biosensor devices and as vehicles for diverse detection schemes. "Heparin biochips" were constructed for applications in techniques such as SPR to measure the extent of heparin−protein interactions.[283,284] In such applications, it was observed that the biosensor response was often affected by the method of heparin immobilization on the solid surface.[284] Covalent attachment of glycosaminoglycans such as heparin and heparin derivatives has been problematic because of the presence of only a single reducing-end amine group.[283] Original methods for surface immobilization of heparin were proposed, including covalent attachment of heparin on an evanescent wave biosensor cuvette,[285] binding as an albumin conjugate on a functionalized polystyrene surface,[286] and on a SPR biochip.[283] Evanescent wave biosensors have been used for studying heparin−protein interactions.[285] Optical sensing of heparin/albumin thin films was used to measure modifications of film thickness by the pH of the solution.[287] SPR analysis was also carried out to systematically evaluate interactions between collagens and different heparin derivatives.[288]

QCM has been applied for detection of various biological saccharide-binding reagents. There has been, however, some skepticism as to the accuracy and applicability of the technique for analysis of molecular recognition, partly related to problems arising from immobilization and positioning of large biomolecules on the sensor surface.[52] A procedure for incorporation of α-galactose antigen on a microbalance surface resulting in a rigid and sensitive recognition biofilm was recently described.[289] In that work, SAMs of α galactose were prepared by thiol-tail derivatization, allowing construction of a highly reproducible and selective lectin sensor.

Carbohydrate−protein binding has an additional advantage when utilized in biosensor design. This is due to the fact that one of the most important criterion for efficient, reversible surface immobilization of biomolecules in sensor devices is whether such molecules retain their biological functions. This issue is particularly important in biosensors based on enzymatic reactions.[290] The optimal design should permit high affinity of the enzyme to the surface to avoid loss; however, the attachment should not be too strong as to not allow enzyme elution and regeneration.[291] Chemical or physical adsorption techniques are often inadequate for such requirements, and biospecific methods are also problematic. For example, binding based on the avidin−biotin system is too strong (binding constant K_{ass} in the order of 10^{15}), and antibody−hapten association, while in the correct binding-strength range, is highly dependent upon the immuno system and solution conditions. Lectin−carbohydrate binding ($K_{ass} = 10^6-10^7$), on the other hand, offers a practical route for reversible immobilization of enzymes and recognition elements in biosensors.[292] Koneke et al. demonstrated the use of con A for reversible immobilization of glucoenzymes within a fluoride ion-sensitive field-effect transistor (FET).[291] Enzyme-reloading in the biosensor assembly was achieved through removal of the lectin-bound glucoenzymes by elution with soluble mannosides.[291]

Carbohydrate−lectin binding is central to other biosensor designs. Galanina et al. have synthesized and compared radioactively and fluorescently labeled carbohydrate conjugates for detection of cell-expressed lectins.[293] The technique was based on the coupling of the saccharide moiety to a soluble polyacrylamide spacer, onto which were attached the

reporter molecules. This synthesis approach was reported to achieve optimal binding of mammalian cells to the carbohydrate ligands, without interference from the spacer arms and the molecular labels. The different molecular components further aided in prevention of nonspecific binding of the cells. The technique was easily amenable to conducting experiments in a standard 96-well plate setup and also for cell- and tissue-staining applications. Organic chemistry synthesis approaches have been employed for creation of carbohydrate conjugates used in electrochemical biosensors.[294,295] Kitov et al. have synthesized a hexadecanyl−polysacchride conjugate to facilitate incorporation of the carbohydrate recognition element within a hydrophobic film.[294] The carbohydrate−protein recognition pair in other designs perturbed the electron-transfer properties of a self-assembled alkaneoid film that constituted the biosensor.[295]

3.4 Carbohydrates in SPR

SPR has become a powerful and widely used analytical technique for evaluating and quantifying biomolecular interactions. SPR measures binding interactions between molecules immobilized on the surface of a biosensor chip and their soluble counterparts through optically monitoring changes of the refractive index in the vicinity of the sensor surface (Figure 12).[296,297] General reviews on the subject of SPR analysis of carbohydrates and glycoconjugates are available.[298] Below, we summarize some of the research activities concerning carbohydrate SPR biosensor applications.

One of the detriments for the use of SPR in carbohydrate analysis has been whether effecient immobilization of the molecular recognition elements on the sensor chips is feasible. While a number of chemical processes have been introduced to immobilize proteins on the biochip surface,[299] similar procedures for carbohydrates have been limited. SPR sensors attained carbohydrate immobilization through the bridging biotin−avidin system.[300,301] Nonspecific interactions with avidin, however, become problematic in such arrangements.[283] Direct binding through covalent attachment of conjugated carbohydrates has been reported.[283] Ordered multilayers of heparin/albumin could serve as biocompatible films in SPR applications.[302] Neoglycoconjugates, consisting of synthesized molecules of glycosides and carrier molecules such as proteins or lipids, were used as affinity ligands for deposition on SPR sensor surfaces, although these molecules also exhibited relatively low affinities.[303] Recent studies attempted to construct stable and tightly bound carbohydrate layers through nanoscale coatings on solid surfaces.[169] Such systems could have potential uses in varied biosensor applications.

Numerous experiments designed for studying carbohydrate recognition using SPR biosensors have been reported. The technique was applied for analysis of carbohydrate−antibody recognition involving individual saccharide molecules[304] or oligosaccharide antigens on bacterial surfaces,[305] interactions between oligosaccharides and integral membrane proteins,[306] pattern receptor recognition by glucans in human monocytes,[307] substrate recognition by saccharide-digesting enzymes,[308] or the effect of clustering of glycosidic units.[309]

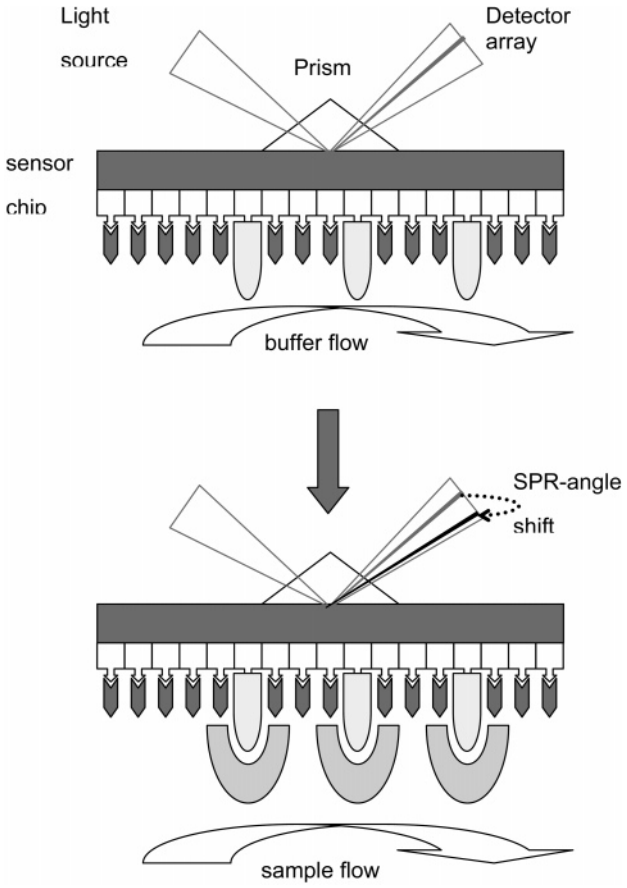

Figure 12. Schematic representation of a SPR biosensor. The ligand is immobilized on the sensor surface (above). When the analyte in a sample solution binds to the ligand, the refraction index of the surface is modified, resulting in a shift of the angle of refracted light.

SPR biosensor chips have been developed for capture and detection of vesicles containing glycolipids and other membrane-bound carbohydrate receptors.[163] This application required initial physical immobilization of the carbohydrate-containing vesicles, followed by addition of the complementary receptors, which were detected by the SPR signal. The method was demonstrated for detection of CT through vesicle-incorporated GM1 ganglioside.[163] This extension of the SPR technique is important because numerous carbohydrate species are bound or displayed on cell surfaces through hydrophobic residues. Such applications, however, necessitate efficient immobilization of the vesicles without destroying them, which could pose technical difficulties.

SPR-based biosensors have been used for detection of carbohydrate derivatives, such as glyocolipids and glycoproteins. The envelope glycoprotein gp41 of HIV was employed for studying antibody binding to the glycoprotein and the effect of serum on the recognition process.[310] Binding and kinetic profiles of the interaction between platelet glycoproteins and fibrinogen were evaluated by application of SPR.[311] Related experiments examined the occurrence and kinetic properties of biochemical reactions involving

carbohydrates, for example, the *in situ* analysis of dextran monolayer degradation by dextranase.[312]

Carbohydrate−lectin interactions have been frequently employed as a basis for SPR biosensor applications. These approaches were aided by the broad knowledge base regarding the pool of saccharide ligands attracted to various lectins. Examples of such SPR applications include steady-state and kinetic analyses of lectin binding to oligosaccharides and glycopeptides,[115,313] analysis of lectin interactions with C and O glycosides linked to a carboxymethyl dextran layer on the SPR sensor surface,[314] carbohydrate-binding activity and specificity of a lectin extracted from bulbs of spring crocus,[315] structural basis for the unusual carbohydrate-binding specificity of jacalin, the seed lectin from jack fruit (*Artocarpus integrifolia*),[316] and others. Lectin−glycolipid binding formed the basis of surface immobilization procedures in miniaturized SPR sensors.[317]

SPR was used for detection of carbohydrates in physiological solutions at high sensitivities.[318] A SPR sensor for heparin featured a surface that was coated either with protamine or polyethylene imine. Importantly, the degrees of heparin affinities were dependent upon the receptor species coating the surface in each case. The sensor performance was also found to be affected by incubation time, heparin dilution, and the presence of other components in the analyte solution. Nonspecific adsorption had to be additionally overcome by optimization of the experimental conditions, overall indicating that the intrinsic high sensitivity of the SPR technique could also pose problems for carbohydrate-binding analysis. Aside from detection of carbohydrates in varied solution environments, heparin and its derivatives have been employed as recognition elements in SPR biosensors. SPR was used to evaluate heparin binding to chemokines, a process believed to be central to chemokine functionality.[319] The relative degree of avidin binding to heparin and its derivatives was also evaluated using SPR biosensors.[320] Heparin and heparan sulfate were used as substrates for studying membrane interactions and host entry of HSV.[321] Another application employed heparin-modified gold surfaces for analysis of low-density lipoproteins (LDL).[322]

SPR has been additionally used for determination of glycosylation changes in proteins. SPR analysis of glycoproteins has been generally achieved through immobilization of the proteins on the sensor surface by using antibodies and identification of carbohydrate epitopes through binding of specific lectins.[323] It was also reported that modifications of the affinity between the biosensor-immobilized proteins in the cell-culture supernatant and added lectins allowed analysis of glycoprotein concentrations and changes in protein glycosylation.[323]

Evaluation of protein binding to surface-immobilized LPS was carried out using specially designed SPR biosensors, because of the importance of LPS constituents in affecting protein binding to varied cell surfaces.[324,325] Biosensor chip surfaces derivatized with different quantities of LPS were used for determination of peptide- and protein-binding constants.[326] Immobilization of LPS in these sensor chips was achieved thorough attachment of the biotinylated saccharide molecules to streptavidin-coated sensor surfaces. The protein affinities to LPS in such assays were evaluated through the changes in mass close to the sensor surface.

While most oligosaccharide immobilization techniques have been based on the avidin−biotin high-affinity system, other methods were reported. Catimel et al. described antibody detection by SPR, which was carried out through direct immobilization of gangliosides onto the sensor surface by hydrophobic interactions.[327] The advantage of this type of approach was the forestalling of chemical derivatization of the saccharide molecules or of the sensor surface, leading to simplification of biosensor construction. In a different modification of the SPR sensor chip, complete vesicles containing ganglioside GM1 were surface-immobilized, deriving affinity and kinetic information upon binding of CT.[163]

Other chemical methods were introduced to immobilize and display carbohydrates and glycoconjugates on SPR biosensor surfaces. Stein et al. reported on modifying a carboxymethyldextran surface to couple the lipid-anchored contact site A (csA) of a homophilic adhesion glycoprotein of the bacterium *Dictyostelium discoideum*.[328] The carboxy groups in the derivatized layer were modified to enable hydrophobic binding of the glycoprotein via its lipid anchor to the dextran matrix. Alternatively, the researchers employed covalent binding through a perfluorophenylazide-derived hydrophobic cross linker. Titration experiments verified that the bound csA molecules reacted with antibodies that recognize either the native or the denatured glycoprotein; thus, they most likely adopt a native state in the sensor surface environments.[328]

In addition to detection of carbohydrate-binding species, SPR has been used for studying various parameters contributing to such interactions. SPR has been applied, for example, to assess modulation by pH, divalent cations, and polyamines on the high-affinity binding of antibodies to polysialic acid (PSA) expressed on the vertebrate neural cell adhesion molecule (NCAM).[329] In such experiments, the sensitivity of the optical signal generated by the sensor response facilitated identification of slight changes in the binding events.

4. Concluding Remarks

The increasing awareness of the biological importance of oligosaccharide derivatives and growing interest in glycobiology applications have clearly become a major driving force toward development of new techniques for carbohydrate characterization. This review summarized the large body of recent experimental work dedicated to construction of biosensors and bioassays designed to detect and analyze carbohydrates and glycoconjugates, and sensors utilizing carbohydrates for detection of other soluble biomolecules.

The complexity and high variability of carbohydrate structures have often placed formidable barriers toward their practical applications; however, these properties might as well open new avenues to

biosensor applications specifically based on the differences among carbohydrate groups and their biological expression. Varied carbohydrate biosensor designs have been based on the molecular recognition and specific binding encountered between polysaccharides and other macromolecules, particularly proteins. Such molecular interactions, including carbohydrate−lectin, carbohydrate−toxin, or saccharide−enzyme affinities, play significant roles in diverse biosensor devices and bioassays, either those aiming to detect and/or analyze oligosaccharides or others that rely on embedded carbohydrates for detection of other biomolecules.

The diverse and proliferating literature on carbohydrate biosensors points to promising directions for future progress in the field. The increased synthetic capabilities and sophisticated biochemical techniques aiming to interfere with biosynthetic and cellular pathways responsible for carbohydrate production could have a major impact in the design of novel cellular-based biosensors, in the same way that genetic engineering has revolutionized genetic analysis and screening. Chemical routes for fine tuning the selectivity and targeting in biosensor design are another high-potential direction. Overall, understanding and harnessing the intrinsic complexity of carbohydrate structures is the underlying factor for development and utilization of oligosaccharide biosensor designs and applications.

5. Abbreviations

AFM	atomic force microscopy
b-SiA	bound sialic acid
CT	cholera toxin
con A	concanavalin A
ELISA	enzyme-linked immunosorbent assay
FGF	fibroblast growth factor
FPA	fluorescent polarization assay
FRET	fluorescence resonance energy transfer
GFP	green fluorescent protein
HSV	herpes simplex virus
HPRG	histidine−proline-rich glycoprotein
HIV	human immunodeficiency virus
ISEFT	ion selective field effect transistor
LPS	lipopolysaccharides
MS	mass spectrometry
mAb	monoclonal antibody
PET	photoinduced energy transfer
PPD	polarized photometric detection
PDA	polydiacetylene
QCM	quartz crystal microbalance
SLeA	sialylated Lewis antigen
SPR	surface plasmon resonance
TFA	trifluoroacetic acid

6. References

(1) Feizi, T. *Glycoconjugate J.* **2001**, *17*, 553.
(2) Sturgeon, R. J. *Carbohydr. Chem.* **1983**, *14*, 5.
(3) Mislovicova, D.; Gemeiner, P.; Sandula, J.; Masarova, J.; Vikartovska, A.; Docolomansky, P. *Biotechnol. Appl. Biochem.* **2000**, *31*, 153.
(4) Electricwala, A. *Biochim. Biophys. Acta* **1989**, *990*, 53.
(5) Gemeiner, P.; Docolomansky, P.; Vikartovska, A.; Stefuca, V. *Biotechnol. Appl. Biochem.* **1989**, *28*, 155.
(6) Perdomo, J.; Hinkers, H.; Sundermeier, C.; Seifert, W.; Martinez Morell, O.; Knoll, M. *Biosens. Bioelectron.* **2000**, *15*, 515.
(7) Curey, T. E.; Salazar, M. A.; Oliveira, P.; Javier, J.; Dennis, P. J.; Rao, P.; Shear, J. B. *Anal. Biochem.* **2002**, *303*, 42.
(8) Adams, E. W.; Ueberfeld, J.; Ratner, D. M.; O'Keefe, B. R.; Walt, D. R.; Seeberger, P. H. *Angew. Chem.* **2003**, *42*, 5317.
(9) Healey, B.; Li, G.; Walt, D. R. *Biosens. Bioelectron.* **1997**, *12*, 521.
(10) Matsumoto, K.; Kamikado H.; Matsubara H.; Osajima Y *Anal. Chem.* **1988**, *60*, 147.
(11) Baldwin, R. P. *J. Pharm. Biomed. Anal.* **1999**, *19*, 69.
(12) Updike, S. J.; Hicks, G. P. *Nature* **1967**, *214*, 986.
(13) Johnson, D. C.; LaCourse, W. R. *Anal. Chem.* **1990**, *62*, 589A.
(14) Santos, L. M.; Baldwin, R. P. *Anal. Chem.* **1987**, *59*, 1766.
(15) Neuburger, G. G.; Johnson, D. C. *Anal. Chem.* **1987**, *59*, 150.
(16) Colon, L. A.; Dadoo, R.; Zare R. N. *Anal. Chem.* **1993**, *65*, 476.
(17) Zhou, W.; Baldwin, R. P. *Electrophoresis* **1996**, *17*, 319.
(18) Shen, Z.; Warren, C. D.; Newburg, D. S. *Anal. Biochem.* **2000**, *279*, 37.
(19) Yamamoto, A.; Wataya, T.; Hayakawa, K.; Matsunaga, A.; Nishimura, M.; Miyazaki, M. *J. Pharm. Biomed. Anal.* **1997**, *15*, 1383.
(20) Whitham, K. M.; Hadley, J. L.; Morris, H. G.; Andrew, S. M.; Nieduszynski, I. A.; Brown, G. M. *Glycobiology* **1999**, *9*, 285.
(21) Anumula, K. R.; Dhume, S. T. *Glycobiology* **1998**, *8*, 685.
(22) He, L.; Sato, K.; Abo, M.; Okubo, A.; Yamazaki, S. *Anal. Biochem.* **2003**, *314*, 128.
(23) Vreeland, V.; Laetsch, W. M. *Planta* **1989**, *177*, 423.
(24) Asher, S. A.; Alexeev, V. L.; Goponenko, A. V.; Sharma, A. C.; Lednev, I. K.; Wilcox, C. S.; Finegold, D. N. *J. Am. Chem. Soc.* **2003**, *125*, 3322.
(25) James, T. D.; Shinkai, S. *Top. Curr. Chem.* **2002**, *218*, 159.
(26) Wang, W.; Gao, X.; Wang, B. *Curr. Org. Chem.* **2002**, *6*, 1285.
(27) James, T. D.; Linnane, P.; Shinkai, S. *Chem. Commun.* **1996**, *3*, 281.
(28) Tsukagoshi, K.; Shinkai, S. *J. Org. Chem.* **1991**, *56*, 4089.
(29) Shinmori, H.; Takeuchi, M.; Shinkai, S. *J. Chem. Soc., Perkin Trans. 2* **1996**, *1*, 1.
(30) Ward, C. J.; Ashton, P. R.; James, T. D.; Patel, P. *Chem. Commun.* **2000**, *3*, 229.
(31) Moore, A. N. J.; Wayner, D. D. M. *Can. J. Chem.* **1999**, *77*, 681.
(32) Norrild, J. C.; Sotofte, I. *J. Chem. Soc., Perkin Trans. 2* **2002**, *2*, 303.
(33) Roydhouse, R. H. *J. Biomed. Mater. Res.* **1968**, *2*, 265.
(34) Laun, H. M. *Makromol. Chem., Macromol. Symp.* **1992**, *56*, 55.
(35) Lee, B.; Kim, Y.; Lee, H.; Yi, J. *Microporous and Mesoporous Mater.* **2001**, *50*, 77.
(36) Kugimiya, A.; Yoneyama, H.; Takeuchi, T. *Electroanalysis* **2000**, *12*, 1322.
(37) Gao, S.; Wang, W.; Wang, B. *Bioorg. Chem.* **2001**, *29*, 308.
(38) Striegler, S.; Dittel, M. *Anal. Chim. Acta* **2003**, *484*, 53.
(39) D'Souza, S. F. *Biosens. Bioelectron.* **2001**, *16*, 337.
(40) Held, M.; Schuhmann, W.; Jahreis, K.; Schmidt, H.-L. *Biosens. Bioelectron.* **2002**, *17*, 1089.
(41) Bousse, L. *Sens. Actuators, B* **1996**, *B34*, 270.
(42) Svitel, J.; Curilla, O.; Tkac, J. *Biotechnol. Appl. Biochem.* **1998**, *27*, 153.
(43) Capila, I.; Linhardt, R. J. *Angew. Chem., Int. Ed.* **2002**, *41*, 390.
(44) Despotis, G. J.; Gravlee, G.; Filos, K.; Levy, J. *Anesthesiology* **1999**, *91*, 1122.
(45) van Kerkhof, J. C.; Bergveld, P.; Schasfoort, R. B. M. *Biosens. Bioelectron.* **1995**, *10*, 269.
(46) Zhong, Z.; Anslyn, E. V. *J. Am. Chem. Soc.* **2002**, *124*, 9014.
(47) Wiskur, S. L.; Anslyn, E. V. *J. Am. Chem. Soc.* **2001**, *123*, 10109.
(48) Sugawara, M.; Hirano, A.; Buhlmann, P.; Umezawa, Y. *Bull. Chem. Soc. Jpn.* **2002**, *75*, 187.
(49) Maccarana, M.; Casu, B.; Lindahl, U. *J. Biol. Chem.* **1993**, *268*, 23898.
(50) Liljeblad, M.; Lundblad, A.; Ohlson, S.; Pahlsson, P. *J. Mol. Recognit.* **1998**, *11*, 191.
(51) O'Sullivan, C. K.; Guilbault, G. G. *Biosens. Bioelectron.* **1999**, *14*, 663.
(52) Davis, K. A.; Leary, T. R. *Anal. Chem.* **1989**, *61*, 1227.
(53) Janshoff, A.; Galla, H.-J.; Steinem, C. *Membr. Sci. Technol. Ser.* **2003**, *7*, 991.
(54) Cheng, T.-J.; Lin, T.-M.; Chang, H.-C. *Anal. Chim. Acta* **2002**, *462*, 261.
(55) Gadzekpo, V. P. Y.; Buhlmann, P.; Xiao, K. P.; Aoki, H.; Umezawa, Y. *Anal. Chim. Acta* **2000**, *411*, 163.
(56) Sugawara, M.; Kojima, K.; Sazawa, H.; Umezawa, Y. *Anal. Chem.* **1987**, *59*, 2842.
(57) Dai, S.; Esson, J. M.; Lutze, O.; Ramamurthy, N.; Yang, V. C.; Meyerhoff, M. E. *J. Pharm. Biomed. Anal.* **1999**, *19*, 1.
(58) Buhlmann, P.; Pretsch, E.; Bakker, E. *Chem. Rev.* **1998**, *98*, 1593.
(59) Ma, S. C.; Yang, V. C.; Fu, B.; Meyerhoff, M. E. *Anal. Chem.* **1993**, *65*, 2078.
(60) Fu, B.; Bakker, E.; Yun, J. H.; Yang, V. C.; Meyerhoff, M. E. *Anal. Chem.* **1994**, *66*, 2250.
(61) Fu, B.; Bakker, E.; Yang, V. C.; Meyerhoff, M. E. *Macromolecules* **1995**, *28*, 5834.
(62) Mathison, S.; Bakker, E. *Anal. Chem.* **1999**, *71*, 4614.
(63) van Kerkhof, J. C.; Bergveld, P.; Schasfoort, R. B. M. *Biosens. Bioelectron.* **1993**, *8*.

(64) Borza, D.-B.; Morgan, W. T. *J. Biol. Chem.* **1998**, *273*, 5493.
(65) Welply, J. K. *Trends Biotechnol.* **1989**, *7*, 5.
(66) Pelkonen, S.; Hayrinen, J.; Finne, J. *J. Bacteriol.* **1988**, *170*, 2646.
(67) Prime, S. B.; Shipston, N. F.; Merry, T. H. *BioMethods* **1997**, *9*, 235.
(68) Thanawiroon, C.; Rice, K. G.; Toida, T.; Linhardt, R. J. *J. Biol. Chem.*, in press.
(69) Lerouxel, O.; Choo, T. S.; Seveno, M.; Usadel, B.; Faye, L.; Lerouge, P.; Pauly, M. *Plant Physiol.* **2002**, *130*, 1754.
(70) Gardner, S. L. B.; M. M.; Fry, S. C. *Phytochemistry* **2002**, *60*, 241.
(71) Ikeda, T.; Shibata, T.; Todoriki, S.; Senda, M.; Kinoshita, H. *Anal. Chim. Acta* **1990**, *230*, 75.
(72) Sun, M.; Lee, C. S. *Biotechnol. Bioeng.* **1998**, *57*, 545.
(73) Weber, P. L.; Kornfelt, T.; Klausen, N. K.; Lunte, S. M. *Anal. Biochem.* **1995**, *34*, 135.
(74) Lerner, L. E. *NMR Spectrosc. Its Appl. Biomed. Res.* **1996**, 313.
(75) Bush, C. A.; Martin-Pastor, M.; Imberty, A. *Ann. Rev. Biophys. Biomol. Struct.* **1999**, *28*, 269.
(76) McReynolds, K. D.; Gervay-Hague, J. *Tetrahedron: Asymmetry* **2000**, *11*, 337.
(77) Nilsson, B. *Prog. Biotechnol.* **1995**, *10*, 29.
(78) Levery, S. B. *Glycopept. Relat. Compd.* **1997**, 541.
(79) Feizi, T.; Stoll, M. S.; Yuen, C.-T.; Chai, W.; Lawson, A. M. *Methods Enzymol.* **1994**, *230*, 484.
(80) Feizi, T. *R. Soc. Chem.* **2002**, *275*, 186.
(81) Stoll, M. S.; Feizi, T.; Loveless, R. W.; Chai, W.; Lawson, A. M.; Yuen, C.-T. *Eur. J. Biochem.* **2000**, *267*, 1795.
(82) de Campos, V. B. *Cell. Mol. Biol.* **1986**, *32*, 527.
(83) Lis, H.; Sharon, N. *Chem. Rev.* **1998**, *98*, 637.
(84) Vijayan, M.; Chandra, N. *Curr. Opin. Struct. Biol.* **1999**, *9*, 707.
(85) Feizi, T. *Immunol. Rev.* **2000**, *173*, 79.
(86) Kim, B.; Cha, G. S.; Meyerhoff, M. E. *Anal. Chem.* **1990**, *62*, 2663.
(87) Bartlett, P. N.; Cooper, J. M. *J. Electroanal. Chem.* **1993**, *362*, 1.
(88) Ballerstadt, R.; Schultz, J. S. *Anal. Chem.* **2000**, *72*, 4185.
(89) Patel, P. D. *Trends Food Sci. Technol.* **1992**, *3*, 35.
(90) Monsigny, M.; Mayer, R.; Roche, A.-C. *Carbohydr. Lett.* **2000**, *4*, 35.
(91) Spicer, S. S.; Naegele, J. R.; Schulte, B. A. *J. Comp. Neurol.* **1996**, *365*, 217.
(92) Bertozzi, C. R.; Kiessling, L. L. *Science* **2001**, *291*, 2357.
(93) Nakagawa, F.; Schulte, B. A.; Spicer, S. S. *Cell Tissue Res.* **1986**, *245*, 579.
(94) Franceschini, V.; Lazzari, M.; Ciani, F. *Brain Res.* **1996**, *725*, 81.
(95) Mahmood, N.; Hay, A. J. *J. Immunol. Methods* **1992**, *151*, 9.
(96) Robinson, J. E.; Holton, D.; Liu, J.; McMurdo, H.; Murciano, A.; Gohd, R. *J. Immunol. Methods* **1990**, *132*, 63.
(97) Nagase, T.; Nakata, E.; Shinkai, S.; Hamachi, I. *Chemistry* **2003**, *9*, 3660.
(98) Nagase, T.; Shinkai, S.; Hamachi, I. *Chem. Commun.* **2001**, *3*, 229.
(99) Hamachi, I.; Nagase, T.; Shinkai, S. *J. Am. Chem. Soc.* **2000**, *122*, 12065.
(100) Ballerstadt, R.; Schultz, J. S. *Methods Biotechnol.* **1998**, *7*, 89.
(101) D'Auria, S.; DiCesare, N.; Staiano, M.; Gryczynski, Z.; Rossi, M.; Lakowicz, J. R. *Anal. Biochem.* **2002**, *303*, 138.
(102) Russell, R. J.; Pishko, M. V.; Gefrides, C. C.; McShane, M. J.; Cote, G. L. *Anal. Chem.* **1999**, *71*, 3126.
(103) Yoshikawa, K.; Omochi, T. *Biochem. Biophys. Res. Commun.* **1986**, *137*, 978.
(104) Tanimoto, T.; Kishimoto, Y.; Ikuta, A.; Nishi, Y.; Miyake, K. *J. Inclusion Phenom. Macrocyclic Chem.* **2002**, *44*, 297.
(105) Taubenberger, J. K.; Layne, S. P. *Mol. Diagn.* **2001**, *6*, 291.
(106) Zeng, X. N.; Yumiko; Murata, T.; Usui, T. *Arch. Biochem. Biophys.* **2000**, *383*, 28.
(107) Barnes, C.; D'Silva, C.; Jones, J. P.; Lewis, T. J. *Sens. Actuators, A* **1992**, *31*, 159.
(108) Krull, U. J.; Brown, R. S.; Koilpillai, R. N.; Nespolo, R.; Safarzadeh-Amiri, A.; Vandenberg, E. T. *Analyst* **1989**, *114*, 33.
(109) Milton, J. D.; Fernig, D. G.; Rhodes, J. M. *Glycoconjugate J.* **2001**, *18*, 565.
(110) Kinning, T.; Edwards, P. *Opt. Biosens.* **2002**, 253.
(111) Cooper, M. A. *Nat. Rev. Drug Discovery* **2002**, *1*, 515.
(112) Rahmoune, H.; Rudland, P. S.; Gallagher, J. T.; Fernig, D. G. *Biochemistry* **1998**, *37*, 6003.
(113) Steinfeld, S.; Penaloza, A.; Decaestecker, C.; Rommes, S.; Andre, S.; Schuring, M.-P.; Danguy, A.; Appelboom, T.; Kiss, R.; Gabius, H.-J. *J. Rheumatol.* **2000**, *27*, 1910.
(114) Koopmann, J.; Hocke, J.; Gabius, H. J. *Biol. Chem. Hoppe-Seyler* **1993**, *374*, 1029.
(115) Hasegawa, Y.; Shinohara, Y.; Sota, H. *Trends Glycosci. Glycotechnol.* **1997**, *9*, S15.
(116) West, C. M. *Mol. Cell. Biochem.* **1986**, *25*, 3.
(117) Rudd, P. M.; Elliott, T.; Cresswell, P.; Wilson, I. A.; Dwek, R. A. *Science* **2001**, *291*, 2370.
(118) Bucala, R.; Vlassara, H.; Cerami, A. *Drug Dev. Res.* **1994**, *32*, 77.
(119) Sangadala, S.; Bhat, U. R.; Mendicino, J. *Mol. Cell. Biochem.* **1992**, *31*, 75.
(120) Helenius, A.; Aebi, M. *Science* **2001**, *291*, 2364.
(121) Feizi, T.; Childs, R. A. *Biochem. J.* **1987**, *245*, 1.
(122) Lee, K. B.; Loganathan, D.; Merchant, Z. M.; Linhardt, R. J. *Appl. Biochem. Biotechnol.* **1990**, *23*, 53.
(123) Ma, J.; Ming, C. Y.; Jing, D.; Cheng, L. S.; Li, H.; Feng, J.; Xiang, C. Y. *Electrochem. Commun.* **1999**, *1*, 425.
(124) Wong, N. K. C.; Kanu, N.; Thandrayen, N.; Rademaker, G. J.; Baldwin, C. I.; Renouf, D. V.; Hounsell, E. F. *Protein Protocols Handbook*, 2nd ed.; 2002, 841.
(125) Goodarzi, M. T.; Fotinopoulou, A.; Turner, G. A. *Protein Protocols Handbook*, 2nd ed.; 2002, 795.
(126) Turner, G. A. *Clin. Chim. Acta* **1992**, *208*, 149.
(127) Cardullo, F.; Diederich, F.; Echegoyen, L.; Habicher, T.; Jayaraman, N.; Leblanc, R. M.; Stoddart, J. F.; Wang, S. *Langmuir* **1998**, *14*, 1955.
(128) Lindemann, D.; Goepfert, P. A. *Curr. Top. Microbiol. Immunol.* **2003**, *277*, 111.
(129) Spear, P. G.; Sarmiento, M.; Manservigi, R. *IARC Sci. Publ.* **1978**, *24*, 157.
(130) Bertucci, C.; Cimitan, S.; Menotti, L. *J. Pharm. Biomed. Anal.* **2003**, *32*, 697.
(131) Lowe, P. A.; Clark, T. J. H. A.; Davies, R. J.; Edwards, P. R.; Kinning, T.; Yeung, D. *J. Mol. Recognit.* **1998**, *11*, 194.
(132) Wyatt, R.; Sodroski, J. *Science* **1998**, *280*, 1884.
(133) Poignard, P.; Saphire, E. O.; Parren, P. W.; Burton, D. R. *Ann. Rev. Immunol.* **2001**, *19*, 253.
(134) Matei, L. *Rev. Roum. Biochim.* **2000**, *36*, 99.
(135) van den Berg, L. H.; Sadiq, S. A.; Lederman, S.; Latov, N. *J. Neurosci. Res.* **1992**, *33*, 513.
(136) Storring, P. L. *Trends Biotechnol.* **1992**, *10*, 427.
(137) Goldstein, D. E.; Wiedmeyer, H. M.; England, J. D.; Little, R. R.; Parker, K. M. *Crit. Rev. Clin. Lab. Sci.* **1984**, *21*, 187.
(138) Peacock, I. *J. Clin. Pathol.* **1984**, *37*, 841.
(139) Taylor, S. C.; Thibault, P.; Tessier, D. C.; Bergeron, J. J. M.; Thomas, D. Y. *EMBO Rep.* **2003**, *4*, 405.
(140) Ni, J.; Singh, S.; Wang, L.-X. *Bioconjugate Chem.* **2003**, *14*, 232.
(141) Yarema, K. J.; Bertozzi, C. R. *Genome Biol.* **2001**, *2*, 0004.1.
(142) Dube, D. H.; Bertozzi, C. R. *Curr. Opin. Chem. Biol.* **2003**, *7*, 616.
(143) Charter, N. W.; Mahal, L. K.; Koshland, D. E., Jr.; Bertozzi, C. R. *Glycobiology* **2000**, *10*, 1049.
(144) Lemieux, G. A.; Yarema, K. J.; Jacobs, C. L.; Bertozzi, C. R. *J. Am. Chem. Soc.* **1999**, *121*, 4278.
(145) Streit, W. J.; Schulte, B. A.; Balentine, J. D.; Spicer, S. S. *J. Histochem. Cytochem.* **1985**, *33*, 1042.
(146) Dell, A.; Morris, H. R. *Science* **2001**, *291*, 2351.
(147) Tietjen, M.; Fung, D. Y. *Crit. Rev. Microbiol.* **1995**, *21*, 53.
(148) Leonard, P.; Hearty, S.; Brennan, J.; Dunne, L.; Quinn, J.; Chakraborty, T.; O'Kennedy, R. *Enzyme Microb. Technol.* **2003**, *32*, 3.
(149) Kaspar, C. W.; Hartman, P. A.; Benson, A. K. *Appl. Environ. Microbiol.* **1987**, *53*, 1073.
(150) March, J. B.; Gammack, C.; Nicholas, R. *J. Clin. Microbiol.* **2000**, *38*, 4152.
(151) Ellis, R. W.; Sobanski, M. A. *J. Med. Microbiol.* **2000**, *49*, 853.
(152) Gray, S. J.; Sobanski, M. A.; Kaczmarski, E. B.; Guiver, M.; Marsh, W. J.; Borrow, R.; Barnes, R. A.; Coakley, W. T. *J. Clin. Microbiol.* **1999**, *37*, 1797.
(153) Sutton, A.; Vann, W. F.; Karpas, A. B.; Stein, K. E.; Schneerson, R. *J. Immunol. Methods* **1985**, *82*, 215.
(154) Akinwolere, O. A.; Kumararatne, D. S.; Bartlett, R.; Goodall, D. M.; Catty, D. *J. Clin. Pathol.* **1994**, *47*, 405.
(155) Nielsen, K.; Gall, D. *J. Immunoassay Immunochem.* **2001**, *22*, 183.
(156) Hirmo, S.; Arturrsson, E.; Puu, G.; Wadstro, T.; Nilsson, B. *J. Microbiol. Methods* **1999**, *37*, 177.
(157) Das, T.; Sen, A.; Kempf, T.; Pramanik, S. R.; Mandal, C.; Mandal, C. *Biochem. J.* **2003**, *373*, 345.
(158) Plebani, M.; Burlina, A. *Clin. Biochem.* **1991**, *24*, 219.
(159) Li, S.; Marquardt, R. R.; Abramson, D. *J. Food Prot.* **2000**, *63*, 281.
(160) Cousin, M. A. *Dev. Ind. Microbiol. Ser.* **1990**, *31*, 157.
(161) Herrington, D. A.; Hall, R. H.; Losonsky, G.; Mekalanos, J. J.; Taylor, R. K.; Levine, M. M. *J. Exp. Med.* **1988**, *168*, 1487.
(162) Lee, Y. C.; Lee, R. T. *J. Biomed. Sci.* **1996**, *3*, 221.
(163) Cooper, M. A.; Hansson, A.; Lofas, S.; Williams, D. H. *Anal. Biochem.* **2000**, *277*, 196.
(164) Carmona-Ribeiro, A. M. *Chem. Soc. Rev.* **2001**, *30*, 241.
(165) Sicchierolli, S. M.; Carmona-Ribeiro, A. M. *J. Phys. Chem.* **1996**, *100*, 16771.
(166) Song, X.; Shi, J.; Swanson, B. *Anal. Biochem.* **2000**, *284*, 35.
(167) Song, X.; Shi, J.; Nolan, J.; Swanson, B. *Anal. Biochem.* **2001**, *291*, 133.
(168) Song, X.; Nolan, J.; Swanson, B. *J. Am. Chem. Soc.* **1998**, *120*, 11514.

(169) Song, X.; Swanson, B. *Anal. Chem.* **1999**, *71*, 2097.
(170) Liebau, M.; Hildebrandt, A.; Hartmann, J.; Rothe, U.; Mtithing, J.; Neubert, R. *Proc. SPIE−Int. Soc. Opt. Eng.* **1988**, *3539*, 188.
(171) Spangler, B. D.; Tyler, B. J. *Anal. Chim. Acta* **1999**, *399*, 51.
(172) Nyquist, R. M.; Eberhardt, A. S.; Silks, L. A., III; Li, Z.; Yang, X.; Swanson, B. I. *Langmuir* **2000**, *16*, 1793.
(173) Sackmann, E.; Tanaka, M. *Trends Biotechnol.* **2000**, *18*, 58.
(174) Puu, G. *Anal. Chem.* **2001**, *73*, 72.
(175) Kelly, D.; Grace, K. M.; Song, X.; Swanson, B.; Frayer, D.; Mendes, S. B.; Peyghambarian, N. *Opt. Lett.* **1999**, *24*, 1723.
(176) Bardeau, J.-F.; Eberhardt, A. S.; Nyquist, R. M.; Parikh, A. N.; Shreve, A. P.; Swanson, B. L. *Synth. Met.* **1999**, *102*, 1452.
(177) Cheng, Q.; Song, J.; Stevens, R. C. *Polym. Prepr.* **2002**, *43*, 128.
(178) Pan, J. J.; Charych, D. *Langmuir* **1997**, *13*, 1365.
(179) Charych, D. H.; Nagy, J. O.; Spevak, W.; Bednarski, M. D. *Science* **1993**, *261*, 585.
(180) Lio, A.; Reichert, A.; Ahn, D. J.; Nagy, J. O.; Salmeron, M.; Charych, D. H. *Langmuir* **1997**, *13*, 6524.
(181) Katz, M.; Tsubery, H.; Kolusheva, S.; Shames, A.; Fridkin, M.; Jelinek, R. *Biochem. J.* **2003**, *375*, 405.
(182) Kolusheva, S.; Kafri, R.; Katz, M.; Jelinek, R. *J. Am. Chem. Soc.* **2001**, *123*, 417.
(183) Kolusheva, S.; Wachtel, E.; Jelinek, R. *J. Lipid Res.* **2003**, *44*, 65.
(184) Rozner, S.; Kolusheva, S.; Cohen, Z.; Dowhan, W.; Eichler, J.; Jelinek, R. *Anal. Biochem.* **2003**, *319*, 96.
(185) Jelinek, R.; Kolusheva, S. *Biotechnol. Adv.* **2001**, *19*, 109.
(186) Charych, D.; Cheng, Q.; Reichert, A.; Kuziemko, G.; Stroh, M.; Nagy, J. O.; Spevak, W.; Stevens, R. C. *Chem. Biol.* **1996**, *3*, 113.
(187) Song, J.; Cheng, Q.; Zhu, S.; Stevens, R. C. *Biomed. Microdevices* **2002**, *4*, 213.
(188) Yamanaka, S. A.; Charych, D. H.; Loy, D. A.; Sasaki, D. Y. *Langmuir* **1997**, *13*, 5049.
(189) Hauschildt, S.; Brabetz, W.; Schromm, A. B.; Hamann, L.; Zabel, P.; Rietschel, E. T.; Muller-Loennies, S. *Handb. Exp. Pharmacol.* **2000**, *145*.
(190) Nicaido, H.; Vaara, M. Outer Membrane. In *Escherichia coli and Salmonella typhimurium*, 1987.
(191) Wiese, A.; Brandenburg, K.; Ulmer, A. J.; Seydel, U.; Muller-Loennies, S. *Biol. Chem.* **1999**, *380*, 767.
(192) Salzer, W. L.; McCall, C. E. *Mol. Aspects Med.* **1988**, *10*, 511.
(193) Ertl, P.; Mikkelsen, S. R. *Anal. Chem.* **2001**, *73*, 4241.
(194) Ertl, P.; Wagner, M.; Corton, E.; Mikkelsen, S. R. *Biosens. Bioelectron.* **2003**, *18*, 907.
(195) Goh, Y. Y.; Frecer, V.; Ho, B.; Ding, J. L. *Protein Eng.* **2002**, *15*, 493.
(196) Sakti, S. P.; Luclum, R.; Hauptmann, P.; Buhling, F.; Ansorge, S. *Biosens. Bioelectron.* **2001**, *16*, 1101.
(197) Desmidt, M.; De Groot, P. A.; Haesebrouck, F.; Ducatelle, R. *Meded. Fac. Landbouwwet., Univ. Gent* **1992**, *57*, 1851.
(198) Feizi, T. *Adv. Exp. Med. Biol.* **1988**, *228*, 317.
(199) Dwek, M. V.; Ross, H. A.; Leathem, A. J. C. *Proteomics* **2001**, *1*, 756.
(200) Ohuchi, N.; Taeda, Y.; Yaegashi, S.; Harada, Y.; Kanda, T.; Mori, S. *Cancer Mol. Biol.* **1994**, *1*, 179.
(201) Ho, J. J.; Kim, Y. S. *Pancreas* **1994**, *9*, 674.
(202) Banerjee, S.; Robson, P.; Soutter, W. P.; Foster, C. S. *Hum. Pathol.* **1995**, *26*, 1005.
(203) Lamerz, R. *Ann. Oncol.* **1999**, *10*, 145.
(204) Feizi, T.; Childs, R. A. *Trends Biochem. Sci.* **1985**, *10*, 24.
(205) Plzak, J.; Smetana, K. Jr.; Betka, J.; Kodet, R.; Kaltner, H.; Gabius, H.-J. *Int. J. Mol. Med.* **2000**, *5*, 369.
(206) Kijima, H.; Kashiwagi, H.; Dowaki, S.; Ohtani, Y.; Tobita, K.; Matsubayasi, H.; Ajioka, Y.; Watanabe, H.; Tsuchida, T.; Yamazaki, H.; Nakamura, M.; Ueyama, Y.; Tanaka, M.; Makuuchi, H. *Int. J. Oncol.* **2000**, *17*, 55.
(207) Nakagoe, T.; Fukushima, K.; Sawai, T.; Tsuji, T.; Jibiki, M.; Nanashima, A.; Tanaka, K.; Yamaguchi, H.; Yasutake, T.; Ayabe, H.; Ishikawa, H. *J. Exp. Clin. Cancer Res.* **2002**, *21*, 363.
(208) Davidson, B.; Berner, A.; Nesland, J. M.; Risberg, B.; Kristensen, G. B.; Trope, C. G.; Bryne, M. *Hum. Pathol.* **2000**, *31*, 1081.
(209) Rye, P. D.; Bovin, N. V.; Vlasova, E. V.; Molodyk, A. A.; Baryshnikov, A.; Kreutz, F. T.; Garinther, W. I.; Schultes, B. C.; Noujaim, A. A.; Madiyalakan, R.; Magnani, J.; Nilsson, O.; Nilsson, K.; Nustad, K.; Norum, L.; Bell, H.; Cao, Y.; Suresh, M. R.; Very, D. L.; Freeman, J. V.; Yeung, K. K.; Hilgers, J. *Tumor Biol.* **1998**, *19*, 390.
(210) Aubeck, R.; Eppelsheim, C.; Braeuchle, C.; Hampp, N. *Analyst* **1993**, *118*, 1389.
(211) Simanek, E. E.; McGarvey, G. J.; Jablonowski, J. A.; Wong, C.-H. *Chem. Rev.* **1998**, *98*, 833.
(212) Devine, P. L.; McGuckin, M. A.; Ward, B. G. *Anticancer Res.* **1992**, *12*, 709.
(213) You, T.; Niwa, O.; Chen, Z.; Hayashi, K.; Tomita, M.; Hirono, S. *Anal. Chem.* **2003**, *75*, 5191.
(214) Rief, M.; Oesterhelt, F.; Heymann, B.; Gaub, H. E. *Science* **1997**, *275*, 1295.
(215) Morris, V. J.; Kirby, A. R.; Gunning, A. P. *Scanning* **1999**, *21*, 287.
(216) Camesano, T. A.; Abu-Lail, N. I. *Biomacromolecules* **2002**, *3*, 661.
(217) Gad, M.; Itoh, A.; Ikai, A. *Cell Biol. Int.* **1997**, *21*, 697.
(218) Camesano, T. A.; Wilkinson K. J. *Biomacromolecules* **2001**, *2*, 1184.
(219) Muirhead, D.; Lead, J. R. *Hydrobiologia* **2003**, *494*, 65.
(220) Li, H.; Rief, M.; Oesterhelt, F.; Gaub, H. E.; Zhang, X.; Shen, J. *Chem. Phys. Lett.* **1999**, *305*, 197.
(221) Razatos, A.; Ong, Y. L.; Sharma, M. M.; Georgiou, G. *J. Biomater. Sci., Polym. Ed.* **1998**, *9*, 1361.
(222) Low, N. H. *Anal. Methods Food Authentication* **1998**, 97.
(223) Low, N. H.; Hageman, L.; Valdez, F. *Fruit Process.* **1998**, *8*, 97.
(224) Snyder, L. R. *J. Chromatogr.* **1971**, *63*, 7.
(225) Cimpoiu, C. *Chromatogr. Sci. Ser.* **2003**, *89*, 81.
(226) Lopez, H. J.; Gonzalez-Castro, M. J.; Naya, A. I.; De la Cruz Garcia, C. *J. Chromatogr. Sci.* **1998**, *36*, 293.
(227) Huber, C. G.; Bonn, G. K. *J. Chromatogr. Libr.* **1995**, *58*, 147.
(228) Bietz, J. A. *Chromatogr. Sci. Ser.* **2002**, *87*, 547.
(229) Sadana, A.; Vo-Dinh, T. *Biotechnol. Appl. Biochem.* **2001**, *33*, 17.
(230) Goetz, H. A.; Knoll, W.; Frank, C. W.; Hawker, C. J. *Polym. Mater. Sci. Eng.* **2001**, *84*, 398.
(231) Tsuchida, A.; Matsuura, K.; Kobayashi, K. *Macromol. Chem. Phys.* **2000**, *201*, 2245.
(232) Diociaiuti, M.; Molinari, A.; Ruspantini, I.; Gaudiano, M. C.; Ippoliti, R.; Lendaro, E.; Bordi, F.; Chistolini, P.; Arancia, G. *Biochim. Biophys. Acta* **2002**, *1559*, 21.
(233) Chevolot, Y.; Martins, J.; Milosevic, N.; Leonard, D.; Zeng, S.; Malissard, M.; Berger, E. G.; Maier, P.; Mathieu, H. J.; Crout, D. H. G.; Sigrist, H. *Bioorg. Med. Chem.* **2001**, *9*, 2943.
(234) Hatanaka, K.; Takeshige, H.; Akaike, T. *J. Carbohydr. Chem.* **1994**, *13*, 603.
(235) Marks, R. S.; Margalit, A.; Bychenko, A.; Bassis, E.; Porat, N.; Dagan, R. *Appl. Biochem. Biotechnol.* **2000**, *89*, 117.
(236) Frank, B. P.; Belfort, G. *J. Membr. Sci.* **2003**, *212*, 205.
(237) Griesser, H. J.; Hartley, P. G.; McArthur, S. L.; McLean, K. M.; Meagher, L.; Thissen, H. *Smart Mater. Struct.* **2002**, *11*, 652.
(238) Dutra, R. F.; Castro, C. M. H. B.; Azevedo, C. R.; Vinhas, E.; Malagueno, E.; Melo, E. H. M.; Lima Filho, J. L.; Kennedy, J. F. *Biosens. Bioelectron.* **2000**, *15*, 511.
(239) Wang, J.; Taha, Z.; Naser, N. *Talanta* **1991**, *38*, 81.
(240) Charych, D. H.; Spevak, W.; Nagy, J. O.; Bednarski, M. D. *Mater. Res. Soc. Symp. Proc.* **1993**, *292*, 153.
(241) Baek, M.-G.; Stevens, R. C.; Charych, D. H. *Bioconjugate Chem.* **2000**, *11*, 777.
(242) Neubauer, A.; Hoedl, C.; Pum, D.; Sleytr, U. B. *Anal. Lett.* **1994**, *27*, 849.
(243) Messner, P.; Kuepcue, S.; Sara, M.; Pum, D.; Sleytr, U. B. *GBF Monogr.* **1991**, *15*, 111.
(244) Sara, M.; Sleytr, U. B. *Micron* **1996**, *27*, 141.
(245) Kupcu, S.; Neubauer, A.; Hoedl, C.; Pum, D.; Sara, M.; Sleytr, U. B. *NATO ASI Ser., Ser. E* **1993**, *252*, 57.
(246) Pum, D.; Sara, M.; Sleytr, U. B. *Immobilised Macromol*, 1993.
(247) Schwarz, M.; Spector, L.; Gargir, A.; Shtevi, A.; Gortler, M.; Altstock, R. T.; Dukler, A. A.; Dotan, N. *Glycobiology* **2003**, *13*, 749.
(248) Gustavsson, P.-E.; Larsson, P.-O. *J. Chromatogr. Libr.* **2003**, *67*, 121.
(249) Hartmann, A.; Bock, D.; Jaworek, T.; Kaul, S.; Schulze, M.; Tebbe, H.; Wegner, G.; Seeger, S. *Proc. SPIE−Int. Soc. Opt. Eng.* **1996**, *2629*, 108.
(250) Ohashi, E.; Karube, I. *Fish. Sci.* **1995**, *61*, 856.
(251) Reiss, M.; Heibges, A.; Metzger, J.; Hartmeier, W. *Biosens. Bioelectron.* **1998**, *13*, 1083.
(252) Ohashi, E.; Karube, I. *J. Biotechnol.* **1995**, *40*, 13.
(253) Ohashi, E.; Koriyama, T. *Anal. Chim. Acta* **1992**, *262*, 19.
(254) David, C.; Millot, M. C.; Renard, E.; Sebille, B. *J. Inclusion Phenom. Macrocyclic Chem.* **2002**, *44*, 369.
(255) Chegel, V.; Shirshov, Yu.; Avilov, S.; Demchenko, M.; Mustafaev, M. *J. Biochem. Biophys. Methods* **2002**, *50*, 201.
(256) Ombelli, M.; Eckmann, D. M.; Composto, R. J. *Mater. Res. Soc. Symp. Proc.* **2002**, *734*.
(257) Chen, R. J.; Bangsaruntip, S.; Drouvalakis, K. A.; Kam, N. W. S.; Shim, M.; Li, Y.; Kim, W.; Utz, P. J.; Dai, H. *Proc. Natl. Acad. Sci. U.S.A.* **2003**, *100*, 4984.
(258) Gavalas, V. G.; Chaniotakis, N. A.; Gibson, T. D. *Biosens. Bioelectron.* **1998**, *13*, 1205.
(259) Meledeo, M. A.; Ibey, B. L.; O'Neal, D. P.; Pishko, M. V.; Cote, G. L. *Proc. SPIE−Int. Soc. Opt. Eng.* **2002**, *4624*, 55.
(260) Gulcev, M. D.; Goring, G. L. G.; Rakic, M.; Brennan, J. D. *Anal. Chim. Acta* **2002**, *457*, 47.
(261) Svitel, J.; Surugiu, I.; Dzgoev, A.; Ramanathan, K.; Danielsson, B. *J. Mater. Sci.: Mater. Med.* **2001**, *12*, 1075.
(262) Howell, S.; Kenmore, M.; Kirkland, M.; Badley, R. A. *J. Mol. Recognit.* **1998**, *11*, 200.
(263) Barie, N.; Rapp, M. *Biosens. Bioelectron.* **2001**, *16*, 979.
(264) Luong, J. H. T.; Brown, R. S.; Male, K. B.; Cattaneo, M. V.; Zhao, S. *Trends Biotechnol.* **1995**, *13*, 457.
(265) Tu, Y.-F.; Chen, H.-Y. *Biosens. Bioelectron.* **2002**, *17*, 19.

(266) Stefan, R.-I.; van Staden, J. F.; Aboul-Enein, H. Y. *Electroanalysis* **1999**, *11*, 1233.
(267) Kalix, S.; Buchenauer, H. *Electrophoresis* **1995**, *16*, 1016.
(268) Brinkman, E.; van der Does, L.; Bantjes, A. *Biomaterials* **1991**, *12*, 63.
(269) O'Connor, S. M.; Andreadis, J. D.; Shaffer, K. M.; Ma, W.; Pancrazio, J. J.; Stenger, D. A. *Biosens. Bioelectron.* **2000**, *14*, 871.
(270) Shi, H.; Tsai, W.-B.; Garrison, M. D.; Ferrari, S.; Ratner, B. D. *Nature* **1999**, *398*.
(271) Shi, H.; Ratner, B. D. *J. Biomed. Mater. Res.* **2000**, *49*, 1.
(272) Wilchek, M.; Bayer, E. A. *Anal. Biochem.* **1988**, *27*, 1.
(273) Ulman, A. *Chem. Rev.* **1996**, *96*, 1533.
(274) Love, K. R.; Seeberger, P. H. *Angew. Chem.* **2002**, *41*, 3583.
(275) Houseman, B. T.; Mrksich, M. *Chem. Biol.* **2002**, *9*, 443.
(276) Houseman, B. T.; Gawalt, E. S.; Mrksich, M. *Langmuir* **2003**, *19*, 1522.
(277) Fukui, S.; Feizi, T.; Galustian, C.; Lawson, A. M.; Chai, W. *Nat. Biotechnol.* **2002**, *20*, 1011.
(278) Alban, S.; Gastpar, R. *J. Biomol. Screening* **2001**, *6*, 393.
(279) Kozlov, I. A.; Mao, S.; Xu, Y.; Huang, X.; Lee, L.; Sears, P. S.; Gao, C.; Coyle, A. R.; Janda, K. D.; Wong, C.-H. *ChemBioChem* **2001**, *2*, 741.
(280) Mammen, M.; Chio, S.-K.; Whitesides, G. M. *Angew. Chem.* **1998**, *37*, 2755.
(281) Evans, S. V.; MacKenzie, C. R. *J. Mol. Recognit.* **1999**, *12*, 155.
(282) Rowe-Taitt, C. A.; Cras, J. J.; Patterson, C. H.; Golden, J. P.; Ligler, F. S. *Anal. Biochem.* **2000**, *281*, 123.
(283) Zhang, F.; Fath, M.; Marks, R.; Linhardt, R. J. *Anal. Biochem.* **2002**, *304*, 271.
(284) Osmond, R. I. W.; Kett, W. C.; Skett, S. E.; Coombe, D. R. *Anal. Biochem.* **2002**, *310*, 199.
(285) Kamei, K.; Wu, X. X. X.; Minami, K.; Huy, N. T.; Takano, R. H.; Kato, S. H. *Anal. Biochem.* **2001**, *295*, 203.
(286) Marks, R. M.; Lu, H.; Sundaresan, R.; Toida, T.; Suzuki, A.; Imanari, T.; Hernaiz, M. J.; Linhardt, R. J. *J. Med. Chem.* **2001**, *44*, 2178.
(287) Brynda, E.; Houska M.; Wikerstal, A.; Pientka, Z.; Dyr, J. E.; Brandenburg A. *Langmuir* **2000**, *16*, 4352.
(288) Munakata, H.; Takagaki, K.; Majima, M.; Endo, M. *Glycobiology* **1999**, *9*, 1023.
(289) Zhang, Y.; Telyatnikov, V.; Sathe, M.; Zeng, X.; Wang, P. G. *J. Am. Chem. Soc.* **2003**, *125*, 9292.
(290) Mattiasson, B. *J. Appl. Biochem.* **1981**, *3*, 183.
(291) Koeneke, R.; Menzel, C.; Ulber, R.; Schuegerl, K.; Scheper, T. *Biosens. Bioelectron.* **1996**, *11*, 1229.
(292) Saleemuddin, M.; Husain, Q. *Enzyme Microb. Technol.* **1991**, *13*, 290.
(293) Galanina, O. E.; Tuzikov, A. B.; Rapoport, E.; Le Pendu, J.; Bovin, N. V. *Anal. Biochem.* **1998**, *265*, 282.
(294) Kitov, P.; Railton, C.; Bundle, D. R. *Carbohydr. Res.* **1998**, *307*, 361.
(295) Willner, I.; Riklin, A.; Shoham, B.; Rivenzon, D.; Katz, E. *Adv. Mater.* **1993**, *5*, 912.
(296) Carvalho, R. M.; Rath, S.; Kubota, L. T. *Quim. Nova* **2003**, *26*, 97.
(297) McDonnell, J. M. *Curr. Opin. Chem. Biol.* **2001**, *5*, 572.
(298) Okazaki, I. *Trends Glycosci. Glycotechnol.* **1998**, *10*, 321.
(299) Rich, R. L.; Myszka, D. G, *Curr. Opin. Biotechnol.* **2000**, *11*.
(300) Shinohara, Y.; Sota, H.; Hasegawa, Y. *Techniques in Glycobiology*; Townsend, R. R.; Hotchkiss, A., T., Jr., Eds.; 1997.
(301) Mach, H.; Volkin, D. B.; Burke, C. J.; Middaugh, C. R.; Linhardt, R. J.; Fromm. J.; Loganathan, D.; Mattsson L. *Biochemistry* **1993**, *32*, 5480.
(302) Brynda, E.; Houska, M. *Protein Architecture*, 2000.
(303) Jungar, C.; Mandenius, C.-F. *Anal. Chim. Acta* **2001**, *449*, 51.
(304) Zou, W.; Mackenzie, R.; Therien, L.; Hirama, T.; Yang, Q.; Gidney, M. A.; Jennings, H. J. *J. Immunol.* **1999**, *163*, 820.
(305) Young, N. M.; Gidney, M. A. J.; Gudmundsson, B.-M. E.; MacKenzie, C. R.; To, R.; Watson, D. C.; Bundle, D. R. *Mol. Immunol.* **1999**, *36*, 339.
(306) Hara-Kuge, S.; Ohkura, T.; Seko, A.; Yamashita, K. *Glycobiology* **1999**, *9*, 833.
(307) Rice, P. J.; Kelley, J. L.; Kogan, G.; Ensley, H. E.; Kalbfleisch, J. H.; Browder, I. W.; Williams, D. L. *J. Leukocyte Biol.* **2002**, *72*, 140.
(308) Shen, B.; Shimmon, S.; Smith, M. M.; Ghosh, P. *J. Pharm. Biomed. Anal.* **2003**, *31*, 83.
(309) Hayashida, O.; Shimizu, C.; Fujimoto, T.; Aoyama, Y. *Chem. Lett.* **1998**, *1*, 13.
(310) Uda, T.; Hifumi, E.; Kubota, N.; Shimizu, K.; Ogino, K. *Denki Kagaku oyobi Kogyo Butsuri Kagaku* **1995**, *63*, 1160.
(311) Huber, W.; Hurst, J.; Schlatter, D.; Barner, R.; Huebscher, J.; Kouns, W. C.; Steiner, B. *Eur. J. Biochem.* **1995**, *34*, 647.
(312) Frazier, R. A.; Davies, M. C.; Matthijs, G.; Roberts, C. J.; Schacht, E.; Tendler, S. J. B.; Williams, P. M. *Langmuir* **1997**, *13*, 7115.
(313) Shinohara, Y.; Kim, F.; Shimizu, M.; Goto, M.; Tosu, M.; Hasegawa, Y. *Eur. J. Biochem.* **1994**, *33*, 189.
(314) Nahalkova, J.; Svitel, J.; Gemeiner, P.; Danielsson, B.; Pribulova, B.; Petrus, L. *J. Biochem. Biophys. Methods* **2002**, *52*, 11.
(315) van Damme, E. J. M.; Astoul, C. H.; Barre, A.; Rouge, P.; Peumans, W. J. *Eur. J. Biochem.* **2000**, *267*, 5067.
(316) Bourne, Y.; Astoul, C. H.; Zamboni, V.; Peumans, W. J.; Menu-Bouaouiche, L.; van Damme, E. J. M.; Barre, A.; Rouge, P. *Biochem. J.* **2002**, *364*, 173.
(317) Whelan, R. J.; Wohland, T.; Neumann, L.; Huang, B.; Kobilka, B. K.; Zare, R. N. *Anal. Chem.* **2002**, *74*, 4570.
(318) Gaus, K.; Hall, E. A. H. *Biosens. Bioelectron.* **1998**, *13*, 1307.
(319) Sadir, R.; Baleux, F.; Grosdidier, A.; Imberty, A.; Lortat-Jacob, H. *J. Biol. Chem.* **2001**, *276*, 8288.
(320) Kett, W. C.; Osmond, R. I. W.; Moe, L.; Skett, S. E.; Kinnear, B. F.; Coombe, D. R. *Biochim. Biophys. Acta* **2003**, *1620*, 225.
(321) Rux, A. H.; Lou, H.; Lambris, J. D.; Friedman, H. M.; Eisenberg, R. J.; Cohen, G. H. *Virology* **2002**, *294*, 324.
(322) Gaus, K.; Hall, E. A. H. *Anal. Chem.* **1999**, *71*, 2459.
(323) Liljeblad, M.; Lundblad, A.; Pahlsson, P. *Biosens. Bioelectron.* **2002**, *17*, 883.
(324) Zhu, Y.; Ho B.; Ding J. L. *Biochim. Biophys. Acta* **2003**, *1611*, 234.
(325) Mueller-Loennies, S.; Brade, L.; MacKenzie, C. R.; Di Padova, F. E.; Brade, H. *J. Biol. Chem.* **2003**, *278*, 25618.
(326) de Haas, C. J. C.; Haas, P. J.; van Kessel, K. P. M.; van Strijp, J. A. G. *Biochem. Biophys. Res. Commun.* **1998**, *252*, 492.
(327) Catimel, B.; Scott, A. M.; Lee, F. T.; Hanai, N.; Ritter, G.; Welt, S.; Old, L. J.; Burgess, A. W.; Nice, E. C. *Glycobiology* **1998**, *8*, 927.
(328) Stein, T.; Gerisch, G. *Anal. Biochem.* **1996**, *35*, 252.
(329) Hayrinen, J.; Haseley, S.; Talaga, P.; Muhlenhoff, M.; Finne, J.; Vliegenthart, J. F. G. *Mol. Immunol.* **2002**, *339*, 399.

CR0300284

Relaxation Dynamics of Semiflexible Polymers

Y. Bohbot-Raviv,[1] W. Z. Zhao,[2] M. Feingold,[2] C. H. Wiggins,[3,5] and R. Granek[4,5,*]

[1]*Department of Materials and Interfaces, Weizmann Institute of Science, Rehovot 76100, Israel*
[2]*Department of Physics and The Ilse Katz Center for Nanotechnology, Ben-Gurion University, Beer Sheva 84105, Israel*
[3]*Department of Applied Physics and Applied Mathematics and Center for Computational Biology and Bioinformatics, Columbia University, 500 West 120th Street, New York, New York 10027, USA*
[4]*Department of Biotechnology Engineering and The Institute for Applied Biosciences, Ben-Gurion University, Beer Sheva 84105, Israel*
[5]*The Kavli Institute for Theoretical Physics, University of California, Santa Barbara, California 93106, USA*

(Received 2 July 2003; published 3 March 2004)

We study the relaxation dynamics of a semiflexible chain by introducing a time-dependent tension. The chain has one of its ends attached to a large bead, and the other end is fixed. We focus on the initial relaxation of the chain that is initially strongly stretched. Using a tension that is self-consistently determined, we obtain the evolution of the end-to-end distance with no free parameters. Our results are in good agreement with single molecule experiments on double stranded DNA.

DOI: 10.1103/PhysRevLett.92.098101 PACS numbers: 87.15.Aa, 87.15.He, 87.16.Ka

Semiflexible polymers, such as DNA, f-actin, and microtubule filaments, are common examples of biomaterials. The near equilibrium dynamics of semiflexible polymers in solutions have been extensively studied experimentally [1] and theoretically [2–4] in the past decade, both because of the possible implications in biology and because their dynamics is rather different from the flexible chain dynamics.

The far from equilibrium dynamics of such systems received much less attention. Perkins *et al.* [5] studied the shape of relaxing DNA that is hydrodynamically stretched. Their results were interpreted by Brochard and co-workers [6], who considered the propagation along the chain of the relaxing tension. However, their work builds on the freely jointed chain model and so does not include bending energy. Therefore, it may not be applied to strongly stretched chains even when their length L is much longer than their persistence length L_p. The strong stretching regime corresponds to tensions $\sigma \gtrsim k_B T/L_p$ associated with extensions above $0.5L$. For such tensions, excess length—associated with bending energy dominated undulations—is being pulled out.

Modern experiments on single DNA molecules often use a bead that is attached to one or both ends of the chain. This allows one to exert a controlled force on the chain by means of optical or magnetic traps [7–10]. When the end is released, the contraction of the chain involves motion of the bead with a time-dependent velocity. The Stokes force acting on the bead, which is transmitted to the DNA as tension, slows down the dynamics [10]. Hence, the interpretation of such experiments requires a detailed theory that describes the dynamics of the DNA-bead complex. The purpose of this Letter is to provide such a description. We introduce a *time-dependent tension* that is used to calculate the end-to-end distance. We solve for this tension by relating it to the Stokes drag acting on the bead, which, in turn, is a result of the DNA contraction. This allows us to fully describe the short time evolution of the end-to-end distance.

A time-dependent tension has been previously introduced [11,12] and, in particular, has been used to describe the propagation of equilibrium tension fluctuations [3]. A key feature in these studies is that the propagation of polymer density (or, equivalently, tension) is given as a ratio of the compression modulus B and a longitudinal drag coefficient. The compression modulus is found to be large and depends on the local tension as $B \sim \sigma^{3/2}$ [12], which leads to a tension propagation time τ_ℓ shorter than the transverse undulation relaxation time by a factor of $4(k_B T/L_p\sigma)^{1/2}$ [12]. For the large tensions considered here, this factor is larger than 10. This implies that tension can be assumed uniform along the chain when we describe the dynamics of transverse undulations. Therefore, the propagation of the tension and the associated longitudinal drag coefficient become irrelevant. Only the slow variables, i.e., the transverse undulations and the bead velocity, limit the motion. The uniform tension assumption is also justified considering the time resolution of our experiment. The tension propagation time is [12] $\tau_\ell \simeq 0.04(k_B T/L_p\sigma)^{1/2}\eta L^2/\sigma$, where η is the solvent viscosity. For the tensions and chain lengths that we use in experiment, $\sigma \simeq 10 k_B T/L_p$ and $L \simeq 20\ \mu$m, this leads to $\tau_\ell \simeq 0.006$ s, significantly shorter than the experimental time resolution, 0.04 s.

The bending energy $\mathcal{H}_o$ of a semiflexible polymer is well described by the wormlike chain (WLC) or Kratky-Porod model [2,3,8]. When an external force, σ, acts at the polymer ends pulling them apart, the energy becomes $\mathcal{H} = \mathcal{H}_o - \sigma z$, where z is the end-to-end distance of the chain. In this model, the chain conformation energy is

$$\mathcal{H} = \frac{\kappa}{2}\int_0^L ds\left(\frac{\partial^2 \mathbf{R}}{\partial s^2}\right)^2 - \sigma z, \tag{1}$$

where $\mathbf{R}(s)$ is the 3D position vector of the s polymer segment, κ is the bending constant, and L is the total arclength of the chain. The term $(\partial^2\mathbf{R})/(\partial s^2)$ evaluates the curvature at point s. When $\sigma = 0$, this energy leads to a persistence length $L_p = \kappa/k_BT$, that describes the arclength over which the local tangents decorrelate. The equilibrium force-extension relation, which results from the WLC model, has been investigated by Marko and Siggia [8] and verified in a wide range of experiments [7,8].

We now consider the dynamics of a chain-bead system. The system we study consists of a large bead attached to an end of a semiflexible polymer, while its other end is fixed. Although the ratio L/L_p can take any value, for $L \gtrsim L_p$ our treatment below applies only to the strong stretching regime, where roughness is small. The WLC Hamiltonian adopted for this case includes a time-dependent tension $\sigma(t)$ that replaces the constant tension σ [11]. $\sigma(t)$ will be identified as the Stokes drag acting on the bead, which is transmitted to the polymer itself as an external force. It acts as a time-dependent Lagrange multiplier conjugated to the extension $z(t)$.

We denote by $\mathbf{R}(s, t)$ the position of a polymer segment s at time t, and by $\mathbf{h}(s, t)$ the 2D component of $\mathbf{R}(s, t)$ perpendicular to the end-to-end vector, $\mathbf{h} = [h^{(\alpha)}, h^{(\beta)}]$. The extension $z(t)$, in the small roughness approximation, is given by

$$z(t) \simeq \int_0^L ds\left[1 - \frac{1}{2}\left(\frac{\partial \mathbf{h}(s, t)}{\partial s}\right)^2\right]. \tag{2}$$

In this approximation, the Hamiltonian of Eq. (1) becomes

$$\mathcal{H}(t) = \frac{1}{2}\int_0^L ds\left[\kappa\left(\frac{\partial^2\mathbf{h}}{\partial s^2}\right)^2 + \sigma(t)\left(\frac{\partial \mathbf{h}}{\partial s}\right)^2\right], \tag{3}$$

where the constant $-\sigma(t)L$ has been omitted.

The stochastic motion of the polymer is described by the Langevin equation for $\mathbf{h}(s, t)$ [4]

$$\frac{\partial \mathbf{h}(s, t)}{\partial t} = \int_0^L ds' \,\Lambda(|s - s'|) \times\left[-\kappa\left(\frac{\partial^4\mathbf{h}}{\partial s'^4}\right) + \sigma(t)\left(\frac{\partial^2\mathbf{h}}{\partial s'^2}\right)\right] + \mathbf{f}(s, t). \tag{4}$$

Here $\Lambda(s) = 1/8\pi\eta s$ is the Oseen hydrodynamic interaction kernel obtained from the diagonal terms of the Oseen tensor and $\mathbf{f}(s, t)$ is thermal white noise. Since the tension $\sigma(t)$ originates from the Stokes friction force acting on the bead, it may be related to the dynamics of the extension $\langle z(t)\rangle$, namely,

$$\sigma(t) = -\zeta\frac{\partial\langle z\rangle}{\partial t}, \tag{5}$$

where $\zeta = 6\pi\eta b$ is the friction constant of the bead of radius b. In Fourier space, Eq. (4) becomes

$$\frac{\partial \mathbf{h}_k(t)}{\partial t} = -\omega_k(t)\mathbf{h}_k(t) + \mathbf{f}_k(t), \tag{6}$$

where $\omega_k(t) = \Lambda_k[\kappa k^4 + \sigma(t)k^2]$ and $\Lambda_k \simeq \ln(1/ka)/4\pi\eta$. Here a is a short length scale cutoff chosen as the thickness of the polymer. The correlation function of $\mathbf{f}_k(t)$ is given by the fluctuation-dissipation theorem

$$\langle f_k^{(\alpha)}(t) f_{-k}^{(\beta)}(t')\rangle = 2k_BTL\Lambda_k\delta_{\alpha\beta}\delta(t - t'), \tag{7}$$

where α and β denote the two transverse directions.

Solving the Langevin Eq. (6) allows us to calculate the equal time undulation correlation function in Fourier space

$$\langle \mathbf{h}_k(t)\cdot\mathbf{h}_{-k}(t)\rangle = \langle \mathbf{h}_k\cdot\mathbf{h}_{-k}\rangle_o e^{-2\Omega_k(t)} + 4k_BTL\Lambda_k\int_0^t dt'\, e^{-2[\Omega_k(t) - \Omega_k(t')]}, \tag{8}$$

where $\Omega_k(t) = \int_0^t dt'\,\omega_k(t')$ and $\langle \mathbf{h}_k\cdot\mathbf{h}_{-k}\rangle_o$ is the initial undulation correlator. Since the polymer is assumed to be initially in equilibrium, we take

$$\langle \mathbf{h}_k\cdot\mathbf{h}_{-k}\rangle_o = \frac{2k_BTL}{\sigma_o k^2 + \kappa k^4}, \tag{9}$$

where σ_o is the initial tension, i.e., the pulling force on the bead *prior* to its release. Accordingly, the mean extension after the release, in the small roughness approximation, is

$$\frac{\langle z(t)\rangle}{L} = 1 - \frac{1}{2L^2}\sum_{k=\pi/L}^{\pi/a} k^2\langle \mathbf{h}_k(t)\cdot\mathbf{h}_{-k}(t)\rangle. \tag{10}$$

The corresponding initial extension is $\langle z(0)\rangle/L = 1 - k_BT/\sqrt{4\kappa\sigma_o}$, as obtained in Ref. [8].

Equation (10) determines the mean end-to-end distance $\langle z(t)\rangle$ at time t given the full history of the tension $\sigma(t')$ at all times $0 < t' < t$. This evolution may be determined uniquely if we identify the physical source of the tension as the Stokes force acting on the bead, Eq. (5). This leads to a set of two equations for the two unknowns $\langle z(t)\rangle$ and $\sigma(t)$. To obtain a single equation, we integrate the Stokes law, Eq. (5), such that

$$\Sigma(t) = \zeta[\langle z(0)\rangle - \langle z(t)\rangle], \tag{11}$$

where $\Sigma(t) = \int_0^t dt'\,\sigma(t')$. Equation (10) becomes an integral equation for $\Sigma(t)$

$$\frac{\Sigma(t)}{\zeta L} = \frac{k_BT}{\pi}\int_{\pi/L}^{\pi/a} dk\frac{[e^{-2\Omega_k(t)} - 1]}{\kappa k^2 + \sigma_o} + \frac{2k_BT}{\pi}\int_{\pi/L}^{\pi/a} dk\,\Lambda_k k^2\int_0^t dt'\, e^{-2[\Omega_k(t) - \Omega_k(t')]}, \tag{12}$$

where $\Omega_k(t) = \Lambda_k[\Sigma(t)k^2 + \kappa t k^4]$.

In order to verify the validity of Eq. (12), we consider the (nonphysical) limit where the polymer feels no drag. This may be achieved by formally taking the limit $\Lambda_k \to \infty$. Using $\lim_{\Lambda\to\infty}\Lambda e^{-\Lambda x} = \delta_+(x)$ and performing the integrations in Eq. (12), we obtain the limiting equation of motion:

$$6\pi\eta b\frac{d\langle z\rangle}{dt} = -k_BT/[4L_p(1-\langle z\rangle/L)^2] = -\sigma_{\rm eq}(\langle z\rangle). \tag{13}$$

Indeed, in this case we expect that the polymer rapidly explores all of its configurations at any given extension, thus passing through quasiequilibrium states as it relaxes. This implies that the forces acting on the bead are the equilibrium polymer force and the Stokes drag force, as described by Eq. (13). While an equation of this type has been previously used to explain the relaxation curve, it failed to quantitatively describe the experimental data [10]. Although reasonable agreement can be obtained using the persistence length as a fitting parameter, the best fitting value is about 3 times larger than the known value, $L_p \approx 50$ nm [10].

An alternative form of Eq. (12), which is convenient for numerical analysis, is obtained by writing $\sigma(t) = \sigma_o - \delta\sigma(t)$ and integrating by parts the terms involving t' explicitly. A further simplification, with little effect on the final result (as verified numerically), is made by replacing k in Λ_k by $k_\xi = 1/\xi$, where $\xi = \sqrt{\kappa/\sigma_o}$. Transforming to dimensionless variables $\tilde{k} = k\xi$, $\tilde{t} = t/\tau$, and $\tilde{\Sigma} = \Sigma/(\sigma_o\tau)$, where $\tau = \xi^2/[2\Lambda_{k_\xi}\sigma_o]$, and defining $C = 3\ln(\xi/a)bL/(\pi\xi L_p)$, leads to

$$\tilde{\Sigma}(\tilde{t}) = C\int_0^{\tilde{t}} d\tilde{t}'\left(1-\frac{d\tilde{\Sigma}(\tilde{t}')}{d\tilde{t}'}\right)\int_{\pi\xi/L}^{\pi\xi/a} d\tilde{k}\frac{\tilde{k}^2}{\tilde{k}^2+1} \times e^{-(\tilde{t}-\tilde{t}')\tilde{k}^4-[\tilde{\Sigma}(\tilde{t})-\tilde{\Sigma}(\tilde{t}')]\tilde{k}^2}. \tag{14}$$

Equation (14) is a nonlinear integrodifferential equation. A straightforward numerical algorithm that uses a single time step has been found to be time consuming. In order to reduce computing time, we divide the total time scale into blocks; each block comprises many integration steps. The time step in each block is constant and doubles from one block to the next. At each time step, Eq. (14) is iteratively solved for $\tilde{\Sigma}(\tilde{t})$. The solution at a given block is based only on half of the data points (i.e., every second point) calculated in the previous block, one quarter of the points calculated in the second previous block, and so on. This algorithm speeds up the computation by about 1.5 orders of magnitude. Once $\tilde{\Sigma}(\tilde{t})$ is found, the extension $z(t)$ is obtained from Eq. (11).

The numerical results were compared to recent measurements on a setup identical to the one described in Refs. [9,10]. We use double stranded DNA from the λ phage (Promega, $L = 16.5$ μm). The DNA is attached at one end to a polystyrene bead (Polysciences) and at the other end to the cover slip at the bottom of the sample. This is obtained using a low pH protocol [9] that allows one to vary L. A laser beam (SDL, $\lambda = 830$ nm) is focused through a 100× objective (Zeiss, 1.3 NA, oil immersion) to give an optical trap. Trapped beads are used to stretch the DNA to extensions that are close to L. After turning off the trap, the relaxation is monitored by tracking the bead at video rate, 25 frames/s, and with low spatial resolution, 0.3 μm. Experiments were performed with different bead sizes, $b = 0.5$, 1, and 1.4 μm.

In Figs. 1–3, we compare the predictions of our theory to the experimental data. In the numerical simulations, we used the viscosity of water at room temperature $\eta = 0.89$ mPs, DNA persistence length $L_p = 50$ nm, and DNA thickness $a = 2$ nm. There are *no free parameters.* The initial extension of the DNA molecule known from

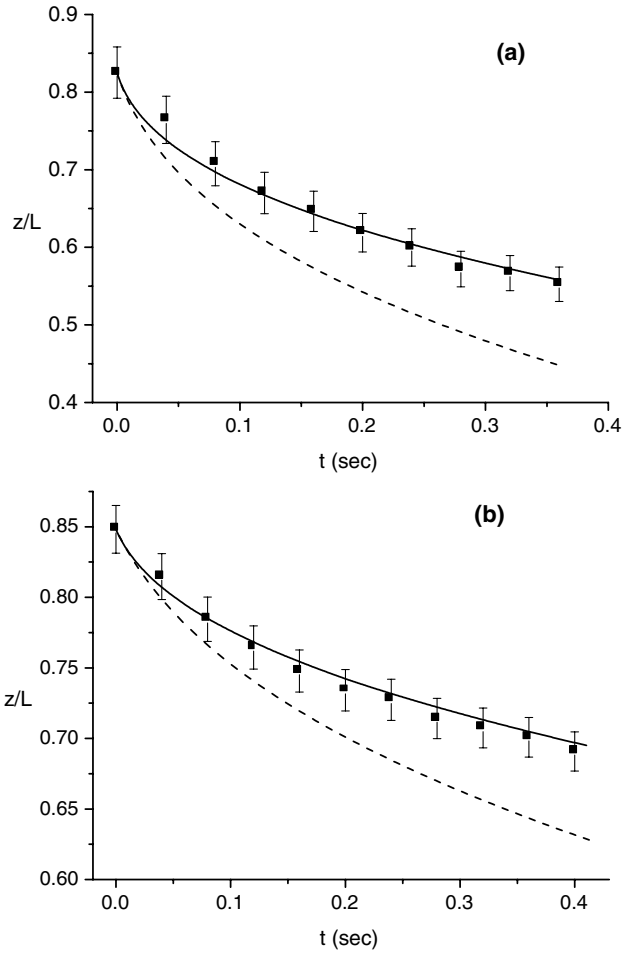

FIG. 1. DNA extension plotted vs time. (a) DNA length $L = 14.5$ μm, bead radius $b = 0.5$ μm, and initial extension $z(0) = 0.825L$; (b) $L = 20.1$ μm, $b = 1.4$ μm, and $z(0) = 0.848L$. The solution of Eqs. (11) and (14) (solid line) and the experimental data points are shown. The computational error in the solid line is about 4% at the longest times shown and diminishes at shorter times. For comparison, the solution of Eq. (13) (dashed line) is also shown.

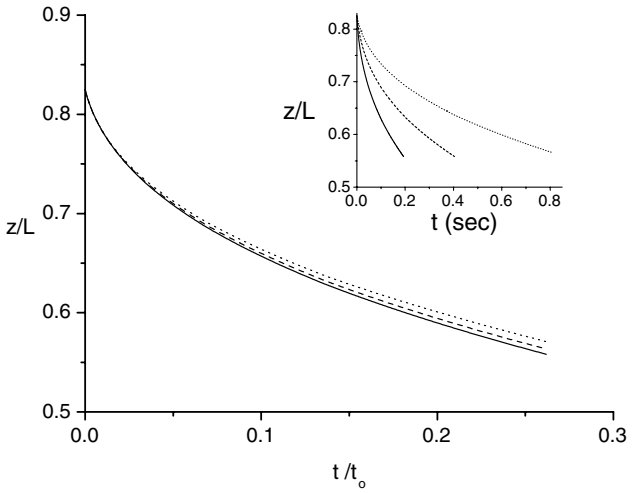

FIG. 2. Theoretical extension, computed from Eqs. (11) and (14), vs the scaled time t/t_o, where $t_o = 6\pi\eta L_p L b/k_B T$, for three different bead radii: $b = 0.25$ μm (full line), $b = 0.5$ μm (dashed line), and $b = 1$ μm (dotted line). $L = 14.5$ μm and $z(0)/L = 0.825$. Inset: Same as above but against the time (unscaled).

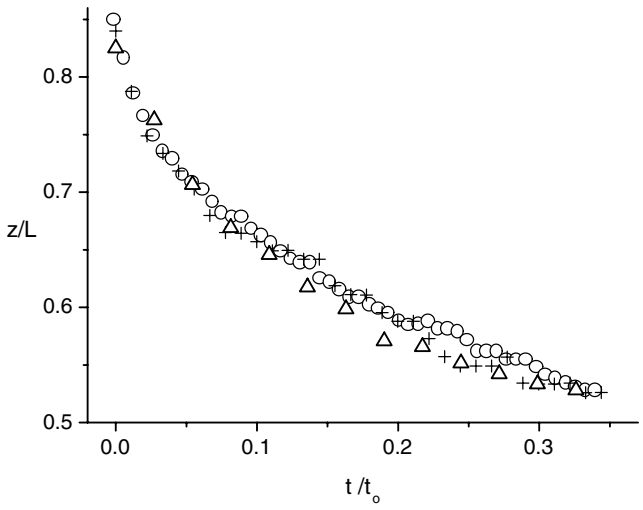

FIG. 3. Experimental results for DNA relaxation. The time axis is divided by t_o. Circles are for $b = 1.4$ μm [same system as for Fig. 1(b)], plusses are for $b = 0.5$ μm [same system as for Fig. 1(a)], and triangles are for a system with $b = 1$ μm, $z(0)/L = 0.84$, and $L = 17.7$ μm.

the experiment determines the initial tension used in the numerical solution, $\sigma_o = k_B T/\{4L_p[1 - z(0)/L]^2\}$. In Figs. 1(a) and 1(b), we plot the relative extension z/L against time t for two systems differing in chain length, bead size, and initial conditions. Good agreement between theory and experiment is found. For comparison, we also show the solution of Eq. (13) (dashed line) which fails to account for the experimental data. Figure 2 shows theoretical predictions for a system with three different bead sizes, with the time rescaled to t/t_o, where $t_o = 6\pi\eta L_p L b/k_B T$, while in the inset we plot the results against time. We find that the collapse of the three theoretical curves is nearly perfect, signifying a weak breakdown of scaling. A nearly perfect scaling is also found when we vary the chain length L. Note that this scaling cannot be inferred directly from Eq. (14), although it is obeyed by the $b \to \infty$ limiting Eq. (13). In Fig. 3, we demonstrate a similar scaling behavior in the experimental data.

In this Letter, we have developed a first principle approach to dynamics of strongly stretched semiflexible chains. This approach employs a time-dependent tension that is uniquely determined by a supplementary physical constraint. By comparing to experiments, we have shown that our theory works well with no free parameters. Our approach may be extended to other problems, e.g., the nonlinear viscoelasticity of actin networks and the dynamics of DNA-protein complexes [13].

We thank R. Baer, D. Chatenay, M. Elbaum, E. Frey, E. Goshen, T. Liverpool, F. MacKintosh, A. Maggs, and D. Morse for useful discussions. This work was supported in part by the National Science Foundation under Grant No. PHY99-07949, and by the Israel Academy of Science and Humanities (Grant No. 263/00).

*Author to whom correspondence should be addressed. Electronic address: rgranek@bgumail.bgu.ac.il

[1] F. Amblard *et al.*, Phys. Rev. Lett. **77**, 4470 (1996); L. Le Goff *et al.*, Phys. Rev. Lett. **89**, 258101 (2002); A. Caspi *et al.*, Phys. Rev. E **66**, 011916 (2002).
[2] F. Gittes and F. C. MacKintosh, Phys. Rev. E **58**, R1241 (1998); E. Farge and A. C. Maggs, Macromolecules **26**, 5041 (1993); K. Kroy and E. Frey, Phys. Rev. E **55**, 3092 (1997.
[3] V. Shankar *et al.*, J. Rheol. **46**, 1111 (2002); T. B. Liverpool and A. C. Maggs, Macromolecules **34**, 6064 (2001); R. Everaers *et al.*, Phys. Rev. Lett. **82**, 3717 (1999).
[4] R. Granek, J. Phys. II (Paris) **7**, 1761 (1997).
[5] T. T. Perkins *et al.*, Science **264**, 822 (1994); **268**, 83 (1995).
[6] F. Brochard-Wyart *et al.*, Europhys. Lett. **26**, 511 (1994); S. Manneville *et al.*, Europhys. Lett. **36**, 413 (1996).
[7] S. B. Smith *et al.*, Science **258**, 1122 (1992); **271**, 795 (1996); P. Cluzel *et al.*, Science **221**, 792 (1996); J. C. Meiners and S. R. Quake, Phys. Rev. Lett. **84**, 5014 (2000); T. R. Strick *et al.*, Science **271**, 1835 (1996).
[8] J. Marko and E. Siggia, Macromolecules **28**, 8759 (1995).
[9] G. V. Shivashankar *et al.*, Proc. Natl. Acad. Sci. U.S.A. **96**, 7916 (1999).
[10] M. Feingold, Physica (Amsterdam) **9E**, 616 (2001).
[11] U. Seifert *et al.*, Phys. Rev. Lett. **77**, 5389 (1996).
[12] F. Brochard-Wyart *et al.*, Europhys. Lett. **47**, 171 (1999).
[13] H. Salman *et al.*, Biophys. J. **80**, 783 (2001).

Fluorescence Correlation Spectroscopy Close to a Fluctuating Membrane

Cécile Fradin,*† Asmahan Abu-Arish,* Rony Granek,*‡ and Michael Elbaum*
*Department of Materials and Interfaces, Weizmann Institute of Science, Rehovot 76100, Israel; †Department of Physics and Astronomy and Department of Biochemistry, McMaster University, Hamilton, Ontario L8S 4M1, Canada; and ‡Department of Biotechnology Engineering and the Institute for Applied Biosciences, Ben-Gurion University of the Negev, Beer-Sheva 84105, Israel

ABSTRACT Compartmentalization of the cytoplasm by membranes should have a strong influence on the diffusion of macromolecules inside a cell, and we have studied how this could be reflected in fluorescence correlation spectroscopy (FCS) experiments. We derived the autocorrelation function measured by FCS for fluorescent particles diffusing close to a soft membrane, and show it to be the sum of two contributions: short timescale correlations come from the diffusion of the particles (differing from free diffusion because of the presence of an obstacle), whereas long timescale correlations arise from fluctuations of the membrane itself (which create intensity fluctuations by modulating the number of detected particles). In the case of thermal fluctuations this second type of correlation depends on the elasticity of the membrane. To illustrate this calculation, we report the results of FCS experiments carried out close to a vesicle membrane. The measured autocorrelation functions display very distinctly the two expected contributions, and allow both to recover the diffusion coefficient of the fluorophore and to characterize the membrane fluctuations in term of a bending rigidity. Our results show that FCS measurements inside cells can lead to erroneous values of the diffusion coefficient if the influence of membranes is not recognized.

INTRODUCTION

Fluorescence correlation spectroscopy (FCS) is a method allowing the study of the dynamics of phenomena involving fluctuations in the fluorescence signal collected from a confocal detection volume. The principle is to compute the autocorrelation function of this signal: each process leading to a variation in fluorescence at a particular timescale will be reflected in the autocorrelation function at the same timescale. FCS was originally introduced to observe chemical reactions in solution (Magde et al., 1972), but many other processes can be studied. The simplest is the free diffusion of fluorescent particles (Aragón and Pecora, 1976; Rigler et al., 1993), where FCS allows retrieving both their diffusion coefficient and their concentration. Rotational diffusion (Ehrenberg and Rigler, 1974; Kask et al., 1987), residence of the fluorophore in a triplet state (Widengren et al., 1995), directed motion (Köhler et al., 2000), and photobleaching (Widengren and Rigler, 1997), among other phenomenon, can also be observed (see e.g., Thompson, 1991, or Webb, 2001 for reviews).

The dimensions of the confocal detection volume can typically be smaller than $0.5 \times 0.5 \times 2\ \mu m^3$, giving submicron spatial resolution in the two lateral directions, and corresponding to a volume of <1 fl, to be compared with the typical length ($\simeq 10\ \mu m$), and volume ($\simeq 1$ pl) of a cell. The photomultipliers or avalanche photodiodes used for FCS experiments can detect single fluorophores with CW excitation intensities of the order of 10 $\mu W/\mu m^2$, levels supposed to be nondamaging for most biological systems. Used in its single-molecule range of application (i.e., with an average of less than one molecule in the detection volume), FCS allows working with concentrations as low as 1 nM. The time resolution of the correlators used to calculate the autocorrelation function in real time can be as low as 10 ns. For all these reasons, there is a very strong interest in applying FCS to biological systems (Berland et al., 1995; Brock et al., 1998; Politz et al., 1998; Schwille et al., 1999; Wachsmuth et al., 2000; Gennerich and Schild, 2000; Cluzel et al., 2000; Dittrich et al., 2001; Nomura et al., 2001).

However, when examining the specific issue of the diffusion of macromolecules inside cells, one invariably observes long time correlations in the autocorrelation function, and faces the difficulty to identify the cause. Anomalous diffusion, on one hand, or slowing down of one part of the fluorophore population, on the other, perhaps by nonspecific binding or compartmentalization, have been proposed as interpretations (Wachsmuth et al., 2000). The cellular medium being crowded by large-scale objects such as lipid membranes (for example the cellular membrane, the endoplasmic reticulum, and the nuclear membrane), mitochondria, or cytoskeleton, it is somewhat obvious that these will influence macromolecular diffusion nearby (see e.g., Zimmerman and Minton, 1993), and hence that their effect should be taken into account when analyzing FCS measurements inside cells. Nevertheless, this complex problem has received limited attention so far. Calculations have been made for diffusion between two rigid membranes in the case of regular FCS experiments (Gennerich and Schild, 2000), and for diffusion and binding close to a single rigid membrane in the case of a nonstandard geometry (FCS used with total internal reflection) (Starr and Thompson, 2001),

Submitted October 17, 2001, and accepted for publication October 16, 2002.

Address reprint requests to Cécile Fradin, Dept. of Physics and Astronomy, McMaster University, 1280 Main St. West, Hamilton, ON L8S 4M1, Canada. Tel.: 1-905-525-9140; Fax: 1-901-546-1252; E-mail: fradin@physics.mcmaster.ca.

0006-3495/03/03/2005/16 $2.00

showing that the restriction of diffusion in one dimension has a strong effect on the residence time measured by FCS, and hence on the extracted diffusion coefficient if this effect is not accounted for. We consider in this paper the case of diffusion close to a single soft membrane (able to undergo fluctuations such as thermal fluctuations) studied by standard FCS. This case will be relevant to most FCS experiments in biological systems, inasmuch as they are usually bounded by soft lipidic membranes, but most particularly to studies of phenomena occurring close to the cellular or nuclear membranes.

MATERIALS AND METHODS

Fluorescence correlation spectroscopy

Set-up

The home-built FCS set-up used for the experiments is a classical one, as described for example in Thompson (1991), based on a modified upright microscope equipped with differential interference contrast imaging. Fluorescence is excited by a CW HeNe laser (1674P, JDS Uniphase, San Jose, CA, USA), whose 543.5-nm wavelength is selected by an excitation filter (HQ545/30, Chroma Technology, Brattleboro, VT, USA). The beam passes through a beam expander, which allows spatially filtering it by placing a 150-μm pinhole at the focus (to keep only the fundamental Gaussian mode of the laser), and to increase its $1/e^2$ waist to a value of 2.8 mm before entering the 6-mm back aperture of a 100× oil objective (Achrostigmat 100 × /1.25, Zeiss, Göttingen, Germany), resulting in a theoretical halfwidth of the focal volume of 300 nm (Rigler et al., 1993). The 750-μm output power of the laser is attenuated by a system of two polarizers to obtain a radiant exposure of order $10\,\mu\mathrm{W}/\mu\mathrm{m}^2$ at the focus. The exact intensity is monitored by an amplified silicon detector (PDA55, Thorlabs, Newton, NJ, USA) measuring the excitation intensity transmitted by the dichroic mirror, which amounts to 10.4% of the actual intensity arriving on the sample. The emitted fluorescence is filtered by an emission filter (HQ610/75, Chroma Technology), focused through a 50-μm diameter pinhole (hence theoretically giving a confocal detection volume with a $1/e^2$ radius of 250 nm, and a half-height of 825 nm (Rigler et al., 1993)), and then detected by a photon counting head (H7421, Hamamatsu Photonics, Shimokanzo, Japan). The output signal is fed into a correlator (Flex99R-12D, Correlator.com, Bridgewater, NJ, USA). The measurement durations for curves (presented in the section FCS measurements near a vesicle membrane) were either 30 s or 60 s. The vertical position of the objective and horizontal position of the sample in one direction can be adjusted by means of home-built piezoelectric-driven objective and sample holder. Monitoring of the objective height and of the sample position is achieved using a multifunctional input/output board (PCI-1200, National Instruments, Austin, TX, USA) and a program written for LabView (Labview 5.1, National Instruments). Analyses of the measured autocorrelation functions were performed with a program using the NonlinearRegress function of Mathematica (Mathematica 4.0, Wolfram Research, Champaign, IL, USA).

Autocorrelation function

The normalized autocorrelation function of a signal $I(t)$ fluctuating around its mean value $\langle I(t)\rangle$ is (adopting the convention that the deviation of any quantity X from its mean value $\langle X\rangle$ will be noted δX):

$$G(t) = \frac{\langle \delta I(0)\delta I(t)\rangle}{\langle I(t)\rangle^2}, \tag{1}$$

where all averages are taken over time and stationarity of the system has been assumed.

In the simple case of one single fluorophore freely diffusing in solution (with a diffusion constant D), an analytical expression of this autocorrelation function can be derived by assuming the intensity profile of the detection volume to be Gaussian (Aragón and Pecora, 1976). This assumption is justified when the laser beam is spatially filtered and underfills the back aperture of the objective. The detectable emission intensity is then written:

$$I_{\mathrm{D}}(\mathbf{r}) = EQI_0 e^{-2x^2/w_0^2} e^{-2y^2/w_0^2} e^{-2z^2/z_0^2} c(\mathbf{r}), \tag{2}$$

where w_0 and z_0 are the radius of the $1/e^2$ contour in, respectively, the radial and axial directions (cf. Fig. 1); Q is the quantum efficiency of the fluorophore and $c(\mathbf{r})$ its concentration; E is the collection efficiency of the optical system; and I_0 the maximum laser intensity in the focal plane.

In the case where the average concentration of the fluorophore is constant over space, and considering a total background intensity $I_{\mathrm{B}}(t)$, one has:

$$\begin{aligned}\langle I(t)\rangle &= \int_{-\infty}^{+\infty} dx \int_{-\infty}^{+\infty} dy \int_{-\infty}^{+\infty} dz\, I_{\mathrm{D}}(\mathbf{r}) + I_{\mathrm{B}}(t) \\ &= \langle c\rangle EQI_0 \left(\frac{\pi}{2}\right)^{3/2} w_0^2 z_0 + \langle I_{\mathrm{B}}(t)\rangle = (1+r)I_{\mathrm{M}}, \end{aligned} \tag{3}$$

writing $I_{\mathrm{M}} = \langle c\rangle EQI_0(\pi/2)^{3/2} w_0^2 z_0$ and introducing the ratio $r = \langle I_{\mathrm{B}}(t)\rangle / I_{\mathrm{M}}$.

Assuming that the background intensity is not correlated in time and that the system is stationary (which ensures that $\langle \delta c(\mathbf{r},0)\delta c(\mathbf{r}',t)\rangle = \langle c\rangle e^{-(\mathbf{r}'-\mathbf{r})^2/4Dt}/(4Dt)^{3/2}$):

$$\begin{aligned}\langle \delta I(0)\delta I(t)\rangle &= \int\int\int_{-\infty}^{+\infty} d\mathbf{r}\, \delta I_{\mathrm{D}}(\mathbf{r}) \int\int\int_{-\infty}^{+\infty} d\mathbf{r}'\, \delta I_{\mathrm{D}}(\mathbf{r}') \\ &= \frac{I_{\mathrm{M}}^2}{\langle c\rangle \pi^{3/2} w_0^2 z_0} \frac{1}{\left(1+4Dt/w_0^2\right)\left(1+4Dt/z_0^2\right)^{1/2}}. \end{aligned} \tag{4}$$

The autocorrelation function is then given by the classical expression (Aragón and Pecora, 1976):

$$G(t) = \frac{1}{(1+r)^2} \frac{1/\langle N\rangle}{(1+t/\tau)(1+t/(S^2\tau))^{1/2}}, \tag{5}$$

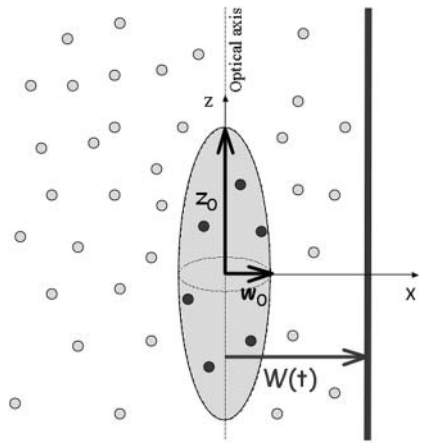

FIGURE 1 Geometry of the considered system. Fluorescent molecules are represented by spheres. Dark gray spheres correspond to molecules in the detection volume, whose fluorescence will be detected by the optical system. The membrane separates space into a region ($x < \langle W\rangle$) containing fluorophores with an average concentration $\langle c\rangle$, and a region ($x > \langle W\rangle$) containing no fluorophores.

where $\tau = w_0^2/4D$ would be the average residence time of a fluorophore in an infinite cylinder of radius w_0, $\langle N\rangle = \langle c\rangle \pi^{3/2} w_0^2 z_0$ is the average number of fluorophores in the effective volume $V_e = \pi^{3/2} w_0^2 z_0$, and $S = z_0/w_0$ is the aspect ratio of the detection volume. At long time this leads to the scaling $G(t) \sim t^{-3/2}$, the probability for a random walking particle in three dimensions to return to the origin.

In practice, one also has to take into account the fact that a fraction T of the fluorophores is in a nonfluorescent triplet state with an average half-life time τ_T, which adds a supplementary contribution to the autocorrelation function (Palmer and Thompson, 1987; Widengren et al., 1995). Finally, the autocorrelation function obtained from the simple free diffusion of a single fluorophore in an infinite solution is correctly described by:

$$G(t) = \frac{1}{(1+r)^2}\left(1 + \frac{Te^{-t/\tau_T}}{1-T}\right)\frac{1/\langle N\rangle}{(1+t/\tau)(1+t/(S^2\tau))^{1/2}}, \tag{6}$$

If the diffusion is obstructed by the presence of obstacles in the solution, it was proposed that this could in some cases be accounted for by considering a mean-square displacement of the particles $r(t)^2 \sim t^\gamma$ (Bunde and Havlin, 1995; Saxton, 1994) where the exponent $\gamma < 1$ characterizes the anomalous diffusion. If the diffusion coefficient D_a of the particles undergoing anomalous diffusion is defined by $\langle r(t)^2\rangle = 6D_a t^\gamma$ (which can be seen alternatively as having a time-dependent diffusion coefficient $D = D_a t^{\gamma-1}$), the autocorrelation function (easily obtained by replacing Dt by $D_a t^\gamma$ in Eq. 6) reads:

$$G(t) = \frac{1}{(1+r)^2}\left(1 + \frac{Te^{-t/\tau_T}}{1-T}\right)\frac{1/\langle N\rangle}{(1+(t/\tau_a)^\gamma)(1+1/S^2(t/\tau_a)^\gamma)^{1/2}}, \tag{7}$$

where the quantity τ_a is again the average residence time of a particle in an infinite cylinder of radius w_0, only this time it is given by $\tau_a = (w_0^2/4D_a)^{1/\gamma}$. The anomalous-diffusion coefficient D_a is in units of m^2/s^γ.

Calibration

The set-up was calibrated each time experiments were carried out by fitting the autocorrelation function obtained from the free diffusion of Rhodamine 610 (Exciton Chemical, Dayton, OH, USA) in water with Eq. 6, and assuming $D = 280\,\mu m^2/s$ (Rigler et al., 1993). Values obtained for the experiments presented here were $\tau = 47\,\mu s$ and $S = 8$, giving for the half-waists of the detection volume $w_0 = 230\,nm$ and $z_0 = 1.8\,\mu m$. The effective volume is then $V_e = 0.53\,fl$.

Vesicle preparation

DOPC (1,2-Di[cis-9-octadecenoyl]-sn-glycero-3-phosphocholine, also known as diC18:1c9, purchased from Avanti Polar Lipids, Alabaster, AL) vesicles were prepared either by gentle hydration (Needham and Evans, 1988) or by electroswelling (Angelova et al., 1992) (the latter method yields a higher proportion of unilamellar vesicles). For gentle hydration, ~50 μl of DOPC dissolved in chloroform (4 mg/ml) was dried on a roughened Teflon plate, after which 5 ml of a 0.1 M Pipes buffer (pH = 7.4) supplemented with 0.2 M glucose was added, and vesicles were grown overnight at 37°C. For electroswelling, the same quantity of the DOPC solution was dried on an Indium Tin Oxide glass plate, and closed by another Indium Tin Oxide plate separated by neoprene spacers. The 1 ml enclosed volume was then filled with 0.1 M sucrose solution. An alternating electric potential was applied, 1 V peak-to-peak amplitude, 10 Hz for 2 h, followed by 1 Hz for 1 h. After 2-h annealing, the vesicle-containing solution was harvested gently. Before experiments, a stock of vesicles was mixed with an equal volume of a 10% hypertonic glucose solution (instead of sucrose), and with a concentration of fluorescent material (either streptavidin labeled with Cy3 dye, purchased from Amersham, [Buckinghampshire England] or tetramethyl rhodamine-labeled 10-kDa dextran, purchased from Molecular Probes, Eugene, OR) at double the desired final concentration. This ensured that the vesicles, filled with a less dense medium, would float upward and fix themselves on the upper coverslip of the sample, making their observation in our upright microscope easier, and allowing to carry out all the FCS experiments within 20 μm of the upper coverslip. Also this way a compartmentalization was created between the inside of the vesicles, void of fluorophore, and the outside of the vesicles, containing fluorophores.

DERIVATION OF THE AUTOCORRELATION FUNCTION IN PRESENCE OF A FLUCTUATING MEMBRANE

General expression in presence of a vertical fluctuating membrane

We first consider a planar membrane separating space into a region void of fluorophore and a region with an average fluorophore concentration $\langle c\rangle$ constant over space, and call $W(t)$ the position of this membrane relative to the center of the detection volume (see Fig. 1). We will assume the membrane to be vertical and perpendicular to the x axis (as shown in Fig. 1) in all the following derivations, and indicate how the results are changed if the membrane is horizontal (perpendicular to the optical axis). We will suppose that the membrane position is varying with time around an average position $\langle W\rangle$: $W(t) = \langle W\rangle + \delta W(t)$ (hence excluding from the calculation drifts in the position of the membrane). We will also assume that the membrane movements are slow enough compared to free diffusion of the fluorophores that we can decouple these two motions (adiabatic approximation). Finally we will neglect all interactions of the membrane with the strong electric field in the vicinity of the laser focus (Bar-Ziv et al., 1995), which should be justified for the very low laser intensities used in FCS experiments.

Average intensity as a function of the distance to the wall

As a fraction of the space enclosed by the detection volume may be devoid of fluorophores, the expression for the average intensity in the detector is different from the one derived in the classical case (Eq. 3), and now depends on the membrane position:

$$\langle I_w(t)\rangle = EQI_0\frac{\pi}{2}w_0 z_0 \times \left\langle \int_{-\infty}^{W(t)} dx\, e^{-2x^2/w_0^2} c(t)\right\rangle + \langle I_B(t)\rangle. \tag{8}$$

Because a negligible coupling between the fluctuations in fluorophore concentration and the fluctuations in position of the membrane has been assumed, one can separate the averaging on c and δW, obtaining:

$$\langle I_w(t)\rangle = I_M \times \left(\left\langle \frac{1+\mathrm{erf}(\sqrt{2}(W(t))/w_0)}{2}\right\rangle + r\right). \tag{9}$$

The intrinsic width of the membrane (head-to-head distance between the polar heads of lipid molecules) is of

the order of 5 nm for phospholipids (Rawicz et al., 2000), which is negligible compared to w_0. Although the roughness of the membrane contributes to the statistical width of the interface, we will consider the case where the amplitude of the membrane fluctuations remains small compared to w_0, which will be the case for membranes with sufficiently high bending rigidity. This hypothesis can be easily verified during experiments by checking that the amplitude of the intensity fluctuations are small compared to the difference in intensity between the inside and the outside of the vesicle. In this case the intensity profile is a simple error function:

$$\langle I_w(t)\rangle = I_M \times \left(\frac{1+\mathrm{erf}(\sqrt{2}\langle W\rangle/w_0)}{2} + r\right). \tag{10}$$

Autocorrelation function

We have now:

$$I_{\langle W\rangle}(t) = I_B(t) + EQI_0 \int_{-\infty}^{+\infty} dy e^{-2y^2/w_0^2} \int_{-\infty}^{+\infty} dz e^{-2z^2/z_0^2} \times \left(\int_{-\infty}^{\langle W\rangle} dx e^{-2x^2/w_0^2} c(\mathbf{r},t) + \int_{\langle W\rangle}^{\langle W\rangle+\delta W(t)} dx e^{-2x^2/w_0^2} c(\mathbf{r},t)\right). \tag{11}$$

Using again the fact that the statistical fluctuations of the interface should be small ($\delta W \ll w_0$), and keeping only first order terms in δW and δc, we get:

$$I_{\langle W\rangle}(t) = \langle I_{\langle W\rangle}(t)\rangle + EQI_0 \int_{-\infty}^{+\infty} dy\, e^{-2y^2/w_0^2} \int_{-\infty}^{+\infty} dz\, e^{-2z^2/z_0^2} \times \left(\int_{-\infty}^{\langle W\rangle} dx\, e^{-2x^2/w_0^2} \delta c(\mathbf{r},t) + \delta W(t) \times e^{-2\langle W\rangle^2/w_0^2} \langle c\rangle\right). \tag{12}$$

Then, considering that the fluctuations of the wall and the movements of the fluorophores are not coupled, and that the background intensity is noncorrelated in time, we obtain:

$$\langle \delta I_{\langle W\rangle}(0)\delta I_{\langle W\rangle}(t)\rangle = (EQI_0)^2 \int_{-\infty}^{+\infty} dy\, e^{-2y^2/w_0^2} \int_{-\infty}^{+\infty} dz\, e^{-2z^2/z_0^2} \int_{-\infty}^{+\infty} dy' e^{-2y'^2/w_0^2} \int_{-\infty}^{+\infty} dz'\, e^{-2z'^2/z_0^2} \times \left(\int_{-\infty}^{\langle W\rangle} dx\, e^{-2x^2/w_0^2} \int_{-\infty}^{\langle W\rangle} dx'\, e^{-2x'^2/w_0^2} \langle \delta c(\mathbf{r},0)\delta c(\mathbf{r}',t)\rangle + \langle c\rangle^2 e^{-4\langle W\rangle^2/w_0^2} \langle \delta W(0)\delta W(t)\rangle_{\mathrm{planar}}\right). \tag{13}$$

The first term corresponds to the diffusion of the fluorophores in solution, modified by the presence of a flat vertical obstacle. It is exactly equal to the autocorrelation function that would be obtained if the obstacle were a fixed, rigid wall ($\delta W(t) = 0$). The second term reflects the influence of the position fluctuations of the obstacle, and has to be added in the case of a soft fluctuating membrane. By its motion, the membrane modulates the number of fluorophores that can be observed in the detection volume, causing fluctuations in the total detected intensity. The related correlations are not due to individual particle motions, as in the case of the first term, but to variations in the number of detected particles (where the diffusional fluctuations have already been averaged). The characteristic times of these correlations will then depend only on the characteristic times of the membrane fluctuations. The subscript of $\langle \delta W(0)\delta W(t)\rangle$ has been added to remind that this function has to be calculated for a membrane that is flat (no curvature and no roughness) at the scale of the detection volume. The total autocorrelation function then reads:

$$G(\langle W\rangle, t) = G_d(\langle W\rangle, t) + G_f(\langle W\rangle, t), \tag{14}$$

where the part corresponding to the modified diffusion of the fluorophore is (for the geometry depicted in Fig. 1):

$$G_d(\langle W\rangle,t) = \left[(EQI_0)^2 \int_{-\infty}^{+\infty} dy\, e^{-2y^2/w_0^2} \int_{-\infty}^{+\infty} dz\, e^{-2z^2/z_0^2} \times \int_{-\infty}^{+\infty} dy' e^{-2y'^2/w_0^2} \int_{-\infty}^{+\infty} dz' e^{-2z'^2/z_0^2} \int_{-\infty}^{\langle W\rangle} dx\, e^{-2x^2/w_0^2} \times \int_{-\infty}^{\langle W\rangle} dx' e^{-2x'^2/w_0^2} \langle \delta c(\mathbf{r},0)\delta c(\mathbf{r}',t)\rangle\right] \Big/ \langle I_{\langle W\rangle}(t)\rangle^2 \tag{15}$$

and the part corresponding to the membrane fluctuations is:

$$G_f(\langle W\rangle, t) = \frac{e^{-4\langle W\rangle^2/w_0^2}}{\pi/2((1+\mathrm{erf}(\sqrt{2}\langle W\rangle/w_0))/2+r)^2} \times \frac{\langle \delta W(0)\delta W(t)\rangle_{\mathrm{planar}}}{w_0^2}. \tag{16}$$

Diffusion term

Derivation of the diffusion term $G_d(\langle W\rangle, t)$ under reflecting boundary conditions

In this section, we calculate $G_d(\langle W\rangle, t)$ from Eq. 15 assuming that the particles are reflected by the membrane. This is equivalent to assuming that the fluorophores do not interact at all with the membrane: they do not (even transiently) bind to it, nor do they diffuse across it. We can consider (Aragón and Pecora, 1976):

$$\langle \delta c(\mathbf{r},0)\delta c(\mathbf{r}',t)\rangle = \langle c\rangle p(\mathbf{r},\mathbf{r}',t), \tag{17}$$

where $p(\mathbf{r},\mathbf{r}',t)$ is the probability to find a fluorophore in $\mathbf{r}'$ at t if it was in $\mathbf{r}$ at $t = 0$.

In the presence of a membrane perpendicular to the x axis (placed in $x = W$), and assuming reflecting boundary

conditions at the membrane surface, (our calculation can be readily adapted to absorbing boundary conditions if particles are adsorbed by the membrane, or semireflective boundary conditions if only part of the particles are reflected by the membrane by modifying Eq. 18 in consequence) this probability is given by:

$$p(\mathbf{r},\mathbf{r}',t)=\frac{1}{(4\pi Dt)^{3/2}}\left(e^{-(x-x')^2/4Dt}+e^{-(x+x'-2W)^2/4Dt}\right)\times e^{-(y-y')^2/4Dt}e^{-(z-z')^2/4Dt}. \quad (18)$$

By integration, and neglecting the time-dependent fluctuations in W (adiabatic approximation) in this term, we get:

$$G_d(\langle W\rangle,t)=\frac{1/\langle N\rangle}{(1+t/\tau)^{1/2}(1+t/(S^2\tau))^{1/2}}\times\frac{1}{((1+\mathrm{erf}(\sqrt{2}\langle W\rangle/w_0))/2+r)^2}\times\frac{2}{\pi^{1/2}w_0}\left(A_{w_0}(\langle W\rangle,t)+B_{w_0}(\langle W\rangle,t)\right), \quad (19)$$

with:

$$A_{w_0}(\langle W\rangle,t)=\frac{1}{2a(t)}\int_{-\infty}^{\langle W\rangle}dx\,e^{-4(b(t)^2/a(t)^2)(x^2/w_0^2)}\times\left[1+\mathrm{erf}\left[\frac{1}{a(t)\sqrt{4Dt}}\left(x+a(t)^2\langle W\rangle\right)\right]\right], \quad (20)$$

and:

$$B_{w_0}(\langle W\rangle,t)=\frac{1}{2a(t)}e^{-4\langle W\rangle^2/b(t)^2w_0^2}\times\int_{-\infty}^{\langle W\rangle}dx\,e^{-(4b(t)^2/a(t)^2)((x+\langle W\rangle/b(t)^2)^2/w_0^2)}\times\left[1-\mathrm{erf}\left[\frac{1}{a(t)\sqrt{4Dt}}(x+(2-a(t)^2)\langle W\rangle)\right]\right], \quad (21)$$

using the notations:

$$a(t)=\left(1+\frac{8Dt}{w_0^2}\right)^{1/2} \quad (22)$$

$$b(t)=\left(1+\frac{4Dt}{w_0^2}\right)^{1/2}. \quad (23)$$

In the particular cases when $\langle W\rangle\to\infty$ (wall infinitely remote) and $\langle W\rangle=0$ (wall in the center of the detection volume), it is straightforward to verify that Eq. 5 is retrieved: the autocorrelation function measured is the same as in the case of free diffusion.

Because $A_{w_0}(\langle W\rangle,0)=\sqrt{\pi}w_0(1+\mathrm{erf}(2\langle W\rangle/w_0))/4$ and $B_{w_0}(\langle W\rangle,0)=0$, the value of the autocorrelation function at $t=0$ is given by:

$$G_d(\langle W\rangle,0)=\frac{1}{\langle N\rangle}\times\frac{(1+\mathrm{erf}(2\langle W\rangle/w_0))/2}{((1+\mathrm{erf}(\sqrt{2}\langle W\rangle/w_0))/2+r)^2}. \quad (24)$$

In the case where the membrane is perpendicular to the optical axis (and at an average distance $\langle Z\rangle$ from the center of the detection volume), it is easy to show that Eq. 19 has to be replaced with:

$$G_d(\langle Z\rangle,t)=\frac{1/\langle N\rangle}{(1+t/\tau)}\times\frac{1}{((1+\mathrm{erf}(\sqrt{2}\langle Z\rangle/z_0))/2+r)^2}\times\frac{2}{\pi^{1/2}z_0}\left(A_{z_0}(\langle Z\rangle,t)+B_{z_0}(\langle Z\rangle,t)\right). \quad (25)$$

Influence of a stationary membrane on G_d

Taken alone (without the fluctuation part G_f), Eq. 19 gives the exact expression for the autocorrelation function measured by FCS in presence of a fixed, rigid, and reflecting wall placed at $x=\langle W\rangle$. Autocorrelation functions calculated from this expression for different representative values of $\langle W\rangle$ are shown in Fig. 2 *a*. They illustrate the two different effects due to the presence of the wall: a change in the geometry of the detection volume, and a change in the diffusion pattern of the molecules.

As the detection volume approaches and touches the wall, part of this volume becomes inaccessible to the fluorescent particles. Hence the average number of fluorophores in the detection volume decreases, leading to an increase in the relative fluorescence fluctuations, and hence to an increase in the value of $G_d(\langle W\rangle,0)$ (Eq. 24). This is balanced by the existence of a nonzero noise level ($r\neq 0$), which prevents the divergence of $G_d(\langle W\rangle,0)$ as $\langle W\rangle$ goes to $-\infty$. (Effects of the membrane on the amplitude of G_d will be discussed in more details in the section on Relative amplitudes of the fluctuation and diffusion terms, and a plot of G_d as a function of $\langle W\rangle/w_0$ can be found in Fig. 5 *a*). The reduction of the effective detection volume has consequences not only on the amplitude of the autocorrelation function, but also on the characteristic time over which it decays, which is closely related to the average residence time of a fluorescent particle in the detection volume. Because the size of the detection volume decreases, the time particles spend diffusing through the detection volume decreases as well.

The other factor, the change in the diffusion pattern of the molecules because of the presence of an obstacle, also influences the residence time of particles in the detection volume. If a particle is reflected by a close by membrane, it can immediately reenter the detection volume. This hence leads to an increase of the residence time of particles in the detection volume, and consequently to an increase of the characteristic decay time of G_d.

The characteristic decay time τ_d of the function G_d can be defined by $G_d(\langle W\rangle,\tau_d)=G_d(\langle W\rangle,0)/2$ (this definition is illustrated in Fig. 2 *a* for one of the autocorrelation functions). In the cases of either free or anomalous diffusion, and for an infinite aspect ratio S of the detection volume, we have, respectively, $\tau_d=\tau$ or $\tau_d=\tau_a$, i.e., τ_d is rigorously equal to

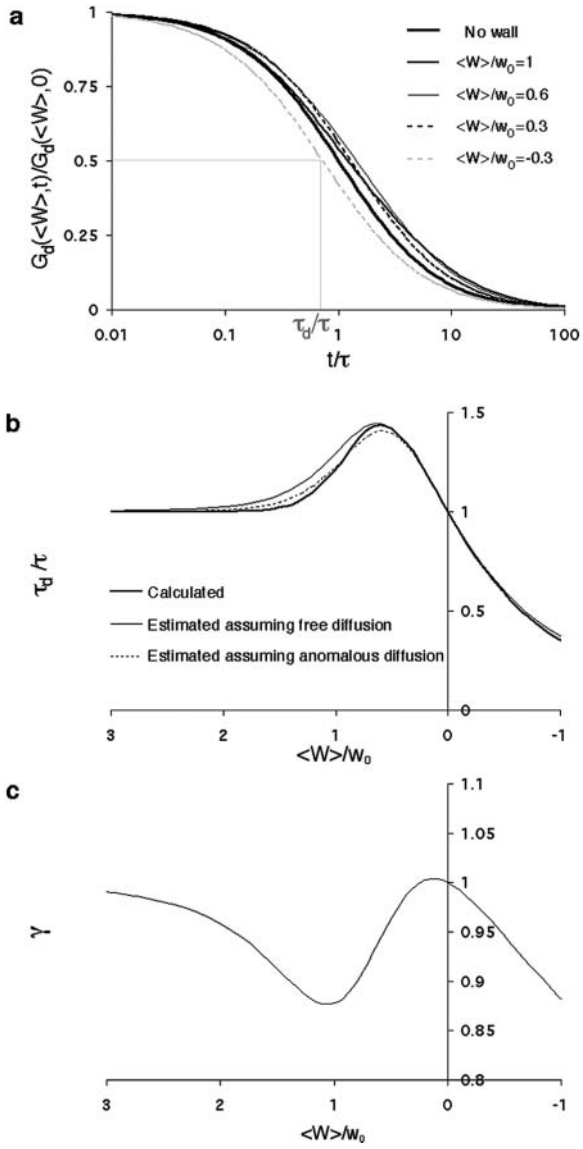

FIGURE 2 (*a*) Autocorrelation functions calculated for different values of $\langle W\rangle/w_0$, normalized by their values at $t = 0$, as a function of t/τ, where $\tau = w_0^2/4D$ is the free-diffusion residence time. The curves have been calculated for a typical value of the detection volume aspect ratio $S = 6.4$. For illustration, the characteristic residence time τ_d, defined by $G_d(\langle W\rangle, \tau_d) = G_d(\langle W\rangle, 0)/2$, is indicated for one of the curves. (*b*) Value of the characteristic residence time τ_d as a function of $\langle W\rangle/w_0$ (*continuous thick line*), compared with the values of the residence time estimated by fitting the autocorrelation functions calculated from Eq. 19 by a free-diffusion autocorrelation function (Eq. 6, *continuous thin line*) or by an anomalous-diffusion autocorrelation function (Eq. 7, *dashed thin line*). All curves have been normalized by the free-diffusion residence time $\tau = w_0^2/4D$. (*c*) Anomalous exponent γ obtained by fitting the autocorrelation functions calculated from Eq. 19 using an anomalous-diffusion model (Eq. 7). Note that for *b* and *c*, the *x* axis has been inverted, so that the plot is read from left to right as the detection volume approaches the membrane.

the average residence time of a particle in the detection volume (a cylinder in those cases). For finite aspect ratios of the detection volume, τ_d is still a very good approximation for the average residence time of the particles in the detection volume. τ_d is plotted in Fig. 2 *b* as a function of $\langle W\rangle/w_0$, and the two contradictory effects mentioned above can be observed: the decrease in the detection volume causes a decrease in the residence time at small and negative $\langle W\rangle/w_0$ (note the $+1$ slope around $\langle W\rangle \simeq 0$, due to the $\langle W\rangle/w_0$ dependence of the cross-sectional area of the detection volume, and hence of the residence time), whereas the reflection of particles on the obstacle causes an increase of the residence time at larger $\langle W\rangle/w_0$. This leads to the existence of a maximum around $\langle W\rangle/w_0 = 0.6$, at which $\tau_d/\tau = 1.43$.

The shape of the autocorrelation function is also modified due to the change in geometry and in diffusion pattern. This can be appreciated by inspection of the curves shown in Fig. 2 *a*. For example, for $\langle W\rangle/w_0 = 0.6$, the fact that molecules might be reflected by the wall and reenter the detection volume is apparent in the tail acquired at longer times by the autocorrelation function when compared to the free-diffusion autocorrelation function.

Consequences for the analysis of FCS measurements

One may try to analyze the autocorrelation functions calculated from Eq. 19 (such as those shown in Fig. 2 *a*) assuming either free or anomalous diffusion of the fluorophores (i.e., assuming either Eq. 6 or Eq. 7 holds true). The average residence times estimated this way (τ in the case of free diffusion and τ_a in the case of anomalous diffusion) are plotted in Fig. 2 *b* together with τ_d. In the case of an anomalous-diffusion model, the actual shape of G_d will be partly accounted for by a change in the anomalous coefficient γ, which allows adjustment of the slope of the autocorrelation function. A plot of γ as a function of $\langle W\rangle/w_0$ is shown in Fig. 2 *c*.

It can be seen from Fig. 2 *b* that the residence times estimated with these simple models are quite comparable to the actual characteristic time τ_d. It would be incorrect, however, to equate them with, respectively, the residence time for free diffusion $w_0^2/4D$ or the residence time for anomalous diffusion $(w_0^2/4Dt^{1-\gamma})^{1/\gamma}$. This would lead to an error in the diffusion constant D that can be as large as 43%, as can be seen in Fig. 3, where diffusion coefficients estimated by using these two models and assuming they are valid (i.e., writing in the first case $D = w_0^2/4\tau$ and in the second case $D = w_0^2/4\tau_a^\gamma t^{1-\gamma}$) are compared to the actual diffusion coefficient.

Figs. 2 and 3 point out that the presence of a simple boundary approaching the detection volume modifies the autocorrelation function in a way that may be misinterpreted as evidence for anomalous diffusion, or more simply that may lead to the extraction of an erroneous diffusion constant.

Fluctuation term

Derivation of the fluctuation term $G_f(\langle W\rangle, t)$ in the case of thermal fluctuations

In this section, we calculate $G_f(\langle W\rangle, t)$ from Eq. 16 assuming the membrane fluctuations are caused by thermal

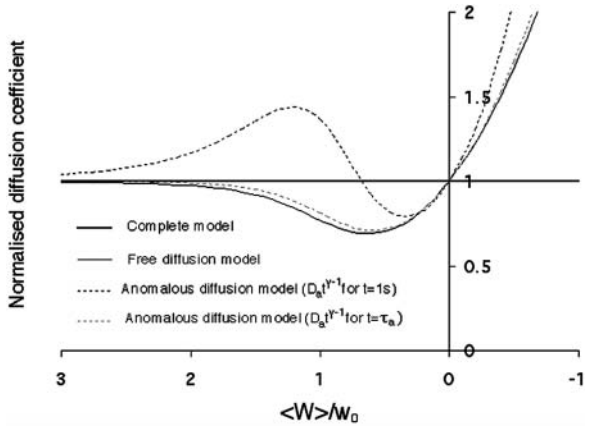

FIGURE 3 Diffusion coefficients (normalized by the actual diffusion coefficient) calculated from the residence times obtained by fitting the autocorrelation functions calculated with Eq. 19 using a hindered-diffusion model (*thick black line*), a free-diffusion model (*thin black line*), or an anomalous-diffusion model. In this last case, the quantity plotted is $D_a t^{\gamma-1}$, for $t = 1$ s (*dashed black line*), and for $t = \tau_a$ (*dashed gray line*).

agitation. This allows us to express G_f in terms of the elastic properties of the membrane.

We have in this case to take into account the fact that the membrane fluctuates at all scales, and that it can no longer be seen as a planar object. Mathematically speaking, it means that the transversal displacement of the membrane $W(t)$ is now also a function of $\mathbf{r_M}$, $\mathbf{r_M}$ being a point on the membrane. To calculate the correlation function $\langle \delta W(0)\delta W(t)\rangle$, it is convenient to decompose $\delta W(\mathbf{r_M}, t)$ into a Fourier sum:

$$\delta W(\mathbf{r_M}, t) = \frac{A}{(2\pi)^2}\int\int d\mathbf{q}\ \delta W_{\mathbf{q}}(t) e^{i\mathbf{q}.\mathbf{r_M}}, \tag{26}$$

where A is the area of the membrane. The integral runs over all modes that can be excited on the membrane, from the mode of smallest wave vector ($q_{\min} \sim 1/R$ in the case of a vesicle of radius R) to the mode of largest wave vector ($q_{\max} \simeq \pi/a$ where a is a typical molecular length).

Henceforth:

$$\langle \delta W(0)\delta W(t)\rangle = \int\int d\mathbf{r_M}\ \delta W(\mathbf{r_M}, 0)\delta W(\mathbf{r_M}, t)$$

$$\langle \delta W(0)\delta W(t)\rangle = \left[\frac{A}{(2\pi)^2}\right]^2 \int\int d\mathbf{r_M} \times \int\int d\mathbf{q}\int\int d\mathbf{q}'\ \delta W_{\mathbf{q}}(0)\delta W_{\mathbf{q}'}(t) e^{i(\mathbf{q}+\mathbf{q}').\mathbf{r_M}}$$

$$\langle \delta W(0)\delta W(t)\rangle = \frac{A}{(2\pi)^2}\int\int d\mathbf{q}\langle \delta W_{\mathbf{q}}(0)\delta W_{-\mathbf{q}}(t)\rangle. \tag{27}$$

In the case of the thermal undulations of a membrane, it has been shown that (Brochard and Lennon, 1975; Zilman and Granek, 1996):

$$\langle \delta W_{\mathbf{q}}(0)\delta W_{-\mathbf{q}}(t)\rangle = \frac{k_B T}{AKq^4} e^{-\omega(q)t}, \tag{28}$$

where K is the rigidity of the layer, η the viscosity of the solvent, and

$$1/\omega(q) = \frac{4\eta}{Kq^3} \tag{29}$$

is the characteristic time associated with the damping of a mode of wave vector q.

We obtain:

$$\langle \delta W(0)\delta W(t)\rangle = \frac{k_B T}{2\pi K}\int_{q_{\min}}^{q_{\max}} dq \frac{e^{-(Kq^3/4\eta)t}}{q^3}. \tag{30}$$

We now have to remember that the correlation function that appears in Eq. 16 is $\langle \delta W(0)\delta W(t)\rangle_{\text{planar}}$, because we were in the case where the membrane was flat at the scale of the detection volume. In the case of a fluctuating membrane, the use of this equation is strictly justified only if the dominating wavelength of the undulations is larger than z_0. In the case of thermal undulations, the dominating wavelength at time t is of order $(Kt/\eta)^{1/3}$ (cf. Eq. 29), which means we must have $t > \eta z_0^3/K$. To overcome this difficulty, we introduce the wave vector $q_{\max}^{\text{FCS}} = 1/w_0$, which marks the limit between undulations whose wavelengths are larger than the detection volume and undulations whose wavelengths are smaller. In the first case, $q < q_{\max}^{\text{FCS}}$, we can consider that the membrane inside the detection volume is moving as whole, and that our derivation of Eq. 16 is correct. In the second case, $q > q_{\max}^{\text{FCS}}$, on the other hand, the membrane will exhibit undulations inside the detection volume, and the net change in effective detection volume will be zero at all times: the FCS experiment is not sensitive to these undulations, and they shouldn't be considered in our calculation. So finally $\langle \delta W(0)\delta W(t)\rangle_{\text{planar}}$ can be written as an integral running only over wave vectors from $q_{\min}$ to $q_{\max}^{\text{FCS}}$:

$$\langle \delta W(0)\delta W(t)\rangle_{\text{planar}} = \frac{k_B T}{2\pi K}\int_{q_{\min}}^{q_{\max}^{\text{FCS}}} dq \frac{e^{-(Kq^3/4\eta)t}}{q^3}. \tag{31}$$

Inserting Eq. 31 into Eq. 16 then leads to:

$$G_f(\langle W\rangle, t) = \frac{e^{-(2\langle W\rangle/w_0)^2}}{((1+\text{erf}(\sqrt{2}\langle W\rangle/w_0))/2 + r)^2}\frac{k_B T}{\pi^2 K w_0^2} \times \int_{q_{\min}}^{q_{\max}^{\text{FCS}}} dq \frac{e^{-(Kq^3/4\eta)t}}{q^3}. \tag{32}$$

The indefinite integral associated with Eq. 32 may be expressed in terms of gamma functions, hence simplifying its numerical computation:

$$\int dq\, e^{-Kq^3 t/4\eta}/q^3 = -e^{-Kq^3 t/4\eta}/(2q^2) + Kqt\gamma[2/3, Kq^3 t/4\eta]/(4\eta(2Kq^3 t/\eta)^{2/3}).$$

Equation 32 equation can be readily adapted to the case where the membrane is perpendicular to the optical axis (and

at a distance $\langle Z\rangle$ on average from the center of the detection volume) by replacing $\langle W\rangle$ by $\langle Z\rangle$ and w_0 by z_0.

The characteristic time of the fastest mode is given by $4\eta/Kq_{\max}^3$, which corresponds, for a membrane of rigidity as low as $10\,k_BT$ in aqueous solution ($\eta = 1.002\times 10^{-3}\,\mathrm{kg\cdot s^{-1}\cdot m^{-1}}$), to ~1 ms. This is one order of magnitude slower than the residence time of a typical fluorophore in the detection volume (~0.1 ms), and hence justifies the separation into diffusion and fluctuation regimes.

The amplitude of this part of the autocorrelation function is given by:

$$G_f(\langle W\rangle,0) = \frac{e^{-(2\langle W\rangle/w_0)^2}}{((1+\mathrm{erf}(\sqrt{2}\langle W\rangle/w_0))/2+r)^2} \times \frac{k_BT}{2\pi^2 K w_0^2}\left[\frac{1}{q_{\min}^2}-\frac{1}{q_{\max}^{FCS^2}}\right]. \quad (33)$$

Dependence of G_f on the bending rigidity of the membrane

It can be seen directly from Eq. 32 that the shape of the function G_f does not depend on $\langle W\rangle$, only its amplitude depends on the membrane position. Furthermore, in the case when $q_{\max}^{FCS} = q_{\min}$, using Eq. 33 and making the change in variable $Q = q/q_{\min}$, G_f can be rewritten as:

$$G_f(\langle W\rangle,t)/G_f(\langle W\rangle,0) = 2\int_1^\infty dQ\,\frac{e^{-Q^3\omega(q_{\min})t}}{Q^3}. \quad (34)$$

It then appears that $G_f(\langle W\rangle,t)/G_f(\langle W\rangle,0)$ has a universal shape if time is normalized by the characteristic time of the smallest wave vector mode $1/\omega(q_{\min}) = 4\eta/Kq_{\min}^3$. This universal shape is shown in Fig. 4. In this case, the characteristic decay time of the autocorrelation function τ_f, defined as $G_f(\langle W\rangle,\tau_f) = G_f(\langle W\rangle,0)/2$, is obtained for $\tau_f \simeq 0.175/\omega(q_{\min})$. The influence of the cutoff of the highest wavevector modes is visible only when we no longer have $q_{\max} \gg q_{\min}$: as can be seen in Fig. 4 (*thin line*), the shape of G_f is then modified. But in general ($q_{\max} \gg q_{\min}$) we have:

$$\tau_f \simeq 0.7\frac{\eta}{Kq_{\min}^3}. \quad (35)$$

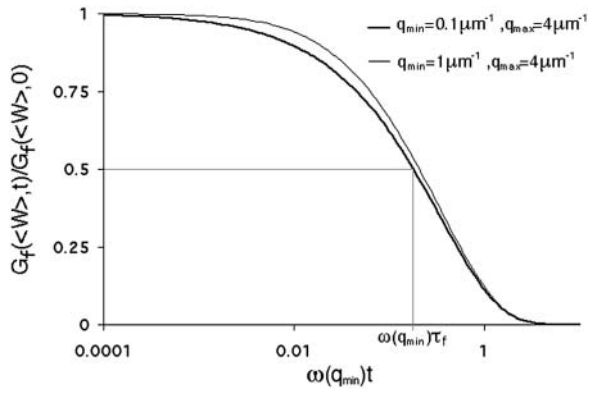

FIGURE 4 Part of the autocorrelation function due to the fluctuations of the membrane, calculated for $q_{\min} = 0.1\ \mu\mathrm{m}^{-1}$ (*thick line*) and for $q_{\min} = 1\,\mu\mathrm{m}^{-1}$ (*thin line*). In both cases, $K = 10\,k_BT$ and $q_{\max} = 4\,\mu\mathrm{m}^{-1}$. The time has been normalized by $1/\omega(q_{\min})$ and the amplitude of the curve by the value of $G_f(\langle W\rangle,0)$ (Eq. 33). The characteristic decay time τ_f of the autocorrelation function calculated for $q_{\min} = 0.1\,\mu\mathrm{m}^{-1}$ is indicated.

The characteristic decay time of G_f is then inversely proportional to the bending rigidity K of the membrane, and to the third power of the smallest wave vector that can be excited on the membrane, $q_{\min}^3$. Measurements of τ_f will therefore give a good estimation of K only if $q_{\min}$ is known with very good precision. This characteristic decay time is very roughly of the order of 1 s for membranes with rigidity in the range 20–500 k_BT, and for $q_{\min} \sim 1/R$ corresponding to a membrane typical size of the order $10\,\mu\mathrm{m}$. This is typically the range of rigidity expected for most biological membranes, inasmuch as the very flexible plasma membrane of red blood cells has been shown to be of order 50 k_BT (Evans, 1983; Hochmuth and Waugh, 1987) (just slightly higher than the rigidity of a simple lipid bilayer), whereas on the other end of the spectrum the rigidity of the supported double bilayer delimitating the nucleus is expected to be as high as 1000 k_BT (Helfer et al., 2000). This shows that the thermal fluctuations of biological membranes should lead to long time correlations, causing the appearance of tails in the autocorrelation functions measured by FCS.

The amplitude $G_f(\langle W\rangle,0)$ of G_f is inversely proportional to K and to $q_{\min}^2$ (cf. Eq. 33, in the case when $q_{\min} \ll q_{\max}$). Estimations of K based on the measurements of $G_f(\langle W\rangle,0)$ will hence be more precise than those based on the measurements of τ_f. For each autocorrelation function measured, those two estimations are independent.

Relative amplitudes of the fluctuation and diffusion terms

The amplitude $G_d(\langle W\rangle,0)$ and $G_f(\langle W\rangle,0)$ depends strongly on $\langle W\rangle/w_0$. This dependence, as well as that of the amplitude of the total correlation function $G(0)$, is shown in Fig. 5 *a*. As the detection volume approaches the membrane, the relative contribution of the fluctuation term over that of the diffusion term (see Fig. 5 *b*) increases dramatically (meanwhile, the signal-to-noise ratio is decreasing). A tail corresponding to the fluctuation term will be visible in the autocorrelation function whenever $G_f(\langle W\rangle,0)/G_d(\langle W\rangle,0)$ stops being negligible, i.e., roughly when $\langle W\rangle < w_0$ (Fig. 5 *b*) or, if one considers a membrane perpendicular to the optical axis (at an average distance $\langle Z\rangle$ from the center of the detection volume), when $\langle Z\rangle < z_0$. Because z_0 is typically $\simeq 1-5\ \mu\mathrm{m}$ in an FCS experiment, which is only slightly less than the characteristic dimension of most cells, it will be difficult avoiding having the plasma membrane at a distance $\langle Z\rangle < z_0$ when carrying out an in vivo FCS experiments, meaning it will be difficult avoiding getting tails

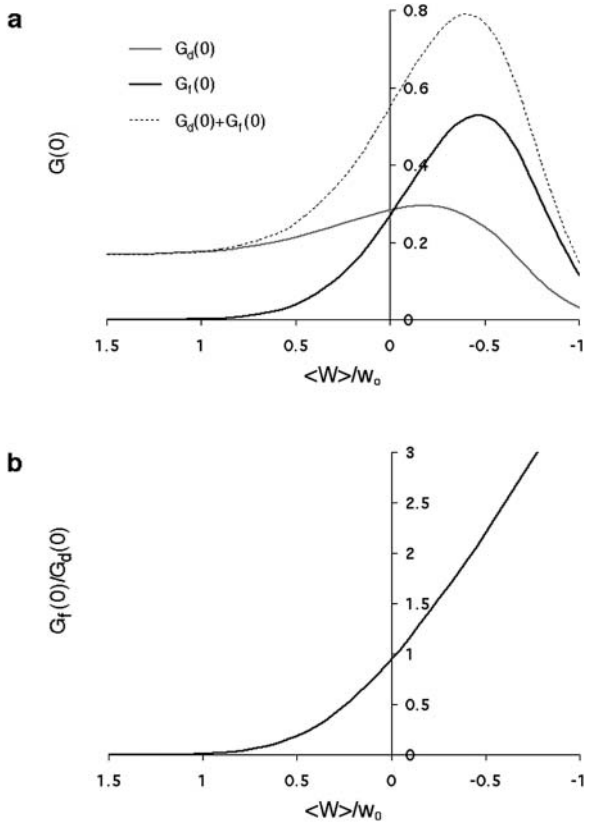

FIGURE 5 (*a*) Amplitude of the two separate contributions (*gray line*: diffusion term, Eq. 24; *black line*: membrane fluctuations term, Eq. 33) and of the complete autocorrelation function (*dashed line*). The curves have been calculated for $w_0 = 230$ nm, $S = 8$, $\langle c \rangle = 15$ nM, $K = 1000\ k_BT$, and $q_{min} = 0.1\ \mu m^{-1}$. (*b*) Relative amplitude of the membrane fluctuation term $G_f(0)$ to the diffusion term $G_d(0)$, calculated for the same set of parameters as in *a*. Note that the *x* axis has been inverted as in Figs. 2 and 3.

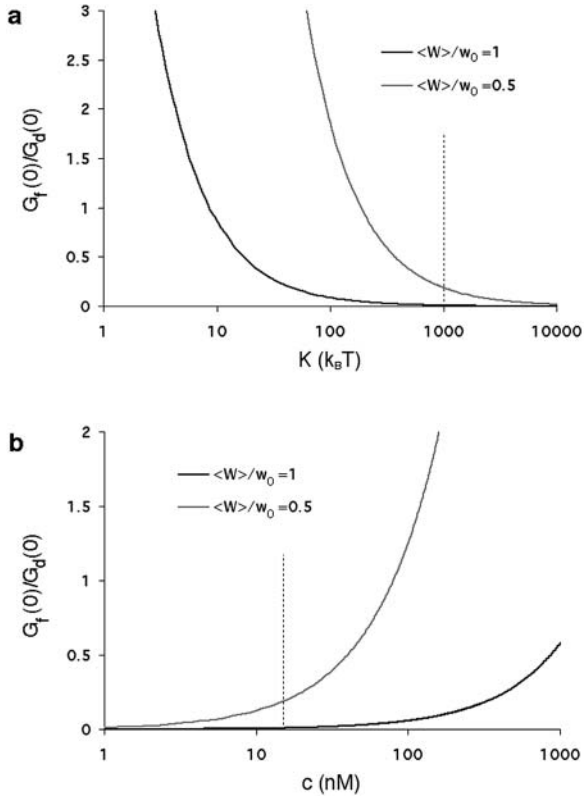

FIGURE 6 (*a*) Variation of the relative amplitude of the two terms $G_f(0)/G_d(0)$ with the bending rigidity of the membrane K (all other parameters as in Fig. 5), for two particular distances of the detection volume to the membrane: $\langle W \rangle / w_0 = 1$ (*gray line*) and $\langle W \rangle / w_0 = 0.5$ (*black line*). The dashed line indicates the value of K used for the curves of Fig. 5. (*b*) Variation of $G_f(0)/G_d(0)$ with the fluorophore concentration (other parameters values as in Fig. 5), again for $\langle W \rangle / w_0 = 1$ (*gray line*) and $\langle W \rangle / w_0 = 0.5$ (*black line*). The dashed line indicates the value of $\langle c \rangle$ used for the curves of Fig. 5.

in the autocorrelation function (provided the plasma membrane indeed separates a fluorescent environment from a nonfluorescent environment, which will be the case if the cell contains fluorophores and the outside medium does not).

Three other factors play a part in the relative amplitude of the two terms: the bending rigidity of the membrane ($G_f(\langle W \rangle, 0) \propto 1/K$), the average concentration of the fluorophore ($G_d(\langle W \rangle, 0) \propto 1/\langle c \rangle$), and the wavevector of the longest mode that can be excited on the membrane ($G_f(\langle W \rangle, 0) \propto 1/q_{min}^2$). The more rigid the membrane, the less important its fluctuations will be. On the other hand, the higher the fluorophore concentration, the smaller the diffusion term will be. The membrane fluctuation term will then become very apparent at large $\langle c \rangle$. This is illustrated in Fig. 6. Note that even for biological membranes, whose rigidity is expected to be very high in some cases, in the range 50 k_BT–1000 k_BT (Helfer et al., 2000), and for small fluorophore concentrations (as low as 10 nM), the fluctuation term should be detectable.

MEASUREMENTS NEAR A VESICLE MEMBRANE

DOPC vesicles were prepared with both low ($\simeq$ 10 nM) and high ($\simeq$ 500 nM) concentrations of fluorophores outside the vesicles, to ascertain the influence of this parameter on the existence and amplitude of the fluctuation term. Two different types of fluorescent species were used (a fluorescent streptavidin and a fluorescent 10-kDa dextran, see section ''Materials and Methods'') to detect an eventual influence of fluorophore interaction with the membrane (transient binding or membrane penetration for example). Dextrans should be particularly inert. Experiments were performed at 25°C. At this temperature the unsaturated lipid used is in the fluid L_α phase (Koynova and Caffrey, 1998). FCS measurements were carried out in the equatorial plane of several different giant vesicles (one of them is shown in Fig. 7 *a*), with radii varying between 5 μm and 15 μm. During the experiment, the sample was moved step by step so that the focus of the laser would come progressively closer to the membrane and eventually cross it. At each point the intensity

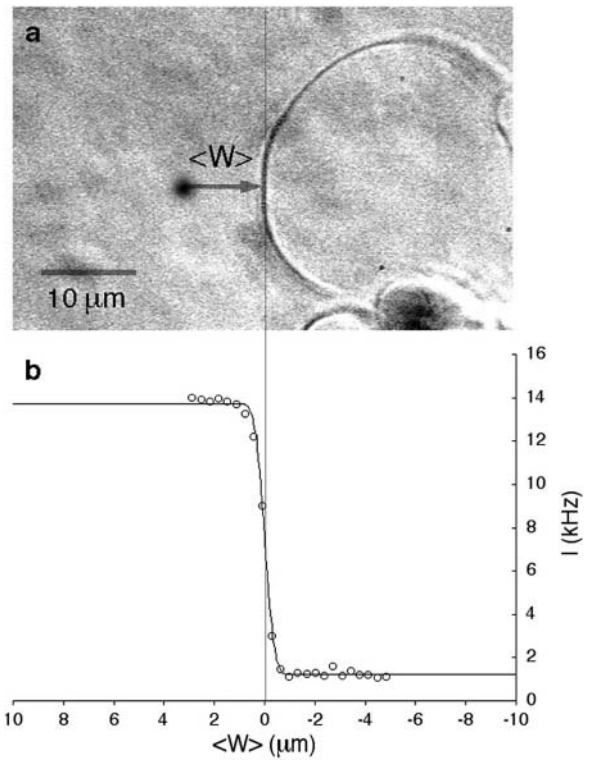

FIGURE 7 (*a*) DIC photograph of one of the vesicles used for the presented experiments. The radius of the vesicle is 14.4 μm, giving $q_{\min} = 6.9 \times 10^4 \mathrm{m}^{-1}$ if $q_{\min} = 1/R$. (*b*) Measured average intensity profile coming from the fluorescence of the Cy3-streptavidin present outside the vesicle, as a function of the distance $\langle W \rangle$ of the detection volume from the membrane (*circles*). The line is only a guide to the eye. The maximum signal intensity is $I_M = 12.5$ kHz, and the relative amount of noise is $r = 0.1$. Note that the scales of figures *a* and *b* are different and that the *x* axis in *b* runs from positive to negative values.

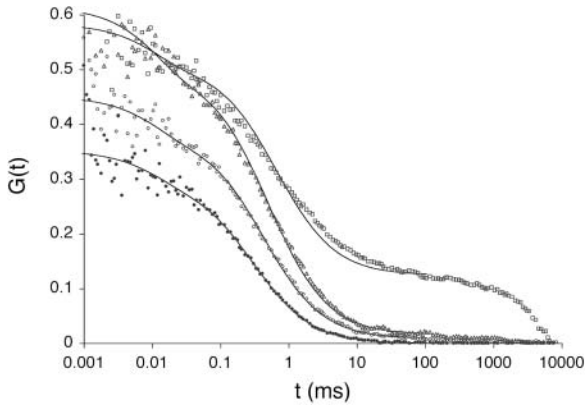

FIGURE 8 Typical measured autocorrelation functions, for a 6.8-nM concentration of Cy3-streptavidin outside a vesicle, and for different position of the membrane relative to the detection volume: membrane infinitely remote (*black dots*), $\langle W \rangle = 0.44\, w_0$ (*empty circles*), $\langle W \rangle = 0.28\, w_0$ (*empty triangles*), and $\langle W \rangle = 0.09\, w_0$ (*empty squares*). These positions have been calculated from the measured average intensity using Eq. 10. As explained in the text, continuous black lines are fits obtained using Eq. 36.

was measured for a given period of time, and the autocorrelation function of the signal computed. Typical autocorrelation curves (streptavidin, low concentration), obtained for different distances of the detection volume to the membrane, are shown in Fig. 8.

To test the mechanical and optical stability of our set-up, we also performed FCS measurements close to a fixed rigid wall, constituted by the side of a glass coverslip. None of the effects that we observed in the vicinity of the vesicle membranes and that we attribute to membrane fluctuations could be observed in this case (see section ''Amplitude of the fluctuation term''), ruling out mechanical or optical instability as the cause of these effects.

Intensity profile across the membrane

Fig. 7 *b* shows a typical intensity profile measured as a function of position, with steps of 35 μm, and a counting time of 30 s. It shows that a signal is obtained outside the vesicle, whereas only a background noise is observed inside the vesicle, demonstrating the nonpermeability of the lipid bilayer to the fluorescent species, in this case a 66-kDa Cy3-streptavidin. A similar observation was made with the 10-kDa dextran also used in our experiments, even at the highest used concentration, although we observed that free dyes such as rhodamine tend to penetrate the membranes and slowly fill the vesicles. The amplitude of the intensity fluctuations was always small compared to the average intensity outside the vesicles (data not shown), showing that the roughness of the membrane was small enough to justify the use of Eq. 10. As the precision on the sample position was not good enough to fit the intensity profile of Fig. 7 *b* with this equation, we simply used it to deduce from the measured average intensity the normalized distance $\langle W \rangle / w_0$ of the detection volume to the wall. Values for the parameters I_M and r are needed for this. They were derived by identifying the average intensity outside the vesicle and far from the membrane with $(1+r)I_M$, and the average intensity inside the vesicle and far from the membrane with rI_M. The relative level of background intensity r evaluated this way was found to vary from $r = 0.04$ for a fluorophore concentration around 500 nM ($I_M \simeq 700$ kHz) to $r = 0.1$ for a fluorophore concentration around 5 nM ($I_M \simeq 10$ kHz, see Fig. 7 *b*).

Free diffusion of the fluorescent species

FCS measurements were performed outside and far from any vesicle ($\langle W \rangle / w_0 = \infty$) to characterize the free diffusion of the fluorescent species in the buffer supplemented with sucrose and glucose. All the autocorrelation curves measured far from the membrane were very satisfactorily described assuming a free-diffusion model, and using the corresponding Eq. 6 (see for example the curve represented by *black diamonds* in Fig. 8). Fitting these curves with this equation, we find the average residence time of the Cy3-streptavidin in

the detection volume to be $\tau = 0.300 \pm 0.005$ ms, implying a diffusion coefficient of the fluorophore in the sucrose/glucose buffer $D = 44 \pm 1\,\mu m^2/s$. For the measurements presented here (Figs. 7–11), we also find $G(0) = 0.275 \pm 0.005$, corresponding to an average number of fluorophores in the detection volume $\langle N \rangle = 2.2 \pm 0.2$ and to a concentration $\langle c \rangle = 6.8 \pm 0.5$ nM (assuming $r = 0.1$ as suggested by the intensity curve shown in Fig. 7 *b*). Each Cy3-streptavidin molecule yields an average intensity of 5.7 ± 0.3 kHz. For the parameters related to the triplet state of this fluorophore, the fits gave: $T = 0.16 \pm 0.02$ and $\tau_T = 11 \pm 3\,\mu s$. For the 10-kDa dextran, we find $\tau = 0.150 \pm 0.005$ ms, corresponding to $D = 88 \pm 2\,\mu m^2/s$. Results for two different concentrations of this fluorophore are presented (Figs. 9 and 10): a low concentration measured to be 23 ± 1 nM and a high concentration measured to be 490 ± 2 nM. In both cases the average intensity per molecule is 3.7 ± 0.1 kHz. The triplet state is characterized by $T = 0.16 \pm 0.02$ and $\tau_T = 17 \pm 10\,\mu s$ at low intensity and $T = 0.17 \pm 0.02$ and $\tau_T = 8 \pm 5\,\mu s$ at high intensity.

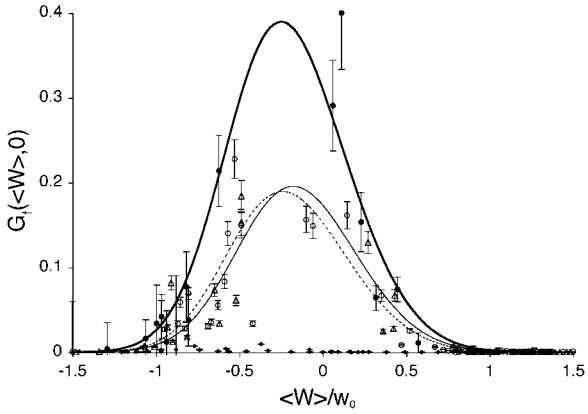

FIGURE 10 Amplitude of the membrane fluctuations contribution in the autocorrelation function as a function of $\langle W \rangle / w_0$, for a 6.8-nM concentration of streptavidin (*filled circles*), and 23.8-nM (*open squares*) and 490-nM (*open triangles*) concentrations of dextran. The radii of the vesicles were, respectively, 14.4 μm, 9.1 μm, and 7.3 μm. The best fits using Eq. 33 are indicated (*bold continuous line*, *continuous line*, and *dotted line*). The small filled lozenge symbols along the horizontal axis correspond to the measured amplitude of the fluctuation term in the case of a fixed, rigid wall.

Measured autocorrelation functions and amplitude of the different contributions

Autocorrelation functions

Fig. 8 shows typical autocorrelation functions, measured at low concentration of Cy3-streptavidin, far away from the membrane (*filled symbols*) and close to the membrane ($\langle W \rangle / w_0 < 1.5$, *empty symbols*). Far from the membrane, the only characteristic time observed is the one coming from the free diffusion of the streptavidin molecules through the detection volume ($\tau = 0.3$ ms). Close to the membrane, two characteristic times can be observed, one at short timescales (τ_d ($\langle W \rangle$) $\simeq 0.5$ ms) corresponding to the modified diffusion of the fluorophore close to the membrane, and one at long timescales ($\tau_f \simeq 5$ s) attributed to thermal fluctuations of the membrane. Because of the three orders of magnitude difference in their respective characteristic times, these two contributions can be clearly distinguished. In this case (low concentration of the fluorophore) the contribution of the diffusion term is dominant, although the fluctuation term is very clearly visible. To evaluate the respective amplitudes of both contributions, and check that they obey Eqs. 24 and 33, the autocorrelation functions were first fit from 0.002 ms to 200 ms (i.e., for $t = \tau_f$, where it can be considered that $G(t) = G_d(t) + G_f(0)$) with a modified form of Eq. 10, fixing τ_T to the value found in the case of free diffusion (so that the change in shape of the diffusion contribution could not be compensated for by a mistaken τ_T), and adding a constant baseline corresponding to $G_f(\langle W \rangle, 0)$:

$$G(t) = \left(1 + \frac{Te^{-t/\tau_T}}{1-T}\right)\left(\frac{G_d(\langle W \rangle,0)}{(1+t/\tau)(1+t/(S^2\tau))^{1/2}} + G_f(\langle W \rangle,0)\right). \quad (36)$$

This simple fit allows to retrieve values for $G_d(\langle W \rangle, 0)$ and $G_f(\langle W \rangle, 0)$. Several of these fits are shown in Fig. 8.

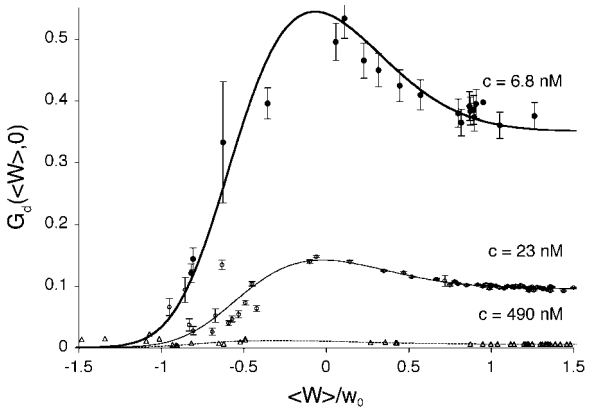

FIGURE 9 Amplitude of the fluorophore diffusion contribution of the autocorrelation function, as a function of $\langle W \rangle / w_0$, for a 6.8-nM concentration of streptavidin (*filled circles*), and 23.8-nM (*open squares*) and 490-nM (*open triangles*) concentrations of dextran. The best fits using Eq. 24 are indicated (*bold continuous line, continuous line*, and *dotted line*, respectively).

Amplitude of the diffusion term

The amplitude of the diffusion contribution as a function of position is shown in Fig. 9 for the three different systems studied (Cy3-streptavidin at low concentration and 10-kDa dextran both at low and high concentration). The three curves obey Eq. 24, as can be seen in the figure. Values for the

relative noise contribution r can be obtained from this fit, independently from the value obtained from the intensity profile, and found to be systematically slightly higher in the first case (ranging from $r = 0.16 \pm 0.03$ at low fluorophore concentration to $r = 0.060 \pm 0.004$ at high fluorophore concentration) than in the second case (see section ''Intensity profile across the membrane''). This might be due to the fact that noise gets higher close to the membrane, perhaps due to some adsorption of fluorophores to the lipid bilayer or scattering of light at the membrane. As expected, the amplitude of this term is extremely sensitive to the concentration of the fluorophore, being inversely proportional to the average number of particles present in the detection volume.

Amplitude of the fluctuation term

The amplitude of the membrane fluctuation contribution as a function of position is shown in Fig. 10, for the same three systems than in Fig. 9, and for the case of the immobile glass wall. The striking feature here is that the amplitude of this term does not depend on concentration: in fact, for the two measurements done with the 10-kDa dextran at very different concentrations, the amplitude is exactly the same. This demonstrates that the origin of this term cannot be attributed to any phenomenon involving particle correlation, which would always give rise to correlations having an amplitude proportional to the inverse of the particle concentration (as for particle diffusion). In the important case of transient binding of the fluorophore to the membrane, which can lead to intensity correlations as well, the eventual corresponding term in the autocorrelation function would have a very small amplitude at high concentration (see for example the exact derivation that can be found in (Starr and Thompson, 2001)), exactly as in the case of the fluctuation term (cf. Fig. 9). On the contrary, we have here a concentration-independent term, which is in agreement with our attribution of the signal to membrane fluctuations restricting access of the fluorophores to the detection volume in a time-correlated manner. The effect vanishes completely in the case of an immobile wall. Our measurements also suggest that the amplitude of this term is linked to the size of the vesicle, as expected from Eq. 33 that links $G_f(\langle W \rangle, 0)$ to the vesicle diameter $R \sim 1/q_{min}$: the two measurements made with the smaller vesicles ($R = 7.3 \pm 0.2\,\mu$m and $R = 9.1 \pm 0.2\,\mu$m, cf. Fig. 10) exhibit smaller amplitudes for this term than the one made with a larger vesicle ($R = 14.4 \pm 0.3\,\mu$m). This is in agreement with our model, as a larger vesicle is expected to undergo more fluctuations (as modes with larger wavelengths are allowed to propagate on the surface, i.e., as q_{min} is smaller), which will cause the fluctuation term to have a larger amplitude. The curves of Fig. 10 can be satisfactorily fit by Eq. 33, as can be seen in the figure. The fits allow attributing values for the relative noise ratio r (independently from the other two measurements presented in sections ''Intensity profile across the membrane'' and ''Amplitude of the diffusion term'') and to the quantity $k_BT/(2\pi^2 K w_0^2 q_{min}^2)$. If we further assume that $q_{min} = 1/R$, we respectively retrieve for the three different vesicles studied: $K = 810 \pm 190\,k_BT$ (vesicle obtained by gentle hydration, $R = 14.4\,\mu$m), $K = 330 \pm 100\,k_BT$, and $K = 400 \pm 120\,k_BT$ (vesicles obtained by electroswelling, $R = 9.1$ and $7.3\ \mu$m). The difference in elasticity between the vesicles obtained by gentle hydration and those obtained by electroswelling is probably due to the fact that in the first case the vesicles tested were multilamellar whereas in the second case unilamellar vesicles were selected (by minimal optical contrast using differential interference contrast optics). It might also be due to the difference in osmotic pressure between the inside and outside of the vesicles achieved for this second set of experiments: a lower osmotic pressure inside the vesicle will cause an increase of the surface area over volume ratio of the vesicle, resulting in an enhancement of the fluctuations (not taken into account in our calculations) and an increase in the value of $G_f(\langle W \rangle, 0)$, which we might mistake for a smaller bending rigidity. Other measurements on similar systems have typically yielded lower values: $K = 21\,k_BT$ for unilamellar DOPC vesicles (micropipette aspiration) (Rawicz et al., 2000), and $\sim 100\ k_BT$ for a stack of lipidic dipalmitoylphosphatidylcholine membranes (using electric-field induced bending deformation of cylindrical tubes) (Mishima et al., 2001). Discrepancy with our measurements may come from the model-dependent estimation of q_{min}. If we assume instead that $q_{min} = 4/R$, we extract an experimental value $K = 51 \pm 12\,k_BT$ for the vesicle obtained by gentle hydration and $K = 21 \pm 7$ and $K = 25 \pm 8$ for the vesicles obtained by electroswelling, in good agreement this time with other experiments. Because of the ambiguity on q_{min}, which cannot be lifted, it is difficult to extract exact absolute bending rigidities of the membranes from the measurement of $G_f(\langle W \rangle, 0)$, but their relative propensity to fluctuate can be readily observed: on Fig. 10, the difference between the soft lipid bilayer membranes (*filled circles*, *open squares*, and *open triangles*) and the rigid wall (*filled lozenges*), for example, is striking.

Fit of one autocorrelation function and derived values of *K* and *D*

Fig. 11 shows an example of an autocorrelation function (measured for Cy-3 streptavidin at low concentration, for a vesicle radius $R = 14.4\,\mu$m, and for $\langle W \rangle / w_0 = 0.6$) fit by the complete diffusion model derived in this paper. For this fit, Eqs. 19 and 32 were inserted into Eq. 14, and the multiplicative term $(1 + Te^{-t/\tau_T}/(1 - T))$, accounting for the residence of the fluorophores in their triplet state, was added. To avoid too many free parameters, the value of τ_T was fixed to 11 μs (value measured far from the vesicle), and q_{min} was fixed to 0.69 μm^{-1} (expected value supposing $q_{min} = 1/R$), whereas $\langle N \rangle$, T, r, D, and K were allowed to vary. From the fit we retrieve $D = 43.8 \pm 1.5$, and

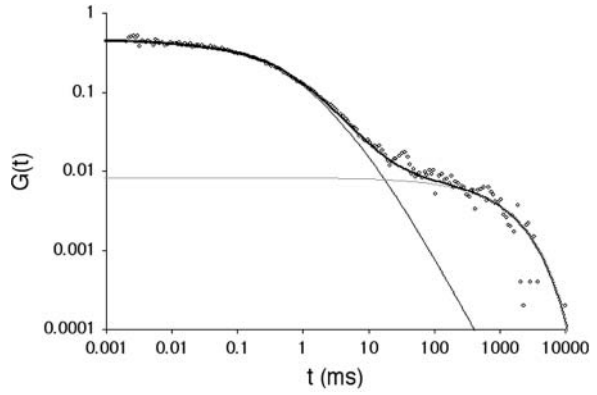

FIGURE 11 Autocorrelation function (on a log-log scale) measured for a 6.8-nM concentration of Cy3-streptavidin outside a vesicle at $\langle W\rangle/w_0 = 0.6$ (*gray open symbols*), and best fit obtained using the complete model derived in this paper (*thick black line*). The diffusion part G_d (*thin black line*) and fluctuation part G_f (*thin gray line*) of the fit are also shown. The diffusion coefficient retrieved from the fit is $D = 43.8 \pm 1.5\ \mu m^2/s$, whereas the bending rigidity is $K = 720 \pm 400\, k_B T$ (assuming $q_{min} = 1/R$).

$K = 720 \pm 400\, k_B T$. The diffusion coefficient of the molecules close to the membrane is measured to be equal to the diffusion coefficient infinitely far from the membrane, and the value measured for the bending rigidity is consistent with the one derived from the amplitude of the fluctuation term (see previous section and Fig. 10). The precision obtained on K is not very good, as instabilities in the vesicle position prevented measurement of the autocorrelation functions over a time much larger than the characteristic time of the fluctuations themselves. Also, once again, K depends on our estimation of q_{min}. If we assume $q_{min} = 4/R$, then we retrieve a much smaller value of the bending rigidity: $K = 11 \pm 7\, k_B T$. It can clearly be seen in Fig. 11 that the fluctuation term G_f, calculated assuming that thermal fluctuations of the membrane were responsible for the observed long-term correlations, indeed describes very correctly the part of the autocorrelation function obtained at large times.

The measured value of the diffusion coefficient is to be compared with those obtained using either a free-diffusion model or an anomalous-diffusion model to fit the diffusion part of the autocorrelation function (i.e., substituting either Eq. 6 or Eq. 7 for G_f in Eq. 14, and keeping Eq. 32 to describe the part due to the membrane fluctuations). In these cases also, we fixed $\tau_T = 11\ \mu s$ and $q_{min} = 0.69\ \mu m^{-1}$. Using the free-diffusion model, we find $D = 33.9 \pm 1.1$, and $K = 1500 \pm 850\, k_B T$. Using the anomalous-diffusion model, we get $D = 39.3 \pm 1.7$, $K = 1600 \pm 300\, k_B T$, and $\gamma = 0.85 \pm 0.02$. In both cases, the diffusion coefficient obtained is significantly lower than the value measured from free diffusion far away from the vesicle membrane. This is the expected result: an increase of the residence time due to the modification of the particle diffusion by the membrane, mistaken for a decrease of the diffusion coefficient, as discussed in section ''Derivation of the diffusion term under reflecting boundary conditions''. In the case of the anomalous-diffusion model, we observe also that the change in slope of the autocorrelation function, as compared to a free-diffusion autocorrelation function, is mistaken for anomalous diffusion. The obtained anomalous exponent $\gamma = 0.85$ is even lower than the one predicted for $\langle W\rangle = 0.6$ (cf. Fig. 2 *c*), probably because fitting the fluctuation term at the same time as the diffusion term allowed for larger admissible range for γ.

When the center of the detection volume passes through the time-averaged membrane position ($\langle W\rangle/w_0 < 0$), we observe residence times and autocorrelation functions shapes that cannot be explained by our model, suggesting either interactions of the fluorophores used with the membrane, or, more likely, noise levels too high to obtain meaningful curves in this region.

CONCLUSIONS

We have shown that when FCS measurements are carried out close to a membrane, the usual expression for the autocorrelation function has to be modified, and in the case of a fluctuating membrane separating two media with different concentrations of fluorophores, a new term should be added. For a soft membrane undergoing thermal fluctuations, the latter term depends only on the bending rigidity and surface area of the membrane, and has a characteristic decay time much larger than the one corresponding to the diffusion of the fluorophores.

To illustrate our calculation, we performed FCS measurements in the proximity of phospholipid bilayer vesicles. We observed both the modification of the diffusion term according to our calculation (except very close to the membrane, where binding or adsorption of the fluorophore on the membrane, which we have neglected, might play a role), and the appearance of a long decay-time membrane fluctuation term in the autocorrelation function. As expected, the amplitude of the first term was observed to depend inversely on the concentration of fluorophores, whereas the amplitude of the second term was independent of that quantity. We were able to extract from these measurements both the correct diffusion coefficient of the fluorophore and an estimation of the bending rigidity of the membrane.

The modification of the diffusion term, due to the presence of a vertical obstacle in one direction of space, becomes dramatic as soon as $\langle W\rangle/w_0 \simeq 1.5$, that is before the detection volume even touches the obstacle. Far from the membrane it is caused primarily by the reflection of the fluorophores on the obstacle leading to enhanced correlations, and close to the membrane by the reduction of the effective detection volume. Consequently, the shape of the correlation function is modified, and the average residence time is no longer linked to the diffusion coefficient by the simple relation: $D = w_0^2/4\tau$, as is the case for free diffusion. Erroneous interpretations of the nature of the observed

diffusion may easily be assigned, if this effect is not acknowledged. The issue is particularly acute for studies inside living cells, where membrane barriers abound. It could be useful to investigate whether other types of analysis of the fluorescence fluctuations (Qian and Elson, 1990; Chen et al., 1999; Kask et al., 1999) might prove more reliable for in vivo studies.

The fact that the membrane fluctuations themselves have an influence on the autocorrelation function, causing correlations to appear at characteristic times of order roughly 1 s for typical biological membranes, could account for many of the long time tails observed in autocorrelation functions when taking measurements in cells. In fact, our calculation shows that any soft membrane delimiting regions with different concentrations of fluorophore will lead to long time correlations in the autocorrelation function measured by FCS. Because the amplitude and characteristic time of the term coming from the membrane fluctuations depend on its elasticity, FCS provides a way to estimate this parameter. Absolute measurements are difficult though, because they depend on the model used to describe the membrane fluctuations, and are altered by the absence (even in the case of a spherical membrane) of an exact relationship between the membrane surface area and wave vector of the larger mode propagating on the membrane. Nevertheless, this method might prove to be an interesting way for evaluating the out-of-plane elasticity of biological membranes, inasmuch as it is sensitive to high bending rigidities ($\sim 100\ k_BT$–$1000\ k_BT$), and contrary to traditional methods (such as light or x-ray scattering) it can be used in situ on biological membranes, even those, as the nuclear membrane or endoplasmic reticulum for example, that are buried inside the cell. It is also noninvasive, which might be an advantage compared to methods relying on deformation of the membrane or insertion of a bead as a tracer (Dimova et al., 2000; Helfer et al., 2000). Finally, it allows spatial resolution in the plane perpendicular to the optical axis. This last feature could be useful in the case of membranes exhibiting domain segregation, or in the case of cell membranes, whose elastic properties depend on the local cytoskeleton arrangement and membrane protein composition and concentration (Discher et al., 1994).

APPENDIX: RELATIONSHIP BETWEEN $G_f(t)$ AND THE $t^{2/3}$ DEPENDENCE OF A MEMBRANE TRANSVERSE MSD

The transverse mean-square displacement (MSD) of a membrane has been shown (Zilman and Granek, 1996; Granek, 1997) to behave as $t^{2/3}$ for $\eta a^3/K \ll t \ll \eta L^3/K$, where L is the characteristic size of the membrane, and a a typical molecular length. This means that a particle attached to the membrane undergoes anomalous diffusion in the direction perpendicular to the membrane, with an anomalous exponent $\gamma = 2/3$. We discuss in this appendix how this is related to our experiment.

The quantity measured by FCS in the case when fluorescent particles are present on only one side of the membrane is related to the mean autocorrelation function of the membrane position in the transverse direction, $\langle W(0)W(t)\rangle$, which is in turn related to the transverse MSD of the membrane $\langle (W(t) - W(0))^2\rangle$ by:

$$\langle W(0)W(t)\rangle = \langle W(t)^2\rangle - \frac{1}{2}\langle (W(t) - W(0))^2\rangle. \qquad (37)$$

An approximate expression for the MSD can be found (Granek, 1997) provided that we are in the time range $1/\omega(q_{\max}) \ll t \ll \eta 1/\omega(q_{\min})$ ($q_{\min} = \pi/L$ and $q_{\max} = \pi/a$ are the same quantities that have been defined in section ''Derivation of the fluctuation term''), which ensures that we are far from both cutoffs in term of excitable wavelengths on the membrane, and that the limits of the integration that has to be performed over all modes (which is exactly the same as in Eq. 32) can be set to zero and infinity, respectively. However in our case G_f is proportional to $\langle W(0)W(t)\rangle_{\text{planar}}$, which is the autocorrelation function if only the modes for which $q < q_{\max}^{\text{FCS}} = 1/w_0$ (and to which the FCS experiment is sensitive) contribute. In this case, the same approximate form is found for the corresponding MSD:

$$\langle (W(t) - W(0))^2\rangle_{\text{planar}} = \frac{1}{\pi}\frac{k_BT}{K}\int_{q_{\min}}^{q_{\max}^{\text{FCS}}} dq \frac{1 - e^{-\omega(q)t}}{q^3} \simeq 0.17\left[\left(\frac{k_BT}{K}\right)^{1/2}\frac{k_BT}{\eta}t\right]^{2/3}, \qquad (38)$$

but the approximation is valid only for $1/\omega(q_{\max}^{\text{FCS}}) \ll t \ll 1/\omega(q_{\min})$.

It can also be shown (Granek, 1997) that the MSD reaches a saturation value at long times (as the autocorrelation function of $\langle W(0)W(t)\rangle$ goes to zero), which is:

$$W(t)^2 \simeq \frac{1}{2\pi q_{\min}^2}\frac{k_BT}{K}. \qquad (39)$$

It follows from the previous equations, and from the fact that $G_f(t) \propto \langle W(0)W(t)\rangle_{\text{planar}}$, that within the correct time range:

$$G_f(t) = G_f(0)\left[1 - 0.17\pi q_{\min}^2\left(\frac{K}{\eta}t\right)^{2/3}\right]. \qquad (40)$$

In our case, this expression will be valid only if $1/\omega(q_{\max}^{\text{FCS}}) \ll t \ll \eta 1/\omega(q_{\min})$, where $q_{\max}^{\text{FCS}} \simeq 1/w_0$ is the cutoff imposed by our experiment, much before we reach the molecular cutoff.

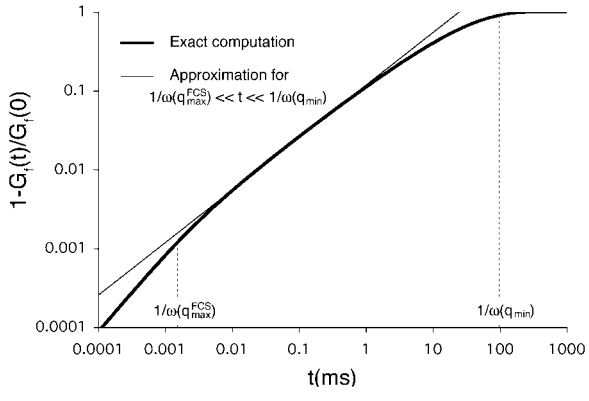

FIGURE 12 Log-log plot of the quantity $1 - G_f(t)/G_f(0)$ as calculated exactly with our model from Eqs. 32 and 33 (*thick continuous line*), and approximated expression using the $t^{2/3}$ dependence of the transversal MSD of a membrane in the time range $1/\omega(q_{\max}) \ll t \ll 1/\omega(q_{\min})$ (*thin continuous line*). The dashed lines indicate the respective positions of $1/\omega(q_{\max})$ and $1/\omega(q_{\min})$.

The $t^{2/3}$ dependence of the transverse MSD of membranes has been indirectly observed in the stretched exponential decay of the dynamic structure factor measured by light-scattering experiments (Nallet et al., 1989; Sigaud et al., 1993). To check if it could directly be seen with FCS, we plotted the quantity $1 - G_f(t)/G_f(0)$ (as calculated from Eqs. 32 and 33) on a log-log scale (Fig. 12). It can be seen that the curve as indeed a slope 2/3 over the range of time $1/\omega(q_{max}^{FCS}) \ll t \ll \eta 1/\omega(q_{min})$. This time range can be increased, to observe this power law, by increasing $1/\omega(q_{min})$ (using larger vesicles), inasmuch as $1/\omega(q_{max}^{FCS})$ is fixed by the optical resolution w_0. For high concentrations of fluorophores (and hence disappearance of the diffusion term in the autocorrelation function), and for a large q_{min}, it should hence be possible to observe by FCS the $t^{2/3}$ time dependence of the membrane transverse MSD.

The authors gratefully acknowledge A. Gennerich for helpful discussions, and D. Zbaida for help with vesicle preparation.

This work was supported by the Israel Science Foundation-Charles H. Revson Foundation and by the Dr. Joseph Cohn Minerva Center for Biomembrane Research. C.F. acknowledges support from the European Union as a Marie-Curie fellowship recipient. M.E. is incumbent of the Delta Career Development Chair.

REFERENCES

Angelova, M. I., S. Soléau, P. Méléard, J. F. Faucon, and P. Bothorel. 1992. Preparation of giant vesicles by external AC electric fields. Kinetics and applications. *Prog. Colloid Polym. Sci.* 89:127–139.

Aragón, S. R., and R. Pecora. 1976. Fluorescence correlation spectroscopy as a probe of molecular dynamics. *J. Chem. Phys.* 64:1791–1803.

Bar-Ziv, R., T. Frisch, and E. Moses. 1995. Entropic expulsion in vesicles. *Phys. Rev. Lett.* 75:3481–3484.

Berland, K. M., P. T. So, and E. Gratton. 1995. Two-photon fluorescence correlation spectroscopy: method and application to the intracellular environment. *Biophys. J.* 68:694–701.

Brochard, F., and J. F. Lennon. 1975. Frequency spectrum of the flicker phenomenon in erythrocytes. *J. Phys. France.* 11:1035–1047.

Brock, R., M. A. Hink, and T. M. Jovin. 1998. Fluorescence correlation microscopy of cells in the presence of autofluorescence. *Biophys. J.* 75: 2547–2557.

Bunde, A., and S. Havlin. 1995. Fractals and Disordered Systems. Springer-Verlag, Berlin.

Chen, Y., J. D. Müller, P. T. So, and E. Gratton. 1999. The photon counting histogram in fluorescence fluctuation spectroscopy. *Biophys. J.* 77:553–567.

Cluzel, P., M. Surette, and S. Leibler. 2000. An ultrasensitive bacterial motor revealed by monitoring signaling proteins in single cells. *Science.* 287:1652–1655.

Dimova, R., B. Pouligny, and C. Dietrich. 2000. Pretransitional effects in dimyristoylphosphatidylcholine vesicle membranes: optical dynamometry study. *Biophys. J.* 79:340–356.

Discher, D. E., N. Mohandas, and E. A. Evans. 1994. Molecular maps of red cell deformation: hidden elasticity and in situ connectivity. *Science.* 266:1032–1035.

Dittrich, P., F. Malvezzi-Campeggi, M. Jahnz, and P. Schwille. 2001. Accessing molecular dynamics in cells by fluorescence correlation spectroscopy. *Biol. Chem.* 382:491–494.

Ehrenberg, A., and R. Rigler. 1974. Rotational Brownian-motion and fluorescence intensity fluctuations. *Chem. Phys.* 4:390–401.

Evans, E. 1983. Bending elastic modulus of red blood cell membrane derived from buckling instability in micropipet aspiration tests. *Biophys. J.* 43:27–30.

Gennerich, A., and D. Schild. 2000. Fluorescence correlation spectroscopy in small cytosolic compartments depends critically on the diffusion model used. *Biophys. J.* 79:3294–3306.

Granek, R. 1997. From semi-flexible polymers to membranes: anomalous diffusion and reptation. *J. Phys. II France.* 7:1761–1788.

Helfer, E., S. Harlepp, L. Bourdieu, J. Robert, F. C. MacKintosh, and D. Chatenay. 2000. Microrheology of biopolymer-membrane complexes. *Phys. Rev. Lett.* 85:457–460.

Hochmuth, R. M., and R. E. Waugh. 1987. Erythrocyte membrane elasticity and viscosity. *Annu. Rev. Physiol.* 49:209–219.

Kask, P., K. Palo, D. Ullmann, and K. Gall. 1999. Fluorescence-intensity distribution analysis and its application in biomolecular detection technology. *Proc. Natl. Acad. Sci. USA.* 96:13756–13761.

Kask, P., P. Piksarv, Ü. Mets, M. Pooga, and E. Lippmaa. 1987. Fluorescence correlation spectroscopy in the nanosecond time range: rotational diffusion of bovine carbonic anhydrase B. *Eur. Biophys. J.* 14: 257–261.

Köhler, R. H., P. Schwille, W. W. Webb, and R. H. Hanson. 2000. Active protein transport through plastid tubules: velocity quantified by fluorescence correlation spectroscopy. *J. Cell Sci.* 113:3921–3930.

Koynova, R., and M. Caffrey. 1998. Phases and phase transitions of phosphatidylcholines. *Biochim. Biophys. Acta.* 1376:91–145.

Magde, D., E. Elson, and W. W. Webb. 1972. Thermodynamic fluctuations in a reacting system-measurement by fluorescence correlation spectroscopy. *Phys. Rev. Lett.* 29:705–708.

Mishima, K., S. Nakamae, H. Ohshima, and T. Kondo. 2001. Curvature elasticity of multilamellar lipid bilayers close to the chain-melting transition. *Chem. Phys. Lipids.* 110:27–33.

Nallet, F., D. Roux, and J. Prost. 1989. Hydrodynamics of lyotropic smectics—a dynamics light-scattering study of dilute lamellar phases. *J. Phys. France.* 50:3147–3165.

Needham, D., and E. Evans. 1988. Structure and mechanical properties of giant lipid (DMPC) vesicle bilayers from 20°C below to 10°C above the liquid crystal-crystalline phase transition at 24°C. *Biochemistry.* 27:8261–8269.

Nomura, Y., H. Tanaka, L. Poellinger, F. Higashino, and M. Kinjo. 2001. Monitoring of in vitro and in vivo translation of green fluorescent protein and its fusion proteins by fluorescence correlation spectroscopy. *Cytometry.* 44:1–6.

Palmer, A. G., and N. L. Thompson. 1987. Theory of sample translation in fluorescence correlation spectroscopy. *Biophys. J.* 51:339–343.

Politz, J. C., E. S. Browne, D. E. Wolf, and T. Pederson. 1998. Intranuclear diffusion and hybridization state of oligonucleotides measured by fluorescence correlation spectroscopy in living cells. *Proc. Natl. Acad. Sci. USA.* 95:6043–6048.

Qian, H., and E. L. Elson. 1990. On the analysis of high-order moments of fluorescence fluctuations. *Biophys. J.* 57:375–380.

Rawicz, W., K. C. Olbrich, T. McIntosh, D. Needham, and E. Evans. 2000. Effect of chain length and unsaturation on elasticity of lipid bilayers. *Biophys. J.* 79:328–339.

Rigler, R., Ü. Mets, J. Widengren, and P. Kask. 1993. Fluorescence correlation spectroscopy with high count rate and low background: analysis of translational diffusion. *Eur. Biophys. J.* 22:169–175.

Saxton, M. J. 1994. Anomalous diffusion due to obstacles: a Monte Carlo study. *Biophys. J.* 66:394–401.

Schwille, P., U. Haupts, S. Maiti, and W. W. Webb. 1999. Molecular dynamics in living cells observed by fluorescence correlation spectroscopy with one- and two-photon excitation. *Biophys. J.* 77:2251–2265.

Sigaud, G., C. W. Garland, H. T. Nguyen, D. Roux, and S. T. Milner. 1993. Spinodal decomposition in 2-component smectics. *J. Phys. II France.* 3:1343–1355.

Starr, T. E., and N. L. Thompson. 2001. Total internal reflection with fluorescence correlation spectroscopy: combined surface reaction and solution diffusion. *Biophys. J.* 80:1575–1584.

Thompson, N. L. 1991. Fluorescence correlation spectroscopy. *In* Topics in Fluorescence Spectroscopy, Vol. 1: Techniques. J. R. Lakowicz, editor. Plenum Press, New York. 337–378.

Wachsmuth, M., W. Waldeck, and J. Langowski. 2000. Anomalous diffusion of fluorescent probes inside living cell nuclei investigated by spatially-resolved fluorescence correlation spectroscopy. *J. Mol. Biol.* 298:677–689.

Webb, W. W. 2001. Fluorescence correlation spectroscopy: inception, biophysical experimentations, and prospectus. *Appl. Opt.* 40:3969–3983.

Widengren, J., Ü. Mets, and R. Rigler. 1995. Fluorescence correlation spectroscopy of triplet states in solution: a theoretical and experimental study. *J. Phys. Chem.* 99:13368–13379.

Widengren, J., and R. Rigler. 1997. Mechanisms of photobleaching investigated by fluorescence correlation spectroscopy. *Bioimaging.* 4: 149–157.

Zilman, A. G., and R. Granek. 1996. Undulations and dynamic structure factor of membranes. *Phys. Rev. Lett.* 77:4788–4791.

Zimmerman, S. B., and A. P. Minton. 1993. Macromolecular crowding: biochemical, biophysical, and physiological consequences. *Annu. Rev. Biophys. Biomol. Struct.* 22:27–65.

Generic Approach for Dispersing Single-Walled Carbon Nanotubes: The Strength of a Weak Interaction

Rina Shvartzman-Cohen,[†] Yael Levi-Kalisman,[‡] Einat Nativ-Roth,[†] and Rachel Yerushalmi-Rozen*[,†,‡]

Department of Chemical Engineering and The Ilse Katz Center for Meso- and Nanoscale Science and Technology, Ben Gurion University in the Negev, 84105 Beer Sheva, Israel

Received March 12, 2004. In Final Form: May 31, 2004

A generic noncovalent approach for dispersing high concentrations of individual single-walled carbon nanotubes (SWNT) in organic as well as aqueous solutions of synthetic block copolymers is presented. It is suggested that a weak, long-ranged entropic repulsion among polymer-decorated tubes acts as a barrier that prevents the tubes from approaching the attractive part of the intertube potential. The method opens a new route for utilization of block copolymers as compatibilizers for SWNT, improving the incorporation of de-agglomerated SWNT into target polymeric matrixes.

Introduction

Single-walled carbon nanotubes (SWNT) currently attract scientific and technological attention because of their superior properties and emerging applications in nanoelectronics and in the field of nanocomposites.[1]

A major barrier for SWNT utilization in nanocomposites is their poor solubility and low dispersability in aqueous and organic liquids, leading to difficulties in their manipulation and incorporation into different matrixes. The resulting SWNT-based materials exhibit a strength, modulus, and conductivity much lower than expected.[2]

The low dispersability stems from the tendency of as-prepared SWNT to assemble into bundles or ropes that contain hundreds of well-aligned SWNT arranged in a close-packed triangular lattice,[3] due to van der Waals attraction. The over-micrometer-long ropes further entangle into networks. A recent calculation[4] suggests that the typical intertube attraction is on the order of 36 kT for every nanometer of overlap between adjacent tubes, leading to cohesive energy of a few thousands of kT per micrometer-long tubes. Unlike the case of classical colloids, the attraction is short-ranged and decays to a negligible value over a distance of a few nanometers.

Current approaches for dispersing and exfoliating bundled SWNT into individual tubes include covalent modifications,[5−7] $\pi-\pi$ interactions,[8,9] surfactant adsorption,[10,11] and more. Most of these methods are designed to reduce the short-range attraction between adjacent tubes via the introduction of a repulsive interaction of similar strength. Consequently, these treatments often lead to modification of the structural, electronic, and mechanical properties of the tubes.[12−14]

To overcome this problem, a significant effort was invested in the development of noncovalent dispersing methods,[15] mainly based on physical adsorption of polymers.[16−18] While quite a few examples were reported, the underlying mechanism in each of these studies was believed to rely on specific interactions between a given polymer and the SWNT. For example, it was suggested[16] that tight SWNT−polymer association (known as "wrapping") leads to screening of the hydrophobic interaction in aqueous solutions and consequential dispersion of tubes.

Here, we present a generic, single-step method for dispersing individual SWNT in aqueous and organic liquids: a powder of as-prepared SWNT is sonicated in a solution of a synthetic block copolymer, forming a black inklike stable dispersion. While the gentle sonication leads to exfoliation of SWNT into individual tubes,[19] selective adsorption of the block copolymer triggers a repulsion among the polymer-decorated SWNT and stabilizes the exfoliated SWNT in the dispersion. X-ray scattering and

* Corresponding author. E-mail: rachely@bgumail.bgu.ac.il.

[†] Department of Chemical Engineering, Ben Gurion University in the Negev.

[‡] The *Ilse Katz* Center for Meso- and Nanoscale Science and Technology, Ben Gurion University in the Negev.

(1) Dresselhaus, M. S., Dresselhaus, G., Avouris, Ph., Eds. *Carbon Nanotubes*; Topics in Applied Physics 80; Springer-Verlag: Berlin, 2001.

(2) Baughman, R. H.; Zakhidov, A. A.; de Heer, W. A. *Science* **2002**, *297*, 787−792.

(3) Thess, A.; Lee, R.; Nikolaev, P.; Dai, H.; Petit, P.; Robert, J.; Xu, C.; Lee, Y. H.; Kim, S. G.; Rinzler, A. G.; Colbert, D. T.; Scuseria, G. E.; Tomanek, D.; Fisher, J. E.; Smalley, R. E. *Science* **1996**, *273*, 483−487.

(4) Girifalco, L. A.; Hodak, M.; Lee, R. S. *Phys. Rev. B* **2000**, *62*, 13104.

(5) Chen, J.; Hamon, M. A.; Hu, H.; Chen, Y.; Rao, A. M.; Eklund, P. C.; Haddon, R. C. *Science* **1998**, *282*, 95−98.

(6) Boul, P. J.; Liu, J.; Mickelson, E. T.; Huffman, C. B.; Ericson, L. M.; Chiang, I. W.; Smith, K. A.; Colbert, D. T.; Hauge, R. H.; Margrave, J. L.; Smalley, R. E. *Chem. Phys. Lett.* **1999**, *310*, 367.

(7) Ausman, K. D.; Piner, R.; Lourie, O.; Ruoff, R. S.; Korobov, M. J. *Phys. Chem. B* **2000**, *104*, 8911−8915.

(8) Coleman, J. N.; Dalton, A. B.; Curran, S.; Rubio, A.; Barklie, R. C.; Blau, W. J. *Adv. Mater.* **2000**, *12*, 213−216.

(9) Shin, M.; Wong, N.; Shi Kam, Chen, R. J.; Li, Y.; Dai, H. *Nano Lett.* **2000**, *2*, 285−288.

(10) Vigolo, B.; Penicaud, A.; Coulon, C. Sauder, R.; Pailler, C.; Journet, P.; Bernier, P.; Poulin, P. *Science* **2000**, *290*, 1331.

(11) O'Connel, M. J.; Bachilo, S. M.; Huffman, C. B.; Moore, V. C.; Strano, M. S.; Haroz, E. H.; Rialon, K. L.; Boul, P. J.; Noon, W. H.; Kittrell, C.; Ma, J.; Hauge, R. H.; Weisman, R. B.; Smalley, R. E. *Science* **2002**, *297*, 593−596.

(12) Zheng, M.; Jagota, A.; Strano, M. S.; Santos, A. P.; Barone, P.; Chou, S. G.; Diner, B. A.; Dresselhaus, M. S.; McLean, R. C.; Onoa, G. B.; Samsonidze, G. G.; Semke, E. D.; Usrey, M.; Walls, D. J. *Science* **2003**, *302*, 1545−1548.

(13) Monthioux, M.; Smith, B. W.; Claye, A.; Fischer, J. E.; Luzzi, D. E. *Carbon* **2001**, *39*, 1251.

(14) Garg, A.; Sinnott, S. B. *Chem. Phys. Lett.* **1998**, *295*, 273−278.

(15) Moore, V. C.; Strano, M. S.; Haroz, E. H.; Schmidt, J.; Talmon, Y.; Hauge, R. H.; Smalley, R. E. *Nano Lett.* **2003**, *3*, 1379.

(16) O'Connell, M. J.; Boul, P. J.; Ericson, L. M.; Huffman, C.; Wang, Y. H.; Haroz, E. H.; Kuper, C.; Tour, J.; Ausman, K. D.; Smalley, R. E. *Chem. Phys. Lett.* **2001**, *342*, 265−271.

(17) Chen, J.; Liu, H.; Weimer, W. A.; Halls, M. D.; Waldeck, D. H.; Walker, G. C. *J. Am. Chem. Soc.* **2002**, *124*, 9034.

(18) Bandyopadhyaya, R.; Nativ-Roth, E.; Regev, O.; Yerushalmi-Rozen, R. *Nano Lett.* **2002**, *2*, 25−28.

(19) Strano, M. S.; Morre, V. C.; Miller, M. K.; Allen, M. J.; Haroz, E. H.; Kittrell, C.; Huage, R. H.; Smalley, R. E. *J. Nanosci. Nanotechnol.* **2003**, *3*, 81−85.

10.1021/la049344j CCC: $27.50
Published on Web 06/24/2004

electron microscopy indicate that the SWNT do not bundle upon drying and may be redispersed in the pure solvent to form highly concentrated dispersions of individual SWNT and small bundles. We demonstrate that diblock and triblock copolymers of very different structures and compositions act efficiently as stabilizers and may be tailored so as to disperse the tubes in a variety of solvents.

Experimental Section

Materials. *SWNT.* Two types of SWNT were used: select grade nanotubes (SWNT1) and AP grade (SWNT2), which were purchased from Carbolex, University of Kentucky, Lexington, KY, U.S.A. The nanotubes were synthesized by arc-discharge and used as received. According to the specifications by the manufacturer, the as-prepared select grade consists of 85 vol % pure SWNT, while the AP grade consists of 50−70 vol % SWNT. The samples contain graphite, carbon impurities, and catalyst (cobalt and nickel, ca. 20 nm in diameter), the average diameter of the tubes is 1.3 nm, and the typical length is in the range of hundreds of nanometers.

Block Copolymers. Details of the water-soluble polymers [poly(ethylene oxide)100-*b*-poly(propylene oxide)65-*b*-poly(ethylene oxide)100, PEO-PPO-PEO (F-108), of molecular weight 12 600 g/mol, and PE10,500, poly(ethylene oxide)-*b*-poly(propylene oxide), PPO-PEO, of molecular weight 6500 g/mol] are given in Supporting Information (Tables 1 and 2). The block copolymer soluble in organic solvents, poly(styrene-*b*-*tert*-butyl acrylate) diblock copolymer (P745: PS-tbuAC), molecular weight of polystyrene 1900 g/mol and acrylate 31 900 g/mol, was purchased from Polymer Source, Canada. Poly(ethyleneoxide-*b*-poly(dimethylsiloxane)-*b*-ethyleneoxide) triblock copolymer (PEO-PDMS-PEO) was kindly donated by M. Gottlieb.[20] Each PEO block is of molecular weight 2000 g/mol, and the PDMS block is of 12 000 g/mol.

Solvents. Analytical grade organic solvents were used: heptane, ethanol, toluene, 2-propanol (Frutarom, Israel), and Millipore water (10^{18} Ω/cm).

Methods. *Preparation.* Dispersions were prepared by dissolving a block copolymer in a selective solvent (aqueous or organic) to form solutions of desired concentrations. A powder of as-prepared nanotubes was sonicated at very mild conditions (50 W, 43 kHz) for 15−20 min in the polymeric solution (these conditions were shown not to damage the tubes or the polymers).[18,21]

Characterization. Electron Microscopy. The dispersed SWNT were characterized via direct imaging of the aqueous dispersions using cryo-transmission electron microscopy (cryo-TEM).[22] Dried polymer-coated powders were imaged by high-resolution transmission electron microscopy (HRTEM).

In the cryo-TEM method, a drop of the solution was deposited on a transmission electron microscope (TEM) grid (300-mesh Cu grid) coated with a holey carbon film (Lacey substrate, Ted Pella, Ltd.). The excess liquid was blotted, and the specimen was vitrified by a rapid plunging into liquid ethane precooled with liquid nitrogen, in a controlled environment vitrification system. The samples were examined at −178 °C using a FEI Tecnai 12 G^2 TWIN TEM equipped with a Gatan 626 cold stage, and the images were recorded (Gatan model 794 charge-coupled device camera) at 120 kV in low-dose mode.

Wide-Angle X-ray Scattering (WAXS). The measurements were carried out by a Philips X-ray powder diffractometer (PW-1050/70) at 40 kV/28 mA with Cu Kα (λ = 1.54 Å) radiation and a graphite monochromator. The scattering vector $q = 4\pi/\lambda$ (sin θ), where θ is the scattering angle.

Results and discussion

In Figure 1 we present black, macroscopically homogeneous dispersions obtained by sonication of as-prepared SWNT in different solutions of block copolymers (Figure 1A−E).

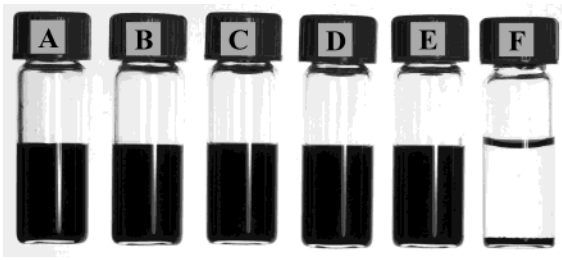

Figure 1. Dispersions of SWNT in polymeric solutions: 1 wt % SWNT1 in a 1 wt % solution of PS-tbuAC (A) in ethanol and (B) in 2-propanol. SWNT2 in solutions of (C) 1 wt % PEO-PDMS-PEO in heptane, (D) 1 wt % PEO-PPO-PEO (F-108) in water, (E) 1 wt % PPO-PEO (PE10,500) in water, and (F) 1 wt % PEO-PDMS-PEO in toluene. Images were taken more than 2 months after preparation.

The observed dispersions are stable for months. The variety of polymers and solvents presented in this work demonstrates the versatility of the approach.

The stable dispersions may be dried (at ambient conditions) and the powder redispersed in the solvent to form an inklike dispersion of SWNT, in concentrations ranging from 0.5 to 30 wt % of polymer-coated SWNT in the solvent. The resulting suspensions are stable over a few months, and centrifugation (at 3500 rpm for 30 min) does not result in precipitation of the nanotubes.

The microscopic structure of stable SWNT dispersions was investigated using cryo-TEM, which is known to preserve the structures present in the bulk solutions[22] (Figure 2A). We observed that the length of the SWNT is well above 1 μm and that the dispersions contain along with the tubes some carbonaceous residues and catalyst particles (Figure 2A). While cryo-TEM provides an overview of the solution composition, HRTEM (Figure 2B) allows one to probe the finer structural details of the dispersed species. The HRTEM images reveal that the structure of the individual SWNT is intact and that the most abundant species in the dispersions are well-separated individual tubes (of a diameter below 2 nm, Figure 2B) and small bundles comprising 2−3 tubes.

To test the aggregation state of dried SWNT, we performed X-ray scattering experiments. A typical WAXS pattern of a powder of high-purity as-prepared SWNT1 is presented in Figure 3A. A characteristic rope structure with peaks at the low-q region (at q = 0.4, 0.85, 1.06, and 1.50 $Å^{-1}$) indicates a two-dimensional triangular lattice with a lattice constant of 1.8 nm[3]. In addition, peaks of graphitic impurities are observed (at q = 1.88 $Å^{-1}$), in good agreement with previous observations. The WAXS spectrum of a dried SWNT1−polymer powder (Figure 3B) is quite different: peaks which result from intertube packing within the ropes in the as-prepared SWNT sample have disappeared, indicating that the dispersed-and-dried powders are composed of nonordered tubes of SWNT (for an additional example, see Supporting Information). The peaks at q = 1.30, 1.61, and 2.35 $Å^{-1}$ characterize the polymer. Redispersion of the powder results in the formation of a stable dispersion of individual SWNT (Figure 2).

Redispersability is a well-known signature of a dispersion mechanism, known as steric stabilization.[23] The mechanism is based on the onset of entropic repulsion among polymer-decorated colloids. Block copolymers are among the more efficient steric stabilizers because they are comprised of chemically distinct and often mutually

(20) Zhang, Z. R.; Gottlieb, M. *Thermochim. Acta* **1999**, *336*, 133.
(21) Bandyopadhyaya, R.; Nativ-Roth, E.; Regev, O.; Yerushalmi Rozen, R. *MRS Proceedings* **2002**, *706*, 46303.
(22) Talmon, Y. In *Cryo techniques in biological electron microscopy*; Steinbrecht, R. A., Zierold, K., Eds.; Springer-Verlag: Berlin, 1987.
(23) Napper, D. H. *Polymeric Stabilization of Colloidal Dispersions*; Academic Press: Orlando, FL, 1993.

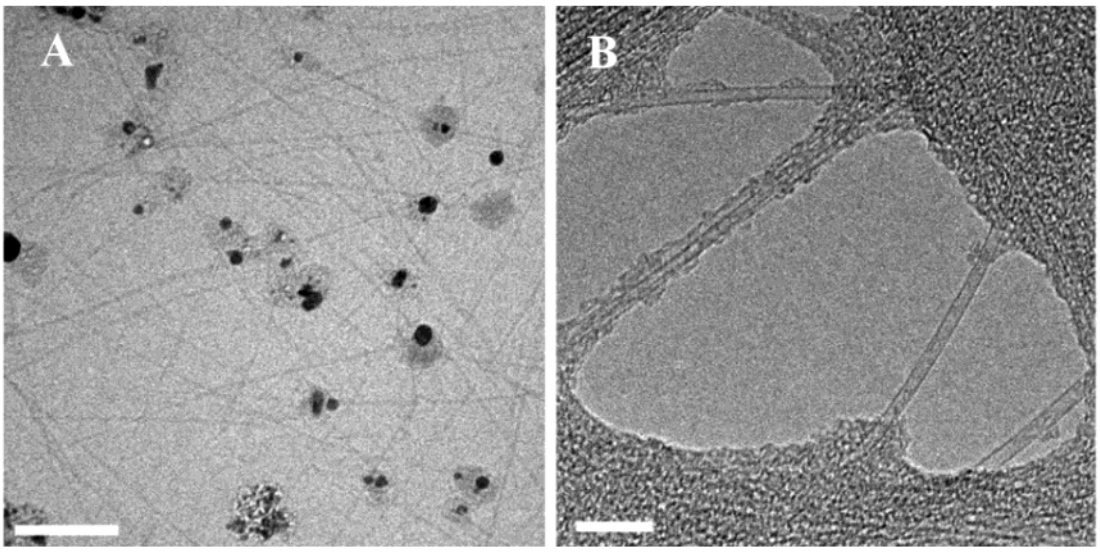

Figure 2. TEM micrographs of concentrated SWNT dispersions prepared by redispersing a powder of the dried dispersion in the pure solvent. (A) Cryo-TEM image of a vitrified aqueous dispersion (1:2.5 wt % of SWNT2/PE10,500). Scale bar = 100 nm. (B) HRTEM image of a dried SWNT2 dispersion prepared by redispersion in ethanol, a dry powder of PS-tbuAC diblock-copolymer-coated SWNT (1:1 wt % SWNT2/PS-tbuAC). Scale bar = 10 nm.

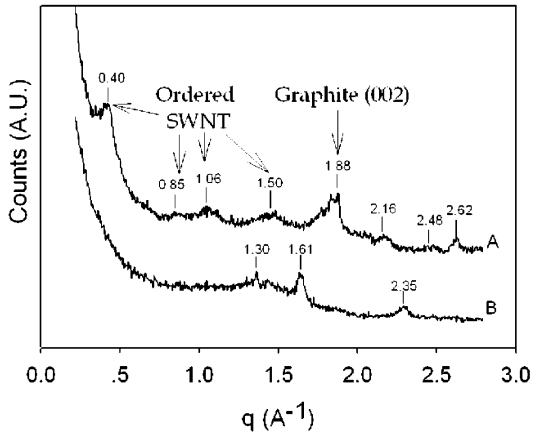

Figure 3. WAXS spectra of a dry powder of a stable dispersion. (A) As-prepared SWNT1 powder exhibiting a typical rope structure. (B) A powder prepared by drying an aqueous dispersion of SWNT1 in a solution of a diblock copolymer (1 wt % SWNT1 in 2.5 wt % of PE10,500).

incompatible moieties (designated A-B and A-B-A for diblocks and triblocks, respectively) that are covalently bonded.[24] A typical scenario for steric stabilization via block copolymers relies on the dual action of the polymer: while one of the blocks (B) anchors the chain to the surface, the other block (A) dangles into the solvent and repels other polymer-decorated objects. It is well-known in the field of colloidal science[23] that the crucial parameter determining the dispersion ability of different block copolymers is solvent selectivity: A selective solvent that acts as a "good solvent" for one of the blocks (i.e., A) dissolves the polymer readily and increases the spatial dimensions of the polymeric chain, while simultaneously acting as a "poor solvent" for the other block (B) that adsorbs onto the colloid.[25]

To test the role of solvent selectivity in SWNT stabilization, we performed two sets of control experiments. In the first, we examined the behavior of block copolymers in a nonselective solvent (a good solvent for both blocks). For example, the triblock copolymer PEO-PDMS-PEO was dissolved in toluene (a good solvent for both PEO and PDMS). We found (Figure 1F and Supporting Information) that SWNT could not be dispersed in these solutions (at polymer concentrations ranging from 1 to 10 wt %). The solutions underwent phase separation, and the tubes coagulated at the bottom of the vial. Note that solutions of the very same polymer in heptane, a selective solvent for the triblock (at similar concentration and temperature), resulted in the formation of a stable dispersion of SWNT (Figure 1C). In a second set of control experiments, we tested the behavior of SWNT in good solvents for homopolymers comprising the blocks: PEO (in water and toluene), PDMS (in heptane and toluene), and PS (in toluene). We found that in these solutions the polymers could not serve as dispersing agents for SWNT. Thus, we conclude that selective interaction of the different blocks with the solvent is essential for stabilization of dispersed SWNT.

Review of a few specific examples where block copolymers lead to dispersion of either bundles or individual tubes implies that they fit well into the framework presented here. For example, we observed a similar behavior to that reported by Moore et al.,[15] where Pluronic triblock copolymers in water, which is a selective solvent for them, lead to dispersion of SWNT (details and additional examples are given in Supporting Information).

The generic method presented here is simple and may be utilized for preparation of stable dispersions of well-separated SWNT in aqueous and organic solvents, at low and high concentrations. The approach is summarized in Figure 4: SWNT held by strong, short-range intertube attraction (Figure 4A) form ropes and bundles (Figure 4B). Gentle sonication causes exfoliation of ropes into individual tubes (Figure 4C). The exfoliated tubes may be stabilized in the liquid media and aggregation may be prevented by introduction of a relatively weak repulsion (of the order of a few kT) at a large distance between the tubes (some tens of nanometers), such as the osmotic (steric) repulsion among the tails of tethered block copolymers in good solvent conditions. The stable dispersions are macroscopically homogeneous (Figure 4D), and

(24) Lodge, T. P. *Macromol. Chem. Phys.* **2003**, *204*, 265.

(25) We note here that the tendency of block B to adsorb onto SWNT is determined by the balance of SWNT−solvent, SWNT−monomer, and polymer−solvent interactions. Issues of polymers adsorption are discussed thoroughly in ref 23, chapter 3.

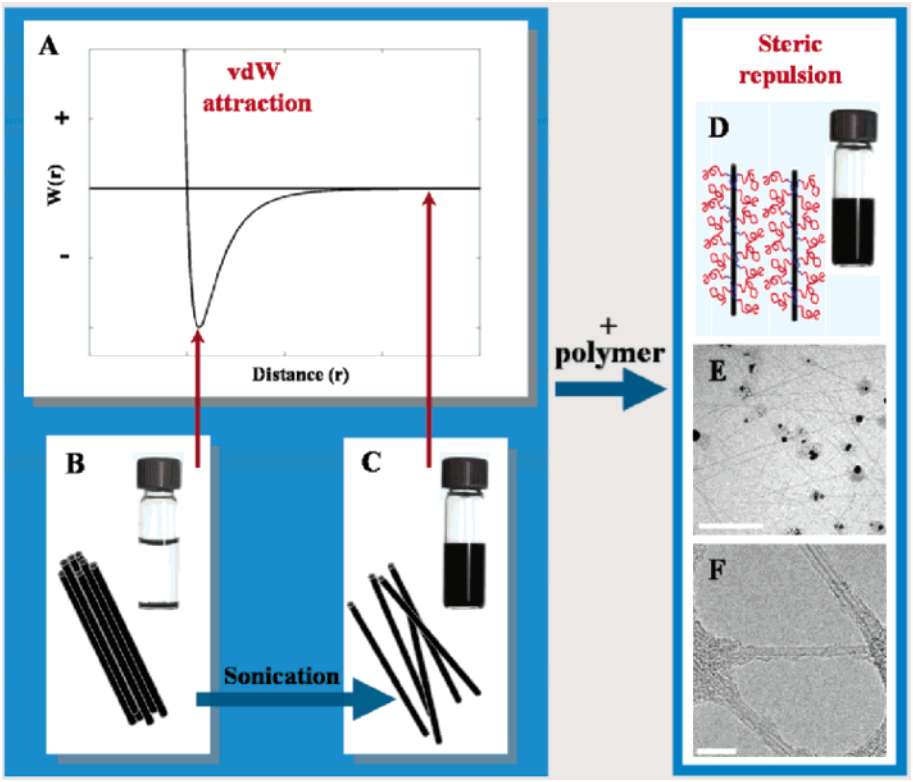

Figure 4. Schematic representation of the concept. (A) Total interaction energy $W(r)$ versus the separation distance r, for two nanotubes, assuming a Lennard-Jones potential $[W(r) = (C_{12}/r^{12}) - (C_6/r^6)]$.[4] The attractive part of the potential leads to crystallization of SWNT in bundles, rendering the material indispersible (A, B). While sonication leads to temporary exfoliation (C),[19] adsorption of block copolymers in a selective solvent stabilizes the exfoliated tubes (D) and prevents re-aggregation. Macroscopic and microscopic imaging of SWNT dispersions indicate that the inklike dispersion is composed of individual tubes and small bundles: (E) cryo-TEM image (scale bar = 100 nm) and (F) HRTEM image (scale bar = 10 nm).[26]

electron microscopy imaging reveals (Figure 4E,F) that they are composed of individual tubes and small bundles. While steric stabilization has long been known as an efficient method for stabilization of colloidal solutions, its applicability to SWNT, where the adhesion forces among the particles are on the order of a few thousands of kT, is somewhat surprising. We suggest that end-tethered polymers may form a barrier and prevent SWNT from approaching the highly attractive (though short-ranged) region of the intertube potential.

The dispersing approach presented here is expected to be highly useful in the preparation of polymer−SWNT composites: because it offers the possibility of selecting a nonadsorbing block that is either identical or compatible with a target polymeric matrix, the dispersing agent may simultaneously act as a compatibilizing agent and adhesion promoter leading to marked strengthening of the SWNT−matrix interface, thus, improving the properties of the resulting nanocomposites. As was discussed before,[27] the typical adhesive fracture energy of a polymer-straightened interface is on the order of 102−103 J/m^2, about 100 times higher than the fracture energy of a carbon−carbon plane.

Acknowledgment. This research was supported by the Israel Science Foundation, the Center of Excellence program (Grant 8003).

Supporting Information Available: Description of additional materials and control experiments. This material is available free of charge via the Internet at http://pubs.acs.org.

LA049344J

(26) A dispersion of 1 wt % SWNT in an aqueous 2.5 wt % solution of a block-copolymer PE10,500 (Figure 4E) was imaged using cryo-TEM, and a dispersion of 1 wt % SWNT in 1 wt % PS-tbuAC solution in ethanol (Figure 4F) was imaged by HRTEM.

(27) de Gennes, P. G. *Can. J. Phys.* **1990**, *68*, 1049.

INTERFACE SCIENCE 11, 199–209, 2003

Effect of Interfaces on the Crystallization Behavior of PDMS

T. DOLLASE*, M. WILHELM AND H.W. SPIESS
Max-Planck-Institut für Polymerforschung, Ackermannweg 10, 55128 Mainz, Germany

Y. YAGEN, R. YERUSHALMI-ROZEN† AND M. GOTTLIEB
Department of Chemical Engineering, Ben-Gurion-University of the Negev, Beer-Sheva 84105, Israel; The Reimund Stadler Minerva Center for Mesoscale Macromolecular Engineering, Ben-Gurion-University of the Negev, Beer-Sheva 84105, Israel
rachely@bgumail.bgu.ac.il

Abstract. The reversible thermal behavior of a non-entangled semicrystalline polymer, poly(dimethylsiloxane), PDMS, was investigated in the presence of sub-micron particles. Filled polymer systems of this type are characterized by a large surface-to-volume ratio but lack the external confinement that is typical for a thin film geometry. Differential-scanning calorimetry (DSC) measurements indicate that the presence of the nanometric solid additives enhances the crystallization rate as compared to native PDMS melts. Different types of additives and surface interactions resulted in a similar effect, suggesting that the origin of the enhanced crystallinity is non-specific. The effect is attributed to entropic interactions in the boundary layer.

Keywords: polymer crystallization, surface effects in polymers

1. Introduction

Surfaces are known to affect the physical properties of polymers and modify their dynamic behavior [1–7]. In particular, first order thermal transitions (crystallization or melting) and second order relaxation processes (glass formation) of polymers deviate significantly in the vicinity of a surface from their bulk behavior [8–11].

Most polymers form amorphous solids as crystallization requires extensive regularity on a chemical (e.g., tacticity) and topological (branching, crosslinking) level. In a crystallizable polymer, the degree of crystallinity is limited by the presence of topological constraints and disparity in chain lengths. The class of polymers that embodies crystalline domains is known as semi-crystalline polymers [12]. The degree of crystallinty as well as the crystal habit: Structure, size and orientation of the crystals, affect bulk properties of the polymeric materials, and are therefore important parameters for most applications [13].

Polymer crystallization from the melt involves ordering at different length scales: It is often observed that aggregates of crystals, originating from a common center, form spherulites (Fig. 1(a)). Each of the crystallites is constructed of lamellar layers (Fig. 1(b)), formed by chain folding along the short direction of the layer. Chain folding is the essential step in the transformation of a polymer liquid (the melt) into a crystal.

Along the normal to the lamellar layer crystalline and amorphous regions alternate. The amorphous regions incorporate chain entanglements, branches, side-chains, and chain ends.

When crystallization is induced by cooling of a high molecular-weight polymer melt at a finite rate, the ideal crystalline structure can not be realized, due to the typically slow dynamics of polymer re-organization

*Present address: Tesa AG, Quickbornstrasse 24, 20253 Hamburg, Germany.
†To whom all correspondence should be addressed.

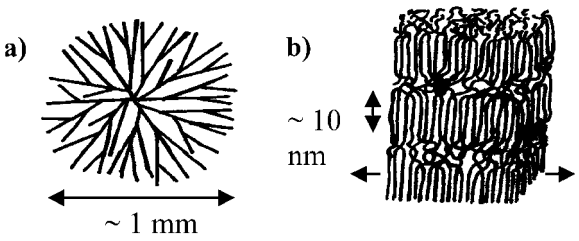

Figure 1. A schematic drawing of polymeric crystallites on two different length scales. (a) Spherulites—the diameter of fully developed spherulites ranges from several microns to centimeters. Throughout the spherulite amorphous (white) and crystalline (black) regions alternate. (b) Typical lamellar structure. The thickness is in the order of 10 nm.

and topological constraints. The latter is often much longer than the experimental time-scale. As a consequence, the structures that develop at a given temperature, and a given cooling rate, are the fastest ones to assemble and grow, rather than those of the lowest free energy. Being dominantly controlled by kinetics, structure, properties, and the degree of crystallinity, are affected by the crystallization temperature, cooling rate, and last, but not-least, the initial conformational state of the chains [12].[1]

Classical theories of polymer crystallization such as the Hoffman-Lauritzen model [14, 15], describe the process as a sequence of two steps: Primary nucleation and growth, with nucleation being the rate-determining step [16]. Nucleation is classified as either homogeneous [17] or heterogeneous. Crystal growth takes place by piecewise incorporation of macromolecular chains on a pre-existing crystal surface, known as secondary nucleation [15].

A different model for the growth mechanism of crystals was suggested by Sadler [18]: In his model the elementary step leading to crystallization is reversible attachment and detachment of chain sequences. The model suggests that the growth process evolves by natural selection of the configurations which lead to growth of the crystalline face. Both models assume that the lamellar crystallites grow into the melt, and there exists a well-defined interface between the ordered phase and the melt, in a similar manner to crystallization of small molecules.

A conceptually different model was recently described by Strobl and coworkers [19, 20]. They suggested that in some cases, polymer crystallization from the melt evolves by cooperative ordering over large regions. Here mesoscopic domains of preordered molten chains separate regions of crystalline and non-oriented molten material. In this approach crystallization is viewed as a disorder-order transition, similar to that observed in two-dimensional monolayers [21]. The process involves the formation of a novel phase referred to as granular crystalline phase characterized by local ordering. It should be noted that the concept of weakly ordered phases was discussed in the context of linear chains crystallization (see for example ref. 22).

The effect of solid micro-particles such as dispersed granular filler on polymer crystallization was investigated in a considerable number of calorimetric studies [13]. It was observed that the presence of particles affect the resulting crystallite size, degree of crystallinity as well as crystallization temperature, T_c, and melting temperature, T_m [23]. These observations are of technical importance in the field of composites and reinforced materials.

In the framework of the classical models of crystallization it was suggested that solid surfaces enhance crystallinity by locally reducing the critical enthalpy for nucleation, an effect known as heterogeneous nucleation [16]. Yet many of the observations cannot be explained by a local reduction of enthalpy.

In the study described here we examine the effect of surfaces on the calorimetric response of a practically non-entangled semicrystalline polymer, poly(dimethylsiloxane), PDMS [24]. Particles are dispersed in a melt, therefore exhibit a large surface-to-volume ratio which emphasizes the effect of interfacial interactions. Yet, unlike a thin-film configuration, finite size and external confinement do not play a dominant role in this system. The experiments monitor the crystallization and glass-transition characteristics in the presence of four different types of interfaces, some of which are enthalpically attractive. Thus, we are able to examine the specific and general aspects of the interfacial interaction, in the context of PDMS crystallization.

The structure of the article is as follows: We describe the preparation and characterization of the samples, introduce the experimental technique, discuss the results and compare them with theoretical predictions.

2. Experimental Section

Materials and Sample Preparation: PDMS from three different sources was used: PDMS 16,000 g mol^{-1} (PDMS 16k) was synthesized by living ring-opening polymerization by T. Wagner at the Max-Planck-Institut für Polymerforschung, Mainz, Germany.

PDMS 15,000 g mol^{-1} (PDMS 15k) was purchased from Polymer Source, Dorval, Canada and PDMS 8,850 g mol^{-1} (PDMS 8.8k) was purchased from PSS Germany (we report all molecular weight data in terms of the number average, M_n; the polydispersity of all polymers was $M_w/M_n = 1.1$, determined by GPC). These molecular weights are roughly of the order of the entanglement length, M_e, of PDMS and we regard PDMS 16k as practically non-entangled.[2]

Fumed silica Cab-o-Sil M7D particles (Cabot Corp., Boston, U.S.A.) were used. These particles form three-dimensional aggregates of an average size of 250 nm consisting of individual particles of 10–20 nm in diameter and with a surface area of 200 ± 25 m^2 g^{-1}. The silica aggregates were employed with three different modifications: (a) as dried particles, (b) saturated with water (c) dried and coated by a fluorinated silane. The first type of particles was dried by heating at 200°C *in vacuo* for 24 hours. Loss of water was monitored by the decrease in the intensity of the water band at 3440 cm^{-1} using FTIR spectroscopy. Fluorination was carried out by immersion of pre-dried particles for 3 hours at ambient temperature in a solution (90% isooctane, Merck, 10% choroform, Frutarom, both HPLC grade) of 1H,1H,2H,2H-perfluorodecyltrichlorosilane, PFDTS (Lancaster). The solvent was then evaporated and the particles were rinsed in chloroform, filtered and dried at 100°C *in vacuo* over night. Surface coverage was estimated from FTIR measurements which were carried out by mixing 5 mg of particles in 100 mg of KBr. The IR spectra of the coated particles exhibited three extra bands at 650, 700 and 900 cm^{-1} corresponding to C-F bending vibrations and additionally a characteristic band slightly below 3000 cm^{-1} revealing C-H stretching modes. No peak was observed at 3440 cm^{-1} indicating the absence of water on the particle surface. PDMS does not wet a surface coated with PFDTS and forms a contact angle of $45^\circ \pm 1$ (advancing) and $35^\circ \pm 1$ (receding).

Controlled Porous Glass (CPG) [25, 26] was purchased from Schott, Hofheim, Germany, in a hydrophilic and hydrophobic form. The hydrophilic glass is a powder of borosilicate which carries Si-OH groups on the surface. In the hydrophobic glass 25% of the OH-groups are exchanged by $C_8H_{17}O$-groups. Both materials are characterized by an average particle size of 30–60 μm and an average pore size of about 100 nm.

The filled polymer mixtures were prepared by stirring of the filler particles in a solution of PDMS in heptane (HPLC grade, Aldrich) for at least 5 hours at ambient temperature. The solvent was then evaporated and the suspension was dried for 24 hours at 85°C. In this study we used a particle concentration of 10 wt% in PDMS. The distribution of the filler particles in the polymeric matrix was characterized by freeze-fracture transmission-electron microscopy (FFTEM). Samples were prepared by placing a filled polymer melt between two copper disks and vitrifying the sample by plunging it into liquid propane, cooled by liquid nitrogen. A Balzers BAF 400 freeze-fracture apparatus was used for fracturing and replication at about 130 K. For electron microscopy Pt/C was deposited at an angle of 45°. The PDMS was removed from the replica using a 1:1 (v/v) mixture of THF and methanol. The clean replica was then imaged in a CEM 902 transmission-electron microscope. In Fig. 2 we present typical images of water-saturated M7D particles dispersed in PDMS 15k. We observe that the particles are well dispersed, and that the inter-aggregate distance is of the order of 1 μm.

Experimental Technique: Differential-scanning calorimetry (DSC) served as the main experimental tool in this study. This is a thermoanalytical technique that records heat flux changes as a function of time [27, 28]. First-order phase transitions like melting or crystallization appear in the thermogram as peaks while a glass transition shows up as a step. In this study we performed experiments at constant rates where the sample was nominally cooled or heated at a constant rate, β ($dT/dt = \beta = \text{constant}$, where T is temperature and t is time). Unless stated otherwise the cooling rate was $\beta = -5$ K min^{-1} and the heating rate $\beta = +5$ K min^{-1}. The experiments were performed in a Mettler Toledo Thermal Analysis System TA 8000, equipped with a DSC 820 module hooked up to a liquid N_2 cooling device. Purge gas was dry N_2 (80 ml min^{-1}). Melting temperature and enthalpy of fusion calibration were carried out using indium (Mettler) and heptane (HPLC grade, Aldrich). We report glass-transition temperatures as midpoints and first-order phase transition temperatures as peak temperatures. All data are normalized with respect to the mass of PDMS and for β when required.

3. Results

A thermogram of pure PDMS 15k including cooling and heating scans is shown in Fig. 3(a), and the numerical data are presented in Table 1. The cooling curve reveals a small and broad exothermal crystallization peak at −88.9°C and a baseline offset at

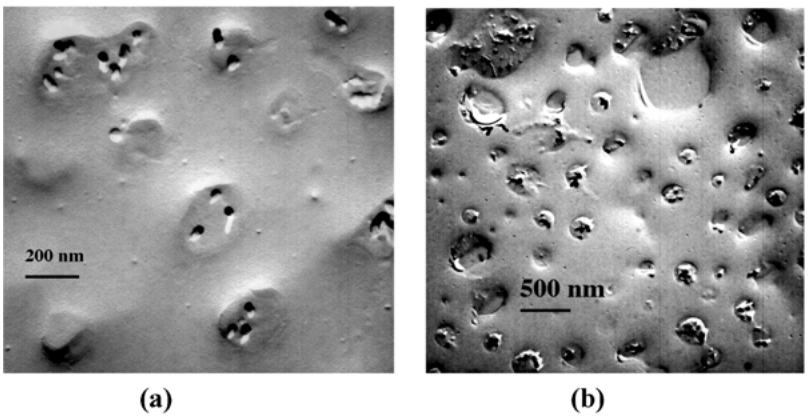

Figure 2. Freeze-fracture TEM micrographs of a sample containing 10 wt% of water-saturated M7D at two different magnifications. (a) M7D particles with an effective size of ∼250 nm constist of aggregates of smaller native particles (∼20 nm). (b) Indication of a random dispersion of M7D particles in PDMS. The measurements were carried out by Prof. Oren Regev and Mr. Klaus Horbaschek in the laboratory of Prof. Heinz Hoffmann at Bayreuth University.

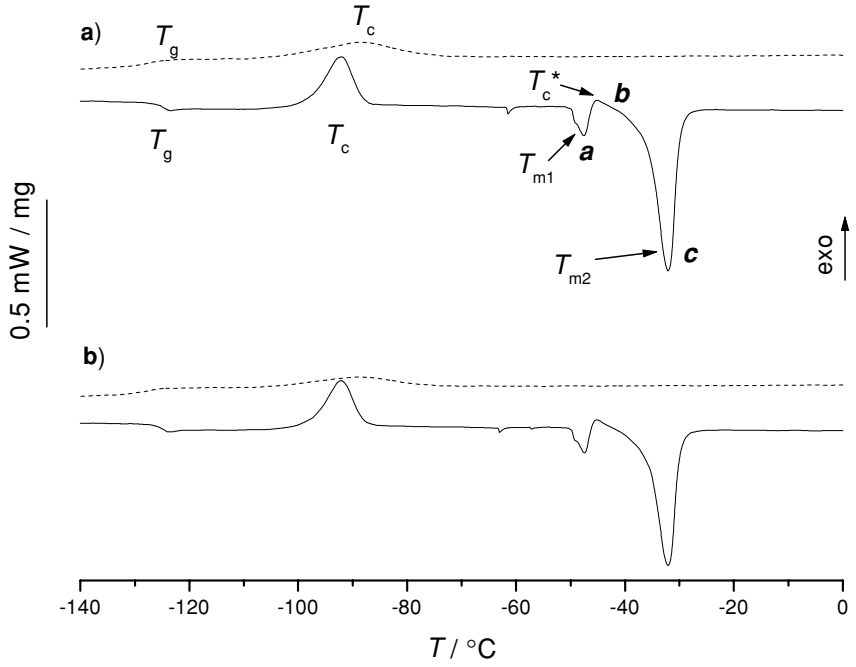

Figure 3. DSC thermogram of pure PDMS 15k. Dashed line is a cooling curve, solid line is a heating curve: (a) first run, (b) subsequent second run. In the cooling curve we observe an exothermal peak T_c and a glass transition at T_g. In the heating curve we observe a glass transition, T_g, an exothermic peak, the so-called cold crystallization, T_c, two melting peaks, T_{m1} (***a***) and T_{m2} (***c***), and a recrystallization exotherm, T_c^* (***b***). Numerical values are given in Table 1.

−125.0°C that is due to a glass transition. In the heating curve we observe, T_g, and a narrow and relatively large exothermic peak, the so-called cold crystallization, T_c, at −92.3°C. At yet higher temperatures we detect two melting peaks, labelled (***a***) and (***c***) in Fig. 3(a) and an additional crystallization exotherm, (***b***), at −45.2°C situated just between the two melting peaks. This is in agreement with previous studies of PDMS [29–33]. At the given cooling rate of $-5\ \mathrm{K\ min^{-1}}$ the crystallization of PDMS is almost completely quenched as indicated by the very small crystallization exotherm observed during the cooling scan and most of the crystallizable

Table 1. Thermal data for non-filled PDMS obtained by DSC at a cooling rate of -5 K min^{-1} and a heating rate of $+5$ K min^{-1}. Data are given for two subsequent runs to show reproducibility.

	1st cooling	2nd cooling
T_c	$-88.9°C$	$-87.8°C$
T_g	$-125.0°C$	$-124.6°C$
	1st heating	2nd heating
T_g	$-128.0°C$	$-128.0°C$
T_c	$-92.3°C$	$-92.2°C$
T_{m1}	$-47.5°C$	$-47.4°C$
T_c*	$-45.2°C$	$-45.3°C$
T_{m2}	$-32.1°C$	$-32.1°C$

material solidifies to form an amorphous glass. In the heating scan a step in the baseline is observed which indicates a glass transition. The now fluid material is in a supercooled state and eventually the viscosity becomes low enough that chains can rearrange to form crystallites. This phenomenon is observed as cold crystallization at T_c. The resulting crystallites melt during a complex melting pattern [34 and references therein]. In Fig. 3(b) we present a subsequent measurement of the very same sample, following the cooling and heating sequence described above. We observe that the second thermogram is almost identical to the first, indicating reproducibility and the absence of memory effects and hysteresis. The thermograms presented in Fig. 3 and the experimental conditions under which the experiments were performed serve as the reference for the investigation of the particle-filled PDMS systems described below.

A thermogram of PDMS filled with 10 wt% non-dried M7D particles is presented in Fig. 4(a) and of PDMS filled with 10% dried M7D particles in Fig. 4(b) (data given in Table 2). The first significant observation in the DSC curves is the appearance of a sharp exotherm in the cooling scan. This feature is attributed to induced crystallization since the subsequent heating scan does not reveal a glass transition nor a cold crystallization peak but exhibits melting endotherms. We may therefore conclude that in this system crystallites form already during the cooling scan. The loss of the glass transition in the heating scan by itself is not a sufficient indication for a high degree of crystallization during the cooling curve: The initial calorimetric value of the step-like T_g feature is rather low and broadening can easily push it down below the detection limit of the calorimeter. The subsequent cold crystallization exotherm (or its absence) is much easier to monitor and evaluate. In addition, the crystallization exotherm is easily detected during the cooling scan. Hence, both cooling and heating scans have to be evaluated in order to obtain a complete thermal picture.

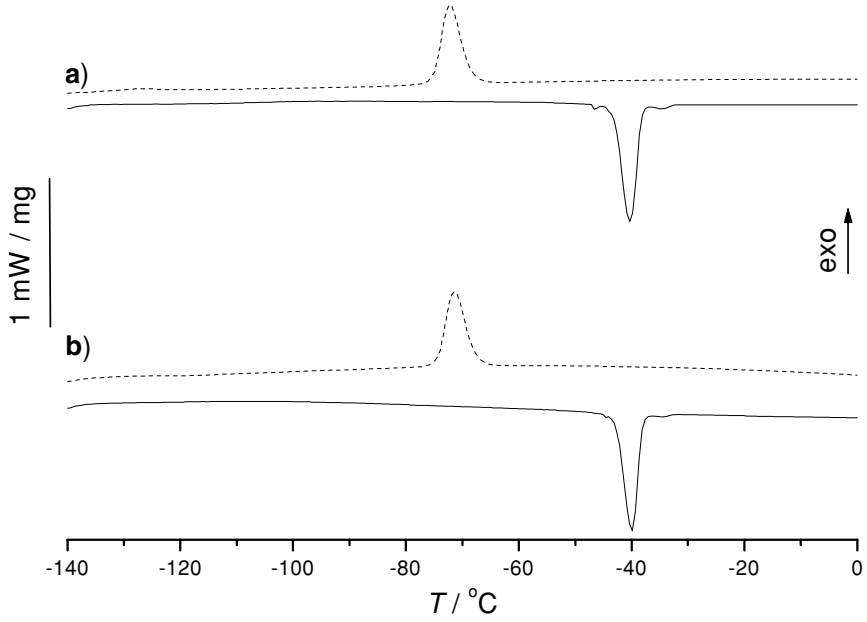

Figure 4. DSC thermograms of PDMS 15k filled with (a) 10 wt% dried M7D silica particles and (b) 10 wt% water-saturated M7D silica particles. Numerical values are specified in Table 2.

Table 2. Thermal data for the filled PDMS systems obtained by DSC at a cooling rate of -5 K min^{-1} and a heating rate of $+5$ K min^{-1}. Data are normalized with respect to the mass of PDMS.

	M7D dried	M7D water-saturated	M7D fluorinated	Hydrophilic CPG	Hydrophobic CPG
T_c	$-72.2°$C	$-71.4°$C	$-75.6°$C	$-72.3°$C	$-72.5°$C
ΔH_c	$+28.7$ J g^{-1}	$+27.5$ J g^{-1}	$+25.6$ J g^{-1}	$+26.6$ J g^{-1}	$+25.6$ J g^{-1}
T_m	$-40.3°$C; $-34.5°$C	$-40.0°$C	$-42.1°$C; $-33.6°$C	$-40.6°$C; $-33.5°$C	$-41.0°$C
ΔH_m	-28.1 J g^{-1}; -0.5 J g^{-1}	-30.0 J g^{-1}	-25.0 J g^{-1}; -2.4 J g^{-1}	-29.2 J g^{-1}; -6.8 J g^{-1}	-28.2 J g^{-1}

To examine the effect of sample preparation on the thermal behavior of the filled systems, a control experiment was performed. Pure PDMS was subjected to the preparation procedure used for the filled systems, without adding filler particles, and DSC curves were measured. No effect was observed when the thermograms of the resulting samples were compared to those of the untreated PDMS.

To test the effect of the cooling rate on the thermal features introduced above, a sequence of DSC experiments in which the cooling rate was varied from $\beta = -2$ K min^{-1} to a fast quench (in liquid nitrogen) was performed. Cooling was followed by a constant heating rate of $\beta = +5$ K min^{-1}. The resulting heating scans are presented in Fig. 5. We observe that crystallization takes place during cooling only at the two lowest cooling rates ($\beta = -2$ K min^{-1} and $\beta = -5$ K min^{-1}, Fig. 5(a) and (b)). Consequently, a loss of T_g and T_c during the heating scan is observed. This indicates that the high degree of crystallization was only achieved during the slow cooling process. The corresponding exotherm can readily be seen in the cooling curve (not given here). For a cooling rate of $\beta = -10$ K min^{-1} (Fig. 5(c)) a small T_g can be monitored and additionally a cold crystallization exotherm is observed in the heating scan. This implies that the crystallization process is partially quenched. For the quasi-infinite cooling rate (Fig. 5(d)) the heating curve resembles that of pure PDMS at intermediate cooling rates, i.e., the crystallization process is

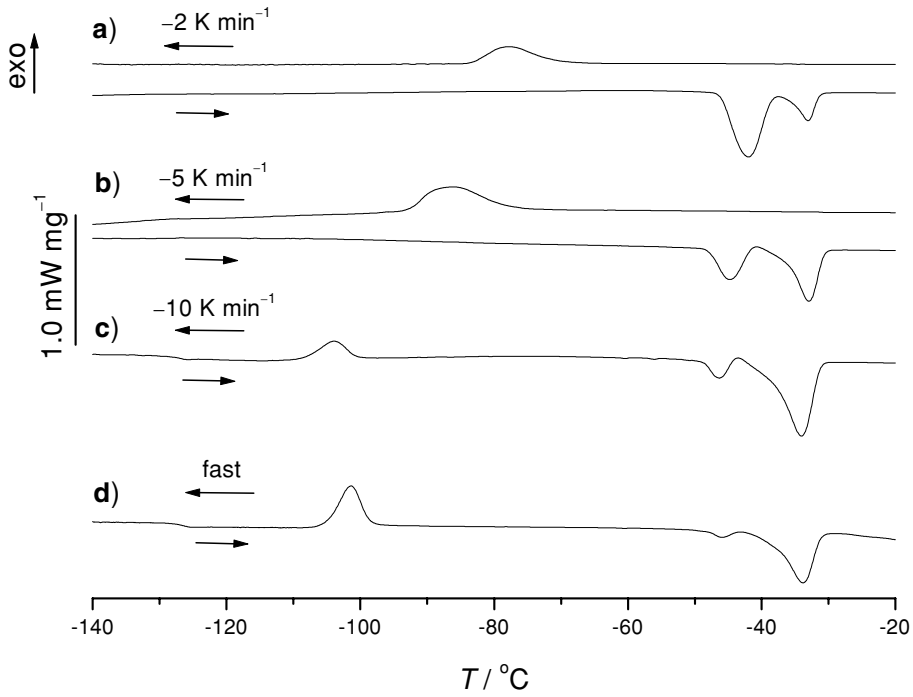

Figure 5. Heating scans of PDMS 16k filled with wt-10% water-saturated M7D silica particles. For the four scans the cooling rate, (a) -2 K min^{-1}, (b) -5 K min^{-1}, (c) -10 K min^{-1}, and (d) quasi-infinite (sample quenched in liquid nitrogen), prior to the heating curve was varied. The heating rate was always $+5$ K min^{-1}.

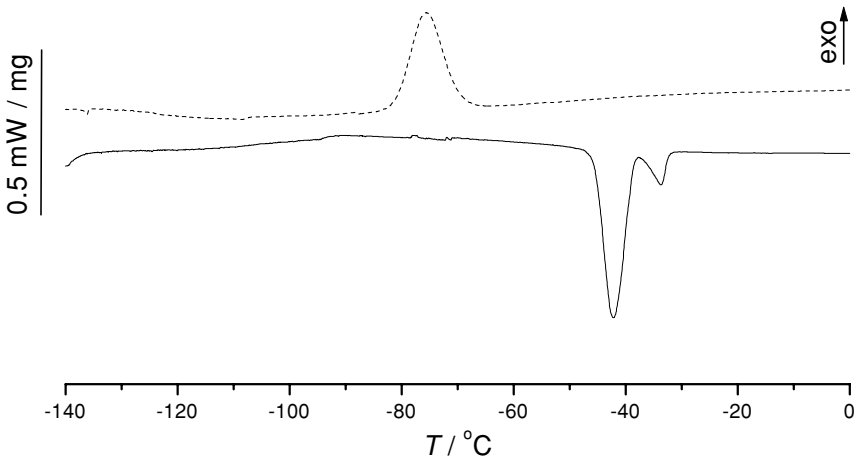

Figure 6. DSC thermogram of PDMS 15k + wt-10% fluorinated M7D silica particles. Numerical values are specified in Table 2.

basically quenched during the cooling cycle. Similar studies were carried out on pure PDMS. In contrast to the filled materials pure PDMS did not exhibit significant crystallization during the cooling cycle down to a cooling rate of $\beta = -2\,\mathrm{K\,min^{-1}}$. We note here that under isothermal conditions crystallization was observed at $T \leq -60^{\circ}$ C.

In Fig. 6 we present DSC thermograms of PDMS filled with fluorinated M7D silica particles. Data is given in Table 2. As previously mentioned, the PDMS melt does not wet the modified surface (contact angle of 45 ± 1). Yet, similar to the behavior presented in Fig. 5, an exothermic peak is found in the cooling curve, suggesting an enhanced tendency towards crystallization in the presence of the fluorinated additives as well. In this system subsequent cooling/heating cycles showed also similar behavior.

The studies described above were extended to the investigation of a different filler system, namely porous glass, CPG. The corresponding thermograms are given in Fig. 7 (and the data in Table 2). Both hydrophilic and hydrophobic CPG affected the crystallization behavior

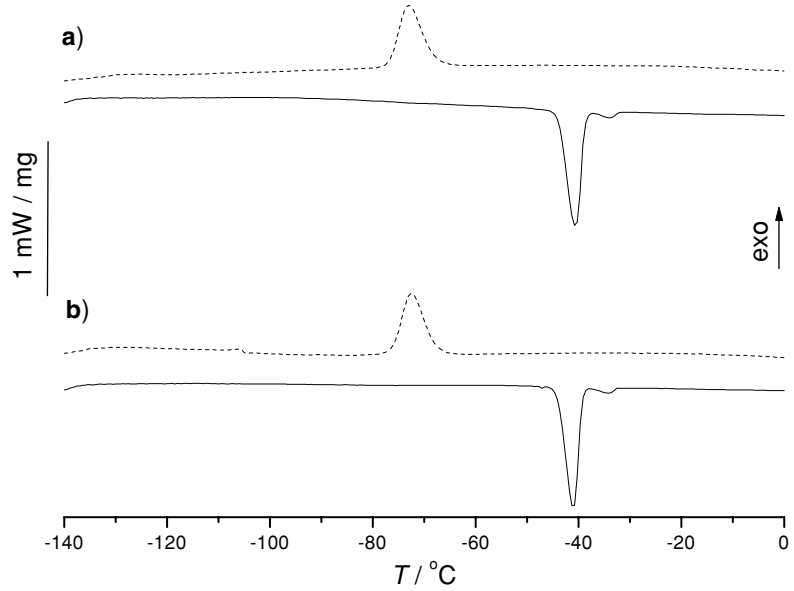

Figure 7. DSC thermograms of PDMS 15k filled with (a) wt-10% hydrophilic CPG and (b) wt-10% hydrophobic CPG. Numerical values are specified in Table 2.

of PDMS in a manner similar to that of the silica particles. In particular, at a given cooling rate the presence of either hydrophilic or hydrohobic CPG resulted in an enhanced crystallization rate, as indicated by the appearance of an exotherm in the cooling curve, and the disappearance of T_g and T_c in the heating curve.

4. Discussion

In this paper we describe an investigation of the effect of surfaces on the thermal behavior of a semicrystalline, practically non-entangled polymer melt. The model system is comprised of a low concentration of sub-micron particles or porous glass (CPG) embedded in the polymer melt. We find that, at a given cooling rate, solid additives regardless of their surface chemistry, enhance the crystallization rate of PDMS as measured in DSC experiments. The effect—within the range of our experiments—does not depend on the nature of the interactions between polymer chains and particle surfaces. In the following we discuss the observations and our interpretations starting from the pure PDMS system.

Thermal behavior of pure PDMS: The observed thermograms of pure PDMS are in agreement with previous observations [29–33]. In particular, the characteristic two-peak melting pattern (Fig. 3), typical of long chain polymers, is observed [34].

The effect of cooling rate: It is known that the cooling rate strongly affects the degree of crystallinity of semicrystalline materials [35, 36]. Crystallization is quenched by a fast cooling rate, leading to the formation of an amorphous glass while a slow cooling process enhances the crystallinity. According to models of polymer crystallization the actual crystallization rate, k_{cryst}, ($X^{-1}\mathrm{d}X/\mathrm{d}t$ where X is the crystal volume fraction), may be estimated by the following considerations: Polymer crystallization is possible within a temperature range bounded by an upper and a lower temperature. To allow for a certain degree of supercooling necessary for crystallization, the upper temperature has to be somewhat lower than the temperature at which the Gibbs free energy favors crystallization. The lower temperature is determined by the viscosity below which chain mobility (e.g., chain diffusion, prealignment, conformational changes) is hindered to the level preventing further chain rearrangements. Complete crystallization occurs in a DSC cooling experiment carried out at a rate, β, only if the crystallization rate fulfills $k_{\text{cryst}} \gg \beta \cdot \Delta T^{-1}$. Here ΔT is the difference between the two critical crystallization temperatures. One may obtain the upper critical crystallization temperature from the onset of the crystallization exotherm and the lower critical temperature from the onset of the cold-crystallization process in a heating-scan performed at the same rate of temperature change. In our case we find a ΔT of 30 K. For the given cooling rate of $\beta = -5\ \mathrm{K\ min^{-1}}$ the material has 6 min to complete the crystallization process. For pure PDMS this cooling rate is apparently too fast. The crystallization rate has been estimated from isothermal experiments and found to be $k_{\text{cryst}} < 0.003\ \mathrm{s^{-1}}$. Our observations indicate that filled PDMS readily crystallizes under these conditions and hence, $k_{\text{cryst}} > 0.003\ \mathrm{s^{-1}}$. PDMS turns out to be a particularly suitable polymer for the investigation of cooling rates via DSC experiments, probably due to its exceptionally high flexibility combined with the low crystallization temperature [37].

Surface effects: Different types of surfaces exhibiting a range of interfacial energies, were investigated. We studied the effect of "attractive surfaces" such as non-coated silica particles (Fig. 4) and hydrophilic CPG (Fig. 7(a)) that are known to adsorb PDMS from the melt, probably due to their silanol surface groups [25]. "Non-attractive" surfaces that are not wetted by and do not adsorb PDMS from the melt, such as the fluorinated silica particles, water-saturated particles, and hydrophobic CPG were investigated as well. The key observation of the present study is that independently of the surface chemistry, the very presence of the surfaces enhances the crystallization rate of PDMS.

The effect of filler particles on the thermal behavior of PDMS was investigated extensively before [22, 39–41]. In some of these studies it was found that filler particles enhanced crystallization, and the results were interpreted as evidence for heterogeneous nucleation. In other studies it was concluded that the presence of solid particles does not affect the crystallization [39], and in others that the degree of crystallinity is reduced [40]. In some of these studies, however, the samples were prepared in a way as to remove non-adsorbed polymers so that only a surface layer of adsorbed polymers was present [41]. In other experiments the samples were quenched into the solid phase, rather than cooled slowly. As was discussed above, and observed in this study (Fig. 5), a fast quench leads to vitrification of the melt and dominates over the tendency of solid additives to induce crystallinity.

Although these phenomena are experimentally particularly easy to address using PDMS samples, we

believe that our observations are not unique to PDMS and should be considered for semicrystalline polymers in general. In the systems studied here, entropic effects obviously predominate. This, however, will not always be the case. Indeed, as was suggested by Cabane and coworkers a highly crystallizable polymer such as polyethylene oxide, PEO, may be affected differently by the presence of additives [42]. Depending on the chemistry involved, the balance of enthalpic and entropic effects may be different for different semicrystalline materials.

The fact that our results are deduced from DSC measurements suggests that the effects are non-local and result in a surface-induced bulk crystallization. In Fig. 2 we presented the TEM image of M7D particles embedded in a PDMS melt. In these samples, the inter-particle distance is of the order of a micron (10 wt% filler content). It is therefore evident that the inter-particle regions constitute a significant fraction of the sample.

Relation to models of crystallization: In the classical models such as that by Lauritzen and Hoffman [14] a description of spherulitic growth rate G (cm s^{-1}) is given by the expression:

$$G = G_0 \exp\left(-\frac{U^*}{R(T - T_0)}\right) \exp\left(-\frac{K_g}{T(T - T_m)}\right)$$

where T is the isothermal crystallization temperature, G_0 takes into account the geometric parameters of both the polymer chain and the crystalline lamella. U^* denotes the free energy of activation that governs the rate of chain segments transport to the growth front, with a temperature dependence similar to that of the viscosity. K_g is a nucleation constant, and $T - T_m$ the degree of under-cooling. In general, for this type of temperature dependence, the rate of crystallization passes through a maximum, as the temperature increases from the glass transition temperature (where U^* becomes infinite) to the vicinity of the melting temperature, where $T - T_m = 0$.

The crystallization rates, as deduced from the DSC measurements presented here, are consistent with the predicted acceleration of the crystallization rate with temperature reduction (in the range between the melting point and the glass-transition temperature), as indicated by the cold crystallization (for example, Fig. 2). At the same time, the accelerated rate of crystallization of the filled materials, as deduced from the DSC measurements, is not consistent with other aspects of the kinetic equation: The filled PDMS is characterized by a significantly higher viscosity than that of the native material. A higher viscosity of the crystallizing material should decrease the mobility, and therefore should have caused a reduction of the crystallization rate, unlike the observations. In addition, we recall that in some of the systems PDMS does not wet the particles, so in the framework of the classical theories of nucleation, we do not expect the particles to serve as efficient centers for epitaxial crystallization, or sites for heterogeneous nucleation.

The role of entropy: The observations may be rationalized by realizing the important role of entropy in polymer-surface interactions. It is known that surfaces act as a strong perturbation to the melt, and may modify the free energy landscape of the system. Two of the specific mechanisms by which entropic interactions act, are enrichment of chain ends at the vicinity of the surface [43], and the enhancement of orientational ordering of polymeric coils due to the presence of a surface [44–48]. Indeed, filler-induced deformation of polymer chains has recently been detected by small-angle neutron scattering (SANS) in polysilicate filled PDMS [49]. When the chain dimensions were approximately the same magnitude as the filler particle diameters, the scattering results showed a decrease in the radius of gyration, R_g for all filler concentrations. For longer chains and low filler concentration an increase in chain dimension was observed, in semi-quantitative agreement with the results of Monte Carlo simulations [50]. In our study, the filler particles are much larger in diameter than the coil dimensions with R_g in the range of 3.5 nm [49]. However, a recent molecular dynamic computer simulation by Starr et al. [47] suggested that in the vicinity of a surface (either attractive or non-attractive) polymer coils become slightly elongated and significantly flattened.

Local ordering at the molecular level as result of the hindered dynamics, was recently observed by solid-state NMR measurements. At temperatures between $T_g + 50$ K and $T_g + 150$ K it was demonstrated that on time scales of a few tens of milliseconds up to the terminal relaxation time, polymer melts that experience other types of constraints such as entanglements [50] exhibit substantial long-lived ordering, which increase in the presence of confinement such as rigid blocks in block copolymers [51].

The experimental and theoretical results described in these studies were concerned with amorphous polymers and are related to the effect of surfaces on the glass-transition temperature. Yet, we believe that

similar effects, of pure entropic nature, are important for crystallization: In line with the experimental observations presented in this work, we suggest that regions of non-random chain conformations on intermediate length scales [52] may play an important role in the early stages of crystallization, even if the orientational ordering of these regions does not match that of the lowest energy crystalline phase. These regions may offer a different pathway for crystallization by allowing the system to bypass kinetic barriers that delay crystallization in a native melt.

Finally, we address the issue of adsorbing surfaces. In this case short range interactions (hydrogen bonding in our system) lead to adsorption of a polymeric monolayer. The solid/melt interface is replaced by a surface coated by a fluffy polymeric layer resulting in entropic repulsion at the interface between the melt and the adsorbed layer. This type of interaction is consistent with the effect of the non-adsorbing surfaces.

5. Summary and Conclusions

To summarize, we found that particles and porous glass with a high surface area and different types of surface interactions accelerate the crystallization rate of non-entangled PDMS melts, as observed in DSC experiments. The effect does not depend on the specific type of interfacial interaction between the additives and the polymer, but is rather affected by the presence of a surface. We suggest that the origins of the effect are entropic, i.e. the conformational space of the chains is modified by the presence of the surface. The mechanism how this change affects crystallization and in particular the role of chain ends and/or the distortion of the chain dimensions in boundary layers remains to be clarified in the future.

Acknowledgments

We would like to thank Profs. J. Baschnagel, G. Strobl, B. Cabane, and I. Szleifer for illuminating discussions, and Prof. Y. Cohen for his remarks. We also thank Mettler Toledo, and especially Dr. R. Riesen for discussing instrumental aspects with us. We would like to express our gratitude to T. Wagner for synthesizing the PDMS 16K. TD acknowledges a fellowship from the MINERVA foundation. This work was funded through the Infrastructure Research Program of the Israel Ministry of Science and Culture (grant no. 8625), and the United States-Israel Binational Science Foundation (BSF 2000124).

Notes

1. This idea is utilized in industrial processing of polymers such poly (ethylene terephthalate) PET, poly (vinyldene fluoride) (PVDF), and Nylon. During the fiber spinning process crystalline fibers are formed by extrusion of the melt through a set of small circular dies, drawing and fast cooling. The pre-ordered melt forms upon cooling highly crystalline materials.
2. We note that the M_e for PDMS as determined from dynamic mechanical analysis is usually reported to be in the range between 11,300 and 16,600 g mol^{-1} depending on the evaluation details. Since quite a few entanglements per chain are required to yield an observable entanglement effect, the PDMS 16k can be regarded as non-entangled material [38].

References

1. Y. Cohen and S. Reich, Journal of Polymer Science **19**, 599 (1981).
2. N.K. Dutta, N.R. Choudhury, B. Haidar, A. Vidal, J.B. Donnet, L. Delmotte, and J.M. Chezeau, Polymer **35**, 4293 (1994).
3. K.U. Kirst, F. Kremer, and V.M. Litvinov, Macromolecules **26**, 975 (1993).
4. X. Zheng et al., Phys. Rev. Lett. **74**, 407 (1995).
5. V. Arrighi, J.S. Higgins, A.N. Burgess, and G. Floudas, Polymer **39**, 6369 (1998).
6. E.K. Lin, R. Kolb, S.K Satija, and W.L. Wu, Macromolecules **32**, 3753 (1999).
7. V.J. Novotny, J. Chem. Phys. **92**, 3189 (1990).
8. J.L. Keddie, R.A.L. Jones, and R.A. Cory, Europhys. Lett. **27**, 59 (1994).
9. J.L. Keddie, R.A.L. Jones, and R.A. Cory, Faraday Discuss. **98**, 219 (1994).
10. G. Tsagaropoulos and A. Eisenberg, Macromolecules **28**, 6067 (1995).
11. J.A. Forrest, K. Dalnoki-Veress, J.R. Stevens, and J.R. Dutcher, Phys. Rev. Lett. **77**, 2002 (1996).
12. G. Strobl, *The Physics of Polymers*, 2nd ed. (Springer-Verlag, Berlin, 1997).
13. J. Jancar (ed.), Structure-Property Relationships in Thermoplastic Matrices, Adv. Polym. Sci. **139**, 1 (1999).
14. J.D. Hoffman, G.T. Davis, and J.I. Lauritzen, in *Treatise on Solid State Chemistry*, Vol. 3, edited by N.B. Hannay (Plenum Press, 1976), p. 497.
15. L. Mandelkern, in *Crystallization of Polymers* (McGraw Hill, New York, 1994).
16. B. Wunderlich, in *Crystal Nucleation, Growth, Annealing*, Macromolecular Physics, Vol. 2 (Academic Press, New York, 1976).
17. J.D. Hoffman, R.L. Miller, H. Marand, and D.B. Roitman, Macromolecules **25**, 2221 (1992).
18. D.M. Sadler, Nature **326**, 174 (1987).
19. B. Heck, T. Hugel, M. Iijima, and G. Strobl, Polymer **41**, 8839 (2000).
20. G. Strobl, Eur. Phys. J. **E 3**, 165 (2000).

21. K. Zahn, R. Lenke, and G. Maret, Phys. Rev. Lett. **82**, 2721 (1999).
22. E.B. Sirota, Langmuir **14**, 3133 (1998).
23. M.I. Aranguren, Polymer **39**, 4897 (1998).
24. T. Dollase, H.W. Spiess, M. Gottlieb, and R. Yerushalmi-Rozen, Europhysics Letters **60**(3), 390 (2002).
25. W. Haller, J. Am. Ceram. Soc. **57**, 120 (1974).
26. R.K. Iler, *The Chemistry of Silica* (Wiley, New York, 1979).
27. W.W. Wendlandt and P.K. Gallagher, *Thermal Characterization of Polymeric Materials*, edited by E.A. Turi, 2nd ed. (Academic Press, San Diego, 1997).
28. V.B.F. Mathod (ed.), *Calorimetry and Thermal Analysis of Polymers* (C. Hanser, Munich, 1994).
29. A. Yim and L.E.St. Pierre, J. Polym. Sci. Polym. Lett. **8**, 241 (1970).
30. B. Ke, J. Polym. Sci. Polym. Lett. **1**, 167 (1963).
31. C.L. Lee, O.K. Johannson, O.L. Flaningam, and P. Hahn, ACS Polym. Prepr. **10**, 1313 (1969).
32. J.D. Helmer and K.E. Polmanteer, J. Appl. Polym. Sci. **13**, 2113 (1969).
33. J.S. Clarson, K. Dodgson, and J.A. Semlyen, Polymer **26**, 930 (1985).
34. S.L. Liu, T.S. Chung, H. Oikawa, and A. Yamaguchi, Journal of Polymer Science: Part B: Polymer Physics, **38**, 3018 (2000).
35. R. Androsch and B. Wunderlich, Macromolecules **33**, 9076 (2000).
36. K. Armistead and G. Goldbeck-Wood, Adv. Polym. Sci. **100**, 219 (1992).
37. P.C. Hiemenz, *Polymer Chemistry* (Marcel Dekker Inc., New York and Basel, 1984).
38. J.D. Ferry, *Viscoelastic Properties of Polymers*, 3rd ed. (Wiley, New York, 1980).
39. J.E. Mark, J.M. Zeigler, and F.W.G. Fearon (eds.), *Silicon-based Polymer Science* (ACS, Washington, 1990).
40. A. Voeit, J. Polym. Sci. Macromol. Rev. **15**, 327 (1980).
41. Y.S. Lipatov and F.G. Fabulyak, Vysokomol. Soyed A **10**, 1605 (1968).
42. R.H. Ebengou and J.P. Cohen-Addad, Polymer **35**, 14 (1994).
43. B. Cabane, private communication.
44. D.T. Wu, G.H. Fredrickson, J.P. Carton, A. Ajdari, and L. Leibler, J Polymer Science: Part B: Polymer Physics **33**, 2373 (1995).
45. J.H. van Vliet and G. ten Brinke, J. Chem. Phys. **93**, 1436 (1990).
46. J. Baschnagel and K. Binder, Macromolecules **28**, 6808 (1995).
47. K. Binder, A. Milchev, and J. Baschnagel, Annu. Rev. Mat. Sci. **26**, 107 (1996).
48. F.W. Starr, T.B. Schroder, and S.C. Glotzer, Phys. Rev. E. **64**, (2001).
49. M.A. Sharaf and J.E. Mark, Polymer **43**, 643 (2002).
50. A.I. Nakatami, W. Chen, R.G. Schmidt, G.V. Gordon, and C.C. Han, Polymer **42**, 3713 (2001).
51. R. Graf, A. Heuer, and H.W. Spiess, Phys. Rev. Lett. **80**, 5738 (1998).
52. T. Dollase, R. Graf, A. Heuer, and H.W. Spiess, Macromolecules **34**, 298 (2001).

J|A|C|S
ARTICLES
Published on Web 00/00/0000

Selective Dispersion of Single-Walled Carbon Nanotubes in the Presence of Polymers: the Role of Molecular and Colloidal Length Scales

Rina Shvartzman-Cohen,[†] Einat Nativ-Roth,[†] Ezhil Baskaran,[‡] Yael Levi-Kalisman,[§] Igal Szleifer,*[,‡] and Rachel Yerushalmi-Rozen*[,†,§]

Contribution from the Department of Chemical Engineering, Ben Gurion University in the Negev, 84105 Beer Sheva, Israel; Department of Chemistry, Purdue University, 560 Oval Drive, West Lafayette, Indiana 47907; The Ilse Katz Center for Meso- and Nanoscale Science and Technology, Ben Gurion University in the Negev, 84105 Beer Sheva, Israel

Received June 19, 2004; E-mail: rachely@bgumail.bgu.ac.il; igal@purdue.edu

Abstract: Dimensionality is known to play a key role in the solution behavior of nano- and mesoparticles. In particular, the shape and the range of the attractive van der Waals interparticle potential are determined by the number of microscopic versus mesoscopic dimensions. For single-walled nanotubes (SWNTs), where two of the dimensions are nanoscopic and one is mesoscopic, the intertube attraction is relatively short ranged, albeit very steep. The very large attraction (compared to the thermal energy, K_bT) among long SWNTs leads to aggregation at different levels and constitutes a major barrier for manipulation and utilization of SWNTs. This study demonstrates that it is possible to shape the intertube potential by decorating SWNTs with end-tethered polymers. In good solvent conditions for the polymers, entropic repulsion among the tethered chains generates a free energy barrier that prevents SWNTs from approaching the attractive part of the intertube potential. Consequentially, stable dispersions of individual, well separated SWNTs can be prepared. Investigation of different chain lengths and tethering densities of the polymers as well as the interparticle potentials for nanometric versus mesoscopic particles suggests that polymer-induced steric stabilization provides a generic method for separation of SWNTs from mixtures of colloidal species, as demonstrated experimentally.

Introduction

Stabilization of colloidal dispersions is an old technological problem first attempted in ancient China and Egypt[1] where a natural polysaccharide, Gum Arabic (GA), was used in the preparation of carbon-black ink. Indeed, ink is an example for a typical colloidal system where solid spherical particles are dispersed in a liquid via the adsorption of a polymer. Such dispersions are considered to be stable as long as the individual particles do not aggregate or coagulate, and the approach is known as *steric stabilization.*[2] While the utilization of polymers for stabilization of colloidal dispersions is a few thousands years old, thorough understanding of polymer−colloid interactions has emerged only over the last 30 years or so. An even younger field is that of interactions among polymers and pseudo-one-dimensional nanocolloids, known as single-walled carbon nanotubes (SWNTs).[3] Over the past few years polymers have been utilized for noncovalent dispersing of SWNTs in different media. Yet, an understanding of SWNT−polymers interactions is only beginning to emerge. In the following we present the relevant terms, suggest a model that accounts for the generic nature of polymer−SWNT interactions, predict that the interactions may lead to dimensional selectivity that may be utilized for purification of SWNT, and demonstrate the concept.

Background. A key term in colloidal interactions is the interparticle potential.[4] For noncharged, spherical particles of radii a, it is common to assume that the van der Waals (vdW) interactions are nonretarded[4] and additive. The resulting vdW potential between the particles, $V(r)$, where r is the interparticle distance is described by $V(r) = -A_{\text{eff}}/12a/r$ for $r \ll a$, $V(r) \propto A_{\text{eff}}a/r^6$ for $r \gg a$ and a more complicated expression in the intermediate range.[5] For all separations, r, the interparticle potential is proportional to the particle size, a. The other proportionality constant is A_{ij}, the effective Hamaker constant which depends on the nature of the particles and the intervening liquid.[6] For typical particles, with a radius in the order of a few hundred nanometers, the attractive interaction exceeds the thermal energy at separations larger than the particle radius.

[†] Department of Chemical Engineering, Ben Gurion University in the Negev.
[‡] Purdue University.
[§] The *Ilse Katz* Center for Meso- and Nanoscale Science and Technology, Ben Gurion University in the Negev.

(1) *Encyclopedia Britannica* 257−259; William Benton: Chicago, 1966.
(2) Napper, D. H., Ed.; *Polymeric Stabilization of Colloidal Dispersions;* Academic Press, Inc.: Orlando, FL, 1993.
(3) Dresselhaus, M. S.; Dresselhaus, G.; Avouris, Ph., Eds. *Carbon Nanotubes, Topics in Applied Physics* 80; Springer-Verlag: Berlin, Heidelberg, 2001.
(4) Israelachvili, J., Ed. *Intermolecular and Surface Forces*; Academic Press Inc.: San Diego, 1992.
(5) The nonretarded vdW interaction free energy (W) between two mesoscopic cylinders is $W = AL/12\sqrt{2}D^{3/2}(R_1R_2/R_1 + R_2)^{1/2}$ where A is the Hamaker constant, L, the cylinder length, D, the intercylinder distance, and R_1, R_2 the radius of each of the cylinders. Chapter 11, ref 4.

Thus, long term stability (of either kinetic or thermodynamic origin) can only be imparted by the prevalence of a repulsion of sufficient range and magnitude, such as the long ranged osmotic (steric) repulsion among tethered polymers in good solvent conditions. Among the more efficient steric stabilizers are block-copolymers.[7] Block copolymers are comprised of covalently bonded chemically distinct and often mutually incompatible moieties (designated A−B and A−B−A for diblocks and triblocks, respectively). A typical scenario for steric stabilization via block copolymers relies on the dual action of the polymer due to a selective interaction with the solvent: while one of the blocks (A) anchors the chain to the surface, the other block (B) dangles into the solvent and repels other polymers. It is well-known that with this type of anchoring the density and the molecular weight of the tethered chains dominate the details of the modified interparticle potential.[8,9]

In addition, the properties of colloidal dispersions are affected by the size, shape, and dimensions of the dispersed particles, as these parameters strongly modify the interparticle potential. When dealing with nonspherical particles, such as platelike clays or submicron rods, it is common to assume that their qualitative behavior is well represented in terms of an equivalent sphere, or to account for the geometry.[2] However, these assumptions should be examined carefully when two of the dimensions are nanometric, as is the case for SWNTs.

SWNTs are crystalline graphitic rods, characterized by a diameter in the range 1−2 nm and a typical length of microns[10] resulting in an aspect ratio larger than 1000. Pristine SWNT form vdW crystals, known as "ropes" or "bundles" of typically 100−500 tubes.[3] Bundling was found to act as an obstacle to most applications and results in diminished mechanical and electrical properties as compared to theoretical predictions related to individual SWNT.[11]

A large effort has been invested during the past decade in the development of approaches for dispersing individual SWNT in aqueous and organic media.[12−16] A variety of methods were designed to induce short ranged repulsion among the tubes: these include covalent modifications,[12,13] $\pi-\pi$ interactions,[14,15] surfactant adsorption,[16] and more.[17] Consequentially these treatments were often found to result in modification of the structural, electronic, and mechanical properties of the tubes[18−20]

Due to the shortcomings of these approaches, noncovalent methods mainly based on physical adsorption of polymers were developed. [21−23] While quite a few examples were reported, the underlying mechanism in each of these studies was believed to rely on specific interactions between a given polymer and the SWNTs. For example, it was suggested that tight SWNT−polymer association (known as "wrapping") leads to screening of the hydrophobic interaction in aqueous solutions and consequential dispersion of tubes.[21]

Recently, we presented a generic approach for stabilization of SWNT dispersions in aqueous and organic liquids, using synthetic and natural block copolymers.[24,25] We showed that a large variety of di- and triblock copolymers in selective solvent (aqueous as well as organic) conditions are efficient stabilizers. Following a temporary exfoliation and deagglomeration of SWNT (for example, via gentle sonication)[26] adsorption of block copolymers prevents reaggregation. This observation is somewhat surprising, as the adhesion energy at the minimum of the intertube potential is known to exceed a few thousands of K_bT[27] by far prevailing entropic (steric) repulsion among polymeric chains.

Here we investigate the origins of the observed behavior by determining the intertube potential for SWNTs decorated by end-tethered polymers. For the attractive part we use the intertube potential calculated by Girifalco et. al..[27] For the repulsive part we generalize a molecular theory that explicitly accounts for the conformational degrees of freedom of the polymer chains.[28,29] The results suggest that, due to the steepness and short-ranged nature of the potential, a relatively weak repulsion, such as the osmotic repulsion among tails of tethered copolymers in a good solvent for the tail chains, can stabilize the dispersed SWNTs and prevent SWNTs from approaching the attractive minimum.

Following the theoretical calculations we suggest that polymer−colloid interactions are sensitive to the dimensions of the dispersed particles and the length of the polymeric chains. We demonstrate (experimentally) that polymers, which disperse SWNT, may not disperse fullerens, carbon fibers, and graphite flakes and that this inherent selectivity can be used for purification of SWNT−particle mixtures.

Experimental Section

Materials: Raw SWNTs from three different sources were used in this study. SWNTAP was purchased from Carbolex Inc. USA (SWNTAP http://carbolex.com), SWNTRW was purchased from

(6) Note that the effective Hamaker constant $A_{ij} = \pi^2\alpha_{ij}n_in_j$, where α_{ji} is the effective polarizability, $\alpha_{ij} = (\alpha_{ii}\alpha_{jj})^{1/2}$, and n_i and n_j are the number density of species i and j correspondingly. $A_{eff} = A_{LS} - A_{LL}$, where L represents the liquid, and S, the solid colloidal particles.

(7) Hadjichristidis, N.; Pispas, S.; Floudas, G. *Block Copolymers: Synthetic Strategies, Physical Properties, and Applications*; John Wiley & Sons: Europe, 2003.
(8) Taunton, H. J.; Toprakciaglu, C.; Fetters, L. J; Klein, J. *Macromolecules* **1990**, *23*, 571.
(9) Halperin, A.; Tirrell, M.; Lodge, T. P. *Adv. Polym. Sci*. **1999**, *100*, 39.
(10) Recently SWNTs of a few centimeters were reported: Zhu, H. W.; Xu, C. L.; Wu, D. H.; Wei, B. Q.; Vajtai, R.; Ajayan, P. M. *Science* **2002**, *296*, 884−886.
(11) Baughman, R. H.; Zakhidov, A. A.; de Heer, W. A. *Science* **2002**, *297*, 787.
(12) Chen, J.; Hamon, M. A.; Hu, H; Chen, Y.; Rao, A. M.; Eklund, P. C.; Haddon, R. C. *Science* **1998**, *282*, 95−98.
(13) Ausman, K. D.; Piner, R.; Lourie, O.; Ruoff, R. S.; Korobov, M. *J. Phys. Chem. B* **2000**, *104*, 8911−8915.
(14) Coleman, J. N.; Dalton, A. B.; Curran, S.; Rubio, A.; Barklie, R. C.; Blau, W. J. *Adv. Mater*. **2000**, *12*, 213−216.
(15) Shin, M.; Wong, N.; Shi Kam, Chen, R. J.; Li, Y.; Dai, H. *Nano Lett.* **2000**, *2*, 285−288.
(16) Vigolo, B.; Penicaud, A.; Coulon, C.; Sauder, R.; Pailler, C.; Journet, P.; Bernier, P.; Poulin, P. *Science* **2000**, *290*, 1331−1334.
(17) Zheng, M.; Jagota, A.; Strano, M. S.; Santos, A. P.; Barone, P.; Chou, S. G.; Diner, B. A.; Dresselhaus, M. S.; McLean, R. C.; Onoa, G. B.; Samsonidze, G. G.; Semke, E. D.; Usrey, M.; Walls, D. J. *Science* **2003**, *302*, 1545−48.
(18) Monthioux, M.; Smith, B. W.; Claye, A.; Fischer, J. E.; Luzzi, D. E. *Carbon* **2001**, *39*, 1251.
(19) Garg, A.; Sinnott, S. B. *Chem. Phys. Lett*. **1998**, *295*, 273−278.
(20) Chen, J.; Liu, H.; Weimer, W. A.; Halls, M. D.; Waldeck, D. H.; Walker, G. C. *J. Am. Chem. Soc*. **2002**, *124*, 9034.
(21) O'Connell, M. J.; Boul, P. J.; Ericson, L. M.; Huffman, C.; Wang, Y. H.; Haroz, E. H.; Kuper, C.; Tour, J.; Ausman, K. D.; Smalley, R. E. *Chem. Phys. Lett.* **2001**, *342*, 265−271.
(22) Chen, J.; Liu, H.; Weimer, W. A.; Halls, M. D.; Waldeck, D. H.; Walker, G. C. *J. Am. Chem. Soc*. **2002**, *124*, 9034.
(23) Star, A.; Steuerman, D. W.; Heath, J. R.; Stoddart, J. F. *Angew. Chem., Int. Ed.* **2002**, *41*, 2508.
(24) Shvartzman-Cohen, R.; Nativ-Roth, E.; Levi-Kalisman, Y.; Yrushalmi-Rozen, R. *Langmuir* **2004**, *20*, 6085−6088.
(25) Bandyopadhyaya, R.; Nativ-Roth, E.; Regev, O.; Yerushalmi- Rozen, R. *Nano Lett.* **2002**, *2*, 25−28.
(26) Strano, M. S.; Moore, V. C.; Miller, M. K.; Allen, M. J.; Haroz, E. H.; Kittrell, C.; Huage, R. H.; Smalley R. E. *J. Nanosci. Nanotechnol*. **2003**, *3*, 81−85.
(27) Girifalco, L. A.; Hodak, M.; Lee, R. S. *Phys. Rev. B* **2000**, *62*, 13104−13110.
(28) Szleifer I.; Carignano, M. A. *Adv. Chem. Phys*. **1996**, *94*, 165−260.
(29) Szleifer I.; Carignano, M. A. *Macromol. Rapid Commun.* **2000**, *21*, 423−448.

Nanoledge France (SWNTRW,www.nanoledge.com), and SWNTK1M was purchased from NanoCarbLab (MedChemLabs division) Russia (www.nanocarblab.com).

The samples contain 40−80 wt % SWNTs, with a typical diameter of 1.3−1.4 nm and length of hundreds of nanometers to tenths of microns. Reported impurities consist of graphite, metal catalyst, and amorphous carbon. The sample designated SWNTK1M was treated by the manufacturer: temperature treatments in air flow were used to remove amorphous carbon and graphite, and acid treatments were used to remove metal particles.

Carbon fibers (Pyrograf III grade PR-24-PS (D 364) prepared via chemical vapor deposition are 30−100 μm long, with a diameter of 60−150 nm and surface area of 50−60 m^2/g, and fullerenes (Buckminsterfullerene 99.5%, Aldrich 37, 964-6, typical diameter 15 nm) were used as received.

Gum Arabic (Aldrich, Acacia 26,077-0) is a highly branched arabinogalactan polysaccharide. Millipore water (resistance of 18.2 MΩ cm) was used. Pluronic triblock: B−A−B triblock copolymer (poly(ethylene oxide)$_{100}$−*b*-poly(propylene oxide)$_{65}$−*b*-poly(ethylene oxide)$_{100}$, PEO−PPO−PEO, F127, of molecular weight 12 600 g/mol were used. The sample was obtained as a gift from BASF AG Germany. A−B diblock copolymer, poly(styrene-b−*tert*-butyl acrylate), PS−*t*buAC, Mn polystyrene 1900 acrylate 31 900 M_w/M_n 1.49, was purchased from Polymer Source Canada (Polymer source, Canada).

Methods. Preparation: Dispersions were prepared by dissolving a polymer in a solvent(aqueous or organic) to form solutions of desired concentrations. As-prepared powder (of SWNTs, carbon fibers of fullerenes) was sonicated at very mild conditions (50 W, 43 kHz) for 15−20 min in the polymeric solution. Centrifugation (3600 rpm, 30 min, room temperature) of the sample was followed by decantation of the supernatant from above the precipitate.

SEM Analysis: Dispersions of SWNTs in GA (both the supernatant and precipitate) were air-dried. The dried materials, as well as the as-received SWNT powders, were ground in a mortar (each one separately), and the powder was fixed to an aluminum stub using double-sided carbon tape and sputter-coated with 1.2 nm thick chromium using an Emitech k575x sputter machine. The samples were examined with an FEI FEG ESEM XL30.

Energy dispersive spectrometry (EDS) analysis: Dried samples (prepared as described above) were sputter-coated with gold and examined by FEI Quanta 200 SEM equipped with a Si/Li detector at 25 kV.

Transmission electron microscopy (TEM) analysis: The dispersed SWNTs were characterized via direct imaging of the aqueous dispersions using cryo-TEM.[30] Dried polymer-coated powders were imaged by TEM.

Samples for TEM imaging were prepared by placing a droplet of the dispersion on a lacey TEM grid (300 mesh Cu: Ted Pella) and allowing the water to evaporate. Imaging was carried out using JEOL 2010 (equipped with Gatan 794 CCD camera) operated at 200 kV.

Samples for cryo-TEM were prepared by placing a droplet on a grid, followed by blotting the excess liquid. Then, the specimen was vitrified by a rapid plunging into liquid ethane precooled with liquid nitrogen, in a controlled environment vitrification system. The vitrified samples were transferred to a cryospecimen holder (Gatan model 626) and examined at −178 °C in low-dose mode. Imaging was carried out using FEI Tecnai 12 G^2 (equipped with Gatan 794 CCD camera) operated at 120 kV.

Theoretical Approach

In this study we apply an extension of the single-chain mean-field theory to study theoretically the role of the polymers in stabilizing dispersions of individual SWNTs and colloidal particles. The predictions from this theory, for the structure and thermodynamic properties of polymers end-tethered to planar, spherical, and cylindrical geometries, have been shown to be in excellent quantitative agreement as compared to experimental observations[31,32] and full-scale computer simulations.[33]

In this approach each polymer molecule is considered in an exact way (within the chosen molecular model), while the intermolecular interactions are considered within a mean-field approximation. Thus, for each polymer conformation the intramolecular and polymer−SWNT interaction are exactly accounted for. The mean-field interactions are determined by the average properties of the polymer chain, in a self-consistent manner. The theory is explained in detail in refs 28 and 29, yet we stress here that we explicitly consider the inhomogeneities of the system in two dimensions and, thus, can calculate SWNT−SWNT interactions and the molecular organization and deformation of the tethered polymers as a function of the distance between SWNTs with the appropriate geometric description.

In Figure 1 we describe the system: it consists of two parallel, infinite SWNTs, of diameter 1 nm each, that are at a distance D from each other. Each SWNT is decorated by N_l end-tethered chains, e.g., poly(ethylene oxide) (PEO). We assume here that chain tethering is irreversible (either due to chemical end-grafting or due to strong adsorption of one of the blocks). The number of polymer chains per unit length is σ_{li}, with $i = 1$ and 2 for nanotube 1 and 2, respectively. The two SWNTs are embedded in a low molecular solvent, e.g., water, of molecular volume ν_w, a good solvent (athermal) environment for PEO. Note the overcrowding of polymers in the intertube region.

This system is geometrically inhomogeneous in the x,y plane. Thus, we write the Helmholtz free energy density, per unit length of nanotube, of the model polymer−solvent−nanotubes system, when the distance between nanotubes is D, by

$$\frac{\beta F(D)}{L} = \sigma_{l1}\sum_{\alpha_1} P(\alpha_1;D)\ln P(\alpha_1;D) + \sigma_{l2}\sum_{\alpha_2} P(\alpha_2;D)\ln P(\alpha_2;D) + \int\int \phi_s(x,y)\ln \phi_s(x,y)\,dx\,dy \quad (1)$$

where $P(\alpha_i;D)$ represents the probability to find a polymer grafted on nanotube i in conformation α_i, when there is another nanotube at distance D. $\phi_s(x,y)$ is the volume fraction of solvent at x,y. The first two terms in the free energy expression represent the conformational entropy of the polymer chains, and the last term is the translational (mixing) entropy of the solvent molecules. There are no attractive interactions because we assume that the solvent is good. Furthermore, the repulsive interactions are separated into intramolecular, polymer−SWNT, and intermolecular. The intramolecular and polymer−SWNT contributions are calculated exactly. The set of conformations considered, α_i, only includes self-avoiding chains that are tethered to the surface of the tube and do not have any segment in the inner region of the SWNT. The intermolecular (hard-core) repulsions are included through local packing constraints,

(30) Talmon, Y. In *Cryo techniques in biological electron microscopy*; Steinbrecht, R. A., Zierold, K., Eds.; Springer-Verlag: Berlin, 1987.

(31) (a) Szleifer, I. *Curr. Opin. Colloid. Interface Sci.* **1996**, *1*, 416−423. (b) Faure, M. C.; Bassereau, P.; Carignano, M. A.; Szleifer, I.; Gallot, Y.; Andelman, D. *Eur. Phys. J. B* **1998**, *3*, 365−375.

(32) Carignano M. A.; Szleifer, I. *Macromolecules* **1995**, *28*, 3197−3204.

(33) Carignano M. A.; Szleifer, I. *J. Chem. Phys.* **1995**, *102*, 8662−8669.

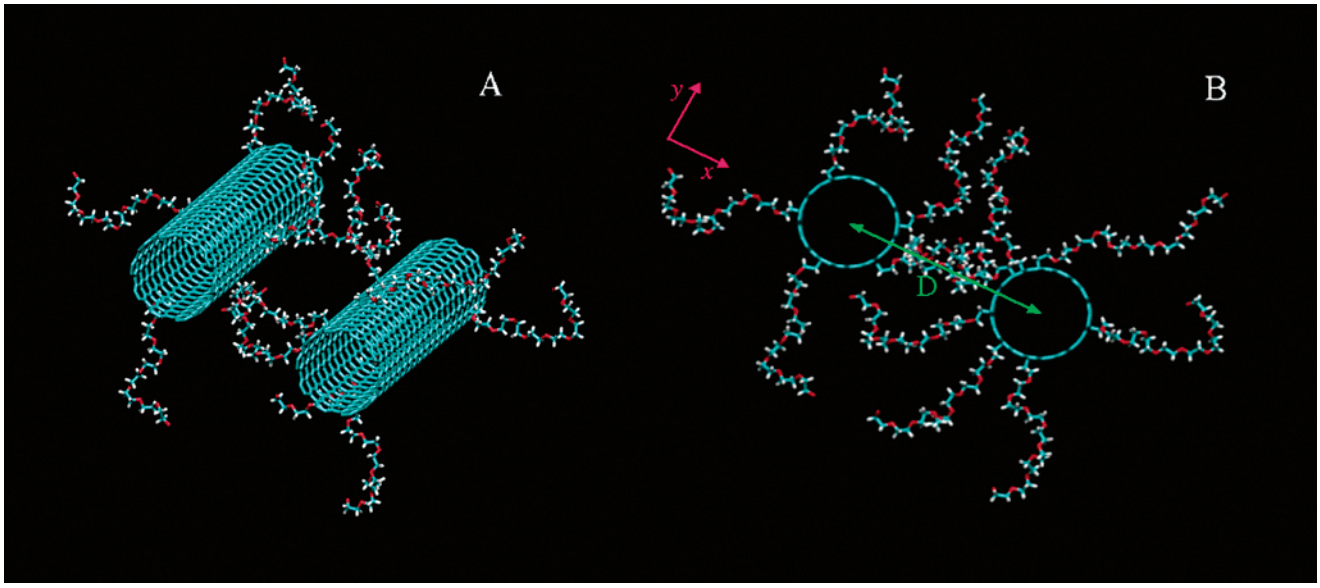

Figure 1. Different views of PEO decorated SWNTs, in good solvent conditions for the PEO chains. (A) A three-dimensional perspective and (B) a projection in the plane perpendicular to the nanotubes' axes. The coordinate system used is that used in the theoretical description, and D is the distance between the SWNT centers.

i.e., incompressibility. Namely, at each region defined between x, $x + dx$ and y, $y + dy$, the volume available is occupied by polymer segments or by solvent molecules

$$\langle\phi_p(x,y)\rangle + \phi_s(x,y) = 1 \qquad (2)$$

for all space but the region inside the nanotubes. The polymer volume fraction contains the sum of contributions from the polymers tethered to SWNT 1 and 2 and is explicitly given by

$$\langle\phi_p(x,y)\rangle = \sigma_{l1}\sum_{\alpha_1} P(\alpha_1;D)\ \upsilon_1(x,y;\alpha_1) + \sigma_{l2}\sum_{\alpha_2} P(\alpha_2;D)\ \upsilon_2(x,y;\alpha_2) \qquad (3)$$

where the first (second) term corresponds to the average volume fraction of the polymers tethered to SWNT 1 (2). $\upsilon_i(x,y;\alpha_i)\,dx\,dy$ is the volume that a polymer molecule in conformation α_i tethered to nanotube i occupies in the region x,y.

The next step is to find the probability of the polymer conformations and the solvent density profile. To this end we minimized the free energy, eq 1, subject to the packing constraints, eq 2 with the use of eq 3. The minimization is carried out with the help of Lagrange multipliers, $\beta\pi(x,y)$, to yield

$$P(\alpha_i;D) = \frac{1}{q_i(D)}\exp[-\beta\int\int\pi(x,y)\upsilon_i(x,y;\alpha_i)\,dx\,dy] \qquad (4)$$

for the probability of chain i in conformation α_i, with $q_i(D)$ being the partition function that ensures the normalization of the probability at each distance D.

The solvent density profile is given by

$$\phi_s(x,y) = \exp[-\beta\pi(x,y)\upsilon_w] \qquad (5)$$

indicating that the Lagrange multipliers are the osmotic pressures at x,y and ensuring that the solvent chemical potential is constant throughout; see refs 28 and 29.

Introducing the explicit expressions for the probabilities, eq 4, and the solvent density profile, eq 5, into the free energy expression, eq 1, we obtain

$$\frac{\beta F(D)}{L} = -\sigma_{l_1}\ln q_1(D) - \sigma_{l_2}\ln q_2(D) - \int\int\pi(x,y)\,dx\,dy \qquad (6)$$

with the partition function of polymer i given by

$$q_i(D) = \sum_{\alpha_i}\exp[-\beta\int\int\pi(x,y)\ \upsilon_i(x,y;\alpha_i)\,dx\,dy] \qquad (7)$$

The last step is to find the Lagrange multipliers. To this end, the explicit expressions for the probability of the chain molecules, eq 4, and the solvent density, eq 5, are introduced into the packing constraints, eq 2 with eq 3. The input necessary to solve the equations include (i) the grafted polymer density on each nanotube, σ_{li}; (ii) The grafted polymers chain conformations, from which the quantities $\upsilon_i(x,y;\alpha_i)\,dx\,dy$ are obtained; and (iii) the distance between SWNTs, D.

In practice we discretize the x,y plane into squares of side length δ, thus converting the integral equations into a set of coupled nonlinear equations. For example, the probability of the polymer chains grafted onto SWNT 1 becomes

$$P(\alpha_i;D) = \frac{1}{q_1(D)}\exp\Big[-\sum_k\sum_l\pi'(k,l)\ n_1(k,l;\alpha_1)\Big] \qquad (8)$$

where the dimensionless osmotic pressure has been defined by $\pi'(k,l) = \int_{(k-1)\delta}^{k\delta}\int_{(l-1)\delta}^{l\delta}\beta\pi(x,y)\,dx\,dy$ and $n_1(k,l;\alpha_1)$ is the number of polymer segments that the polymer in conformation α_1 has in the region k,l.

To model the chains we make use of the rotational isomeric state model previously applied by us[31] to model PEO chains. We allow for three isoenergetic states per bond. The bond length, representing the size of an ethylene oxide monomer, is taken to be 0.3 nm. For each chain length, the conformations are generated once, and that set of self-avoiding chains that are also avoided from the inner region of the SWNTs is used in all the

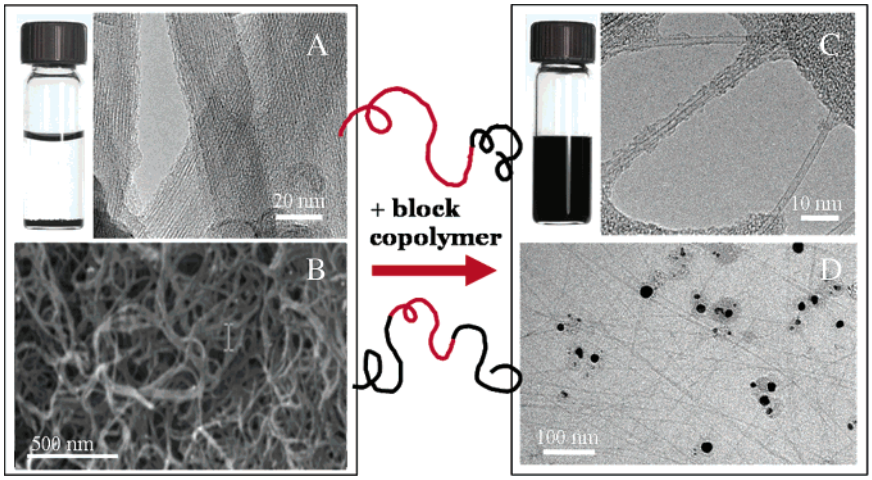

Figure 2. As-prepared SWNTs are highly bundled as observed via (A) TEM and (B) SEM imaging. Sonication leads to temporary exfoliation and deagglomeration of SWNT bundles.[26] In the absence of a dispersing agent, unmodified SWNTs reagglomerate regaining their stable bundled state. In the presence of block copolymers, under specific solvent conditions,[34] SWNTs form stable dispersions of individual tubes, as indicated by HRTEM (C) and cryo-TEM (D) of the dispersions.[35]

calculations presented below. We use a set of 10^5 independent bond sequences, generated by simple sampling. Each bond sequence enters into the calculations at 12 different angles to account isotropically for all the possible orientations with respect to the SWNTs. Indeed we find that for a single SWNT, the distribution of polymer segments is perfectly isotropic in the x,y plane. We have checked that increasing the number of conformations does not change the results presented.

In the calculations we use $\delta = 0.55$ nm and solve a number of nonlinear equations that depend on the chain length: we always reach a large enough intertube distance where the chains tethered to SWNT 1 do not see the chains from SWNT 2. For example, for $n = 50$ the maximal distance between nanotubes is 20δ. Therefore, we solve a system of 2400 nonlinear coupled equations, i.e, 60 in the x direction and 40 in the y direction; see Figure 1. However from symmetry considerations (Figure 1) practically only half of the equations are independent. Thus, for the largest distance we solve 1200 nonlinear coupled equations each with some 10^6 terms (one per chain conformation and angle) via standard numerical methods, for the shortest distance, $D = 2R$, the number of equations reduces to 840 for this chain length.

Results and Discussion

Recently we found that a large variety of synthetic block copolymers[24] and the natural polysaccharide GA[25] efficiently disperse SWNTs in organic as well as in aqueous solutions, up to high concentrations of individual SWNTs. Moreover, the dispersions could be dried and redispersed, preserving the deagglomerated state of the SWNTs. X-ray scattering and TEM provide clear evidence for the individual-tube nature of the dispersed moieties. In Figure 2 we summarize our previous findings (detailed in refs 24 and 25).

In the following we present a detailed theoretical description of the system and examine quantitatively the effect of polymers on the inter-SWNT potential.

In Figure 3 we present the calculated intertube potential for two parallel SWNTs as a function of the intertube distance. The intermolecular interactions between SWNTs are derived using the model by Girifalco et al.[27] A large attractive interaction at short distances is observed, with a minimum of 35 K_bT/nm. The

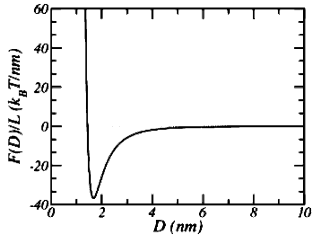

Figure 3. Potential of interaction between two parallel SWNTs as a function of the distance between them, as calculated by Girifalco et al.[27] Note the very deep attractive well when the SWNTs are at contact.

interaction is short ranged and decreases to below K_bT within 5 nm. This is an interesting aspect of SWNT intermolecular behavior, which results from the fact that two of the dimensions of the particles are nanometric.

In the next stage we calculate the intertube potential for SWNTs decorated by (end-tethered)[35] PEO chains of 50, 100, and 150 segments (these chain lengths are relevant to the experimental data), at three different values of surface coverage. Note that in the model presented here we assume that the two polymer blocks play a very different role due to the selectivity of the solvent: the block for which the solvent acts as a poor solvent adsorbs to the SWNTs and anchors the other block, the tail, which dangles into the solvent and is swollen by it (Figure 1). In Figure 4 we present the polymer-induced repulsion among decorated SWNTs, in good solvent conditions for the polymer tails.

Indeed, we observe that the range and strength of the repulsion increase with increasing the length of the grafted chains. The effect of surface coverage is somewhat different: while the strength of the repulsion increases with surface coverage, the range of the interaction is only mildly changed.

(34) The quality of the solvent is characterized by the balance of inter- vs intramolecular interactions. In the mean-field framework the Flory interaction parameter $\chi = \chi_{MS} - {}^1/_2(\chi_{MM} + \chi_{SS})$ is used to describe the balance (where χ_{MM} is the monomer interaction, χ_{MS} is the monomer−solvent interaction, and χ_{SS} is the solvent−solvent interaction). Good solvents are those characterized by low χ, while poor (bad) solvents have a high χ. A detailed description of the approach and a list of good and poor solvents for different polymers can be found in the handbook by Van Krevelen, D. W. *Properties of Polymers*, 3rd ed.; Elesvier: Amsterdam, 1990.

(35) In Figure 2 we present electron microscopy images of as-prepared SWNTs (A) SWNTK1M and (B) SWNTAP and of dispersions of SWNTAP (C) 1 wt % in a solution of 1 wt % of PS-*t*buAC in ethanol and (D) 2.5 wt % of SWNTAP in 1 wt % PE10500 in water. Additional details of the polymers and the dispersions are given in ref 25.

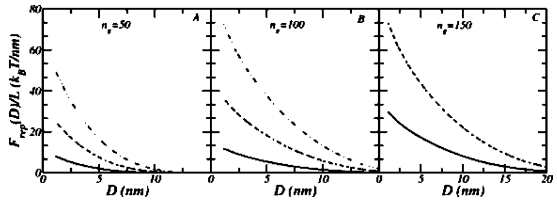

Figure 4. Repulsive component of the interaction between parallel SWNTs with tethered polymers, as a function of the distance between the nanotubes. The steric repulsion due to the tethered polymers is calculated using eq 6. The three graphs correspond to different polymer chain lengths as denoted in the figures. For each polymer molecular weight, the numbers of polymer grafted per unit length are (i) $\sigma_l = 2$ nm^{-1} (full line); (ii) $\sigma_l = 4$ nm^{-1} (dashed line); and (iii) $\sigma_l = 6$ nm^{-1} (dot−dashed line).

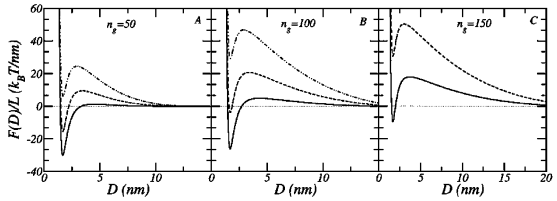

Figure 5. Total interaction energy between parallel SWNTs with tethered polymers. The total interaction is obtained by adding the attractive component, as given in Figure 3, and the repulsive component, Figure 4. The different polymer chain lengths are denoted in the figures, and the lines are as those in Figure 4.

Note the different distance scales for the three polymer chain lengths. For the longest polymer we do not show the highest surface coverage, since the other two already present a very large repulsive interaction.

Examination of the range of SWNT−SWNT attractions presented in Figure 3 and that of the repulsions in Figure 4 suggests that for all chain lengths and surface coverage the range of the repulsive, interpolymer interactions is longer than the range of the intertube attraction.

The overall interaction profile for polymer coated SWNT is presented in Figure 5.

The results of Figure 5, and related calculations, can be used to determine the minimal polymer coverage necessary to stabilize the SWNTs. However, since the position of the maxima changes, one can construct a lower bound limit. Consider for example that in all cases shown the maximum is found around a distance of 3 nm or larger, Figure 5. Then, we take the bound to be 3 nm and determine for each polymer molecular weight the number of polymers per unit length necessary to create a barrier of at least 5kT/nm. We call this quantity σ_l^*. Since the attraction at 3 nm is, from Figure 2, −6kT/nm, we are looking for a repulsive interaction at 3 nm of 11kT/nm. We find the minimal values to be $\sigma_l^* = 3.4$ nm^{-1}, $\sigma_l^* = 2.4$ nm^{-1} and $\sigma_l^* = 1.0$ nm^{-1} for polymers with 50, 100, and 150 segments, respectively. This calculation can in principle be repeated as a function of the CNT diameter and thus obtain the optimal surface modification with polymer chain length.

For the two shortest chain lengths shown above, polymers tethered at low surface coverage present a rather weak repulsion. In all other cases the effective potential exhibits a large barrier (local maxima). Namely, a repulsive energy that is large enough to prevent the SWNTs from reaching the attractive part of the potential at small intertube separations is set up.

While the repulsive part of the effective potential can be modified via the polymer chain length and surface coverage, the short range and steepness of the attractive component of

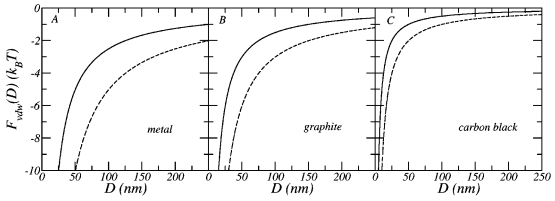

Figure 6. vdW free energy between two spherical particles as a function of interparticle separation (D). The relation was calculated using the expression $W = -A/6DR_1R_2/(R_1 + R_2)$ (ref 4, p 177) for particles of a diameter of 50 nm (full line) and 100 nm (dashed line) of (A) metal, characterized by $A = 5 \times 10^{-19}$ J; (B) graphite, $A = 3 \times 10^{-19}$ J; and (C) carbon black, $A = 1 \times 10^{-19}$ J.

the interaction (Figure 3) imply that the intertube distances at the maximum and minimal free energy are independent of polymer surface coverage and chain length. Therefore, while it is possible to tune the range of the repulsive tail of the potential and the strength of the maximum and minimum, the position of the latter two is fixed.

The results presented in Figure 5 suggest that, in the case of SWNTs, the short range of the attraction gives rise to a simple, generic scenario where steric repulsion among polymers may lead to stabilization of SWNT dispersions. Clearly, the first step in this scenario is to separate the SWNTs (for example, via mild sonication which does not damage the tubes),[24−26] and that enables the tethering of the polymers. Once the polymers are attached to the surface, they present a steric barrier under almost all relevant conditions and thus effectively maintain the nanotubes separated in solutions.

The behavior presented in Figure 5 is fundamental in classical colloidal stabilization. Yet, one point deserves special attention: Unlike classical colloids, SWNTs are molecular objects, with two dimensions in the nanometric range. Thus, the attractive part of the potential is short ranged, and short polymers are able to stabilize the individual tubes (Figure 5). Figure 6 shows the vdW potential between submicron particles. The interaction is significant even at distances larger than the particle's radius showing the colloidal character of the interactions. This is due to the additivity of the vdW interactions as manifested in the Hamaker constant.

To estimate the effect of end-tethered polymers on colloidal particles, we estimated the interaction between parallel planar surfaces decorated by grafted polymers in good solvent conditions. This system provides an upper bound for the repulsive interaction induced by tethered polymers and serves to examine the effect of the strongest possible repulsions. The interactions between grafted polymer layers on planar surface are well described by the Alexander−de-Gennes theory.[37] According to the model, the thickness of the polymer layer, L, is given by $L = cl\sigma^{1/3}n$, where c is a constant of order unity and l is the segment length. The thickness of the layer determines the range of the interaction, and this in turn determines the ability of the polymer layer to prevent flocculation (and stabilize the dispersion). Considering the longest chains with $n = 150$ and $l = 0.3$ nm, we find that the repulsion exceeds K_bT at $D < 45$ nm. Comparison to the potentials presented in Figure 6 suggests that this distance is shorter than the range of the attractive interactions (apart from carbon black, to be discussed below), and

(36) For block copolymers an equivalent assumption is that a triblock copolymer, B−A−B, is tethered to the surface via the A block.
(37) Alexander, S. *J. Phys. (Paris)* **1977**, *38*, 977.

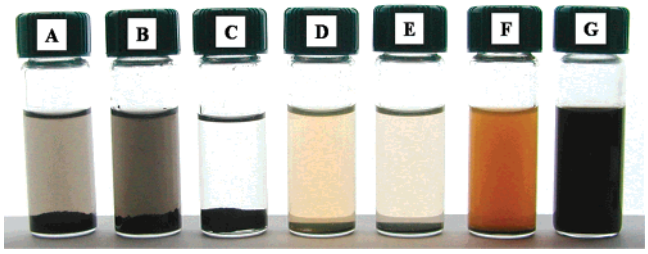

Figure 7. Dispersions of different carbonaceous species following sonication in solutions of 0.5 wt % of carbon fibers in (A) aqueous solution of 5 wt % GA, (B) aqueous solution of 5 wt % F127, and (C) 5 wt % PS-*t*buAC in ethanol. 1.5 wt % of fullerenes in (D) aqueous solution of 5 wt % GA, (E) aqueous solution of 5 wt % F127, and (F) 5 wt % PS-tbuAC in ethanol. (G) 1 wt % of SWNTAP in aqueous solution of 5 wt % F127.

therefore we expect the polymer layer to be ineffective in stabilization of these particles.

To test these ideas, we performed the following set of experiments: Following the procedure described in the Experimental Section, we sonicated carbon fibers and fullerenes in aqueous solutions of GA and F127 and in ethanol solution of PS−*t*buAC at concentrations in the range of 1−10 wt %. An image of vials containing dispersions of the different species is shown in Figure 7.

We observe that carbon fibers (Figure 7A−C) and fullerenes (Figure 7D−F) were not dispersed in the polymer solutions unlike SWNTs (Figure 2 and previous work) but rather coagulated and precipitated, unlike SWNTs under similar conditions (Figure 7G). These observations indicate that the different polymers do not disperse carbon fibers and fullerenes, while they efficiently disperse SWNTs, in accordance with the model presented above. Similar results were obtained for submicron graphite flakes (not shown).

To further test the possibility of using the dimensional selectivity for purification of SWNT−colloidal mixtures, we examined the behavior of as-prepared powders of SWNTs that is known to contain a high percentage of carbonaceous impurities (fullerenes, amorphous carbon, carbon coated metal particles).

A powder containing 40−60 wt % of SWNTs along with carbonaceous impurities and metal catalyst (SWNTAP, SWNTRW) was sonicated in polymeric solutions (GA and Pluronic F127). Dispersions were prepared by sonicating at low power (50 W for 30 min) a powder of as-prepared SWNTs (at concentrations between 0.2 wt % and 10 wt %) in polymer solutions (0.5 wt % to 15 wt %, polymer weight per water weight). A black, homogeneous inklike suspension was obtained, along with a black precipitate. Centrifugation (3600 rpm, 30 min, room temperature) of the sample was followed by decantation of the supernatant from above the precipitate.

Both supernatant and precipitate were imaged by electron microscopy, their composition analyzed via EDS. In Figure 8 we present SEM images of SWNTAP.

The raw powder (Figure 8A) is characterized by the presence of fiberlike entities together with many nontubuline structures. The typical diameter of the fibers is in the range of few tens of nanometers, as expected for ropes where each is composed of many tubes. In Figure 8B we present an image of a powder obtained by drying the supernatant phase of SWNTAP dispersed in GA solution. The sample seems to contain much less of the nontubuline moieties than the raw powder (Figure 8B). The precipitate (Figure 8C) is highly enriched by non-SWNT structures.

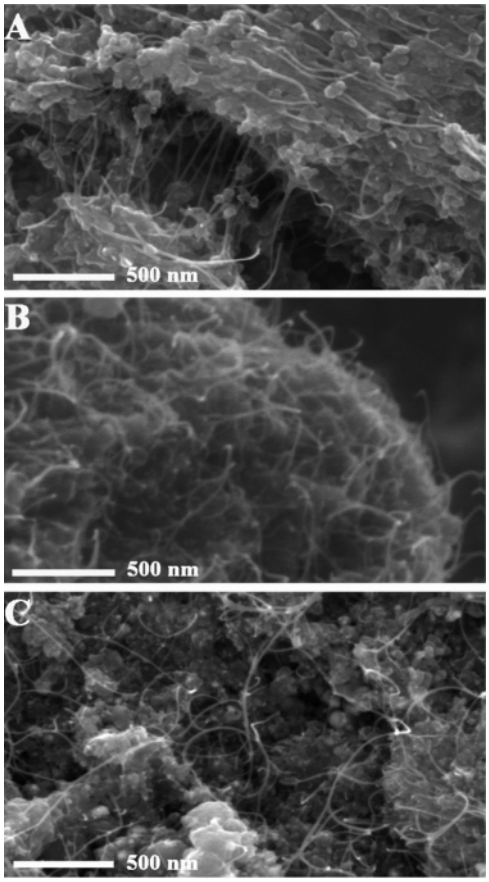

Figure 8. SEM micrographs of (A) as-prepared SWNTAP powder, (B) a dried supernatant phase of a 1 wt % SWNTAP and 1 wt % GA (termed 1:1 wt %) dispersion, and (C) the dried precipitate of the same dispersion. The samples were examined at 10 kV (A) and at 5 kV (B, C).

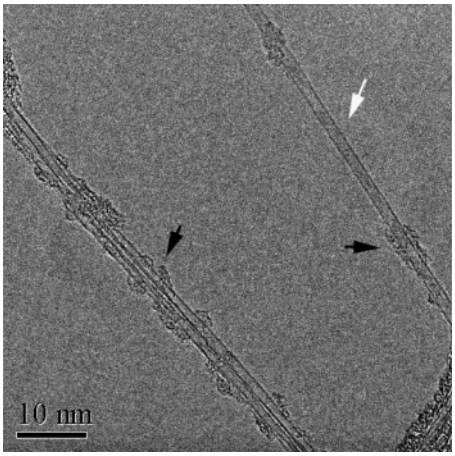

Figure 9. TEM image of redispersed SWNTAP (1:2 wt % SWNTAP to GA in aqueous media). The sample was prepared by drying the supernatant phase and redispersing it in a small volume of water. The white arrow points at an individual tube, and the black arrows indicate carbonaceous species on the tubes.

TEM imaging of the supernatant phase reveals the presence of individual tubes and small bundles containing 2−3 tubes (Figure 9, white arrow). Carbonaceous species that have probably grown onto the tubes during the synthesis[18] are also shown (Figure 9, black arrows).

Table 1. Metal Atom % in Polymer-Treated SWNT Samples (Polymer/SWNT 1:1 wt %) as Measured via EDS

sample	as-prepared	dried supernatant phase	dried precipitate
(a) SWNTAP in GA	5 ± 1.4	2 ± 0.7	7.5 ± 0.8
(b) SWNTRW in GA	2 ± 1.1	0.6 ± 0.2	2 ± 0.8
(c) SWNTAP in F127	5.8 ± 1.4	1.4 ± 0.7	4.7 ± 0.8

The relative metal content of the supernatant phase and the precipitate (obtained by dispersing SWNTAP or SWNTRW at 1:1 weight ratio in aqueous solutions of the polymers) were measured via EDS (Table 1).

The values presented in Table 1 indicate that the relative concentration of metals in the precipitate is significantly higher than that in the supernatant. Additional experimental evidence for the compositional difference between the two phases as observed by thermogravimetric analysis can be found in the Supporting Information.

In a different series of experiments, we collected the precipitate, dried the powder, and redispersed it in water. We observed that though some of the precipitate floated in the liquid, most of it could not be redispersed. This observation indicates that simple partitioning of the carbon soot between the two phases cannot be the origin of the observed effect, but rather the precipitate is composed of nondispersible moieties, suggesting that the interaction between the polymers and SWNTs is selective.

The observed selectivity is an important consequence of the dependence of the intertube potential on the dimensions of the colloidal particles. Using relatively short polymeric chains for steric stabilization, we find that while polymer-decorated SWNTs experience large enough repulsion that results in the formation of stable dispersions, carbonaceous particles (of similar density) but of submicron diameter will coagulate and flocculate.

Similar observations were reported for other polymers and solvents: Yudasaka et al. reported selective dispersion of SWNTs (prepared via laser ablation) by poly(methyl methacrylate) (PMMA) in monochlorobenzene solutions.[38] A. B. Dalton et al. reported the selective dispersion of SWNTs (prepared via arc discharge) in toluene solutions of poly(*p*-phenylenevinylene-*co*-2,5-diotoxy-*m*-phenylenevinylene) (PmPV).[39] We believe that these observations may be rationalized by the model presented here.

The last point relates to carbon black. The calculations presented in Figure 6 suggest that for carbon black particles with a radius of 50 and 100 nm the range and depth of the attractive interaction are much reduced. This is a direct manifestation of the lower values of the effective Hamaker constant due to the relatively low particle density (high porosity). Indeed previous studies[40] indicate that Pluronic polymers disperse well carbon black in aqueous solutions, and as was described in the Introduction, dispersion of carbon black in GA solutions is one of the earliest demonstrations of steric stabilization.

(38) Yudaska, M.; Zhang, M.; Jabs, C.; Ijima, S. *Appl. Phys. A* **2000**, *71*, 449−451.

(39) Dalton, A. B.; Blau, W. J.; Chambers, G.; Coleman, J. N.; Henderson, K.; Lefrant, S.; McCarthy, B.; Stephan, C.; Byrne, H. J. *Synth. Met.* **2001**, *121*, 1217−1218.

Conclusions

We previously found experimentally that it is possible to stabilize dispersed individual SWNTs in aqueous and organic solvents using relatively short tethered polymers in selective solvents. The theory presented here suggests that this behavior originates from the combination of the short range and steepness of the attractive component of the SWNT−SWNT potential, together with the range of polymer-induced repulsion. We also observed that for different colloidal particles the range of the attractive interactions is determined by the number of microscopic vs mesoscopic dimensions. For SWNTs where two of the dimensions are nanoscopic and one is mesoscopic, the attractive potential is relatively short ranged, albeit very steep. Therefore, even short polymer chains can produce a long enough repulsive potential that results in large enough repulsive barriers to stabilize a dispersion of the individual tubes. In the case of submicron colloidal particles the attractive vdW potential is proportional to the product of the Hamaker constant and the particle radius. Typically, this product results in a significant attraction at distances larger than the size of the particles. Therefore, the polymer chain length and surface coverage necessary for inducing steric repulsion in colloidal dispersions are much higher than those required for dispersion of SWNTs.

The effect described above suggests that polymers offer a generic pathway for stabilization of SWNT dispersions, and a proper choice of the polymer molecular weight may result in dimensional selectivity enabling purification of SWNTs from mixtures of non-nanometric objects.

Acknowledgment. This research was supported by the Israel Science Foundation, the Center of Excellence Program (Grant No. 8003) and at Purdue by the National Science Foundation Grant CTS-0338377 and the Indiana 21st Century Research and Technology Fund. The authors thank Dr. Marcelo Carignano for insightful discussions and for the preparation of Figure 1.

Supporting Information Available: TGA behavior of the supernatant phase and the precipitate was studied. Mass change was measured as a function of the temperature during a heating procedure from 40 °C to 1000 °C at a rate of 10 °C min^{-1} under a constant flow of air (200 mL min^{-1}). The amount of the metal catalyst in each phase is revealed by the weight remain without being burned up to 1000 °C. TGA traces of the supernatant and the precipitate phases indicate that the relative concentration of metals in the precipitate is significantly higher than in the supernatant.

JA046377C

(40) Lin, Y.; Alexandridis, P. *J. Phys. Chem. B* **2002**, *106*, 10834−10844.

NANO LETTERS

2002
Vol. 2, No. 1
25−28

Stabilization of Individual Carbon Nanotubes in Aqueous Solutions

Rajdip Bandyopadhyaya, Einat Nativ-Roth, Oren Regev,* and Rachel Yerushalmi-Rozen*

Department of Chemical Engineering and The Ilse Katz Center for Meso and Nanoscale Science and Technology, Ben Gurion University of the Negev, 84105 Beer Sheva, Israel

Received September 12, 2001; Revised Manuscript Received October 15, 2001

ABSTRACT

Single-wall carbon nanotubes pack into crystalline ropes that aggregate into tangled networks due to strong van der Waals attraction. Aggregation acts as an obstacle to most applications, and diminishes the special properties of the individual tubes. We describe a simple procedure for dispersing as-produced nanotubes powder in aqueous solutions of Gum Arabic. In a single step, a stable dispersion of full-length, well separated, individual tubes is formed, apparently due to physical adsorption of the polymer.

Single-wall carbon nanotubes (SWNT) are expected to exhibit superior mechanical and electrical properties[1−4] as a direct consequence of the nanometric dimensions of the individual tube. Yet, as-produced SWNTs align parallel to each other and pack into crystalline ropes, due to strong intertube van der Waals attraction. Ropes that are typically composed of 100 to 500 tubes pack in a triangular lattice with a lattice constant of $a = 1.7$ nm.[5] The ropes further aggregate into tangled networks. Aggregation was found to act as an obstacle to most applications, diminishing the special mechanical and electrical properties of the individual tubes.[6,7]

The observed reduction in desired properties together with the difficulties in manipulating bundled nanotubes have motivated recent attempts to develop methods that will enable solubilization, dispersion, and separation of SWNTs. Covalent[8,9] and ionic[6,10] modifications resulted in a limited success: dispersion of either SWNT fragments or ropes[10] (rather than individual tubes) in organic media and formation of polymer−nanotube composites[11] were reported. Often, it was observed that the band electronic structure of the native tubes was disrupted by these modifications,[12,13] and in some cases the inherent crystalline structure of the individual tube was severely damaged.[14]

An alternative, which does not involve covalent or ionic interactions, is offered by physical adsorption of long chain polymers.[15,16] In this letter we describe a simple procedure, which relies on nonspecific physical adsorption of a natural polymer, Gum Arabic (GA),[17] for dispersing as-produced powder of entangled SWNT ropes into individual, well-separated tubes.

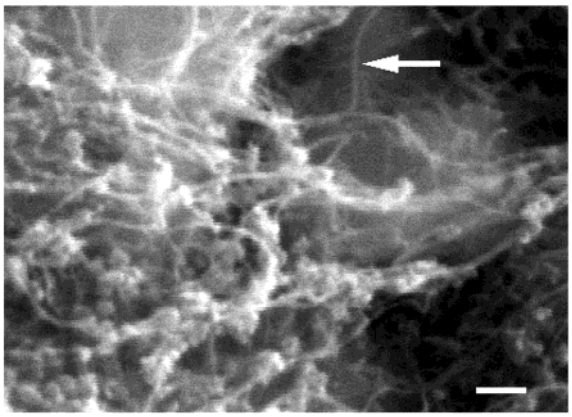

Figure 1. SEM micrograph (Au spattered, JSM-35CF, JEOL, operated at 25kV) of as-produced[20] nanotube powder. The arrow points to a single rope protruding out of the entangled network. Typical rope diameter is in the range of 30−50 nm. Scale bar, 200 nm.

In a single step, as-produced SWNT powder is dispersed in an aqueous solution of GA, a water soluble polysaccharide produced by Acacia Senegal trees,[17,18] and a stable dispersion of individual, full-length tubes is formed. The dispersion may then be dried and redispersed at high concentrations of the powder in pure water, resulting in the reformation of a stable dispersion of individual tubes.

The dispersion method is based on an ancient Egyptian recipe, first used 5000 years ago for preparation of carbon-black ink:[19] GA is dissolved in water to form solutions of 0.5 wt % to 15 wt %. A powder of as-produced nanotubes,[20] which contains a bundled network of ropes (Figure 1), is

* Corresponding authors. E-mail: oregev@bgumail.bgu.ac.il; rachely@bgumail.bgu.ac.il.

10.1021/nl010065f CCC: $22.00
Published on Web 11/22/2001

Figure 2. Vials containing aqueous dispersions of SWNT (0.05 wt %) after 3 months of incubation at room temperature: (A) 2 wt % GA; (B) 5 wt % GA; (C) 5 wt % SDS; (D) 15 wt % SDS; (E) 5 wt % CTAC; (F) 15 wt % CTAC. Note that a uniform dispersion (indicative of a single phase) is observed in A and B while in the other vials the carbon nanotubes coagulate at the bottom.

sonicated at very mild conditions (50 W, 43 kHz) for 15−20 min in the polymeric solutions and a black (of concentrations between 0.2 wt % to 3 wt %), homogeneous ink-like suspension is obtained.

The suspension may then be dried in air, at ambient conditions, and redispersed in pure water in concentrations ranging from 0.5 wt % to 15 wt % (carbon nanotubes powder weight per water weight). The resulting suspensions are stable over few months, and centrifugation (at 4500 rpm for 30 min) does not result in precipitation of the nanotubes. The method is applicable to either SWNT or multiwall nanotubes (MWNT).[1]

To investigate the origin of the dispersing power of GA solutions on carbon nanotubes, we tested surfactants that vary in charge and molecular weight. Negatively charged sodiumdodecyl sulfate (SDS), positively charged cetyltrimethylammoniumchloride (CTAC) and dodecyltrimethylammoniumbromide (DTAB), nonionic pentaoxoethylenedodecyl ether ($C_{12}E_5$), a polysaccharide (Dextrin), and a long chain synthetic polymer poly(ethylene oxide) (PEO) were compared with GA.[21] We found that none of these materials could act as an efficient dispersing agent for nanotubes in aqueous solutions. In Figure 2 we present an image of some of the dispersions of SWNT in solutions of surfactants and GA. We observe that dispersions of nanotubes in GA are homogeneous, while the other solutions are phase separated with coagulated tubes at the bottom of the vial.

To test the aggregation state of the tubes in the dried powder, we performed X-ray scattering experiments. A typical wide-angle X-ray scattering pattern (WAXS) of as-produced powder[20] is presented in Figure 3a. In Figure 3b we present a WAXS spectrum of SWNT powder following dispersion in GA solution and drying. The peaks that result from intertube packing within the ropes in the as-synthesized SWNT (Figure 3a) have disappeared, leaving only the graphite peaks (most probably MWNT).[1] This observation suggests that the ropes in the dispersed-and-dried powder are well separated into individual tubes of either SWNT or MWNT.

The microscopic structure of the stable, concentrated, redispersed solution of carbon nanotubes was further investigated using cryotransmission electron microscopy (cryo-

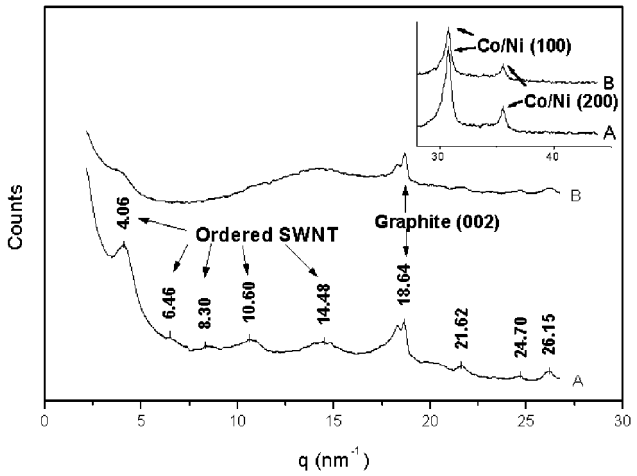

Figure 3. Wide-angle X-ray spectra of (a) as-produced SWNT powder[20] exhibiting a typical rope structure: the peaks at the low-q region indicate a two-dimensional triangular lattice with a lattice constant of 1.8 nm. In addition, multiwall graphitic objects can be seen (at $q = 18.64$ nm^{-1}) in good agreement with previous observations.[5] (b) A powder prepared by drying a dispersion of 3 wt % SWNT in 15 wt % aqueous solution of GA. The intertube reflections have disappeared. The inset presents the reflections of the Co/Ni catalyst used in the synthesis of SWNT.[19] The measurements were carried out by a Philips X-ray powder diffractometer (PW-1050/70) at 40 kV/28 mA with Cu Kα ($\lambda = 0.154$ nm) radiation and graphite monochromator. The scattering vector $q = 4\pi/\lambda \sin\theta$, where θ is the scattering angle.

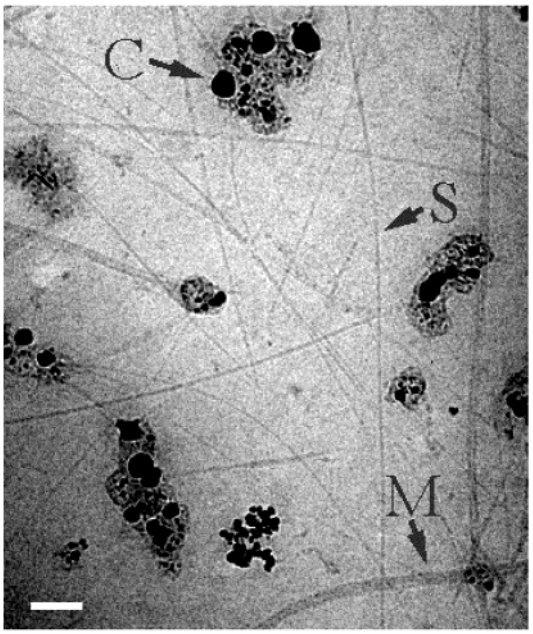

Figure 4. Cryo-TEM micrograph of a highly concentrated dispersion of SWNT, prepared by redispersing a dry powder of GA coated SWNT (obtained by drying a solution of 3 wt % SWNT in 15 wt % GA solution) in pure water. The sample was imaged at −170 °C (under focus of 4 μm) using JEOL 1200EXII TEM equipped with a Gatan 626 cold stage. The arrows indicate flexible SWNT (S), the Co/Ni catalyst (C), and most probably MWNT (M). Scale bar, 50 nm.

TEM).[22,23] Figure 4 presents a cryo-TEM image of redispersed nanotubes. Well separated SWNT, of a diameter below 2 nm, are clearly observed, along with some residues,

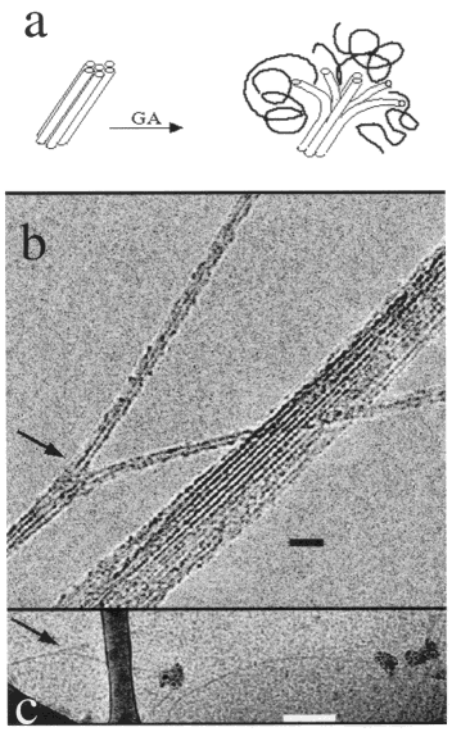

Figure 5. Rope-to-single-tube transition due to adsorption of GA: (a) schematic presentation; (b) high-resolution TEM (JEOL 2010 operated at 200 kV) image of dried solution of 0.05 wt % SWNT in 1 wt % GA (scale bar, 10 nm); (c) cryo-TEM image of 0.05 wt % SWNT in 5 wt % GA (scale bar, 100 nm). Arrows in (b) and (c) show the location of bifurcation.

including the catalyst (note the catalyst scattering pattern in the inset of Figure 3). The length of the SWNT is well above a micron. Similar images were observed in dispersed solutions prior to drying.

These observations demonstrate that adsorption of GA leads to disruption of the intertube interactions in the crystalline ropes, as schematically presented in Figure 5a. The high-resolution TEM image in Figure 5b presents a small bundle during the process of exfoliating. Adjacent to it is either a MWNT or a nonexfoliated bundle. A similar image was observed in the cryo-TEM image presented in Figure 5c. In both figures we observe that the intact structure of full-length SWNT is preserved throughout the process.

The method described above leads to the formation of homogeneous dispersions of individual carbon nanotubes. Drying and re-dispersion of the polymer coated tubes results in highly concentrated dispersions of well-separated tubes.

The spontaneous redispersion of the dried carbon nanotube powder in pure water and the stability of highly concentrated dispersions are signatures of what is known in modern colloid science as steric stabilization.[24] In this mechanism, entropic repulsion among polymeric chains is utilized for stabilization of colloids: In good solvent conditions,[25] polymer chains tend to avoid each other so as not to constrain the conformational space available to each of them. Thus, polymer coated objects experience a repulsive force. In the system described here, GA adsorbs to the aggregated nanotubes, which are of a much smaller dimension than the characteristic radius of the polymeric chains, R_F,[26] and activates a repulsive force at a distance of $2R_F$.[28] At this distance the polymer-induced repulsive force dominates over the vdW attraction[29] between the embedded nanotubes. Consequently, the overall intertube potential becomes repulsive and the nanotube dispersion becomes thermodynamically stable.[24]

An additional consequence of GA adsorption is the exfoliating of ropes into individual tubes. We suggest that the activation of steric repulsion among the polymer coated tubes allows the disassembly of ropes into individual tubes due to a net gain in translational entropy: For a rope that contains about 100 tubes, a 2-fold increase in translational entropy may be achieved.[30]

To conclude, we present a simple method for unbundling as-produced (unmodified, long) carbon nanotubes in aqueous solutions of Gum Arabic. The resulting stable dispersion may be dried into an "instant" ready-for-use powder of individual carbon nanotubes. The unbundling and stabilization of the single tubes in solution is demonstrated unequivocally by a combination of X-ray scattering and cryo-TEM imaging. While the former indicates the loss of intertube ordering, i.e., the disruption of the ropes, the latter provides a direct visualization of the individual SWNT.

The use of GA for stabilization of SWNT dispersions offers a few advantages. Disruption of the interrope packing, leading to dispersion of the tubes, will enable the testing of isolated tube properties and comparison to theoretical predictions. From the practical point of view, the Gum Arabic molecules that adsorb to the carbon nanotubes may act as adhesion promoters leading, to the formation of highly adhesive interfaces between individual tubes and a polymeric matrix.[31]

Acknowledgment. We thank A. Klug and J. Klein for illuminating comments. This research was supported by the FIRST foundation of the Israel Academy of Science and Humanities. R.Y.-R. gratefully acknowledges the support of The Joseph and May Winston Foundation Career Development Chair in Chemical Engineering.

References

(1) *Science of Fullerens and Carbon Nanotubes*; Dresselhaus, M. S., Dresselhaus, G., Eklund, P. C., Eds.; Academic Press: San Diego, 1996.
(2) Yao, Z.; Dekker, C.; Avouris, Ph. *Top. Appl. Phys.* **2001**, *80*, 147.
(3) Salvetat, J. P. et al. *Phys. Rev. Lett.* **1999**, *85*, 944.
(4) Kociak, M. et al. *Phys. Rev. Lett.* **2001**, *86*, 2416.
(5) Thess, A. et al. *Science* **1996**, *273*, 483.
(6) Vigolo, B. et al. *Science* **2000**, *290*, 1331.
(7) Kwon, Y. K.; Saito, S.; Tomanek, D. *Phys. Rev. B* **1998**, *58*, R13314.
(8) Hamon, M. A. et al. *Adv. Mater.* **1999**, *11*, 834.
(9) Riggs, J. E.; Guo, Z.; Carroll, D. L.; Sun Y−P. *J. Am. Chem. Soc.* **2000**, *122*, 5879.
(10) Chen, J. et al. *J. Phys. Chem.* **2001**, *105*, 2525.
(11) McCarthy, B. et al. *Synth. Met.* **2001**, *121*, 1225.
(12) Chen, J. et al. *Science* **1998**, *282*, 95.
(13) Boul, P. J. et al. *Chem. Phys. Lett.* **1999**, *310*, 367.
(14) Monthioux, M. et al. *Carbon* **2001**, *39*, 1251.
(15) Coleman, N. et. al. *Adv. Mater.* **2000**, *12*, 213.
(16) Star, A. et. al. *Angew. Chem., Int. Ed. Engl.* **2001**, *40*, 1721.
(17) Gum Arabic (Aldrich Acacia 26,077−0) is a highly branched arabinogalactan polysaccharide. It was found that the material is mainly composed of two components: 70−80% of arabingalactan,

forming a highly branched structure with a hydrodynamic radius, R_h, of about 5 nm and about 20% of an arabingalactan−protein complex with R_h values ranging from 25 to 50 nm. While the composition of the material is known, its conformation has not yet been elucidated, and the origins of its surface activity are not well understood.
(18) Picton, L.; Bataille, I.; Muller, G. *Carbohydr. Polym.* **2000**, *42*, 23.
(19) *Encyclopedia Britannica* 257−259 (William Benton: Chicago, 1966).
(20) Select grade nanotubes (SWNT) were purchased from Carbolex, University of Kentucky, Lexington, Kentucky. The nanotubes were synthesized by arc discharge. According to the specifications by the manufacturer, the powder consists of 85 vol % pure SWNT, graphite, carbon impurities and catalyst (Cobalt and Nickel, ca. 20 nm in diameter).
(21) SDS, CTAC, and DTAB Aldrich, Dextrin (260754 DEXTRIN 60% 9000 g/mole, 30% 3000 g/mol, and the reminder a low molecular weight fraction) were purchased from Sigma-Aldrich. PEO (M_w = 304 600 g/mol) was purchased from Polymer Source Inc., Canada. $C_{12}E_5$ was purchased from Nikko chemicals, Japan. We found that Dextrin and PEO solutions (at similar molar concentrations to 0.5 wt % GA), as well as $C_{12}E_5$ and DTAB solutions at concentrations ranging from 0.05% to a few percent do not stabilize the nanotubes.
(22) In this method, a drop of the solution is placed on a lacey TEM grid and vitrified in liquid ethane.
(23) Bellare, J. R.; Davis, H. T.; Scriven, L. E.; Talmon, Y. J. *Electron. Microsc. Technol.* **1988**, *10*, 87.
(24) *Polymeric Stabilization of Colloidal Dispersions;* Napper, D. H., Eds.; Academic Press: Orlando Florida, 1993.
(25) A solvent in which solvent-chain interactions are preferred over chain−chain interaction, resulting in an extended configuration of the polymeric coil.[24]
(26) R_F is the Flory radius of the polymer.[24] In the relevant experimental conditions it is in the range of 25 to 50 nm.[18]
(27) Aubouy, M.; Raphael, E. *Macromolecules* **1998**, *31*, 4357.
(28) Klein, J.; Luckham, P. *Nature* **1982**, *300*, 429.
(29) *Intermolecular and Surface Forces*; Israelachvili, J., Ed.; Academic Press: San Diego, 1992.
(30) In a model describing a dilute monatomic gas, the entropy, S, of N independent objects scales as $S \sim Nk_b\ln(A + V/N)$, where N is the number of objects, k_b is the Boltzmann constant, A describes the system (see, for example, Hill, T. L. *Statistical Thermodynamics*; Addison-Wesley: Reading Massachusetts, 1960). V is the volume. The quantity in brackets is of order 10^3 or more, but the logarithm is of order unity. Hence $S = O(Nk_b)$, i.e., the entropy increases monotonically with the number of objects.
(31) de-Gennes, P. G. *J. Phys.* **1990**, *68*, 1049.

NL010065F

distortion therefore explains the magnetoelectric coupling. Application of the electric field transfers the sample into a single-domain state with maximum field **D** for which transition into the $P6_3\underline{cm}$ phase leads to the largest possible energy gain from $H_{ME} = \hat{\alpha}\mathbf{DB}$. According to ref. 13 and Fig. 4a up to 40% (Ho^{3+}: 3–4μ_B) of the rare-earth spins are ordered. The increase defining T_{Ho} in Figs 2a and 4 is due to Ho^{3+}–Ho^{3+} exchange in the *x*–*y* plane which complements the Ho^{3+}–Mn^{3+} interaction.

Transition into the magnetoelectric $P6_3\underline{cm}$ phase corresponds to modification of the inter-planar Mn^{3+}–Mn^{3+} exchange paths stabilizing the three-dimensional magnetic order. With the Mn^{3+} ions at $x = \frac{1}{3}a$, the inter-planar Mn^{3+}–Mn^{3+} exchange is nearly perfectly frustrated. Frustration is overcome by the ~2% movement of the Mn^{3+} ions revealed in Figs 1 and 4b. Depending on the shift being positive or negative, either the exchange path favouring formation of the $\underline{6}_3$ axis (above T_{Ho} at $E = 0$) or the exchange path favouring formation of the 6_3 axis (below T_{Ho} at $E = 0$ and below T_N at $E = \pm E_0$) is strengthened. Figure 4c shows that the electric dipole moment is modified along with the magnetic transition which is another manifestation of magnetoelectric interaction on the microscopic scale.

Thus we have observed how multifold magnetic ordering in $HoMnO_3$ is controlled by a static electric field. Ferromagnetic Ho^{3+} ordering is deliberately activated or deactivated, and the ferromagnetic component is controlled by the sign of the electric field. The driving mechanism for phase control are microscopic magnetoelectric interactions originating in the interplay of Ho^{3+}–Mn^{3+} interaction and ferroelectric distortion. With their potential for giant magnetoelectric effects, magnetic ferroelectrics are most favourable for technological applications of magnetoelectric switching, which is reflected by the current push for novel compounds and concepts to understand this class of materials[27,28]. On the basis of the work presented here, promising candidates for controlled magnetoelectric switching[10] are compounds with electronic states close to the ground state which are energetically lowered by magnetoelectric contributions in an applied electric or magnetic field. Therefore frustrated systems or systems in the vicinity of phase boundaries or quantum critical points[29] are prime candidates for magnetic phase control by an electric field or vice versa. □

Received 19 April; accepted 8 June 2004; doi:10.1038/nature02728.

1. Prinz, G. A. Magnetoelectronics applications. *J. Magn. Magn. Mater.* **200,** 57–68 (1999).
2. Ohno, H. *et al.* Electric-field control of ferromagnetism. *Nature* **408,** 944–946 (2000).
3. Asamitsu, A., Tomioka, Y., Kuwahara, H. & Tokura, Y. Current switching of resistive states in magnetoresistive manganites. *Nature* **388,** 50–52 (1997).
4. O'Dell, T. H. *The Electrodynamics of Magneto-electric Media*, (North-Holland, Amsterdam, 1970).
5. Schmid, H. On a magnetoelectric classification of materials. *Int. J. Magn.* **4,** 337–361 (1973).
6. Nan, C. W. *et al.* A three-phase magnetoelectric composite of piezoelectric ceramics, rare-earth iron alloys, and polymer. *Appl. Phys. Lett.* **81,** 3831–3833 (2002).
7. Srinivasan, G., Rasmussen, E. T., Levin, B. J. & Hayes, R. Magnetoelectric effects in bilayers and multilayers of magnetoresistive and piezoelectric perovskite oxides. *Phys. Rev. B* **65,** 134402 (2002).
8. Kimura, T. Magnetic control of ferroelectric polarization. *Nature* **426,** 55–58 (2003).
9. Van Aken, B. B., Palstra, T. T. M., Filippetti, A. & Spaldin, N. A. Origin of ferroelectricity in magnetoelectric $YMnO_3$. *Nature Mater.* **3,** 164–170 (2004).
10. Hur, N. *et al.* Electric polarization reversal and memory in multiferroic material induced by magnetic fields. *Nature* **429,** 392–395 (2004).
11. Coeuré, P., Guinet, F., Peuzin, J. C., Buisson, G. & Bertaut, E. F. in *Proc. Int. Meeting on Ferroelectricity* (ed. Dvorák, V.) 332–340 (Institute of Physics of the Czechoslovak Academy of Sciences, Prague, 1996).
12. Fiebig, M. *et al.* Determination of the magnetic symmetry of hexagonal manganites by second harmonic generation. *Phys. Rev. Lett.* **84,** 5620–5623 (2000).
13. Sugie, H., Iwata, N. & Kohn, K. Magnetic ordering of rare earth ions and magnetic-electric interaction of hexagonal $RMnO_3$ (R = Ho, Er, Yb or Lu). *J. Phys. Soc. Jpn* **71,** 1558–1564 (2002).
14. van Aken, B. B. *Structural Response to Electronic Transitions in Hexagonal and Ortho-Manganites.* Thesis, Reiksuniv. Groningen (2001).
15. Fiebig, M., Lottermoser, Th. & Pisarev, R. V. Spin-rotation phenomena and magnetic phase diagrams of hexagonal $RMnO_3$. *J. Appl. Phys.* **93,** 8194–8197 (2003).
16. Leute, S., Lottermoser, Th. & Fröhlich, D. Nonlinear spatially resolved phase spectroscopy. *Opt. Lett.* **24,** 1520–1522 (1999).
17. Maichle, J. K., Ihringer, J. & Prandl, W. Simultaneous structure refinement of neutron, synchrotron and x-ray powder diffraction patterns. *J. Appl. Crystallogr.* **21,** 22–28 (1998).
18. Ihringer, J. A quantitative measure for the goodness of fit in profile refinements with more than 20 degrees of freedom. *J. Appl. Crystallogr.* **28,** 618–619 (1995).
19. Rebmann, C., Ritter, H. & Ihringer, J. Standard uncertainty of angular positions and statistical quality of step-scan intensity data. *Acta Crystallogr. A* **54,** 225–231 (1998).
20. Fiebig, M., Fröhlich, D., Lottermoser, Th. & Maat, M. Probing of ferroelectric surface and bulk domains in ferroelectric $RMnO_3$ (R = Y, Ho) by second harmonic generation. *Phys. Rev. B* **66,** 144102 (2002).
21. Fox, D. L., Tilley, D. R., Scott, J. F. & Guggenheim, H. J. Magnetoelectric phenomena in $BaMnF_4$ and $BaMn_{0.99}Co_{0.01}F_4$. *Phys. Rev. B* **21,** 2926–2936 (1980).
22. Scott, J. F. Phase transitions in $BaMnF_4$. *Rep. Prog. Phys.* **42,** 1055–1084 (1979).
23. Ascher, E., Riedel, H., Schmid, H. & Stössel, H. Some properties of ferromagnetic nickel-iodine boracite $Ni_3B_7O_{13}I$. *J. Appl. Phys.* **37,** 1404–1405 (1966).
24. Fiebig, M., Degenhardt, C. & Pisarev, R. V. Interaction of frustrated magnetic sublattices in $ErMnO_3$. *Phys. Rev. Lett.* **88,** 027203 (2002).
25. Kritayakirana, K., Berger, P. & Jones, R. V. Optical spectra of ferroelectric-antiferromagnetic rare earth manganates. *Opt. Commun.* **1,** 95–98 (1969).
26. Dzyaloshinskii, I. E. Thermodynamic theory of 'weak' ferromagnetism in antiferromagnetic substances. *Sov. Phys. JETP* **5,** 1259–1272 (1957).
27. Fiebig, M., Eremenko, V. & Chupis, I. (eds) *Magnetoelectric Interaction Phenomena in Crystals* (Kluwer, Dordrecht, 2004).
28. Zheng, H. *et al.* Multiferroic $BaTiO_3$-$CoFe_2O_4$ nanostructures. *Science* **303,** 661–663 (2004).
29. Saxena, S. S. *et al.* Superconductivity on the border of itinerant-electron ferromagnetism in UGe_2. *Nature* **406,** 587–591 (2000).

Acknowledgements We thank K. Kohn and K. Hagdorn for samples, and the DFG and the BMBF for financial support. M. F. thanks T. Elsässer for continuous support.

Competing interests statement The authors declare that they have no competing financial interests.

Correspondence and requests for materials should be addressed to M.F. (fiebig@mbi-berlin.de).

Demixing in simple fluids induced by electric field gradients

Yoav Tsori, François Tournilhac & Ludwik Leibler

Laboratoire Matière Molle & Chimie (UMR 167 CNRS-ESPCI), Ecole Supérieure de Physique et Chimie Industrielles, 10 rue Vauquelin, 75231 Paris CEDEX 05, France

Phase separation in liquid mixtures is mainly controlled by temperature and pressure, but can also be influenced by gravitational, magnetic or electric fields. However, the weak coupling between such fields and concentration fluctuations limits this effect to extreme conditions[1–3]. For example, mixing induced by uniform electric fields is detectable only at temperatures that are within a few hundredths of degree or less of the phase transition temperature of the system being studied[4–7]. Here we predict and demonstrate that electric fields can control the phase separation behaviour of mixtures of simple liquids under more practical conditions, provided that the fields are non-uniform. By applying a voltage of 100 V across unevenly spaced electrodes about 50 μm apart, we can reversibly induce the demixing of paraffin and silicone oil at 1 K above the phase transition temperature of the mixture; when the field gradients are turned off, the mixture becomes homogeneous again. This direct control over phase separation behaviour depends on field intensity, with the electrode geometry determining the length-scale of the effect. We expect that this phenomenon will find a number of nanotechnological applications, particularly as it benefits from field gradients near small conducting objects.

The driving force for separation in liquid mixtures is the preference of constituent molecules to be in contact with their own species[8]. At high temperatures, however, thermal agitation dominates over enthalpic interactions, and mixing occurs. Figure 1a shows the classic phase diagram of a binary mixture of two liquids, A and B, with phase transition temperature, T_t (blue curve), as a function of the concentration of A (ϕ; where $0 < \phi < 1$). Above T_t

at point 'α', the two liquids are miscible (Fig. 1b); a quench to below T_t, to a point 'β', leads to creation of (say) A-rich droplets in a B-rich continuous phase. The appearance of an interface between demixed phases is a signature of the phase separation transition (Fig. 1c).

The effect of uniform electric fields on liquid phase separation has attracted considerable attention in the past 50 years[1,4–7,9,10]. And yet, even the question of whether the field favours mixing or demixing is still a subject of debate[5,9,11]. Indeed, the shift of the transition temperature caused by uniform fields can originate from the non-linear dependence of dielectric constant on composition[1,4] or from thermal composition fluctuations which in turn induce local electric field fluctuations[10,11]. Theories predict field induced phase separation[1,4,6,11] whereas most experiments show that uniform electric fields favour mixing[4–7]. Still, even for mixtures with a large dielectric constant mismatch, the effect is weak: the critical temperature decreases by about 0.015 K when a field of about 4 MV m^{-1} is applied[4,7]. However, and this is our starting point, the situation is very different when the applied field is non-uniform at a macroscopic scale. For weak fields, the mixture exhibits smooth concentration gradients, as shown schematically in Fig. 1d. This is a molecular analogue of the 'dielectric rise' effect, in which a dielectric liquid is pulled towards a region of high electric field by a dielectrophoretic force[1,12,13]. We show that when the electric field exceeds a critical value, the composition profile changes dramatically: the mixture phase separates, creating a sharp interface (Fig. 1e). Here, demixing originates from the direct coupling between composition and field, and, therefore, the effects are strong. For simple non-polar liquids, demixing can be induced as far as a few degrees above the transition temperature and with easily accessible fields. The new displaced phase lines are shown in green and red curves in Fig. 1a, for two different field amplitudes. The electric field induced demixing may be useful for various optical and chemical applications—and once phase separation is produced, external fields can drive electrohydrodynamic[14] and interfacial instabilities[15,16] or electro-wetting phenomena[17–19]. Upon switching off the electric field, a homogeneous mixture is recovered.

When an electric field is applied to a homogeneous non-conducting mixture, the electrostatic contribution of the free energy is given by F_{es}:

$$F_{es} = -\frac{1}{2}\int \varepsilon(\mathbf{r})\mathbf{E}^2(\mathbf{r})\mathrm{d}^3 r \qquad (1)$$

where ε denotes the dielectric constant, and $\mathbf{E}(\mathbf{r})$ is the local field at point $\mathbf{r}$ obeying the appropriate boundary conditions on the electrodes[1]. In a mixture of liquids A and B with dielectric constants ε_A and ε_B, respectively, ε depends on the composition of the mixture, $\phi(\mathbf{r})$. Local composition variations yield a spatially varying dielectric constant, and the system tries to adjust the mixture concentration and the local field in order to minimize the free energy.

Within a mean field approximation, the concentration profile $\phi(\mathbf{r})$ and local electric field E can be found by minimizing the free energy $F = \int f_b(\phi, T)\mathrm{d}^3 r + F_{es}$, with boundary conditions imposed by the electrode geometry. $f_b(\phi,T)$ is the free-energy density in the absence of electric field yielding the separation temperature $T_t(\phi)$ as shown in Fig. 1 (see Methods).

For arbitrary electrode geometry analytical solution is difficult. The 'wedge' geometry, consisting of two flat and planar tilted electrodes, is particularly simple and brings a useful insight (see Fig. 2a). Indeed, for any concentration profile $\phi(r)$ with azimuthal symmetry, the electric field $\mathbf{E}$ is perpendicular to $\nabla\varepsilon$ and in consequence the field $\mathbf{E}(\mathbf{r})$ is simply given by the solution of the Laplace equation $\nabla\cdot\mathbf{E} = 0$, namely, $E(r) = V/\theta r$, with V being the potential differences across the electrodes and θ the opening angle between them. This great simplification allows to find the composition profile $\phi(r)$ by solving the Euler–Lagrange equation $\delta f_b/\delta\phi - 1/2(\delta\varepsilon/\delta\phi)E^2(r) - \mu = 0$, with μ denoting the chemical potential. The analysis of this equation along classical lines[20] enables us to find the displacement ΔT of the transition temperature by the

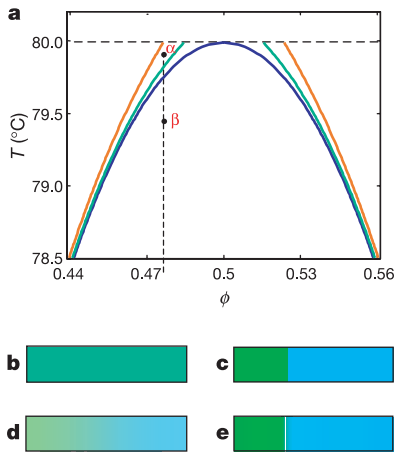

Figure 1 Phase diagram of a symmetric A/B liquid mixture. **a**, Transition temperature $T_t(\phi)$ in the absence of field (blue curve) and with a non-homogeneous field in the wedge geometry (ϕ is the fraction of A in the mixture). The green and red curves correspond to maximum fields of 8 and 15 V μm^{-1}, respectively. **b**, At point 'α' above T_t the mixture is homogeneous. **c**, At point 'β' below T_t the mixture phase separates. Green colour denotes B liquid, blue is A. **d**, Above T_t, a small field gradient induces a small concentration gradient. **e**, Above T_t, a large field gradient provokes phase separation. We used $\varepsilon_A - \varepsilon_B = 5$, $\partial^2\varepsilon/\partial\phi^2 = 5$, $v_0 = 3\times10^{-27}$ m^3 and scaled the critical temperature to be 80 °C.

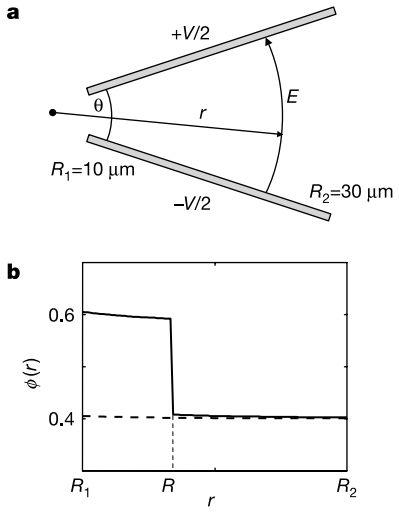

Figure 2 Wedge-shaped model system. **a**, The mixture is put between two flat electrodes with opening angle θ and potential difference V. Far from the edges, the field $E = V/\theta r$ is azimuthal. **b**, At points above the transition (for example, point 'α' of Fig. 1a) and for $\varepsilon_A > \varepsilon_B$, a small voltage V gives rise to a smoothly decaying profile $\phi(r)$, with high ϕ (large ε) at $r = R_1$ and low ϕ (small ε) at $r = R_2$, dashed curve. At the critical voltage V_c, the composition $\phi(R_1)$ becomes unstable. When $V > V_c$ a sharp transition is predicted between high- and low-ϕ regions, solid curve. $\phi(r)$ decays to the bulk average value at large r, here $\phi = 0.4$. We used a standard solution model for the bulk free energy f_b (see Methods section), $T = T_t + 0.2$ °C, $R_2 = 3R_1 = 30$ μm and other parameters as in Fig. 1.

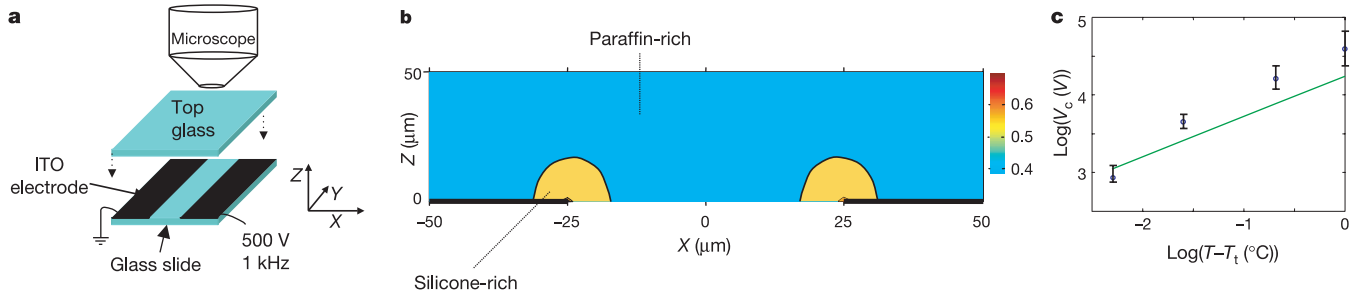

Figure 3 Phase separation with razor-blade electrodes. **a**, Two parts of the bottom glass substrate are coated with a conducting indium tin oxide layer, connected to opposite voltage terminals. The silicone/paraffin mixture between the substrate and the top glass is observed using an optical phase-contrast microscope. **b**, Predicted composition profile $\phi(r)$ in the $x - z$ plane numerically obtained for $V = 150$ V above the threshold. Black lines indicate the two flat electrodes. The silicone-rich phase appears close to the electrode edge, while the paraffin-rich phase is farther away. Here $\phi = 0.45$, $v_0 = 3 \times 10^{-27}\,\mathrm{m}^{-3}$ and $T - T_t = 0.2\,^{\circ}\mathrm{C}$. **c**, Plot of $V_c(T)$ for $T > T_t$. Straight green line (slope 0.5) is model calculation, while points are experimental values with best fit slope 0.7 ± 0.15. Error bars correspond to uncertainty in extrapolation in Fig. 4d.

above non-homogeneous field:

$$\Delta T \approx \frac{v_0}{k_B}\frac{1}{8\pi}\left|\frac{\varepsilon'}{\phi - \phi_c}\right|\left(\frac{V}{\theta R_1}\right)^2 \qquad (2)$$

Here k_B is the Boltzmann constant, v_0 the liquid molecular volume, ϕ_c the critical composition and $\varepsilon' \approx \varepsilon_A - \varepsilon_B$ the derivative of the dielectric constant $\varepsilon(\phi)$ with respect to composition taken at ϕ_c. In equation (2), $r = R_1$ is the position of the inner edge of the wedge (Fig. 2a) where the field is strongest. The transition temperature is thus shifted upwards in the phase diagram (field provokes demixing) and ΔT is proportional to ε' (Fig. 1a). The estimate, equation (2), is valid for compositions ϕ such that $T_t(\phi) + \Delta T \leq T_c$. At compositions ϕ closer to ϕ_c, phase separation occurs at the critical temperature T_c (or just slightly above it when the nonlinear dependence of ε on ϕ plays some role).

The change in T_t by non-uniform fields is large even for mixtures with a weak dielectric constant mismatch, $\varepsilon_A - \varepsilon_B \approx 1$. An estimate with voltage $V = 100$ V, small feature size $R_1 = 10\,\mu$m, $\theta = 1$ and $\phi = 0.4$ ($|\phi - \phi_c| \approx 0.1$) yields an upward shift of about $\Delta T \approx 0.2\,^{\circ}$C. Larger dielectric contrast ε' or smaller distance from the critical composition results in correspondingly larger ΔT.

The phase separation by a non-uniform field is much stronger than the effect of a uniform field. In a uniform field E_0, it can be shown within the same approximations that ΔT is given by $\Delta T \approx \frac{1}{16\pi}(v_0/k_B)\varepsilon'' E_0^2$ (ref. 1). This shift is proportional to the second derivative of dielectric constant with respect to the composition ε'' and relies on second-order coupling of electric field and composition variations. Typically $\varepsilon'' \approx \varepsilon'$, and the shift ΔT in uniform field is about 10 to 50 times smaller than that in non-uniform fields, equation (2). We recall, however, that experimentally for liquid mixtures uniform field causes mixing rather than phase separation.

A useful insight into field-induced separation is gained by analysing the evolution of the composition profile for the wedge electrode geometry. When $\varepsilon' = \varepsilon_A - \varepsilon_B > 0$ and for low voltage V, the composition $\phi(R_1)$ at the inner edge is higher than $\phi(R_2)$ at the outer edge, and the profile $\phi(r)$ is a smoothly decaying function of r (Fig. 2b, dashed curve). However, at a given temperature $T \leq T_c$, there exists a threshold voltage V_c where the behaviour changes markedly. Referring to Fig. 1, the composition $\phi(R_1)$ becomes unstable when it crosses the transition curve $T_t(\phi)$, and separation occurs. An interface between A-rich (high ε) and B-rich (low ε) regions appears at $r = R$ (Fig. 2b, solid curve). The concentration profile then exhibits a sharp jump even though the field, $E(r) = V/\theta r$, still varies smoothly. When the voltage difference V increases, the interface moves towards the outer edge. From equation (2), the critical voltage V_c necessary to produce phase separation scales as $V_c \approx (T - T_t)^{1/2}$.

To test the above predictions, we used the experimental set-up shown in Fig. 3a. We chose to work with razor-shaped electrodes with sharp edges in order to take advantage of the large field gradients present in such a geometry. Figure 3b shows typical concentration profiles calculated by numerical minimization of the total free energy for voltage above the threshold. Two interfaces parallel to each electrode should appear in the region close to the electrode edge. Raising the field (voltage) should displace the interfaces farther from the electrode edge, and should also increase the composition difference between coexisting phases. Lowering the temperature towards T_t while keeping the voltage fixed has a similar effect. As shown in Fig. 3c the threshold voltage V_c and the field at the electrode tips are expected to be low (below the dielectric breakdown) even for temperatures well above T_t.

We worked with two liquid pairs: a mixture of an aromatic silicone oil (polymethylphenylsiloxane) and a low-molecular-mass

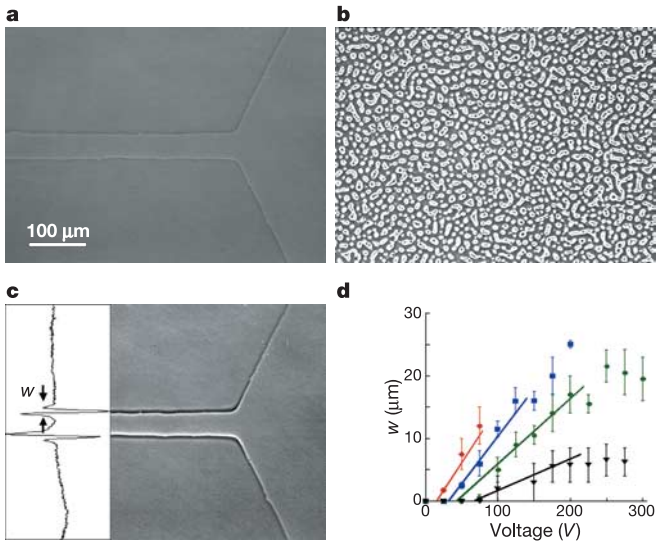

Figure 4 Temperature and voltage dependence of phase separation. **a**, The mixture is in the homogeneous state at $T = T_t + 0.1\,^{\circ}$C, and no voltage is applied. **b**, At $T = T_t - 0.3\,^{\circ}$C, isotropic phase separation occurs, in which drops begin to grow until macro-phase separation. **c**, At $T = T_t + 0.2\,^{\circ}$C and $V = 200$ V, a silicone-rich channel appears along the electrode edges. **d**, Width w of silicone-rich phase close to the edge of the electrodes, plotted as a function of applied voltage V, for temperatures 0.1 (diamonds), 0.3 (squares), 0.5 (circles) and 1 (triangles) °C above T_t. Symbols are experimental data, while solid lines are results of numerical calculation (see Methods section). Error bars correspond to the scatter of three different measurements.

paraffin oil (squalane), and a mixture of low-molecular-mass polydimethylsiloxane and polyisobutylene. We chose these systems because they are non-volatile, non-polar and have a good electric breakdown resistance. We were able to observe electric field induced demixing in both systems despite their modest dielectric constant mismatch.

Below T_t, phase separation is visible across the whole specimen (Fig. 4b). There is no preferential nucleation or wetting at the electrodes. Experiments with the electric field were performed at temperatures above T_t, namely $T - T_t = 0.1$, 0.3, 0.5 and 1 °C. The influence of heating due to dielectric losses and conduction of residual ions was verified to be negligible at the working frequencies. Moreover, heating increases the temperature and opposes demixing.

Phase separation occurs immediately after the electric field is switched on, and interfaces parallel to the electrodes appear (Fig. 4c). Demixing patterns typically evolve over 1 minute, after which a channel of the silicone-rich phase (more polar liquid) is formed along the electrodes' boundaries. This nicely agrees with the numerical calculation for this electrode geometry. When the voltage is switched off, the mixture returns back to its homogeneous state in 4–5 min (Fig. 4a). The phase separation process is reversible and can be repeated many times. The universal character of field induced separation is confirmed by investigations of mixtures of polydimethylsiloxane and polyisobutylene and using different electrode spacing.

The width w of the silicone domain close to the electrode edge increases when the applied voltage is increased or when temperature is reduced closer to T_t. Figure 4d shows a plot of w as a function of V at four temperatures. There is a good agreement between the experimental points and the values obtained by numerically minimizing the free-energy functional. The theoretical and experimental critical voltages V_c, obtained from the extrapolation of each curve to the $w = 0$ axis, also agree reasonably well (Fig. 3c).

The phase separation by non-uniform electric fields is robust and, as indicated by equation (2), can be used on many liquid mixtures well below dielectric breakdown. This complements nicely the gradient field induced phase transitions in colloidal suspensions[21,22] and ferrofluids[23]. Various microfluidic or micro-electromechanical devices could benefit from this effect. For example, a mixture of several components flowing down a channel could be separated and sent off in different channels. Such a separation could provide a new way to reversibly coat the walls of the channel with a preferred chemical species and efficiently control lubrication. Chemically reactive systems could benefit as well, because active species could be isolated from each other or brought together by the electric field, thus achieving better control of reaction kinetics. Phase separation could be also employed to create reversible electro-optic effects in light guiding, scattering, and so on. In this work, non-uniform fields were created by conducting electrodes. Use of holographic optical tweezers techniques[24,25] may open a new field of applications, such as patterning and writing. In all these applications, the reversibility of the process and the dependence on field intensity is a boon. □

Methods

Experimental

Polymethylphenylsiloxane (CAS number: 9005-12-3, Gelest PMM-0025), with a mass average molecular weight of 3,000 g mol^{-1} and a polydispersity index of 2.4, and squalane (CAS number: 111-01-3, purity: 99.8%) were used without further purification. Transparent indium tin oxide (ITO) electrodes 25 nm thick (surface resistivity: 120 Ω per square) were coated on the substrate glass using Shipley SJR 5740 photoresist and HCl/HNO_3 as etchant. Observation cells were made up of the ITO-treated substrate covered with a top glass layer. The temperature was regulated using a Mettler FP80 hot stage, and checked to be stable within ±0.03 °C using a Pt100 probe. Before experiments, the thickness of the empty cell was measured by varying the focus of the microscope. The mixtures were heated about 20 °C above their cloud point temperature before being put in the cell. The cloud point of each specimen was carefully measured through cooling cycles of −1 °C min^{-1} and −0.1 °C min^{-1}.

The high-voltage 1 kHz a.c. source was built from a Sefram 4430 signal generator fitted with an 18 W audio amplifier and a standard 12 V car-engine coil. Optical observations were carried out in phase contrast mode using a Leica DMRD microscope equipped with a filtered (transmission maximum at 544 nm) incandescent source and Fluotar 10 × 0.30 objective. Images were digitized using a JVC 3CCD camera and Eurocard Picolo video board. The width w of the silicone-rich phase near the electrodes was measured from the series of light intensity fringes in the phase contrast image, as defined in the inset of Fig. 4c.

Theoretical

The numerical calculation used in Fig. 2b, Fig. 3b and c, and Fig. 4d is obtained from a variational principle of the total free energy $F = F_b + F_{es}$ with respect to the local concentration ϕ and field E:

$$\frac{\delta f_b(\phi)}{\delta \phi} - \frac{1}{2}\frac{\delta \varepsilon}{\delta \phi}\mathbf{E}^2 - \mu = 0 \quad (3a)$$

$$\nabla\cdot(\varepsilon\mathbf{E}) = 0 \quad (3b)$$

where μ is the chemical potential. The bulk free-energy density f_b is given by a Landau expansion of a standard mean-field symmetric solution model around the critical point[20,26], $\frac{v_0}{k_B T} f_b = \frac{1}{2}\frac{T-T_c}{T_c}\left(\phi - \frac{1}{2}\right)^2 + \frac{4}{3}\left(\phi - \frac{1}{2}\right)^4$, where k_B is the Botlzmann constant, v_0 is the molecular volume, T_c is the critical temperature and $\phi = 1/2$ is the critical composition. Solutions to equations (3a) and (3b) were obtained by a combination of a standard matrix inversion method for the Laplace equation and an iterative gradient scheme for the concentration profile equation.

Received 27 November 2003; accepted 14 June 2004; doi:10.1038/nature02758.

1. Landau, L. D. & Lifshitz, E. M. *Elektrodinamika Sploshnykh Sred* Ch. II, Sect. 18, problem 1 (Nauka, Moscow, 1957).
2. Greer, S. C., Block, T. E. & Knobler, C. M. Concentration gradients in nitroethane+3-methylpentane near the liquid-liquid critical solution point. *Phys. Rev. Lett.* **34,** 250–253 (1975).
3. Moldover, M. R., Sengers, J. V., Gammon, R. V. & Hocken, R. J. Gravity effects in fluids near gas-liquid critical point. *Rev. Mod. Phys.* **51,** 79–99 (1979).
4. Debye, P. & Kleboth, K. Electrical field effect on the critical opalescence. *J. Chem. Phys.* **42,** 3155–3162 (1965).
5. Early, M. D. Dielectric constant measurements near the critical point of cyclohexane-aniline. *J. Chem. Phys.* **96,** 641–647 (1992).
6. Wirtz, D. & Fuller, G. G. Phase transitions induced by electric fields in near-critical polymer solutions. *Phys. Rev. Lett.* **71,** 2236–2239 (1993).
7. Orzechowski, K. Electric field effect on the upper critical solution temperature. *Chem. Phys.* **240,** 275–281 (1999).
8. Rowlinson, J. S. & Swinton, F. S. *Liquids and Liquid Mixtures* (Butterworths, London, 1982).
9. Sengers, J. V., Bedeaux, D., Mazur, P. & Greer, S. C. Behavior of the dielectric constant of fluids near a critical point. *Physica. A* **104,** 573–594 (1980).
10. Amundson, K., Helfand, E., Quan, X. N., Hudson, S. D. & Smith, S. D. Alignment of lamellar block-copolymer microstructure in an electric-field. 2. Mechanisms of alignment. *Macromolecules* **27,** 6559–6570 (1994).
11. Onuki, A. Electric-field effects in fluids near the critical point. *Europhys. Lett.* **29,** 611–616 (1995).
12. Pohl, H. A. *Dielectrophoresis* (Cambridge Univ. Press, Cambridge, UK, 1978).
13. Christen, T. Homogenization of nonuniform electric fields in mixtures of liquid dielectrics. *Appl. Phys. Lett.* **76,** 230–232 (2000).
14. Melcher, J. R. & Taylor, G. I. Electrohydrodynamics—A review of the role of interfacial shear stresses. *Annu. Rev. Fluid Mech.* **1,** 111–146 (1969).
15. Schäffer, E., Thurn-Albrecht, T., Russell, T. P. & Steiner, U. Electrically induced structure formation and pattern transfer. *Nature* **403,** 874–877 (2000).
16. Tsori, Y. & Andelman, D. Thin film diblock copolymers in electric field: Transition from perpendicular to parallel lamellae. *Macromolecules* **35,** 5161–5170 (2002).
17. Berge, B. & Peseux, J. Variable focal lens controlled by an external voltage: An application of electrowetting. *Eur. Phys. J. E* **3,** 159–163 (2000).
18. Comiskey, B., Albert, J. D., Yoshizawa, H. & Jacobson, J. An electrophoretic ink for all-printed reflective electronic displays. *Nature* **394,** 253–255 (1998).
19. Pollack, M. G., Fair, R. B. & Shenderov, A. D. Electrowetting-based actuation of liquid droplets for microfluidic applications. *Appl. Phys. Lett.* **77,** 1725–1726 (2000).
20. Lifshitz, E. M. & Landau, L. D. *Statistical Physics* 2nd edn (Butterworth-Heinemann, New York, 1980).
21. Khusid, B. & Acrivos, A. Effects of interparticle electric interactions on dielectrophoresis in colloidal suspensions. *Phys. Rev. E* **54,** 5428–5435 (1996).
22. Kumar, A., Qiu, Z., Acrivos, A., Khusid, B. & Jacqmin, D. Combined negative dielectrophoresis and phase separation in nondilute suspensions subject to a high-gradient ac electric field. *Phys. Rev. E* **69,** 021402 (2004).
23. Rosensweig, R. E. *Ferrohydrodynamics* (Dover, New York, 1998).
24. Korda, P. T., Taylor, M. B. & Grier, D. G. Kinetically locked-in colloidal transport in an array of optical tweezers. *Phys. Rev. Lett.* **89,** 128301 (2002).
25. Grier, D. G. A revolution in optical manipulation. *Nature* **424,** 810–816 (2003).
26. De Gennes, P. G. *Scaling Concepts in Polymer Physics* (Cornell Univ. Press, Ithaca, New York, 1979).

Supplementary Information accompanies the paper on **www.nature.com/nature**

Acknowledgements We thank D. Andelman and P. G. de Gennes for discussions and suggestions, and R. Bonnecaze and A.-V. Ruzette for comments on the manuscript. We gratefully acknowledge support from ATOFINA.

Competing interests statement The authors declare that they have no competing financial interests.

Correspondence and requests for materials should be addressed to L.L. (Ludwik.leibler@espci.fr).